Current Natural Sciences

Junfang TIAN and Rui JIANG

Car Following Dynamics: Experiments and Models

SCIENCE PRESS
edp sciences

Printed in France

EDP Sciences – ISBN(print): 978-2-7598-3193-7 – ISBN(ebook): 978-2-7598-3194-4
DOI: 10.1051/978-2-7598-3193-7

All rights relative to translation, adaptation and reproduction by any means whatsoever are reserved, worldwide. In accordance with the terms of paragraphs 2 and 3 of Article 41 of the French Act dated March 11, 1957, “copies or reproductions reserved strictly for private use and not intended for collective use” and, on the other hand, analyses and short quotations for example or illustrative purposes, are allowed. Otherwise, “any representation or reproduction – whether in full or in part – without the consent of the author or of his successors or assigns, is unlawful” (Article 40, paragraph 1). Any representation or reproduction, by any means whatsoever, will therefore be deemed an infringement of copyright punishable under Articles 425 and following of the French Penal Code.

The printed edition is not for sale in Chinese mainland.

© Science Press, EDP Sciences, 2023

Preface

The development of traffic flow studies has been almost 90 years since the publication of the seminal Greenshields model. Many traffic phenomena, such as traffic breakdown, traffic oscillations, and hysteresis, have been observed. Hundreds of traffic flow models have been developed to explain and simulate the observations. Some models have been successfully used in transportation engineering applications. However, despite the achievements, the evolution mechanism of traffic flow has not been fully understood, and controversies exist in traffic flow theories. As a consensus, this is largely due to the lack of large-scale high-fidelity traffic data without gaps in information.

The traditional way to collect traffic flow data comes by observing traffic flow passively. Such data have great limitations because the traffic flow is uncontrollable. Moreover, the empirical observations are quite site-specific and contain many confounding factors. On the other hand, *via* traffic experiments, one can control the traffic flow composition and flow rate, reduce the interference of complex factors, and expect to discover the essential characteristics and mechanism of traffic flow evolution.

The complexity of traffic flow evolution is mainly from a car following dynamics and lane-changing behavior. This book offers an account of the car's following dynamics, from the aspect of experiment as well as modeling. The context has been documented in specialized scientific papers, and we hope it can be accessed by a broader readership.

This book consists of six chapters. Chapter 1 is an introduction to the state-of-the-art of traffic flow studies, chapter 2 mainly presents experimental findings of traffic oscillations. Chapter 3 analyzes the car following behaviors. Chapter 4 presents the cellular automaton models and chapter 5 presents the car following models. Finally, the conclusion and outlook are given in chapter 6.

The book is expected to serve as a reference guide on issues of traffic flow studies for students, lecturers, and professionals of engineering and transportation sciences.

DOI: 10.1051/978-2-7598-3193-7.c901
© Science Press, EDP Sciences, 2023

Many people have contributed to the development of the book. We would like to thank Prof. Z. Y. Gao, Prof. S. F. Ma, Prof. H. M. Zhang, Prof. Q. S. Wu, Prof. B. Jia, Prof. M. Treiber, Prof. B. S. Kerner, Prof. X. P. Li, Dr. D. J. Chen, Dr. G. Y. Wang, Dr. M. B. Hu, Prof. T. Wang, Prof. M. Yang, Dr. B. Wang, Dr. S. T. Zheng, Mr. S. R. Zhou, Dr. C. Q. Zhu, Mr. L. D. Gao, Mr. Z. H. Li, Dr. N. Guo, Dr. M. M. Guo, Dr. L. Li, for the scientific discussions and stimulation, and carrying out of the experiments.

This work is supported by the National Natural Science Foundation of China (Grant No. 72222021, 72010107004, 72288101, 71931002).

Contents

Preface III

CHAPTER 1
Introduction 1

1.1 Background 1
1.2 Traffic Flow Data 3
  1.2.1 Vehicle Trajectory Data 3
  1.2.2 Detector Data 3
1.3 Traffic Flow Parameters 5
  1.3.1 Flow Rate 5
  1.3.2 Density and Occupancy 5
  1.3.3 Speed 5
1.4 Fundamental Diagram 6
  1.4.1 Homogeneous, Stationary and Equilibrium Traffic Flow 6
  1.4.2 The Fundamental Diagram 6
  1.4.3 Some Common Fundamental Diagram Models 8
1.5 The Characteristics of Traffic Flow Evolution 12
  1.5.1 Congested Traffic and Phantom Jam 12
  1.5.2 Synchronized Traffic Flow 13
  1.5.3 Traffic Breakdown 14
1.6 Outline of the Book 15
References 16

CHAPTER 2
Traffic Oscillation Analysis 19

2.1 Some Previously Observed Results of Traffic Oscillations 19
2.2 The Platoon Experiments with 25 Cars 20
  2.2.1 Experimental Setup 20
  2.2.2 Spatiotemporal Features 21
  2.2.3 The Concave Growth Patterns 21
2.3 Traffic Oscillation Simulations by Traditional Models 23
  2.3.1 Traditional Models 23

2.3.2 The Initial Convex Growth Pattern in Traditional Models 28
2.4 Empirical Oscillation Analysis 31
2.5 The Platoon Experiment with 50 Cars 37
2.5.1 Experimental Results 39
2.5.2 Corroborating Empirical Observations 44
2.6 The High-Speed Experiment 48
2.6.1 Experimental Setup 48
2.6.2 Experimental Results 50
2.7 The Lightly Congested Flow Experiment 51
2.7.1 Experimental Setup 51
2.7.2 Experimental Results 52
References 58

CHAPTER 3
Car Following Behavior Analysis 61

3.1 The Velocity Distribution Analysis 61
3.2 The Spacing Analysis 61
3.3 The Platoon Length Analysis 65
3.4 The Acceleration Analysis 69
3.5 The Wave Travel Time Analysis 76
3.5.1 Some Observed Features of $\tilde{\tau}_n(t)$ Time Series 79
3.5.2 New Experimental Data Analysis 85
3.6 Indifference Region Analysis 86
3.7 Sensitivity Factor Analysis in Car Following 89
3.8 Stochasticity Factor Analysis in Car Following 91
3.9 Analysis of Competition Between Stochastic and Speed Adaptation Effects 92
References 95

CHAPTER 4
Cellular Automaton Models 97

4.1 The Basic CA Models 97
4.1.1 The NaSch Model 97
4.1.2 The Slow-To-Start Model 99
4.1.3 The Kerner-Klenov-Wolf Model for Synchronized Traffic Flow . . 101
4.2 The Generalized NaSch Models 104
4.2.1 The Comfortable Driving Model and Its Variants 104
4.2.2 Two-State Model and Its Improved Version 109
References 116

CHAPTER 5
Car Following Models 119

5.1 The Extensions of Traditional Models 119
5.2 The Insensitivity Model 120

5.3 The Speed Adaption Model . . . 123
5.4 The Variants of Newell Model . . . 129
  5.4.1 Empirical Congested Pattern Simulation . . . 131
  5.4.2 Vehicle Trajectory Simulation . . . 132
  5.4.3 Platoon Oscillation Simulation . . . 133
5.5 The Improved 2D-ID Model . . . 136
5.6 The E2D-ID Model . . . 140
References . . . 143
Appendix . . . 144

CHAPTER 6

Outlook . . . 147

Chapter 1

Introduction

From the bird's-eye view, the movements of vehicles on the road have fluidity as gas or liquid, thus it is named the traffic flow, which can be characterized by flow, speed, density, etc. Due to the complexity of traffic flow, its evolution mechanism is still not clear. In this chapter, the motivation for traffic flow experiments is discussed. Then two typical types of data used in traffic flow studies, *i.e.*, the vehicle trajectory data and the detector data, are introduced. The fundamental parameters of traffic flow and the fundamental diagram are also introduced. Finally, the empirical characteristics of traffic flow evolution are explained, including congested traffic, phantom jam, synchronized traffic flow and traffic breakdown.

1.1 Background

Traffic congestion has become a worldwide problem, especially in China, due to the process of fast urbanization. It is not sustainable to mitigate traffic congestion *via* increasing transport infrastructure. Scientific theories should be established to improve the operation efficiency of transportation facilities.

Traffic flow theory studies the travel behavior of traffic participants and the spatiotemporal evolution of traffic flow. Based on traffic flow data analysis, this theory describes the characteristics and phenomena of traffic flow, and establishes models which could simulate and predict spatiotemporal patterns of traffic flow. Finally, these models will be used for practical traffic management and control, which aims to provide solutions to alleviate traffic congestion.

With the development of traffic flow studies, some nonlinear dynamics characteristics of traffic flow have been discovered. However, the evolution mechanism of traffic flow has not been fully understood. In particular, the three-phase traffic theory and the fundamental diagram theory are highly controversial. For example, Schönhof and Helbing (2009) published a paper titled "Criticism of three-phase traffic theory", and Kerner (2013) published a paper titled "Criticism of generally accepted fundamentals and methodologies of traffic and transportation theory–A brief review".

It's worth mentioning that in both theories, the sophisticated evolution of traffic flow is closely related to the instability or metastability of traffic flow. In contrast, in

DOI: 10.1051/978-2-7598-3193-7.c001
© Science Press, EDP Sciences, 2023

LWR theory, the sophisticated evolution of traffic flow is usually attributed to "geometric constraint", *i.e.*, different external bottlenecks.

The main difficulty to resolve this controversy is a lack of high-fidelity traffic data that covers congestion from its birth to its death without gaps in information. Most of the data are currently available are collected by point sensors (*e.g.*, loop detectors), and the distance between two neighboring sensors is usually 1–3 km for most freeway sections showing recurrent congestion patterns. As claimed by Treiber *et al.* (2010), "*this is of the same order of magnitude as typical wavelengths of non-homogeneous congestion patterns*" and therefore definitely leads to a loss of information pertaining to the finer features of traffic flow. Daganzo *et al.* (1999) also pointed out that "*no empirical studies to date describe the complete evolution of a disturbance*" and thus we cannot "*explain the genesis of the disturbances or the rate at which they grow*".

The traffic science community has also realized the importance of precise traffic data. As Schönhof and Helbing (2009) claimed, "*In order to finally decide which traffic model provides the best description and what is the true cause of the spatiotemporal organization of the general pattern, it is necessary to have spatiotemporal data of single vehicles ... they will be needed to shed more light on the oldest and most central question of traffic theory, namely what are the real mechanisms and quantitative properties of traffic breakdowns.*"

Studies of this kind could be expensive and technologically challenging. For example, Knoop *et al.* (2008) collected empirical data from a helicopter, using a digital camera to gather high-resolution monochrome images. However, the images cover only 280 m of the motorway and due to the limited stability of the helicopter, only 210 m of the motorway could be used for vehicle detection and tracking. Similarly, the NGSIM data cover only several hundred meters of the highway, which is also very limited.

The traditional way of collecting traffic flow data comes by observing traffic flow passively. Such data have great limitations because the traffic flow is uncontrollable. A common way to test traffic flow models is to examine the spatiotemporal patterns induced by an isolated bottleneck by tuning the bottleneck strength and inflow rate. However, in practice, it is not easy to find an isolated bottleneck. Moreover, neither the bottleneck strength nor the inflow rate can be controlled.

Moreover, the empirical observations *via* cameras are quite site-specific and contain many confounding factors (*e.g.*, geometry such as on-ramps, off-ramps, and weaving area, bottleneck strength, traffic flow composition), which makes it difficult to isolate the dynamical behavior of car-following from those of lane-changing and other interactions. As a result, although there are vast amounts of empirical data, we are unfortunately still unable to understand how traffic dynamics evolve even in very simple scenarios.

Due to the limit of traffic observations, traffic experiments have attracted the interest of researchers. *Via* traffic experiments, one can control the traffic flow composition and flow rate, reduce the interference of complex factors, and extract the essential factors for traffic breakdown, *e.g.*, by performing the experiment near an isolated traffic bottleneck. Thus, one can expect to discover the essential characteristics of traffic flow evolution.

For example, Japanese researchers have conducted several controlled traffic flow experiments on circular roads (Sugiyama *et al.*, 2008). The result shows that even in a circular road without bottlenecks, congestion may occur spontaneously. Their research demonstrates the important role of experimental methods in the study of traffic flow evolution.[1]

We would also like to point out that experimental methods play an important role in complex system research. For example, in the studies of pedestrian flow and the group behavior of animals like ants, experimental methods are broadly applied, which promotes the development of this research.

1.2 Traffic Flow Data

1.2.1 Vehicle Trajectory Data

On the plane, (t, x) or (x, t), vehicle trajectory is the curve representing the corresponding relationship between time t and vehicle position $x(t)$. In general, the trajectory only describes the longitudinal motion of the vehicle and does not contain information about the lateral position and direction of the vehicle. From the vehicle trajectory diagram, not only can we obtain the microscopic information, such as time headway, distance headway and speed, but also can get the macroscopic information of traffic flow operation, such as volume, density, and roadway occupancy rate. For example, the first derivative of the trajectory yields the velocity of the vehicle ($v = dx/dt$), and the second derivative yields the acceleration of the vehicle ($a = d^2x/dt^2$). As shown in figure 1.1, a blue curve shows a vehicle moving forward, stopping for some time, and then moving on. Figure 1.1 shows that the traffic jam gradually forms and propagates upstream. The propagation speed w of the jam can also be identified.

1.2.2 Detector Data

Detector data are usually collected by loop detectors at a fixed location on the road, which are one of the earliest and most proven detection technologies. When a vehicle passes the loop, the vehicle causes a change in the inductance of the signal, so that the arrival and departure of the vehicle can be detected, see figure 1.2.

The detector can directly measure the following variables:

(1) The moment when the front bumper of the vehicle passes the detector $t = t_1$;
(2) The moment when the rear bumper of the vehicle passes the detector $t = t_2$.

---

[1] Note that as early as in the 1950's, Chandler *et al.* (1958) conducted the car-following experiment, aiming to calibrate the parameters of car-following model and evaluate the model performance.

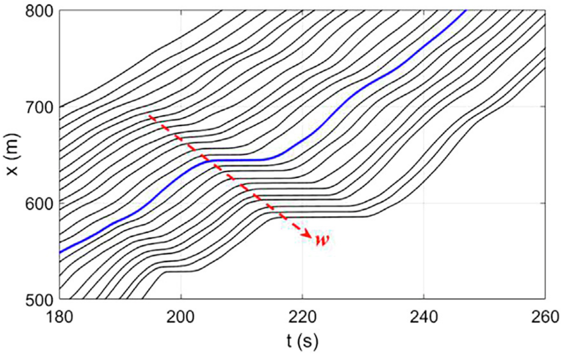

FIG. 1.1 – Vehicle trajectory.

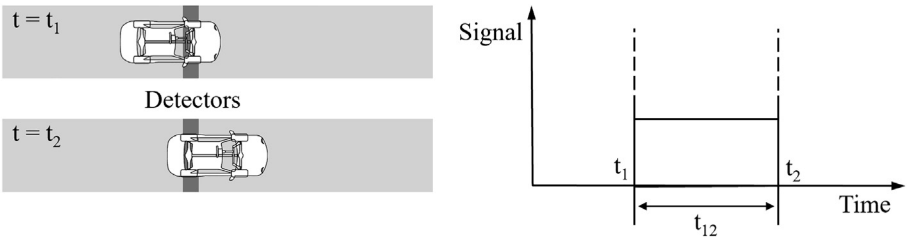

FIG. 1.2 – The illustrations of the loop detector.

It is impossible to obtain important information such as vehicle speed through only one detector, so the double-detectors are often used as a group on the road, and the distance between the two detectors is very close, such as 1 m. Assuming the vehicle moves with constant speed between the two detectors, the vehicle speed v can be calculated based on the time difference of the vehicle passing the two detectors. Based on these variables, the following variables can also be calculated:

(1) Vehicle length l_{veh}: $l_{\text{veh}} = v(t_2 - t_1)$.
(2) Vehicle type: vehicle type can be determined by vehicle length.
(3) Time headway (h): the time difference between the front bumper of two consecutive vehicles arriving at the detector.
(4) Time gap (g): the time difference between the rear bumper of the leading vehicle and the front bumper of the following vehicle.
(5) Space headway (s): the distance between the front bumper of two consecutive vehicles, $s = vh$.
(6) Space gap (d): the distance between the rear bumper of the leading vehicle and the front bumper of the following vehicle, that is space headway minus the length of the front vehicle, $d = s - l_{\text{veh}}$. The calculation of vehicle length, headway, and vehicle spacing assumes that vehicles move with constant speed.

1.3 Traffic Flow Parameters

Flow rate q, speed v and density ρ are the three basic parameters that characterize the macroscopic characteristics of traffic flow.

1.3.1 Flow Rate

(1) Flow rate q: the number of vehicles passing a fixed location on the roadway in unit time,

$$q = \frac{N}{T} \tag{1.1}$$

where T is the observation time interval and N is the number of vehicles passing the location during the interval.

According to the definition of headway, the observation interval T is equal to the sum of the time headways of all vehicles passing during this period, that is $T = \sum_{i=1}^{N} h_i$. Therefore, the flow rate can also be formulated as follows:

$$q = \frac{N}{T} = \frac{N}{\sum_{i=1}^{N} h_i} = \frac{1}{\frac{1}{N}\sum_{i=1}^{N} h_i} = \frac{1}{h} \tag{1.2}$$

where h is the meantime headway.

1.3.2 Density and Occupancy

Density (ρ) is the number of vehicles in a unit length of roadway.

$$\rho = \frac{N}{L} \tag{1.3}$$

where N and L mean the number of vehicles and length of the road section, respectively. Therefore, it is not possible to measure the density directly with detectors.

Occupancy is the ratio of time that vehicles occupy a detector to the observation time interval, which can be expressed as follow:

$$\text{occupancy} = \frac{\sum_{i=1}^{N} (L_i + l_{\text{det}}) \big/ v_i}{T} = \frac{1}{T}\sum_{i=1}^{N}\frac{L_i}{v_i} + \frac{l_{\text{det}}}{T}\sum_{i=1}^{N}\frac{1}{v_i} \tag{1.4}$$

where v_i and L_i are the speed and length of the vehicle i respectively, l_{det} is the size of the detector.

1.3.3 Speed

As mentioned before, speed is the first derivative of the trajectory

$$v = \frac{dx}{dt} = \lim_{(t_2 - t_1)\to 0} \frac{x_2 - x_1}{t_2 - t_1} \tag{1.5}$$

where t_1 and t_2 are two consecutive measurement times, x_1 and x_2 are the positions of the vehicle at time t_1 and t_2 respectively.

In practical applications, the average vehicle speed is widely used. There are two commonly used methods to calculate average vehicle speed: arithmetic average and harmonic average.

(1) Arithmetic average method: average vehicle speed is calculated as follows:

$$\overline{v}_t = \frac{1}{N}\sum_{i=1}^{N} v_i \tag{1.6}$$

where v_i is the speed of vehicle i.

However, this method has a deficiency. Since we calculate traffic density *via* $\rho = q/\overline{v}_t$, the high density is usually underestimated. This is because the arithmetic average method gives the time average speed, while average speed in the relation $q = \rho\overline{v}$ refers to the space average speed.

(2) Harmonic average method: average vehicle speed is calculated as follows:

$$\overline{v}_s = \frac{1}{\frac{1}{N}\sum_{i=1}^{N}\frac{1}{v_i}} \tag{1.7}$$

As above mentioned, the traffic density can be obtained by the equation: $\rho = q/\overline{v}_s$. The attainable range of density calculated by the harmonic average method is much higher than that of the arithmetic average method. However, the harmonic average method also has the deficiency that it is highly sensitive to the measurement error of low speed.

1.4 Fundamental Diagram

1.4.1 Homogeneous, Stationary and Equilibrium Traffic Flow

In homogeneous traffic flow, the parameters (such as speed, density, flow rate, etc.) do not change with location. In stationary traffic flow, the characteristic parameters do not change with time. The homogeneous and stationary traffic flow is called the equilibrium traffic flow.

1.4.2 The Fundamental Diagram

In traffic flow theory, it is usually assumed that the three basic parameters of traffic flow in an equilibrium state have the following relationships:

1. $q = q(\rho)$
2. $v = v(\rho)$
3. $v = v(q)$

Among them, the relationship between flow rate and density is usually called a "Fundamental Diagram". It should be noted that these three relationships represent the same information, that is, one relationship can be inferred from the other two relationships. The three relationships are shown in figure 1.3.

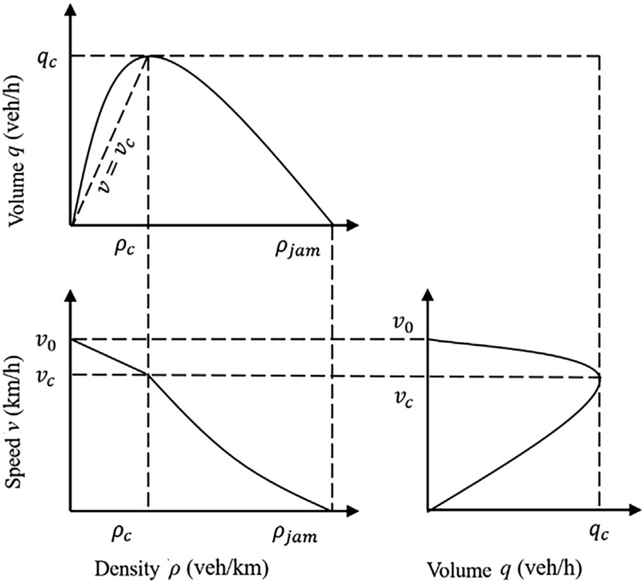

FIG. 1.3 – The relationship of q-v, q-ρ, ρ-v.

Some variables are included in figure 1.3, which are described as follows:

4. Free flow speed v_0; it is the average speed when density tends to zero and the vehicle can run unimpeded; it is equal to the slope of the function $q(\rho)$ at the origin;
5. Capacity q_c; it is the peak on the q-ρ curve, that is, the maximum flow rate;
6. Critical density ρ_c; it is the density at the maximum flow rate, that is, the density at $q = q_c$;
7. Critical speed v_c; it is the speed when the flow reaches the maximum, that is, the average speed when $q = q_c$;
8. Jam density ρ_{jam}; it is the density when the traffic flow is so dense that all vehicles are unable to move ($v = 0$), that is, the density when $v = 0$ and $q = 0$.

1.4.3 Some Common Fundamental Diagram Models

1.4.3.1 Greenshields Model

In 1935, Greenshields *et al.* (1935) proposed one of the oldest models in traffic flow theory. It is based on a simple assumption that the average speed decreases linearly with density. The equation is:

$$v(\rho) = v_0\left(1 - \frac{\rho}{\rho_{\text{jam}}}\right) \tag{1.8}$$

According to the flow-speed-density relationship, the function $q(\rho)$ can be obtained:

$$q(\rho) = \rho v_0\left(1 - \frac{\rho}{\rho_{\text{jam}}}\right) = \rho v_0 - \rho^2 v_0/\rho_{\text{jam}} \tag{1.9}$$

At the capacity, the critical value of ρ is

$$\frac{dq}{d\rho} = v_0 - 2\rho v_0/\rho_{\text{jam}} = 0 \Rightarrow \rho_c = \rho_{\text{jam}}/2 \tag{1.10}$$

Substituting the above equation into equation (1.8), the critical speed can be obtained:

$$v_c = v_0\left(1 - \rho_c/\rho_{\text{jam}}\right) = v_0/2 \tag{1.11}$$

Further, the capacity is:

$$q_c = \rho_c v_c = \frac{1}{4} v_0 \rho_{\text{jam}} \tag{1.12}$$

Substituting the relationship $\rho = q/v$ into equation (1.8), the relationship between flow rate and speed can be obtained:

$$v = v_0\left(1 - (q/v)/\rho_{\text{jam}}\right) \Rightarrow 1 - v/v_0 = (q/v)/\rho_{\text{jam}} \tag{1.13}$$

which can be formulated as

$$q(v) = v\rho_{\text{jam}} - \left(\rho_{\text{jam}}/v_0\right) v^2 \tag{1.14}$$

The three relationships are shown in figure 1.4.

1.4.3.2 Pipes-Munjal Model and Del Castillo-Bennitze Model

The Greenshield model is a concave smooth fundamental diagram model. The Pipes-Munjal model (Munjal and Pipes, 1971) and the Del Castillo-Bennitze model (Castillo and Benítez, 1995) are two other typical concave smooth fundamental diagram models. The fundamental diagrams are shown in figure 1.5. The speed-density relationship of the Pipes-Munjal model is:

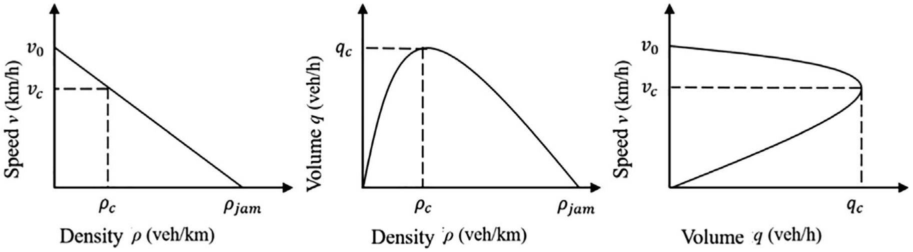

FIG. 1.4 – The q-v, q-ρ, ρ-v diagram of Greenshields model.

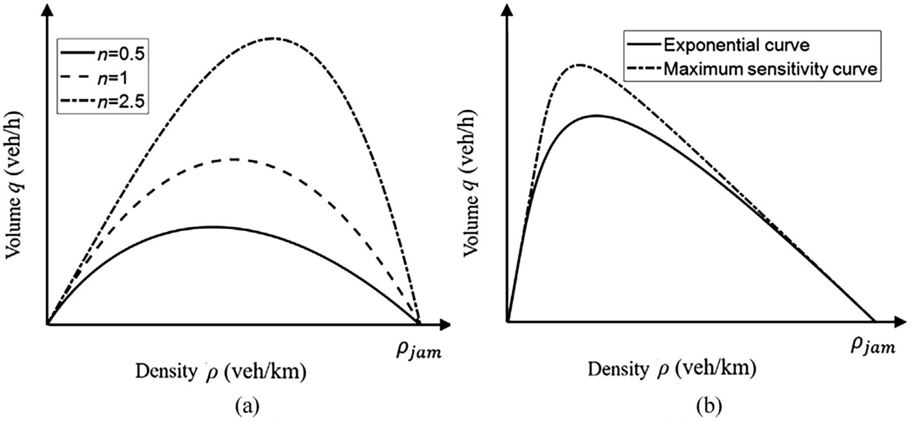

FIG. 1.5 – (a) The fundamental diagram of Pipes-Munjal model. (b) The fundamental diagram of Del Castillo-Bennitze model.

$$v = v_0 \cdot \left[1 - \left(\frac{\rho}{\rho_{\text{jam}}}\right)^n\right] \tag{1.15}$$

where n is a real number greater than 0. There are two speed-density relationships in the Del Castillo-Bennitze model

$$v = v_0 \cdot \left\{1 - \exp\left[\frac{C}{v_0} \cdot \left(1 - \frac{\rho_{\text{jam}}}{\rho}\right)\right]\right\} \text{(Exponential curve)} \tag{1.16a}$$

$$\text{or } v = v_0 \cdot \left\{1 - \exp\left[1 - \exp\left(\frac{C}{v_0} \cdot \left(\frac{\rho_{\text{jam}}}{\rho} - 1\right)\right)\right]\right\} \text{(Maximum sensitivity curve)} \tag{1.16b}$$

where C represents the propagation speed of the motion wave.

1.4.3.3 Triangular or Trapezoidal Fundamental Diagram Model

The cell transmission model often uses a triangular fundamental diagram, as shown in figure 1.6. The function of $q(\rho)$ is represented by two straight lines. The cell transmission model has three parameters: v_0, q_c (or ρ_c) and ρ_{jam}.

$$q(\rho) = \begin{cases} v_0\rho & \text{if } \ \rho \le \rho_c \text{ (free traffic)} \\ \omega\big(\rho_{\text{jam}} - \rho\big) & \text{if } \ \rho > \rho_c \text{ (congested traffic)} \end{cases} \tag{1.17}$$

where $\omega = \frac{q_c}{\rho_{\text{jam}} - \rho_c}$ represents the propagation speed of disturbance.

If the maximum flow limit is considered, the triangular fundamental diagram model is transformed into a trapezoidal fundamental diagram model.

$$q = \min\big\{v_0\rho,\, q_{\max},\, \omega(\rho_{\text{jam}} - \rho)\big\}, \quad 0 \le \rho \le \rho_{\text{jam}} \tag{1.18}$$

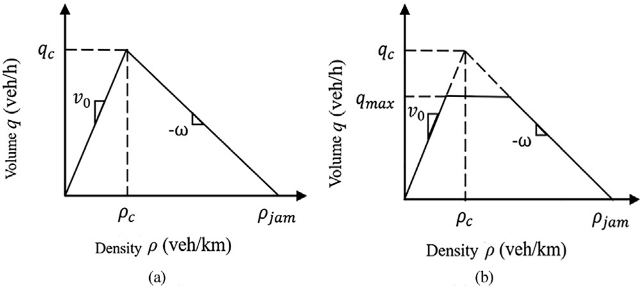

Fig. 1.6 – (a) Triangular fundamental diagram. (b) Trapezoidal fundamental diagram.

1.4.3.4 Fundamental Diagram Model with Inflection Point

In 1993, Kerner and Konhäuser (1993) first used the equilibrium speed-density function with inflection points to prevent the high-order macroscopic traffic flow model from producing traffic density exceeding the jam density. The fundamental diagram is shown in figure 1.7, and its speed-density relationship is

$$v(\rho) = v_0\left[\frac{1}{1 + \exp\left(\frac{\rho/\rho_{\text{jam}} - 0.25}{0.06}\right)} - 3.72 \times 10^{-6}\right] \tag{1.19}$$

In 1998, Lee *et al.* (1998) proposed another fundamental diagram with inflection point, see figure 1.8, whose equilibrium speed-density relationship is

$$v(\rho) = v_0\left(\frac{1 - \rho/\rho_{\text{jam}}}{1 + E\big(\rho/\rho_{\text{jam}}\big)^4}\right) \tag{1.20}$$

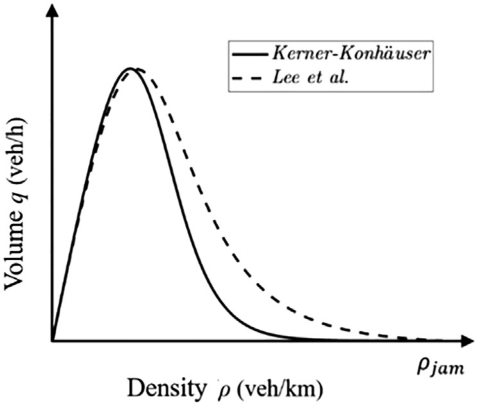

FIG. 1.7 – Fundamental diagram with inflection point.

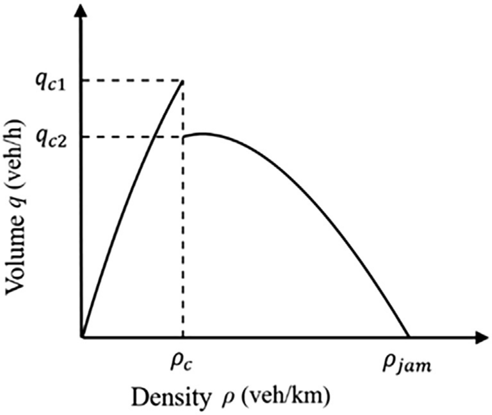

FIG. 1.8 – Example of discontinuous fundamental diagram.

1.4.3.5 Discontinuous Fundamental Diagram Model

Edie (1965) is the first researcher to point out that the fundamental diagram may be discontinuous near the capacity, *i.e.*, the capacity value corresponding to the free flow branch ("free flow capacity", q_{c1}) is higher than the capacity value corresponding to the congested state ("queue capacity" q_{c2}). Thus, there exists a "capacity drop".

$$q(\rho) = \begin{cases} 54.9\rho \cdot \exp(-\rho/163.9) & 0 < \rho \leq 50 \\ 26.8\rho \cdot \ln(162.5/\rho) & 50 < \rho \leq \rho_{\text{jam}} \end{cases} \tag{1.21}$$

1.5 The Characteristics of Traffic Flow Evolution

1.5.1 Congested Traffic and Phantom Jam

Traffic congestion is a very common traffic phenomenon, which is usually caused by traffic bottlenecks such as the on-ramp and off-ramp, lane drop, accidents and slowly moving vehicles. Traffic jam is the kind of congested traffic, in which vehicles move slowly or stop. "Phantom jam" means that the jam happens for unknown reasons. By analyzing a series of aerial photos of the multi-lane traffic flow, Treiterer (1975) presented the experimental evidence of spontaneous traffic jams, see figure 1.9, which shows the generation and propagation of traffic jams.

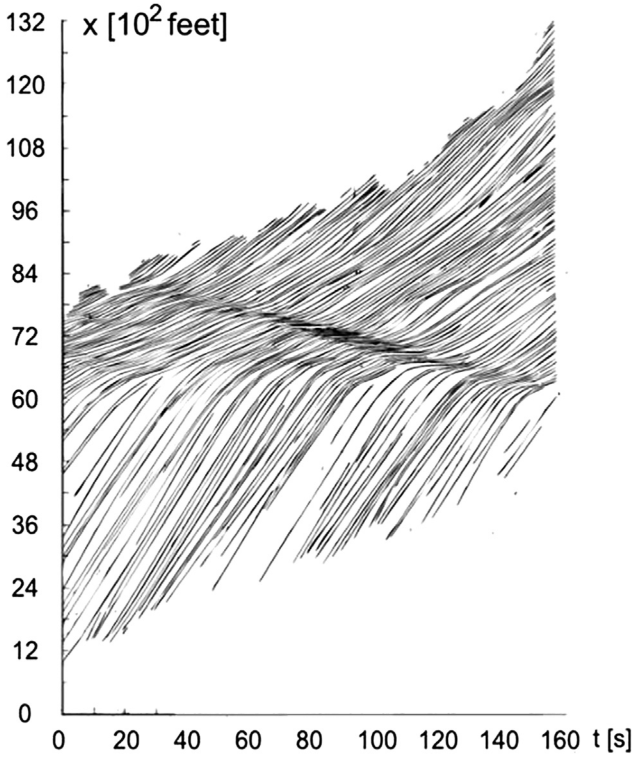

Fig. 1.9 – Vehicle trajectories are extracted from aerial images in Treiterer (1975).

1.5.2 Synchronized Traffic Flow

Based on long-term empirical data analysis, Kerner introduced the three-phase traffic theory (Kerner, 1998, 2004, 2009),[2] which classifies congested traffic into synchronized flow and jams. The synchronized flow is congested traffic without jams. In congested traffic flow, when the speed is not small (or the density is not large), the jam will not appear spontaneously. This "synchronized flow" is stable (see figure 1.10a). With the decrease in speed (or the increase of density), the synchronized flow becomes unstable and jam will appear spontaneously (see figure 1.10b). Apart from the USA, China, synchronized traffic flow has also been reported among different countries, such as in the UK (Rehborn *et al.*, 2011), Germany (Kaufmann *et al.*, 2018; Kerner, 2004; Kerner *et al.*, 2004)), Iran (Kouhi Esfahani *et al.*, 2019), and Singapore (Yang *et al.*, 2016).

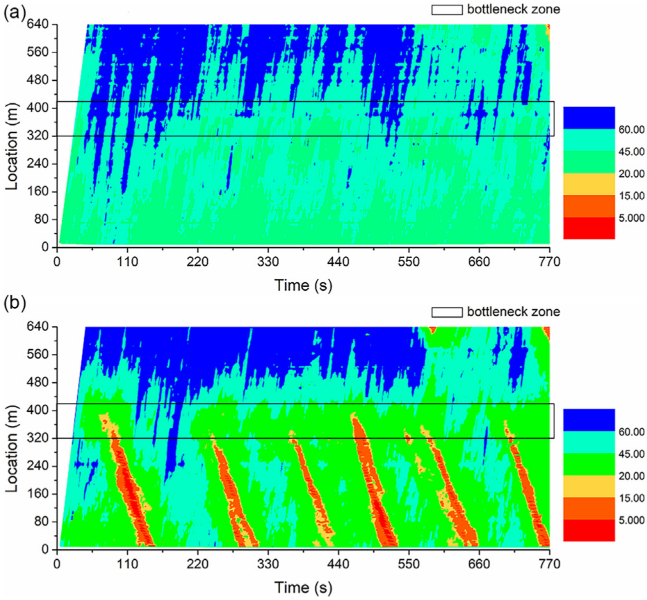

Fig. 1.10 – Spatiotemporal patterns of the velocity on (a) lane 1 (the leftmost lane) and (b) lane 4 from the NGSIM trajectory dataset collected on a 640 m-segment on southbound US 101. The color bar indicates speed (unit: km/h).

---

[2] We would like to mention that there is controversy about "three-phase traffic theory". However, the existence of synchronized flow is not controversial. For example, Schönhof and Helbing (2009) published a paper entitled "criticism of three-phase traffic theory", but Helbing *et al.* (2009) also showed the empirical data of synchronized flow.

Exploring the spatiotemporal characteristics of the synchronized flow shown in figure 1.10a is important, due to that: (1) From the application aspect, the dynamics of the boundaries of the state are different from that of traffic jams (because of the different flows and densities). When it comes to the application of car-following models in traffic management, the models are used to interpolate or extrapolate detector or floating-car observations to estimate the actual or near-future traffic state. Obviously, in order for the estimation to be unbiased, the propagation velocities of the transition fronts between the free flow, congested flow, and jams need to be described correctly; (2) From the congestion formation aspect, it indicates that depending on the bottleneck strength, there are two kinds of congested traffic states after traffic breakdown, *i.e.*, the stable synchronized flow and the unstable one out of which traffic jams emerge spontaneously. The inability of traffic flow simulation models to describe the stable congested traffic implies that jams emerge from unstable congested flow after traffic breakdown occurs, hence these models are not able to explain the traffic breakdown correctly; (3) From the theoretical viewpoint, clarifying the behavioral mechanism of the synchronized flow helps us to understand the complete spectrum of driving behaviors.

1.5.3 Traffic Breakdown

Traffic breakdown, *i.e.*, the onset of traffic congestion, is characterized by an abrupt decrease in speed, a sharp increase in density, and in particular a plummeting drop in capacity (Cassidy and Bertini, 1999; Agyemang-Duah and Hall, 1991). The identification of traffic breakdown can be traced back to the finding of the reverse-lambda-shaped structure of the flow-density data (Edie, 1961; Edie and Foote, 1958). The peak of the "lambda" represents the high free flow states, which are not stable and may rapidly drop into congested flow marked by the other leg of the "lambda" and thus cause traffic breakdown.

Many observations have shown that traffic breakdown happens at merges and lane drops, which are the flow non-conservation bottlenecks (*i.e.*, flow rate per lane differs significantly upstream and downstream of the bottleneck). Athol and Bullen (1973) suggested that the probability of the transition from uncongested to congested flow depends on the flow rate and that the expected time to break down is a declining function of flow. Lorenz and Elefteriadou (2001) made an extensive analysis of the speed and flow rate of more than 40 congestion events and confirmed that breakdown has a probabilistic nature and its occurrence probability increases with increasing flow rate.

Banks (1991) investigated four metered bottlenecks and discovered that the flow drop after the breakdown was of the order of 3 percent overall lanes when data were aggregated over 12 min before and after the breakdown. Hall and Agyemang-Duah (1991) found that the flow drop was of the order of 5–6 percent averaged across all lanes. The duration of this transition period ranged from 6 min to 31.5 min, with an average of 16 min and a median of 15 min. Cassidy and Bertini (1999) reported that the average flow rate after a breakdown can be 10% lower than the flow before a breakdown based on the observations from two freeway bottlenecks in and near

Toronto. Canada. As a result, the onset and dissolution of traffic breakdown are accompanied by a hysteresis effect on the flow-density diagram.[3]

Traffic breakdown also occurs at flow conservation bottlenecks. Koshi (1986) and Koshi *et al.* (1992) reported that some of the tunnels, vertical alignment sags, and S curves on Japanese motorways were recognized as bottlenecks and congestion queues were frequently observed. Speed reduction of vehicles in a platoon happened upstream of these bottlenecks. Related observations were also reported in other places or countries, see *e.g.*, Edie and Foote (1958), Newell (1959), Iwasaki (1991), Tadaki *et al.* (2002), Brilon and Bressler (2004).

In particular, traffic breakdown was also observed on single-lane roads. For example, Shiomi *et al.* (2011) reported a single-lane road breakdown, where the tunnel acts as the bottleneck. In these observations, a capacity drop was reported when a traffic breakdown occurs. Jin *et al.* (2013) analyzed the empirical vehicle platoon data on a single-lane highway section. They found that an abrupt speed drop can occur in the platoon when the speed of the platoon leader is quite high ($\sim$70 km/h), which illustrated that traffic breakdown may be the process in that free flow changes into synchronized flow on the single-lane road.

Based on the empirical data (Kerner, 1998, 2004, 2009; Kerner and Rehborn, 1996a, 1996b, 1997), Kerner claimed that traffic breakdown corresponds to the transition from free flow to synchronized flow (see figure 1.10a for an example) and the spontaneous formation of jams corresponds to the transition from synchronized flow to jams (see figure 1.10b for an example). The direct transition from free flow to jams seldom happens except that bottleneck strength is very strong (Kerner, 2000). Kerner also pointed out that traffic breakdown can be either spontaneous or induced. The latter is usually induced by the propagation of the congested traffic flow that occurred earlier at a downstream road location.

1.6 Outline of the Book

The following contents of the book consist of four chapters. The second chapter deals with traffic oscillations. Three platoon experiments are introduced and the concave growth pattern of traffic oscillations is identified. Moreover, we present the simulations of the traditional car following models, in which inconsistent results will be shown.

The third chapter analyzes the vehicle trajectory data in the experiments. Car following behaviors is investigated by analyzing the speed, spacing, acceleration, wave travel time, etc.

The fourth chapter presents the cellular automaton models that can simulate the concave growth pattern of traffic oscillations. Firstly, the basic cellular automaton models including the NaSch model and a Slow-to-start model are introduced. Then we present the Kerner-Klenov-Wolf model that can reproduce synchronized traffic flow. Finally, two models in the generalized NaSch model class are introduced. It was shown that both models can simulate the concave growth patterns and other empirical observations.

---

[3] However, there were also observations showing that throughput might increase after breakdown (Sun *et al.*, 2014; Dong and Mahmassani 2011; Banks 2009). The origin is still not clear and some possible reasons are: random nature of the breakdown process, a burst of higher flow, the aggressive merging behavior.

The fifth chapter presents the car following models. We remove the fundamental assumption in traditional car-following models so that the spacing of a car could change significantly even if its preceding car moves at a constant speed. As a result, the car following modes could reproduce the concave growth pattern of oscillations. Next, a stochastic speed adaption model and a stochastic variant of the Newell car following model are proposed. Finally, the Two-Dimensional Intelligent Driver Models are introduced.

References

Agyemang-Duah K., Hall F.L. (1991) Some issues regarding the numerical value of freeway capacity, *Proceedings of the international symposium on highway capacity*, pp. 1–15.

Athol P.J., Bullen A. (1973) Multiple ramp control for a freeway bottleneck, *Highw. Res. Rec.* **456**, 50–54.

Banks J.H. (1991) Two-capacity phenomenon at freeway bottlenecks: A basis for ramp metering? *Trans. Res. Rec.* 83–90.

Banks J.H. (2009) Flow breakdown at freeway bottlenecks: Evidence from automated flow analysis, *Trans. Res. Rec.* **2099**, 14–21.

Brilon W., Bressler A. (2004) Traffic flow on freeway upgrades, *Trans. Res. Rec.* **1883**, 112–121.

Cassidy M.J., Bertini R.L. (1999) Some traffic features at freeway bottlenecks, Trans. Res. Part B: Methodol. 33, 0–42.

Castillo J.M.D., Benítez F.G. (1995) On the functional form of the speed-density relationship—II: Empirical investigation, *Trans. Res. Part B: Methodol.* **29**, 391–406.

Chandler R.E., Herman R., Montroll E.W. (1958) Traffic dynamics: Studies in car following, *Oper. Res.* **6**, 165–184.

Daganzo C.F., Cassidy M.J., Bertini R.L. (1999) Possible explanations of phase transitions in highway traffic, *Trans. Res. Part A: Policy and Practice* **33**, 365–379.

Dong J., Mahmassani H.S. (2011) *Predicting flow breakdown probability and duration in stochastic network models: Impact on travel time reliability*, 90th Annual Meeting of the Transportation Research Board, Washington, DC.

Edie L.C. (1961) Car-following and steady-state theory for noncongested traffic, *Oper. Res.* **9**, 66–76.

Edie L.C. (1965) *Discussion of traffic stream measurements and definitions*, Second International Symposium on the Theory of Traffic Flow, London, United Kingdom.

Edie L.C., Foote R.S. (1958) Traffic flow in tunnels, *Highw. Res. Board Proc.* pp. 334–344.

Greenshields B., Bibbins J., Channing W., Miller H. (1935) A study of traffic capacity, *Highw. Res. Board Proc.* p. 468–477.

Hall F.L., Agyemang-Duah K. (1991) Freeway capacity drop and the definition of capacity, *Trans. Res. Rec.* p. 91–98.

Helbing D., Treiber M., Kesting A., Schönhof M. (2009) Theoretical *vs.* empirical classification and prediction of congested traffic states, *Eur. Phys. J. B* **69**, 583–598.

Iwasaki M. (1991) Empirical analysis of congested traffic flow characteristics and free speed affected by geometric factors on an intercity expressway, *Trans. Res. Rec.* **1320**, 242–250.

Jin C.-J., Wang W., Jiang R., Zhang H.M., Wang H. (2013) Spontaneous phase transition from free flow to synchronized flow in traffic on a single-lane highway, *Phys. Rev. E* **87**, 012815.

Kaufmann S., Kerner B.S., Rehborn H., Koller M., Klenov S.L. (2018) Aerial observations of moving synchronized flow patterns in over-saturated city traffic, *Trans. Res. Part C: Emerging Technol.* **86**, 393–406.

Kerner B.S. (1998) Experimental features of self-organization in traffic flow, *Phys. Rev. Lett.* **81**, 3797–3800.

Kerner B.S. (2000) Experimental features of the emergence of moving jams in free traffic flow, *J. Phys. A: Math. Gen.* **33**, L221–L228.

Kerner B.S. (2004) *The physics of traffic: Empirical freeway pattern features, engineering applications, and theory*, Springer Science & Business Media.

Kerner B.S. (2009) *Introduction to modern traffic flow theory and control: the long road to three-phase traffic theory*, Springer Science & Business Media.

Kerner B.S. (2013) Criticism of generally accepted fundamentals and methodologies of traffic and transportation theory: A brief review, *Phys. A: Stat. Mech. Appl.* **392**, 5261–5282.

Kerner B.S., Konhäuser P., (1993) Cluster effect in initially homogeneous traffic flow, *Phys. Rev. E. Stat. Physics, Plasmas, Fluids, and Related Interdisciplinary Topics* **48**, R2335–R2338.

Kerner B.S., Rehborn H. (1996a) Experimental features and characteristics of traffic jams, *Phys. Rev. E* **53**, R1297–R1300.

Kerner B.S., Rehborn H. (1996b) Experimental properties of complexity in traffic flow, *Phys. Rev. E* **53**, R4275–R4278.

Kerner B.S., Rehborn H. (1997) Experimental properties of phase transitions in traffic flow, *Phys. Rev. Lett.* **79**, 4030–4033.

Kerner B.S., Rehborn H., Aleksic M., Haug A. (2004) Recognition and tracking of spatial–temporal congested traffic patterns on freeways, *Trans. Res. Part C: Emerging Technol.* **12**, 369–400.

Knoop V.L., Hoogendoorn S.P., van Zuylen H.J. (2008) Capacity reduction at incidents: Empirical data collected from a helicopter, *Trans. Res. Rec.* **2071**, 19–25.

Koshi M. (1986) Bottleneck capacity of expressways, *J. Japan Soc. Civil Eng.* 371.

Koshi M., Kuwahara M., Akahane H. (1992) Capacity of sags and tunnels on Japanese motorways, *Ite J.* **62**, 17.

Kouhi Esfahani R., Shahbazi F., Akbarzadeh M. (2019) Three-phase classification of an uninterrupted traffic flow: A *k*-means clustering study, *Trans. B: Trans. Dyn.* **7**, 546–558.

Lee H.Y., Lee H.W., Kim D. (1998) Origin of synchronized traffic flow on highways and its dynamic phase transitions, *Phys. Rev. Lett.* **81**, 1130–1133.

Lorenz M.R., Elefteriadou L. (2001) Defining freeway capacity as function of breakdown probability. *Trans. Res. Rec.* **1776**, 43–51.

Munjal P.K., Pipes L.A. (1971) Propagation of on-ramp density perturbations on unidirectional two- and three-lane freeways, *Trans. Res.* **5**, 241–255.

Newell G.F. (1959) A theory of platoon formation in tunnel traffic, *Oper. Res.* **7**, 589–598.

Rehborn H., Klenov S.L., Palmer J. (2011) An empirical study of common traffic congestion features based on traffic data measured in the USA, the UK, and Germany, *Phys. A: Stat. Mech. Appl.* **390**, 4466–4485.

Schönhof M., Helbing D. (2009) Criticism of three-phase traffic theory, *Trans. Res. Part B: Methodol.* **43**, 784–797.

Shiomi Y., Yoshii T., Kitamura R. (2011) Platoon-based traffic flow model for estimating breakdown probability at single-lane expressway bottlenecks, *Trans. Res. Part B: Methodol.* **45**, 1314–1330.

Sugiyama Y., Fukui M., Kikuchi M., Hasebe K., Nakayama A., Nishinari K., Tadaki S.-i., Yukawa S. (2008) Traffic jams without bottlenecks—experimental evidence for the physical mechanism of the formation of a jam, *New J. Phys.* **10**, 033001.

Sun J., Tang K., Zhang S. (2014) Online evaluation of an integrated control strategy at on-ramp bottleneck for urban expressways in Shanghai, *IET Intell. Trans. Syst.* **8**, 648–654.

Tadaki S., Nishinari K., Kikuchi M., Sugiyama Y., Yukawa S. (2002) Analysis of congested flow at the upper stream of a tunnel, *Phys. A: Stat. Mech. Appl* **315**, 156–162.

Treiber M., Kesting A., Helbing D. (2010) Three-phase traffic theory and two-phase models with a fundamental diagram in the light of empirical stylized facts, *Trans. Res. Part B: Methodol.* **44**, 983–1000.

Treiterer J. (1975) Investigation of traffic dynamics by aerial photogrammetry techniques, Ohio Department of Transportation, Columbus, Ohio, pp. Final Report EES-278.

Yang B., Yoon J.W., Monterola C. (2016) Microscopic statistical characterisation of the congested traffic flow and some salient empirical features, arXiv preprint arXiv:1603.04272.

Chapter 2

Traffic Oscillation Analysis

Traffic oscillations refer to the traffic state, in which drivers tend to repeatedly decelerate and accelerate instead of maintaining a stable driving speed. To investigate the properties of traffic oscillations, we have conducted several car-following experiments, in which the leading car moves at a constant speed v_{leading}. In this chapter, firstly, the platoon experiments with 25 cars are introduced, in which v_{leading} varies from 7 km/h to 50 km/h. The concave growth pattern of traffic oscillations is observed. Then the NGSIM empirical data is analyzed, which validates the existence of the concave growth pattern. Next, the platoon experiment with 51 cars and empirical data on the highway is presented. It was found that there exists a critical speed between 30 km/h and 40 km/h, above which, the traffic flow is likely to be stable. Then the high-speed platoon experiment ($v_{\text{leading}} = 60$, 70, 80 km/h) is reported. Finally, the experiment on a circular road that investigates the lightly congested traffic flow is introduced.

2.1 Some Previously Observed Results of Traffic Oscillations

Traffic oscillations usually form at the bottlenecks, such as tunnel sags (Sun *et al.*, 2018), highway lane drops (Bertini and Leal, 2005), and lane changes near merges and diverges (Ahn *et al.*, 2010; Wang and Coifman, 2008; Cassidy and Rudjanakanoknad, 2005). Recent field experiments reveal that traffic oscillations can also arise even in the absence of bottlenecks and lane changes (Stern *et al.*, 2018; Tadaki *et al.*, 2013; Sugiyama *et al.*, 2008). Traffic oscillation, as "a nuisance for all motorists throughout the world", is undesirable (Laval and Leclercq, 2010), leading to traffic instability (Chen *et al.*, 2014; Dong and Mahmassani, 2011; Coifman and Kim, 2011; Kerner *et al.*, 2007), driving discomfort, extra fuel consumption and emission, and more safety risks.

To quantify oscillation characteristics and identify contributing factors, many empirical studies have been performed, which provide solid evidence for nearly periodical patterns of traffic oscillations in congested traffic. Mauch and Cassidy (2002) observed freeway traffic over multiple days on the 10-km stretch of the Queen

DOI: 10.1051/978-2-7598-3193-7.c002
© Science Press, EDP Sciences, 2023

Elizabeth Way. Its findings indicated that oscillations arise only in queues, increase in amplitude, and grow to their full amplitudes while propagating upstream. Laval *et al.* (2009) pointed out that oscillations have typical periods to be somewhere between 2 and 15 min. Gartner *et al.* (2002) studied the relationship between amplitude and period and found that low frequencies are accompanied by high amplitudes and short periods result in small amplitudes. Mauch and Cassidy (2002) found that oscillations propagate at a nearly constant speed of about 22–24 km/h in Canada. Zielke *et al.* (2008) conducted a country-specific analysis of freeway traffic oscillations and pointed out that oscillations propagate at speeds of about 19–20 km/h on the highway OR-217 in the United States, 16 km/h on the highway A9 in Germany, and 14 km/h on the highway M4 in the United Kingdom. Zheng *et al.* (2011) found that regardless of the trigger, the features of oscillation propagations are similar in terms of propagation speed, oscillation duration, and amplitude.

2.2 The Platoon Experiments with 25 Cars

2.2.1 Experimental Setup

The experiment was carried out on January 19, 2013, on a 3.2 km stretch of Chuangxin Avenue in a suburban area in Hefei City, China. See figure 2.1 for the map of the section. There are no traffic lights on the road section. Since the road is in a suburban area and has at least three lanes in each direction, there is no interference from other vehicles that are not part of the experiment.

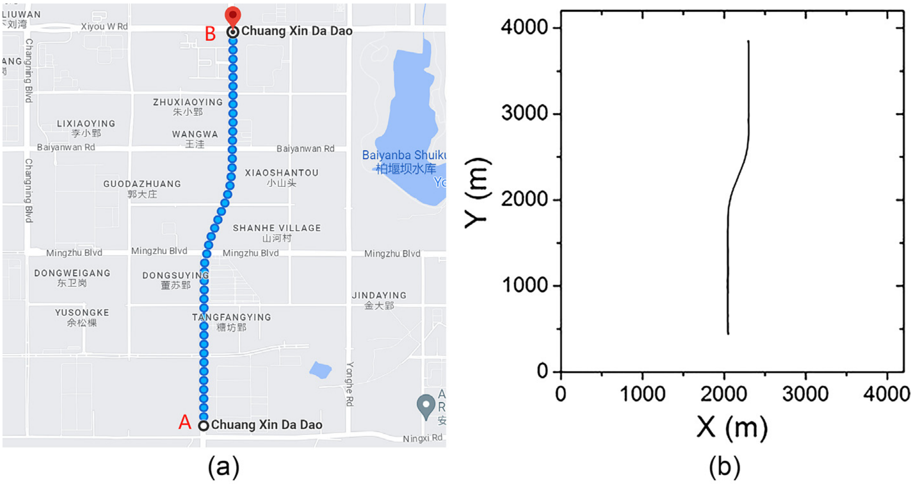

(a) (b)

FIG. 2.1 – (a) Map of the 3.2 km long experiment road section for the 25-car-platoon experiment, which is between points A and B. (b) shows trajectories of cars measured by the GPS.

High-precision difference GPS devices using MSAS (Multi-functional Satellite Augmentation System) were installed on all of the cars to record their locations and velocities every 0.1 s. The measurement errors of the GPS devices were within ±1 m for location and within ±1 km/h for velocity.[4] Once the experiment starts, the driver of the leading car is asked to drive the car at certain pre-determined constant velocity. Other drivers in the experiment are required to drive their cars as they normally do, following each other without overtaking. In two of the runs, the leading driver is asked to firstly drive his car at 15 km/h, then to drive the car without stepping on the gas pedal (the velocity is about 7 km/h in this case), and then to drive the car at 20 km/h. In other runs, the leading driver is asked to accelerate his car to a pre-determined velocity and then maintain the car at this constant velocity as accurately as he can. The leading car is equipped with a cruise control system, which could be switched on when its velocity shown by the speedometer reaches 45 km/h. As a result, the fluctuation of the leading car is very small when its velocity is set at a value greater than or equal to 45 km/h. We note that for safety reasons, the actual velocity of a car is lower than that shown by the speedometer, in particular when the velocity is high. See figure 2.2 for examples of the velocity of the leading car. When reaching the end of the road section, the car platoon decelerates, makes a U-turn, and stops.[5] When all the cars have stopped, a new run of the experiment begins. We have carried out two sets of experiments, in which the sequence of the cars has been changed, see table 2.1. Details of the runs in each set of the experiment are also presented in table 2.1.

2.2.2 Spatiotemporal Features

Figure 2.3 shows some typical spatiotemporal patterns of the traffic flow. One can observe the stripes structure, which exhibits the propagation, growth, dissipation, and merge of disturbances. In figure 2.3a–d, in which the leading car is not very slow, the velocity fluctuation amplitude of the cars in the rear part of the platoon has exceeded 20 km/h. In figure 2.3d, in which the leading car moves with a velocity of around 15 km/h, some cars in the rear part of the platoon have occasionally completely stopped. In figure 2.3e, in which the leading car moves very slowly with a velocity of around 7 km/h, the cars in the rear part of the platoon will have to completely stop from time to time.

2.2.3 The Concave Growth Patterns

To better understand the evolution of the disturbances, figure 2.4 presents the standard deviation σ_v of the time series of the velocity of each car's overall runs of the experiment, in which the leading car is asked to move with the same velocity.

---

[4] The velocity is measured directly *via* the Doppler effect.

[5] Between the first run and the second run in the first set of experiment, the platoon has not stopped after the U-turn. The first run in the first set of experiment is regarded as a test run, and the data have not been used.

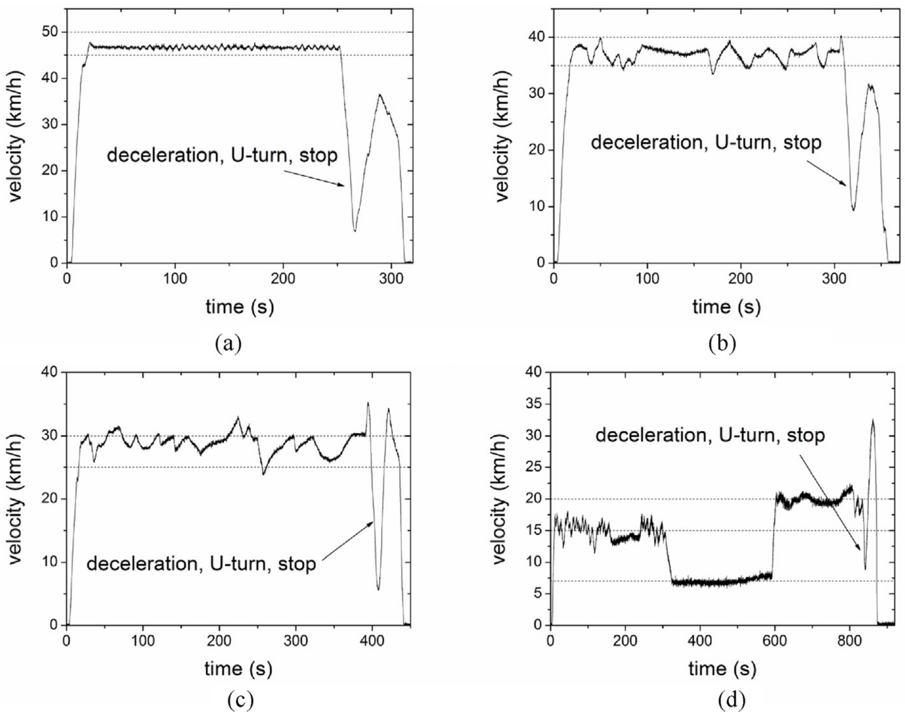

(a) (b) (c) (d)

Fig. 2.2 – The velocity of the leading car. The driver of the leading car is asked to drive at (a) 50 km/h. (b) 40 km/h. (c) 30 km/h. (d) firstly at 15 km/h, then to drive the car without pressing the accelerator pedal (the velocity is about 7 km/h in this case), and then to drive the car at 20 km/h. Note that for safety reasons, the actual velocity of a car is lower than that shown by the speedometer, in particular when the velocity is high. The dashed lines are added visual guides to help read the speeds on the graphs.

Note that the data belonging to the start process, the deceleration, and the U-turn process have been removed. One can see that when the velocity v_{leading} of the leading car is low, σ_v increases almost linearly with car number (figure 2.4a).[6] With the increase of v_{leading}, σ_v becomes increasing in a concave way, *i.e.*, the curve of σ_v bends downward and the increment rate decreases (figure 2.4b–d). In conclusion, a concave growth pattern of oscillations has been identified, *i.e.*, the standard deviations of speed increase in a concave way along the platoon.

---

[6] However, the physical limit of speeds implies that if we had a much longer platoon, the variations of speed of cars in the tail of the platoon would be capped and the line would bend downward, making the overall curve concave shaped. This is confirmed in later 51-car experiment.

Tab. 2.1 – Details of the experiments.

	Car No			Velocity of leading car (km/h)	
Sequence of Car in the platoon	1st set of experiment	2nd set of experiment	Run No. in the experiment	1st set of experiment (12 runs)	2nd set of experiment (23 runs)
1	22	22	1	50	50
2	1	11	2	20	15–7–20
3	2	12	3	45	55
4	3	13	4	30	40
5	4	15	5	55	60
6	5	16	6	40	35
7	6	17	7	55	45
8	7	18	8	35	30
9	8	19	9	60	50
10	9	20	10	25	25
11	10	21	11	45	55
12	11	23	12	30	40
13	12	25	13		50
14	13	1	14		15–7–20
15	14	2	15		55
16	15	3	16		40
17	16	4	17		60
18	17	5	18		35
19	18	6	19		45
20	19	7	20		30
21	20	8	21		50
22	21	9	22		25
23	23	10	23		55
24	24	14			
25	25	24			

2.3 Traffic Oscillation Simulations by Traditional Models

To show whether the concave growth pattern of oscillations can be simulated by the traditional car following models or not, we have conducted several simulations for the following renowned models.

2.3.1 Traditional Models

– **The GM models:**

In the classical General-Motors (GM) family of car-following models (Chandler *et al.*, 1958), the acceleration of a vehicle n is proportional to the velocity difference to the preceding one $n-1$

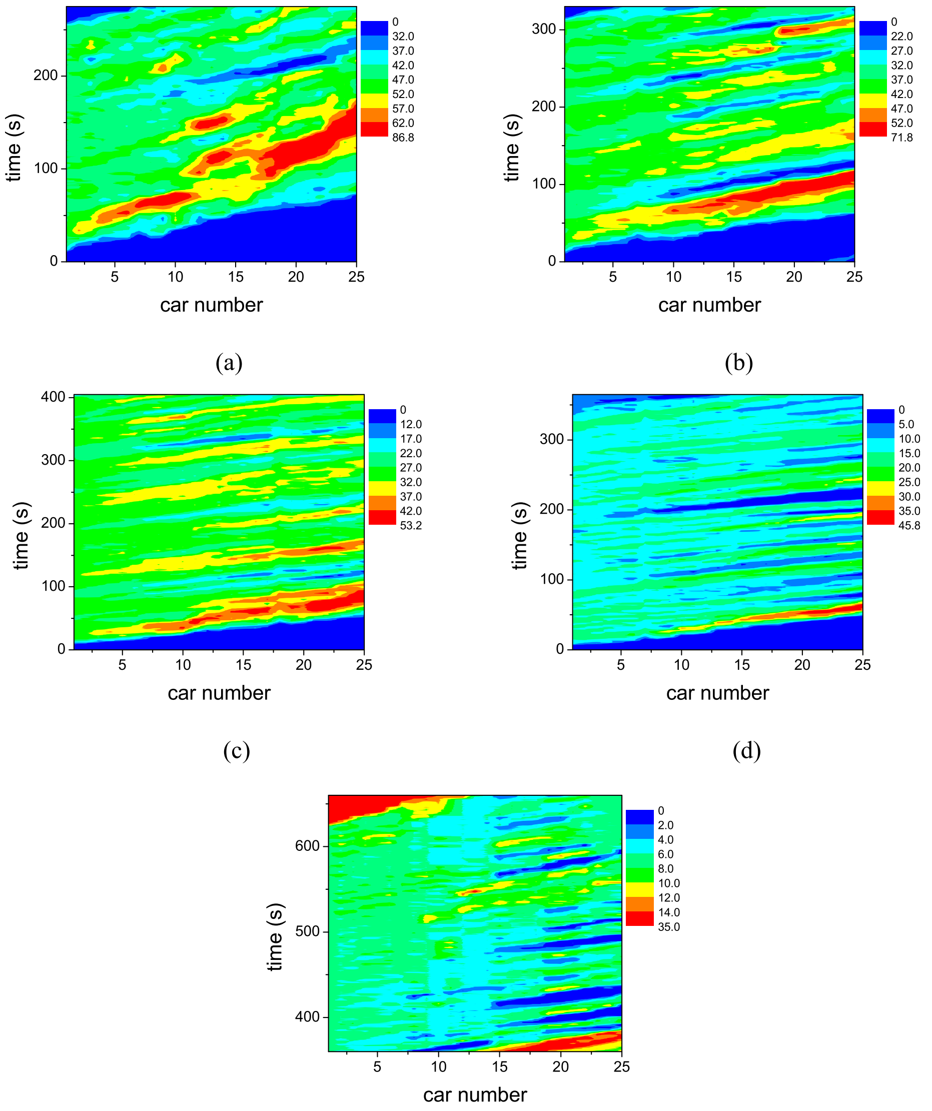

(a) (b)

(c) (d)

(e)

FIG. 2.3 – Typical spatiotemporal patterns of the platoon traffic: car speed shown with different colors (unit: km/h) as function of time and car number.

$$\frac{dv_n(t+\tau)}{dt} = \lambda[v_{n-1}(t) - v_n(t)] \tag{2.1}$$

The stability of traffic flow is related to the sensitivity λ and the reaction time τ: traffic flow is unstable when $\lambda\tau > 1/2$. Here v is velocity of vehicles. This GM model

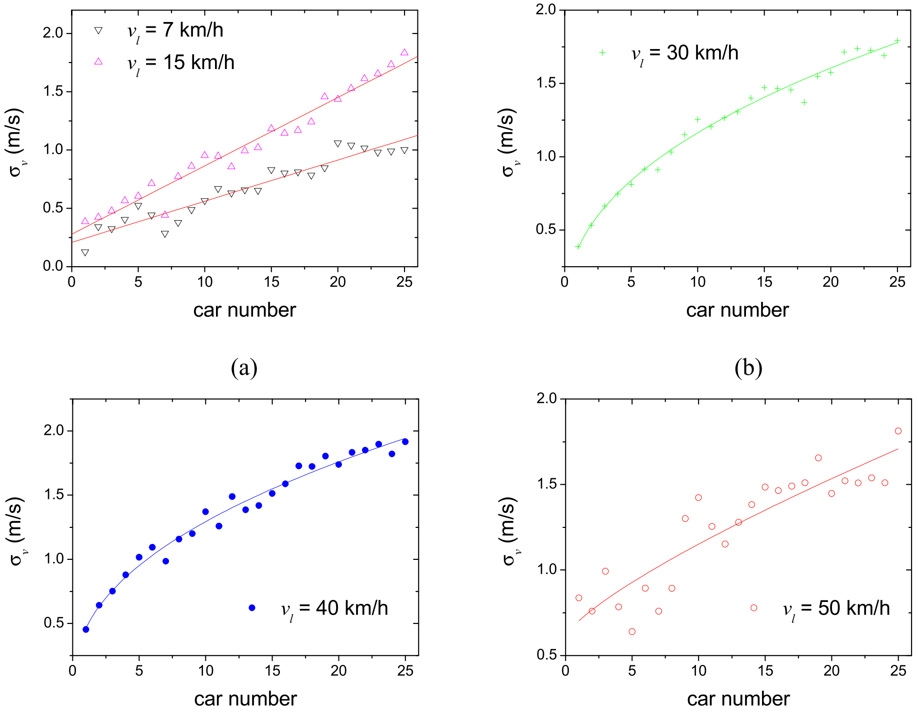

(a) (b)

(c) (d)

FIG. 2.4 – The standard deviation σ_v of the time series of the velocity of each car overall runs of the experiment, in which the leading car is asked to move with the same velocity v_l. The solid lines suggest possible curve fits.

has later been extended to consider the effects of spacing and velocity of the following vehicle on acceleration (Gazis *et al.*, 1959, 1961; Herman *et al.*, 1959):

$$\frac{dv_n(t+\tau)}{dt} = \lambda(v_n(t+\tau))^m[v_{n-1}(t) - v_n(t)]/[x_{n-1}(t) - x_n(t)]^l \qquad (2.2)$$

where m and l are two parameters. A homogeneous traffic state is unstable when $\frac{\lambda\tau v^m}{(\Delta x)^l} > 1/2$. Here Δx is the spacing between vehicles.

In the following simulations, all cars are initially stopped with spacing $\Delta x = 6$ m. Then the leading car accelerates with a constant acceleration of 1 m/s^2 until it reaches the velocity v_l. Then its speed begins to fluctuate with $v = v_l + \xi$, in which ξ is a random number between ± 0.2 m/s. In order to assure that there is no collision and the velocity does not exceed $v_{\max}$, we set $0 \le v \le v_{\max}$ and $v = 0$ if $\Delta x \le$ 6 m.

Figure 2.5a shows the simulation results of the GM model (2.1), in which the parameters used are $\lambda = 0.75$ s^{-1}, $\tau = 0.9$ s, $v_{\max} = 30$ m/s. One can see that the curve of σ_v increases in a convex way. When $v_l = 15$ km/h and 7 km/h, due to the lower bound of zero speed, the curve tends to become concave at the rear part of the platoon. One can imagine that if the platoon is longer, the curve will finally become concave due to the lower bound of zero speed and the upper bound of maximum speed, no matter what v_l is.

Figure 2.5b shows the simulation results of the GM model (2.2), in which the parameters used are $\lambda = 12$ m/s, $\tau = 0.9$ s, m = 0, $l = 1$, $v_{\max} = 30$ m/s. It can be seen that when $v_l = 30$, 40, and 50 km/h, the platoon is quite stable. When $v_l = 15$ km/h and 7 km/h, the curve of σ_v initially increases in a convex way and then tends to be concave due to the lower bound of zero speed.

Figure 2.5c shows the simulation results of the GM model (2.2), in which the parameters used are $\lambda = 4.5$, $\tau = 0.9$ s, $m = 1$, $l = 1$, $v_{\max} = 30$ m/s. Note that with parameter $m = 1$, a stopped car will never start again. Therefore, we modify GM model (2.2) into

$$\frac{dv_n(t+\tau)}{dt} = \max(\lambda(v_n(t+\tau))^m/[x_{n-1}(t) - x_n(t)]^l, \lambda_1)[v_{n-1}(t) - v_n(t)] \tag{2.3}$$

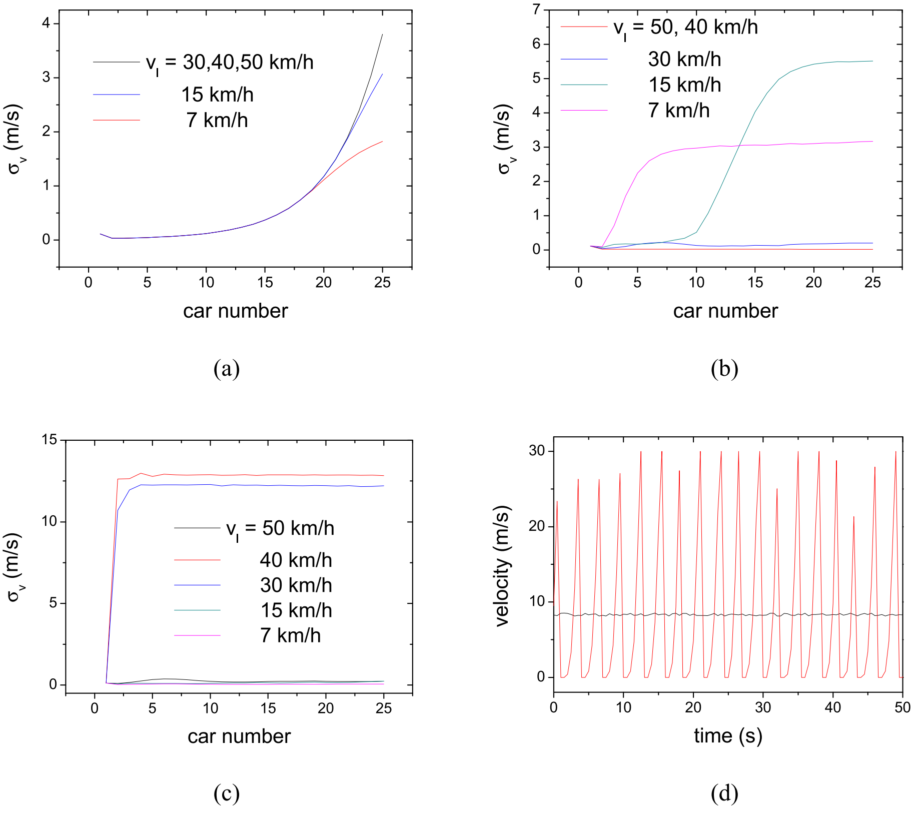

Fig. 2.5 – Simulation results of σ_v in the GM models. (a) Model (1), (b) and (c), model (2). (d) Shows the velocity of the leading car (black line) and the second car (red line), corresponding to panel (c).

and the parameter $\lambda_1 = 0.5\ \text{s}^{-1}$ is used. One can see that when $v_l = 7, 15, 50$ km/h, the platoon is quite stable. When $v_l = 30$ and 40 km/h, the platoon is very unstable and the velocity of the second car has already fluctuated very strongly and unrealistically, see figure 2.5d.

The simulation results demonstrate that the GM models are not able to reproduce the observed experimental features of traffic flow.

– **the Gipps model:**

In the Gipps model, the velocity of vehicle n is calculated (Gipps, 1981)

$$v_n(t+\tau) = \min\left\{ \begin{array}{l} v_n(t) + 2.5a\tau(1 - v_n(t)/v_{\max})\sqrt{0.025 + v_n(t)/v_{\max}}, \\ b\tau + \sqrt{b^2\tau^2 - b\left[2(x_{n-1}(t) - x_n(t) - S) - v_n(t)\tau - v_{n-1}^2(t)\Big/\hat{b}\right]} \end{array} \right\} \tag{2.4}$$

In the simulations, the parameters are $\tau = 2/3$ s, $a = 2\ \text{m/s}^2$, $b = -3\ \text{m/s}^2$, $\hat{b} = -2.5\ \text{m/s}^2$, $S = 6$ m, $v_{\max} = 30$ m/s.

Figure 2.6 shows the simulation results. When $v_l = 7$ and 15 km/h, the platoon is quite stable. When $v_l = 30$, 40, and 50 km/h, the platoon is unstable, and the curve of σ_v increases in a convex way. The feature of the Gipps model is thus not consistent with the experimental results, either.

– **The Optimal Velocity (OV) model** (Bando *et al.*, 1995)**:**

$$\frac{dv_n}{dt} = \kappa[\,V(\Delta x_n) - v_n] \tag{2.5}$$

Here $\Delta x_n = x_{n-1} - x_n$ is the spacing of car n, which follows vehicle $n - 1$. κ is sensitivity parameter.

The OV function used is $V(\Delta x) = 11.6(\tanh(0.086(\Delta x - 25)) + 0.913)$. The unit of length and time are meters and seconds, respectively. The parameters are $\kappa = 1\ \text{s}^{-1}$, $\xi_1 = 0.2\ \text{m/s}^2$. The simulation time step $\Delta t = 0.1$ s.

– **The Full Velocity Difference (FVD) model** (Jiang *et al.*, 2001)**:**

$$\frac{dv_n}{dt} = \kappa[\,V(\Delta x_n) - v_n] + \lambda(v_{n-1} - v_n) + \xi \tag{2.6}$$

where λ is another sensitivity parameter. The OV function and the noise ξ are the same as in the OV model. The parameters are $\kappa = 0.32\ \text{s}^{-1}$, $\lambda = 0.4\ \text{s}^{-1}$, $\xi_1 = 0.2\ \text{m/s}^2$. The simulation time step $\Delta t = 0.1$ s

– **The Intelligent Driver Model (IDM)** (Treiber *et al.*, 2000)**:**

$$\frac{dv_n}{dt} = a\left[1 - \left(\frac{v_n}{v_{\max}}\right)^4 - \left(\frac{s_0 + v_n T + \frac{v_n(v_n - v_{n-1})}{2\sqrt{ab}}}{\Delta x_n - l}\right)^2\right] + \xi \tag{2.7}$$

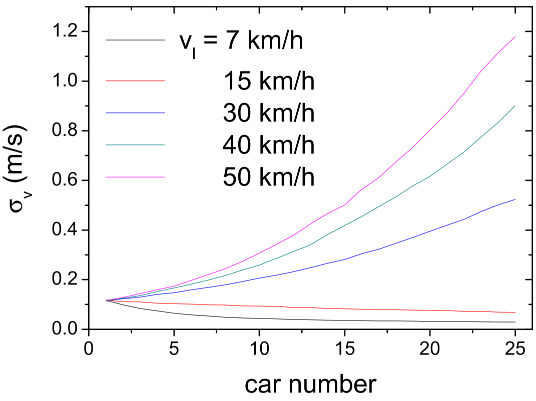

FIG. 2.6 – Simulation results of σ_v in the Gipps model.

where a is maximum acceleration, b is desired deceleration, T is desired time headway, s_0 is the desired gap (bumper-to-bumper distance) between two neighboring cars in a jam, $v_{\max}$ is the maximum velocity, l is car length, ξ is noise as before. The parameters are $v_{\max} = 80$ km/h, $T = 1.6$ s, $a = 0.73$ m/s^2, $b = 1.67$ m/s^2, $s_0 = 2$ m, $l = 5$ m, $\xi_1 = 0.2$ m/s^2. The simulation time step $\Delta t = 0.1$ s.

– **The inertial model** (Tomer *et al.*, 2000)**:**

$$\frac{dv_n}{dt} = A\left(1 - \frac{v_n T + D}{\Delta x_n}\right) - \frac{Z^2(v_n - v_{n-1})}{2(\Delta x_n - D)} - kZ(v_n - v_{\text{per}}) + \xi \tag{2.8}$$

where A is a sensitivity parameter, D is the minimal distance between consecutive cars, v_{per} is the permitted velocity, k is a constant, T is the safety time gap constant, ξ is noise as before. The function Z is defined as $Z(x) = (|x| + x)/2$. The parameters are $A = 5$ m/s^2, $D = 5$ m, $v_{\text{per}} = 80$ km/h, $k = 2$ s^{-1}, $T = 2$ s, $\xi_1 = 0.2$ m/s^2. The simulation time step $\Delta t = 0.1$ s.

Note that in the OV model and the FVD model, the unique relationship between speed and spacing in the steady state is $V(\Delta x)$, which is explicitly given. In the IDM and the inertial model, the relationship is implicitly given, which could be obtained by setting $\frac{dv_n}{dt} = 0$ and $v_n = v_{n-1} = v$.

Figure 2.7 shows the simulation results of the OV model, the FVD model, the IDM, and the inertial model. The results are similar to that of the Gipps model.

2.3.2 The Initial Convex Growth Pattern in Traditional Models

This section generalizes the above simulation analysis to the general models, which can be written as

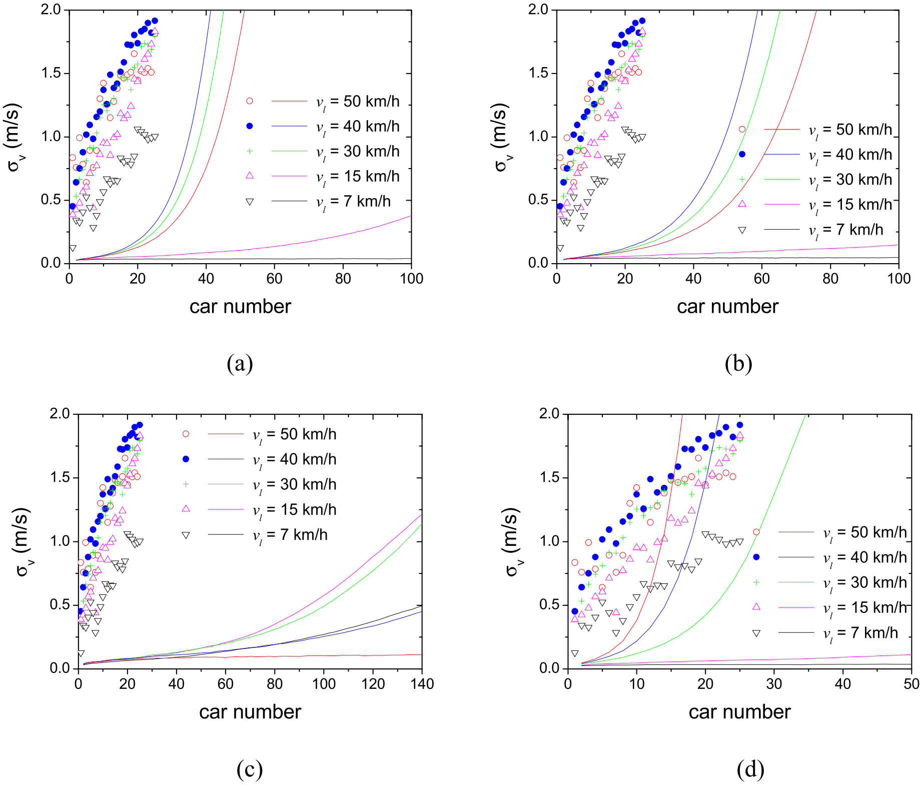

(a) (b)

(c) (d)

FIG. 2.7 – Simulation results (solid lines) of the standard deviation σ_v of the time series of the velocity of each car. (a) The OV model, (b) the FVD model, (c) the IDM, (d) the inertial model.

$$\frac{d}{dt} v_n(t) = f(d_n(t), v_n(t), v_{n-1}(t)) \tag{2.9}$$

$$\frac{d}{dt} d_n(t) = v_{n-1}(t) - v_n(t) \tag{2.10}$$

where $v_n(t)$ is the speed of vehicle n and $d_n(t)$ is the spacing between vehicle n and its preceding vehicle $n-1$. We assume that $f(d_n(t),\ v_n(t),\ v_{n-1}(t)) = 0$ has physical solution. Different formulations of the acceleration function $f(d_n(t),\ v_n(t),\ v_{n-1}(t))$ leads to different models.

Assuming there is a vehicle fleet composed of N vehicles on an open road and the leading vehicle N runs constantly with the speed v_0, then the equilibrium state is as follows:

$$[v_n^e(t),\ d_n^e(t)] = [v_0,\ G(v_0)] \tag{2.11}$$

where $d_n^e(t) = G(v_0)$ is the solution of $f(d_n^e(t), v_0, v_0) = 0$. This state implies that all the vehicles run orderly with the velocity v_0 and space headway $G(v_0)$, which also indicates the unique relationship between velocity and space headway. Then the linearized system around the steady state is

$$\frac{d}{dt}\overline{v_n(t)} = f^{d_n}\overline{d_n(t)} + f^{v_n}\overline{v_n(t)} + f^{v_{n+1}}\overline{v_{n-1}(t)} \tag{2.12}$$

$$\frac{d}{dt}\overline{d_n(t)} = \overline{v_{n-1}(t)} - \overline{v_n(t)} \tag{2.13}$$

where

$$\overline{v_n(t)} := v_n(t) - v_0 \tag{2.14}$$

$$\overline{v_{n-1}(t)} := v_{n-1}(t) - v_0 \tag{2.15}$$

$$\overline{d_n(t)} := d_n(t) - G(v_0) \tag{2.16}$$

and

$$\begin{cases} f^{d_n} = \dfrac{df}{d(d_n)}\Big|_{d_n=G(v_0),v_n=v_0,v_{n-1}=v_0} \\ f^{v_n} = \dfrac{df}{d(v_n)}\Big|_{d_n=G(v_0),v_n=v_0,v_{n-1}=v_0} \\ f^{v_{n-1}} = \dfrac{df}{d(v_{n-1})}\Big|_{d_n=G(v_0),v_n=v_0,v_{n-1}=v_0} \end{cases} \tag{2.17}$$

Applying the Laplace transformation to both the left-hand-side and the right-hand-side of equations (2.12) and (2.13), the relation between velocity disturbance of vehicle n and $n-1$ can be derived

$$L(\overline{v_n(t)}) = H(s)L(\overline{v_{n-1}(t)}) \tag{2.18}$$

$$H(s) = \frac{f^{d_n} + sf^{v_{n-1}}}{s^2 - sf^{v_n} + f^{d_n}} \tag{2.19}$$

where L denotes the Laplace transformation. According to the control theory, the increase of the velocity disturbance from vehicle $n-1$ to n is determined by the transfer function $|H(j\omega)|$ for a disturbance wave with angular frequency ω. Thus, when $|H(j\omega)| > 1$, the amplitude of the disturbance wave propagating from the leading vehicle 1 to the following vehicle $N-n$ increases with ratio $|H(j\omega)|^n$; when $|H(j\omega)| < 1$, the amplitude of disturbance decays with ratio $|H(j\omega)|^n$. Since $|H(j\omega)|^n$ is a convex function of n when $|H(j\omega)|^n > 1$, the small disturbances always increase in a convex way in the initial stage.

For a real traffic system, we have to consider the external disturbances for all $\omega \in [0, +\infty)$. In this case, we are not able to prove rigorously that the disturbance grows in a concave way since components with different angular frequencies may destructively interfere with each other. Nevertheless, the numerical simulation above shows that the disturbance initially does grow in a concave way, which implies that interference among components with different angular frequencies might be trivial. Wang *et al.* (2020) proved that a linear stochastic car-following model with common parameter settings yields (i) concave growth of the speed oscillation magnitudes and (ii) reduction of oscillation frequency as oscillation propagates upstream.

In traditional models, linear instability of the steady-state solution leads to unstable traffic flow, which leads to the initially convex growth pattern of oscillations. This contradicts the observed concave growth pattern, which implies that the mechanism triggering traffic jams in these models is questionable. Further theoretical investigations (Wang *et al.*, 2020; Ngoduy *et al.*, 2019; Treiber and Kesting, 2018; Li *et al.*, 2014) also support the findings.

2.4 Empirical Oscillation Analysis

We analyzed the US-101 trajectory data sets of the Next Generation Simulation program (NGSIM, 2006), which were collected on a 640 m segment on the south-bound direction of US-101 (Hollywood Freeway) in the vicinity of Lankershim Avenue in Los Angeles, California on June 15th, 2005. The data collected were from 07:50 am to 08:35 am. Figure 2.8 provides a schematic illustration of the location for the vehicle trajectory datasets. There are five main lanes throughout the section, and an auxiliary lane is present between the on-ramp and off-ramp. In order to minimize the impact of bottlenecks on traffic flow, only the leftmost lane is analyzed. The following criteria are used to filter suitable oscillations from the empirical data:

1. The formation process of oscillation should be comprised.
2. The speed of the leading vehicle should be as steady as possible. In other words, the standard deviation of the speed of the leading vehicle should be as small as possible.
3. Trajectories involved in jams propagating from the downstream section of the investigated area were abandoned.

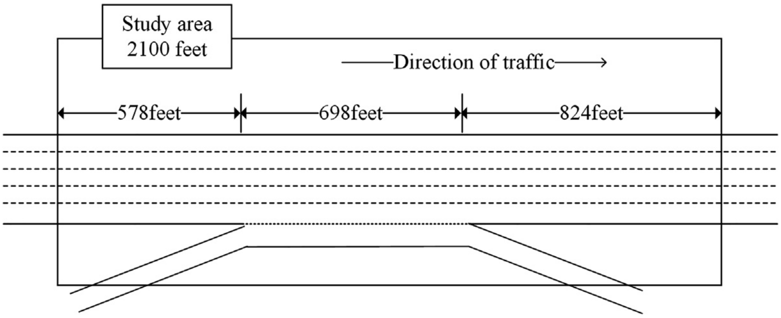

Fig. 2.8 – The sketch of US-101 study area.

With these criteria, 9 oscillations have been selected, see figures 2.9, 2.10, 2.12, and 2.14a. Trajectories of vehicles appearing on the lane only shortly (due to lane changing) have not been considered. To understand the evolution of the disturbances, standard deviations of the time series of the velocity of each vehicle have been analyzed and shown in figures 2.11, 2.13, and 2.14b. The standard deviations increase in a concave way in all examples, as observed in the car-following experiments in Jiang *et al.* (2015); Jiang *et al.* (2014).

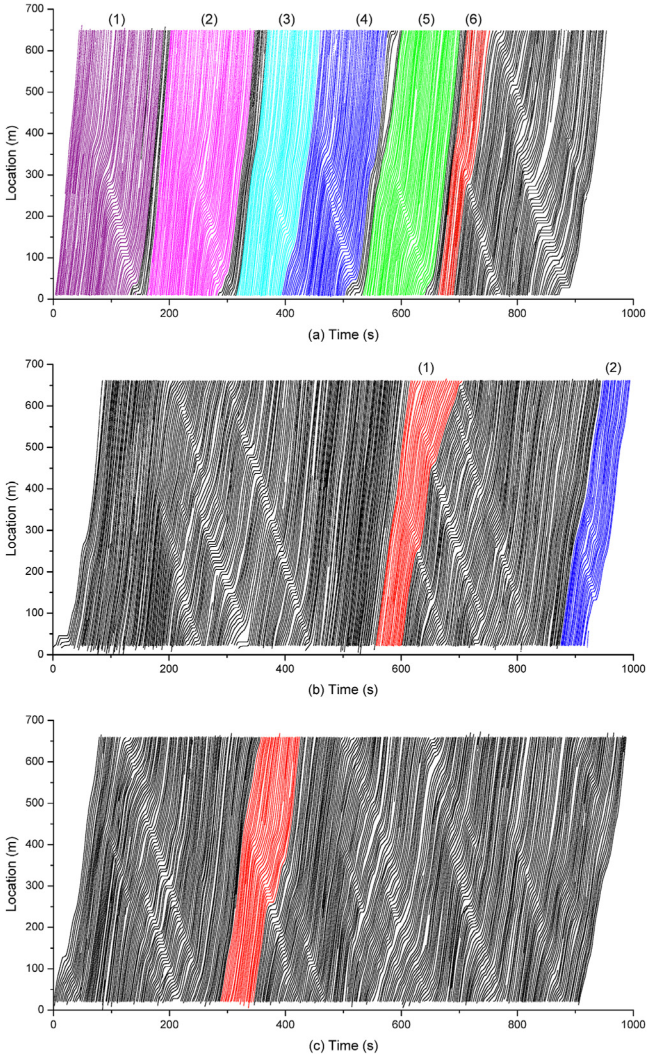

Fig. 2.9 – The NGSIM trajectories during the time interval. The time interval: (a) 07:50 am–08:05 am, (b) 08:05 am–08:20 am, (c) 08:20 am–08:35 am, for the leftmost lane at the location shown by figure 2.8. The colored trajectories have been selected and analyzed.

Figure 2.15a presents the standard deviation data in all examples in a single plot. Since the standard deviation of the speed of the leading vehicle differs from each other in different examples (see figure 2.16a), each set of data has been shifted horizontally to make the dataset match each other. With the shifts, all datasets collapse into a single concave curve, which indicates a universal evolution law of oscillations. We note that there are deviated data marked by the ellipse. This is due to the impact of lane-changing vehicles. For the vehicle indicated by the red trajectory in figure 2.10a,

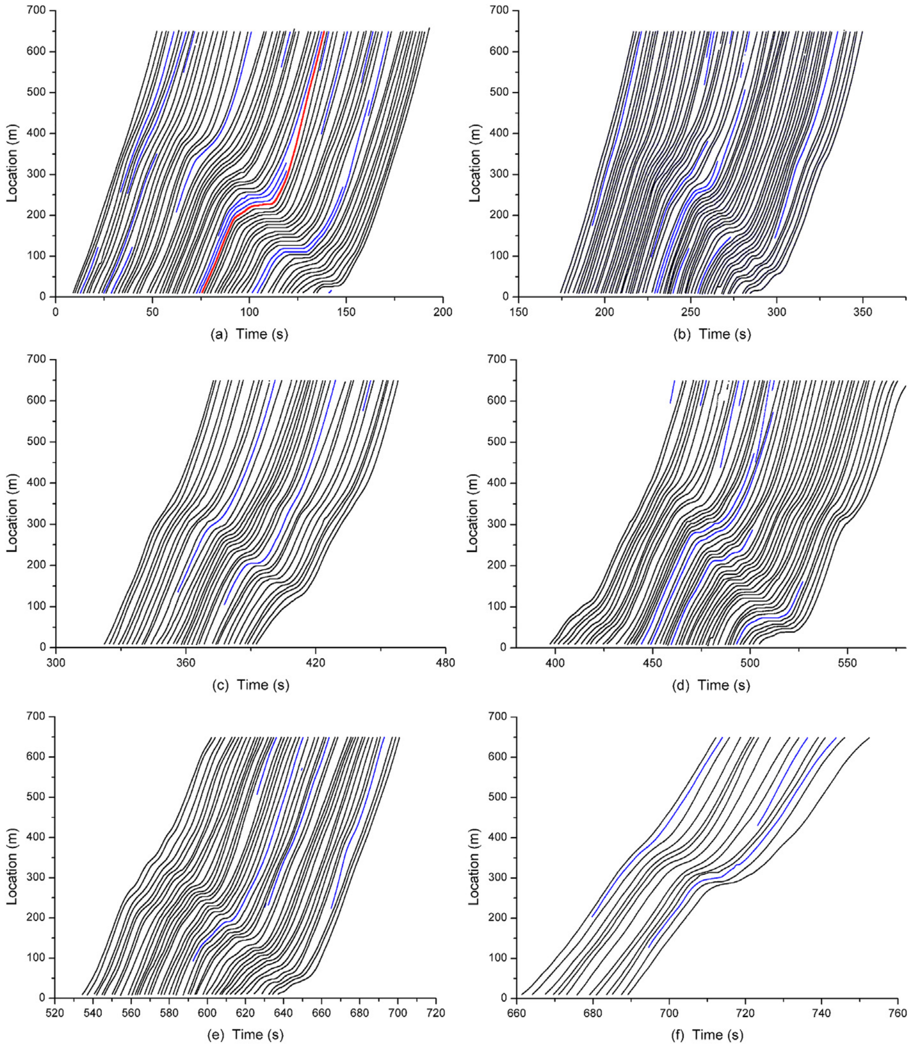

FIG. 2.10 – The NGSIM trajectories during the time interval 07:50 am–08:05 am. (a–f) corresponds to (1–6) in figure 2.9a. Trajectories in black and red have been used for analysis. Trajectories in blue have been abandoned since vehicles only move shortly (due to lane changing) on the lane.

two consecutive vehicles in its front have changed to the neighboring lane. This leads to a large acceleration of the vehicle. However, this deviation occurs only locally and does not change the global concave growth pattern.

The average speed of the leading vehicle in the 9 examples in the NGSIM data is 38 km/h, which indicates that the oscillations can be regarded as evolving from traffic flow with an average speed of 38 km/h. We compare the results with that of $v_{\text{leading}} = 40$ km/h in the 25-car experiment. As mentioned before, the actual

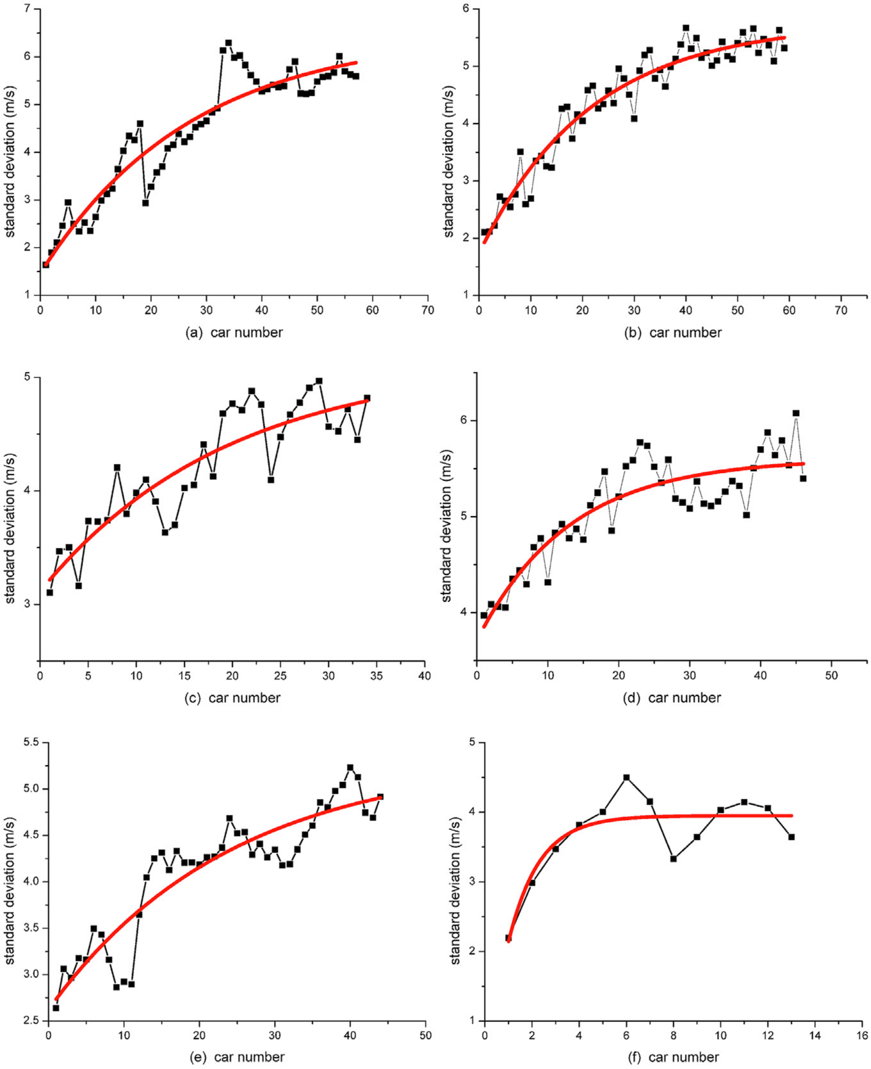

Fig. 2.11 – The standard deviation of the time series of the speed of each vehicle corresponds to figure 2.10. Car number 1 is the leading car. The red line is a fitting line, which shows the evolution concavity of traffic oscillations.

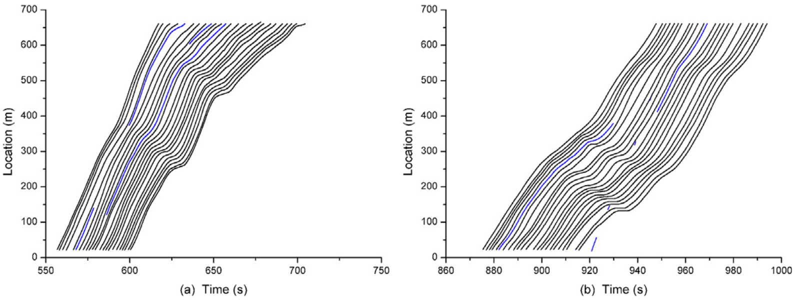

Fig. 2.12 – The NGSIM trajectories during the time interval 08:05 am–08:20 am. (a, b) corresponds to (1, 2) in figure 2.9b.

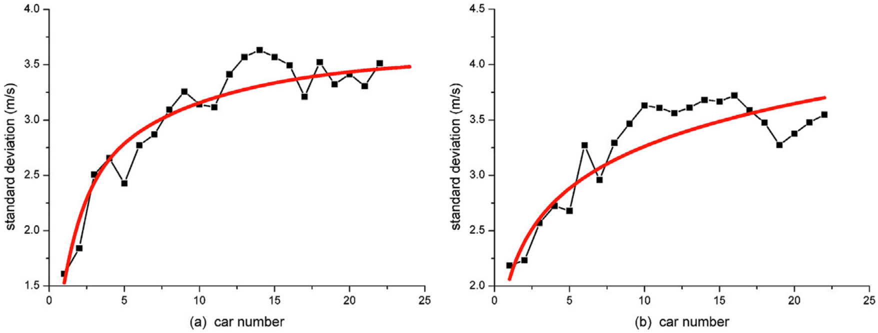

Fig. 2.13 – The standard deviation of the time series of the speed of each vehicle corresponds to figure 2.12. Car number 1 is the leading car.

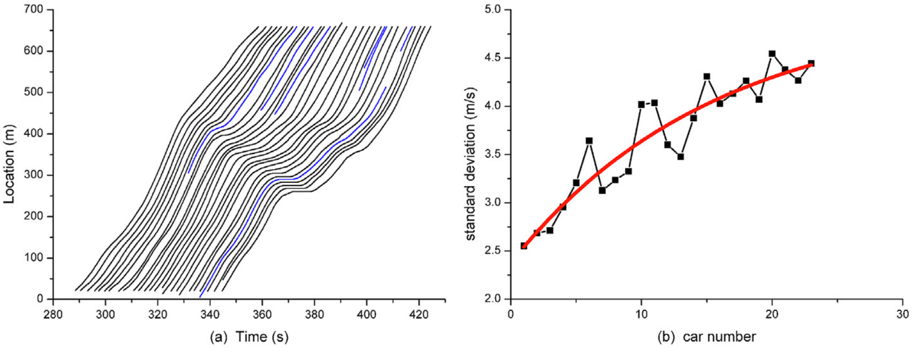

Fig. 2.14 – (a) The NGSIM trajectories and (b) the standard deviation of the time series of the speed of each vehicle during the time interval 08:20 am–08:35 am. (a) Corresponds to the red trajectories in figure 2.9c.

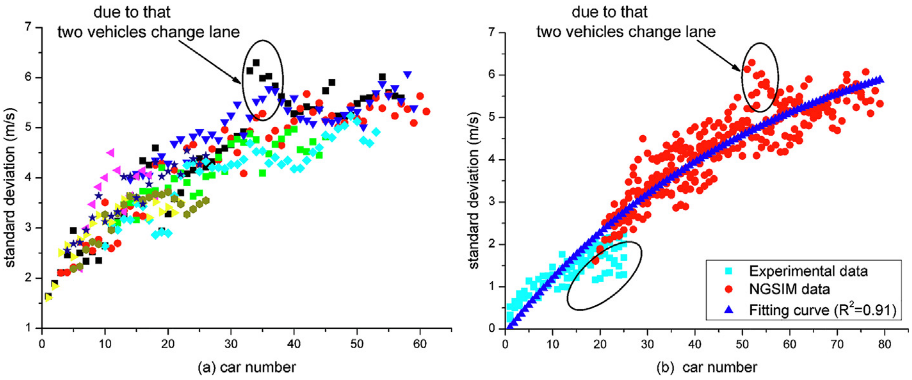

FIG. 2.15 – (a) The standard deviation of the time series of the speed of each vehicle in all empirical examples. (b) Merges the empirical data and the experimental data.

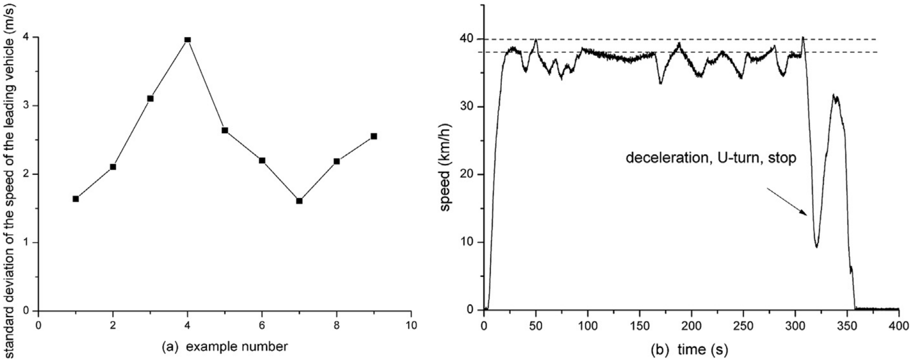

FIG. 2.16 – (a) The standard deviation of the leading vehicle in the 9 empirical examples. (b) The speed of leading vehicle in one run of the traffic experiment. The driver was asked to drive at 40 km/h, but the actual speed is smaller than 40 km/h. The two dashed lines show 40 km/h and 38 km/h.

velocity of a car is lower than that shown by the speedometer, in particular when the velocity is high. When the speedometer shows 40 km/h, the actual speed is about 38 km/h, see figure 2.16b.

Figure 2.17 shows the standard deviation of each car under $v_{\text{leading}} = 40$ km/h. We show the results of each run in figure 2.17. One can see that for each run of the experiment, the evolution of standard deviation disperses, which is similar to the NGSIM data. However, the results under different runs can be fitted by a single concave curve.

Next, we merge the empirical data and the experimental data in a single plot. Since the standard deviation of the speed of the leading vehicle is close to zero in the traffic experiment, we shift horizontally the empirical dataset to make the two datasets

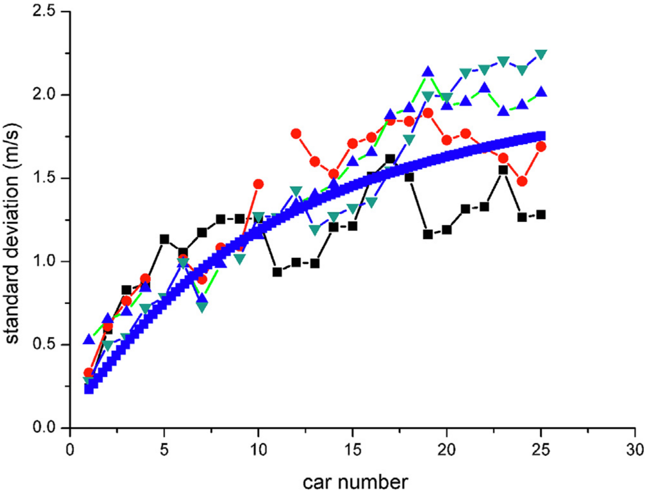

FIG. 2.17 – The standard deviation of the time series of the speed of each vehicle in the car following experiments. Car number 1 is the leading car. The required velocity of the leading car v_l is 40 km/h. The actual velocity is about 38 km/h. Each symbol line represents the experimental result of one run and the heavy line is the fitting curve. The discontinuity of some symbol lines is due to the absence of experimental data since the data were collected by GPS and the signal has been lost temporarily.

match each other, see figure 2.15b. The two datasets are highly compatible and can be fitted by a single concave curve. Note that the cars in the experiment were led by a moving bottleneck, and there is no lane changing. In contrast, in empirical data, traffic oscillations were induced by fixed bottlenecks and vehicles can change lanes. Thus, the compatibility of the two datasets demonstrates that the growth pattern of oscillations is not affected by the type of bottleneck and lane-changing behavior.

We note that the experimental data marked by the ellipse deviate a little from the fitting curve in figure 2.15b. This might be because there is no cut-in in the experiment. Therefore, some drivers leave an averagely larger spacing in front than driving on multilane roads, which lowers the growth rate of the standard deviation of the speed of his/her car.

2.5 The Platoon Experiment with 50 Cars

The platoon experiment with 50 cars was carried out on December 15, 2013, on the runway and taxiway of the old airport (which was closed) in Hefei, China to further investigate the evolution of traffic oscillation along the longer platoon. See figure 2.18a for the map of the airport. The trajectories of cars measured by the GPS devices are shown in figure 2.18b. One can see that the runway and taxiway are about 3 km long.

In the experiment, the platoon has 51 cars. Since we have only 27 GPS devices, we cannot install the GPS on each car. In the experiment, the GPS devices were installed on the leading car and every two cars, *i.e.*, on cars with numbers 1, 2, 3, 6,

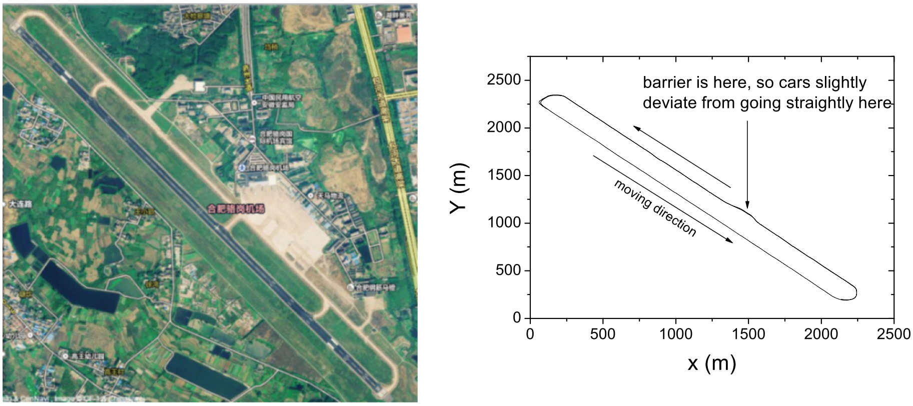
barrier is here, so cars slightly
deviate from going straightly here
moving direction
Y (m)
x (m)
0
500
1000
1500
2000
2500
0
500
1000
1500
2000
2500

(a) (b)

FIG. 2.18 – (a) Map of the airport. (b) The trajectories of cars measured by the GPS installed in the cars.

7, 10, 11, 14, 15, 18, 19, 22, 23, 26, 27, 30, 31, 34, 35, 38, 39, 42, 43, 46, 47, 50, 51. Note that due to the GPS device problem or signal problem, sometimes the speed and/or location data of some cars are missing.

We have carried out two sets of experiments, in which the sequence of the cars has been changed. In the first set of the experiment, the car sequence is from 1 to 51. In the second set of the experiment, the car sequence is 1, 22–51, 12–21, 2–11.

The vehicles initially stopped bumper-to-bumper in the two sets of the experiment. Then the leading car was instructed to move according to a given velocity profile, and other cars were instructed to move following each other. The leading car is equipped with a cruise control system, which could be switched on when its velocity shown by the speedometer reaches 25 km/h. The x location and the velocity profile of the leading car in the two sets of the experiment are shown in figure 2.19. We have classified the time series of the two sets into 23 intervals so that the deceleration caused by vehicle turning is eliminated.[7]

In intervals 1, 2, 3, 9, 18, and 23, the leading car moves at 30 km/h.[8] Interval 1 has been regarded as a test run and the data have not been used. In intervals 14 and 16, the leading car also moves at 30 km/h. However, the driver of the leading car has been asked to decelerate and then accelerate to 30 km/h again to examine the effect of the disturbance of the leading car. Details of the speed of the leading car in all intervals are summarized in table 2.2.

---

[7] If the speed is small, the cars do not need to decelerate when turning at the two ends of the experiment track. Therefore, we did not classify interval 11 into two intervals.

[8] Due to safety reason, the speed shown by the speedometer is a little smaller than the real speed. The difference vanishes when the speed is small. Since the speedometer is not digital, the driver cannot distinguish small speed difference from the speedometer. Thus, the speed of the leading car in the intervals that the drivers are asked to drive at the same speed, might be slightly different.

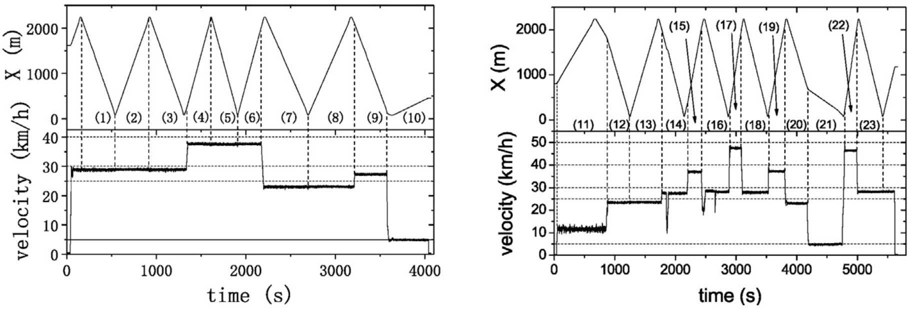

(a) (b)

FIG. 2.19 – The x location and the velocity of the leading car in the two sets of the experiment and the classification of intervals. (a) Set 1, (b) set 2.

TAB. 2.2 – Speed of leading car in the intervals.

Interval No	Speed of leading car
10, 21	5 km/h
11	12 km/h
7, 8, 12, 13, 20	25 km/h
1, 2, 3, 9, 18, 23	30 km/h
14, 16	30 km/h (with disturbance)
4, 5, 6, 15, 19	40 km/h
17, 22	50 km/h

2.5.1 Experimental Results

We present the experiment results in the ascending order of leading speed. Figures 2.20 and 2.21 show the velocities of several typical cars in which the leading car moves at the speed of 5 km/h and 12 km/h, respectively. One can see that the traffic flow is obviously unstable and vehicles in the rear part of the platoon move in a stop-and-go way, which confirms the conclusion of the previous 25-car-platoon experiment (Jiang *et al.*, 2015).

Figures 2.22 and 2.23 show the trajectory diagrams of the cars in the intervals where the leading car moves at a constant speed of 25 km/h and 30 km/h, respectively. Since the cars move almost straight, we show only the change of x location over time. One can see the formation, propagation, and growth of traffic disturbances. Stoppage of cars has been often observed in the rear part of the 51-car platoon. This indicates that the traffic flow is also unstable. But it is noted that the stoppage of cars has not been observed in all intervals even when the prevailing flow condition is not stable and the appearance of stoppage is irregular. This indicates that traffic flow instability is probabilistic.

Figure 2.24 shows the trajectory diagrams of the cars in intervals 14 and 16. One can see that the initial disturbance of the leading car in interval 14 has quickly

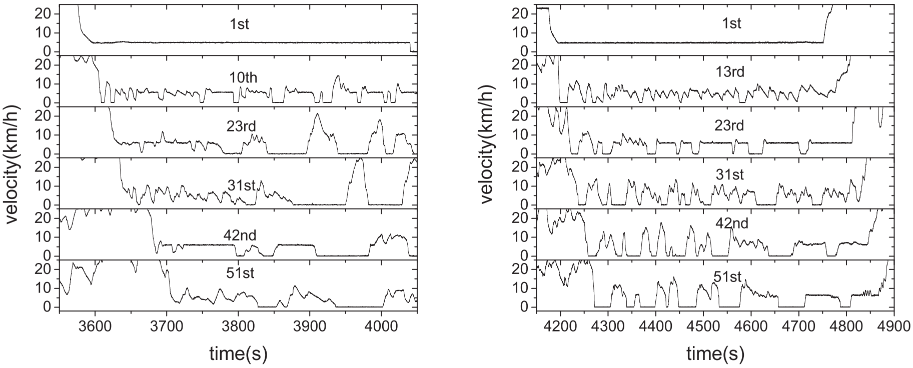

(a) (b)

FIG. 2.20 – Velocities of several typical cars in which the leading car moves with a speed of 5 km/h. (a) Interval 10, (b) interval 21.

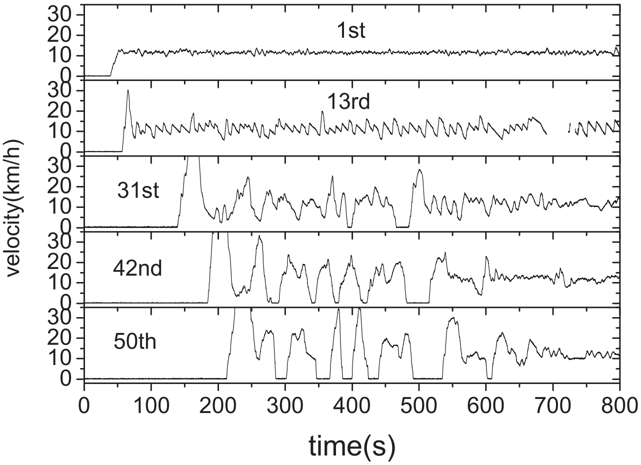

FIG. 2.21 – Velocities of several typical cars in which the leading car moves with a speed of 12 km/h in interval 11.

dissipated. In interval 16, the initial disturbance is so small that it can hardly be identified in the trajectory diagram. But some later disturbances grow in the platoon and eventually cause a stoppage toward the rear of the platoon. This means that a small disturbance is not necessarily able to induce traffic instability even when flow conditions are prone to be unstable, which also implies that the instability is related to the stochastic nature of traffic flow rather than a speed or density threshold alone.

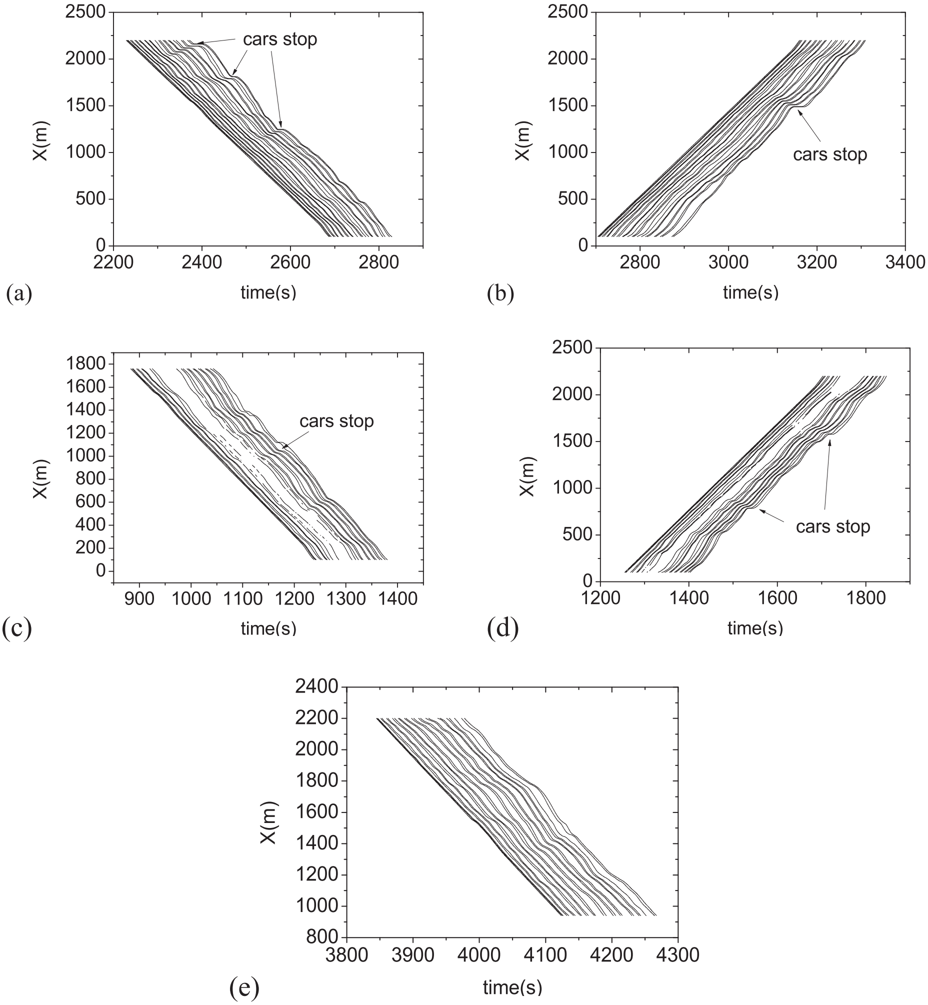

Fig. 2.22 – Trajectory diagrams in which the leading car moves at 25 km/h. (a) Interval 7, (b) interval 8, (c) interval 12, (d) interval 13, (e) interval 20. Large gaps in the trajectories in (c) and (d) are due to the GPS device problem or signal problem, which results in the missing location data of some cars.

Figures 2.25 and 2.26 show the trajectory diagrams of the cars in which the leading car moves at the speed of 40 km/h and 50 km/h, respectively. One can see the propagation and growth of traffic disturbances are quite different from that in figures 2.22–2.24. In most cases, the disturbances are being dampened or absorbed, while they grow in some cases along the platoon but the growth eventually tapers off and never caused traffic stoppage. This implies that once the travel speed exceeds a certain threshold, the ability of traffic to cope with small disturbances becomes sufficiently strong that the traffic flow becomes stable.

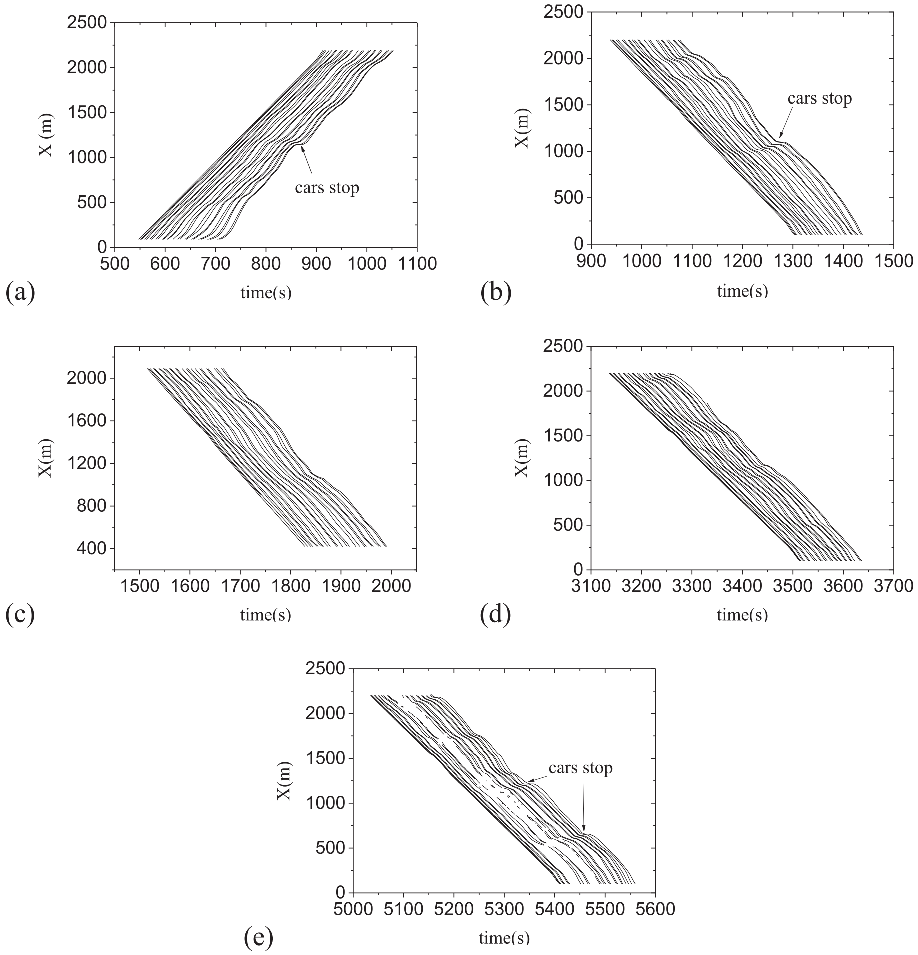

FIG. 2.23 – Trajectory diagrams in which the leading car moves at 30 km/h. (a) Interval 2, (b) interval 3, (c) interval 9, (d) interval 18, (e) interval 23. Large gaps in the trajectories in (e) are due to GPS device problem or signal problem.

Figure 2.27 shows the standard deviations of the velocity of each car along the platoon. To calculate the standard deviation of the velocity of the cars, we use only stationary state data in each interval. One can see that the results corresponding to the first half of the platoon are close to the previous experimental results[9], which indicates that the 51-car-platoon experiment has reproduced and confirmed the previous findings. When the leading car moves at 5 km/h, the standard deviation

---

[9] Note that in previous 25-car-platoon experiment, the leading car moves with 7 km/h and 15 km/h, which are slightly larger than 5 km/h and 12 km/h in the present 51-car-platoon experiment.

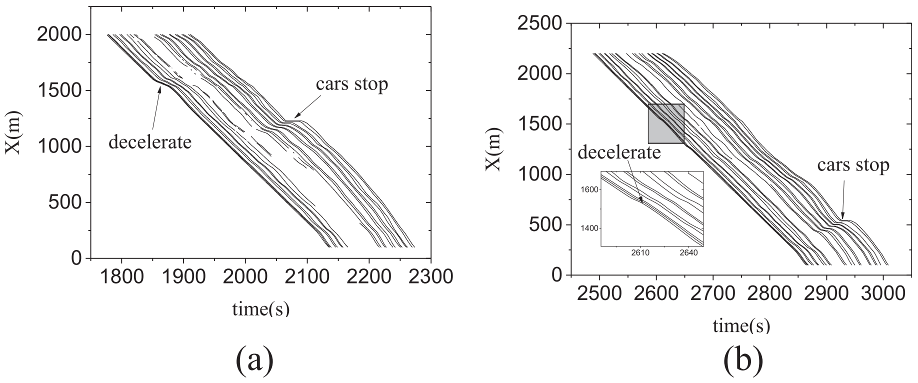

Fig. 2.24 – Trajectory diagrams in which the leading car moves at 30 km/h, but has decelerated and accelerated to 30 km/h again. (a) Interval 14, (b) interval 16. Large gaps in the trajectories are due to the GPS device problems or signal problems.

notably bends down in the second half of the platoon, which means the stop-and-go traffic has almost fully developed, see figure 2.27a. In contrast, when the leading car moves at 12 km/h, the stop-and-go traffic has not yet fully developed, thus the standard deviation still increases quickly in the second half of the platoon, see figure 2.27b.

Figure 2.27c and d show that when the leading car moves at 30 km/h or lower, the standard deviation increases rather quickly along the platoon, all the way to the last vehicle. On the other hand, when the leading car moves at 40 km/h or more, the standard deviation also increases quickly for the first 10–15 cars in the platoon but tapers off along the platoon. The standard deviation is almost flat in the rear of the 51-car-platoon,[10] see figure 2.27e and f.

Based on the findings, we argue that traffic instability might mainly depend on traffic flow speed. It is likely that there exists a critical speed between 30 km/h and 40 km/h for Chinese drivers (the specific value probably depends on the type of drivers and roads).[11] Above the critical speed, the traffic flow is likely to be stable. In contrast, below the critical speed, traffic flow is unstable and will finally lead to the formation of traffic jams.

---

[10] Note that in interval 22, the leading car accelerates from 5 km/h to 50 km/h. The following cars react slowly to the acceleration, as can be seen from figure 2.26b. The cars have to accelerate to a quite large speed to catch up with the preceding cars. Removing the non-stationary state, the stationary state is quite short for cars in the rear part of the platoon. To calculate the standard deviation of the velocity of the cars, we use only stationary state data. In term of this situation, we have not used the data in interval 22 to calculate the standard deviation.

[11] It has been experimentally demonstrated that in pedestrian flow, cultural difference has a significant quantitative impact: German participants is more sensitive to density than Indian (Chattaraj *et al.*, 2009). Therefore, similarly, the critical speed might also depend on the culture background of drivers.

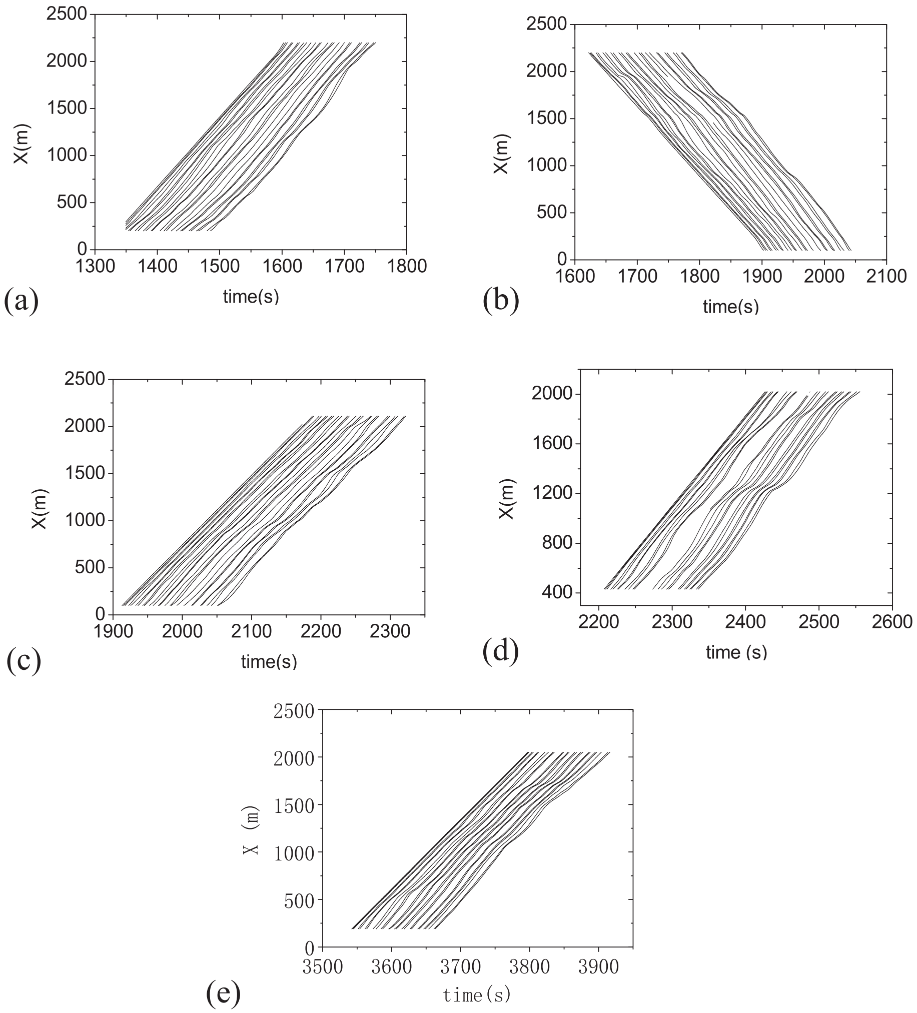

Fig. 2.25 – Trajectory diagrams in which the leading car moves at 40 km/h. (a) Interval 4, (b) interval 5, (c) interval 6, (d) interval 15, (e) interval 19. Large gaps in the trajectories in (d) are due to the GPS device problem or signal problem.

2.5.2 Corroborating Empirical Observations

We have also analyzed the traffic data from the Nanjing Airport Highway, which also supports our experimental findings. This section shows some examples.

The Nanjing Airport Highway is a four-lane highway (with two lanes in each direction) connecting the urban districts of Nanjing with the Lukou Airport. The speed limit on this highway is 120 km/h. There are 40 cameras along the 28-km-long highway, and the studied section is shown in figure 2.28. In this paper, all data presented are taken from the outbound direction heading to the airport. The bottlenecks

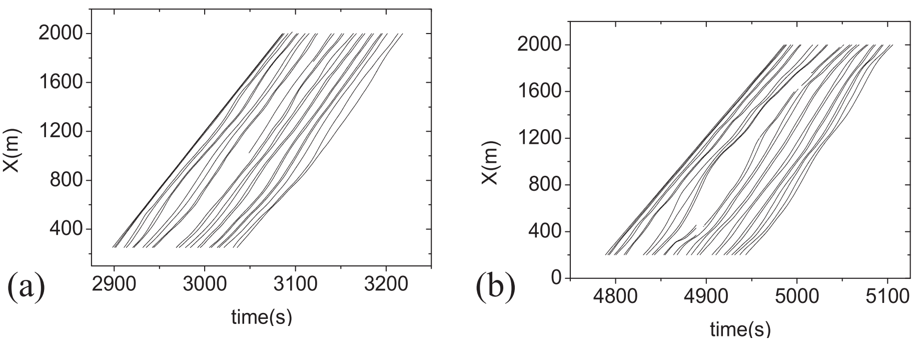

FIG. 2.26 – Trajectory diagrams in which the leading car moves at 50 km/h. (a) Interval 17, (b) interval 22. Some large gaps in the trajectories are due to the GPS device problem or signal problem.

formed by upstream and downstream ramps were not active during the observation period, and low-speed traffic flows were all induced by moving bottlenecks.

The velocity of each vehicle is extracted from the videos using the Autoscope Rackvision Terra system. We checked the videos and corrected some obvious errors by the Tracker software. Only data collected on the left lane is used in the subsequent analysis because Autoscope Rackvision Terra was unable to produce reliable data on the right lane (at cameras 06 and 07, images of vehicles on the right lane were frequently covered by those on the left lane and therefore cannot be correctly recognized by the software).

Firstly, we show two examples that when the average traffic speed is above a critical value, the traffic flow is stable.

Example 1: Figure 2.29a shows the snapshot of a moving bottleneck. In this case, the low-speed traffic flow is induced by a moving bottleneck, which is a highway maintenance vehicle (HMV) and it moves at a very slow but constant velocity (18 km/h). The HMV moves along the emergency lane but still affects main lane traffic as a moving bottleneck and low-speed traffic flow appear behind the HMV. The average velocity of these vehicles is about 47 km/h. Figure 2.29b shows the time series of single-vehicle velocities in this case. One can see that the traffic flow is stable and the fluctuation of velocities is small.

Example 2: In this example, the HMV travels at the same speed as in example 1, but it travels on the left shoulder, see figure 2.30a. Hence it affects main lane traffic more seriously than the HMV in example 1. Consequently, the average velocity of the induced congested flow is about 40 km/h, lower than that in example 1. One can see that congested flow is also stable, see figure 2.30b.[12]

---

[12] We notice that there is a velocity drop at about 7:58. Unfortunately, due to a lack of videos between the cameras, the exact origin of the velocity drop cannot be known. One possible reason might be an over-deceleration of drivers when the vehicles move from high speed traffic into low speed traffic.

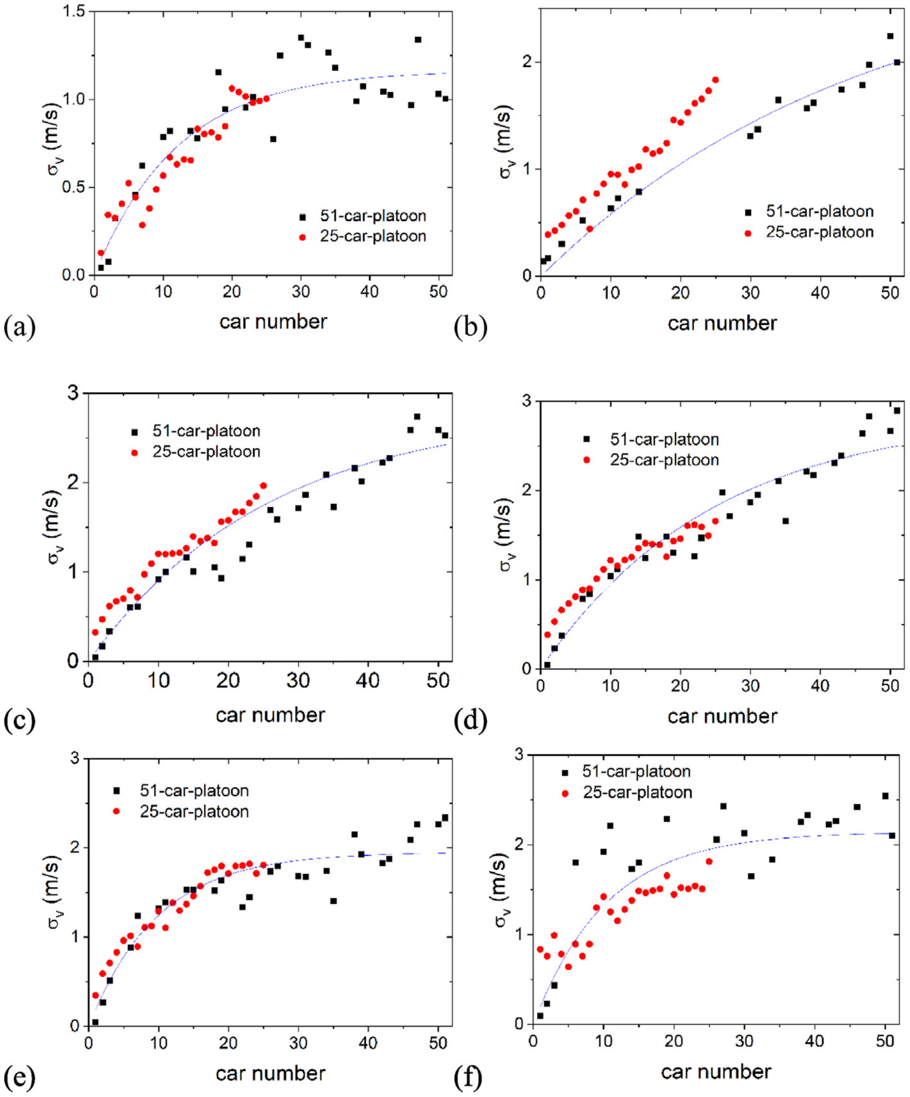

Fig. 2.27 – The standard deviation of the velocity of each car along the platoon averaged over intervals. The black squares show the present results of a 51-car-platoon experiment. The red circles show the previous results of the 25-car-platoon experiment. The blue line is the fitted curve. The leading car moves at the speed of (a) 5 km/h, (b) 15 km/h, (c) 25 km/h, (d) 30 km/h, (e) 40 km/h, (f) 50 km/h.

Next, we show one example that when the speed is below a critical speed, the traffic flow is unstable.

Example 3: In this example, the HMV travels also at 18 km/h. However, since the HMV moves in the middle of the left lane (figure 2.31a), it affects main lane traffic

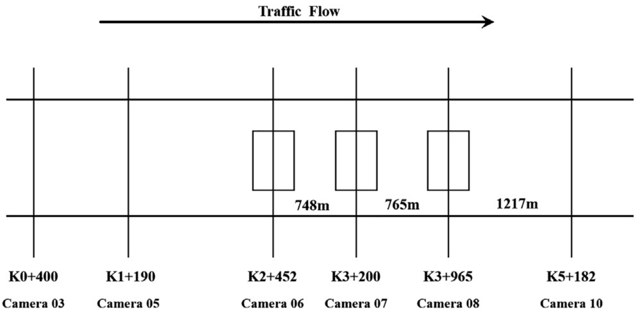

FIG. 2.28 – The sketch of part of the Nanjing Airport Highway and locations of the cameras. Here KX + Y is widely used in transportation engineering in China and it means that the camera is 1000X + Y m away from the highway end (the end in the urban district of Nanjing airport highway). Distances between cameras 06, 07, 08, and 10 are shown in the sketch.

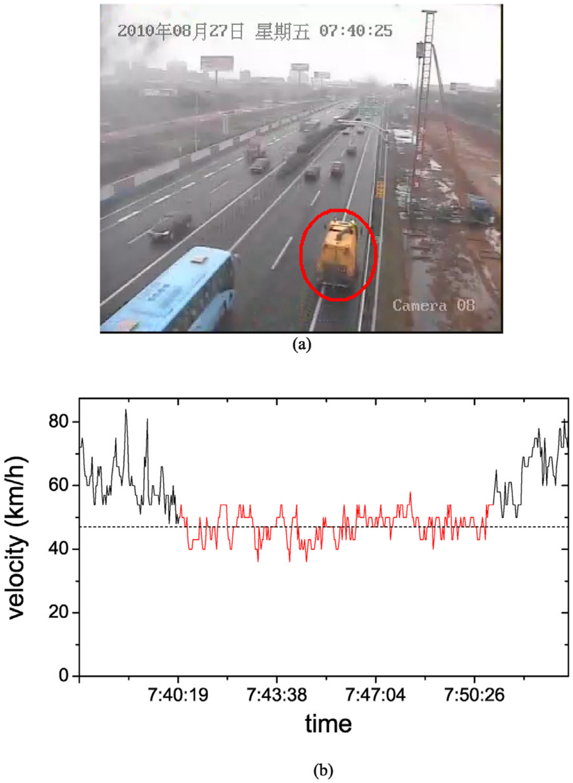

FIG. 2.29 – (a) The screenshot of a moving bottleneck on the Nanjing Airport Highway, as indicated by the red circle. (b) The corresponding vehicle-level velocities on the left lane. The dashed line shows a velocity of 47 km/h.

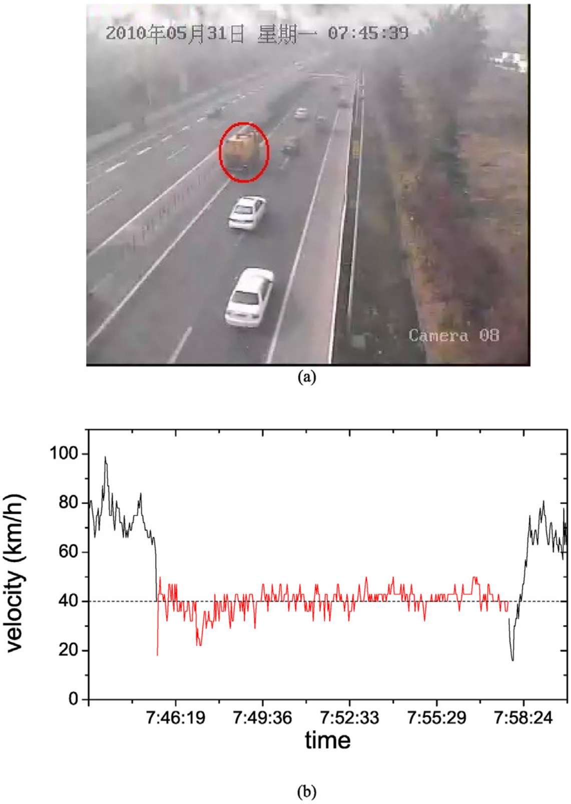

FIG. 2.30 – (a) The screenshot collected at camera 08, May 31, 2010, 7:45:39 am; (b) The corresponding vehicle-level velocities. The line shows a velocity of 40 km/h.

much more severely than the other two cases: the traffic flow speed is about 30 km/h. In this case, traffic flow is unstable and a jam is induced,[13] see figure 2.31b.

2.6 The High-Speed Experiment

2.6.1 Experimental Setup

Previous experiments are conducted with the speed of the leading vehicle of the platoon lower than 60 km/h. In this section, the high-speed experiments were carried out on the Xinqiao airport highway in Hefei, China on September 19, 2014.

---

[13] The cars have stopped as observed from the videos. However, Autoscope cannot detect the zero velocity when the car stops, since it measures the time that a car passes two nearby locations. Thus, only the starting velocity which is a little larger than zero can be recorded.

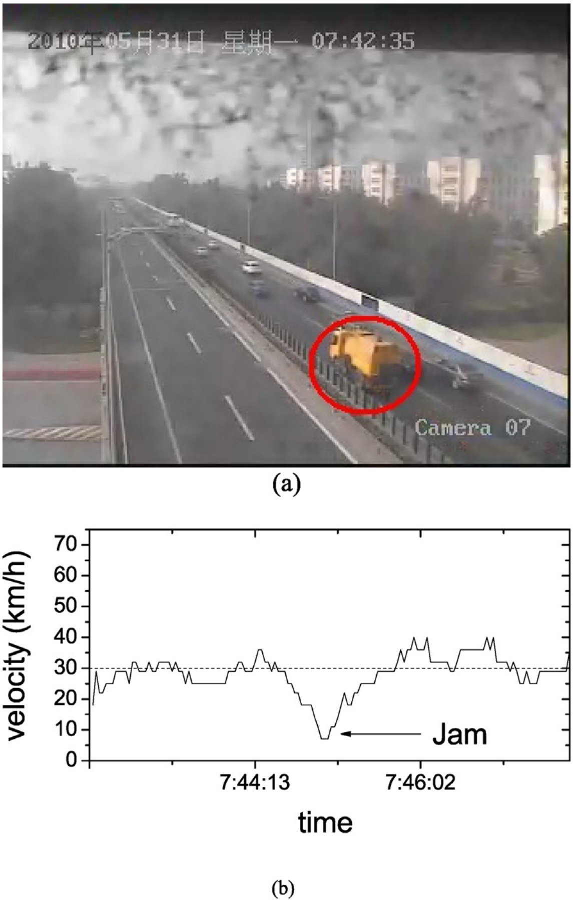

Fig. 2.31 – An example in which a jam is induced. (a) The screenshot shows the moving bottleneck; (b) the corresponding vehicle-level velocities. The dashed line shows the velocity of 30 km/h.

See figure 2.32a for the map of the highway. The trajectories of cars measured by GPS were shown in figure 2.32b. A one-way journey from the toll station to the airport is approximately 15 km. The highway has three lanes in each direction, and the traffic on the highway is very dilute. Therefore, there is no interference from other vehicles that are not part of the experiment.

In the experiment, the platoon has 11 cars. In the odd/even runs, the platoon goes from the toll station/airport to the airport/toll station. Due to the loop road in the airport area (see inset in figure 2.32b), the platoon must decelerate but they do not need to stop. In the toll-station area, the platoon starts at zero speed. For example, one can refer to figure 2.32c, which shows the leading car speed in runs 1

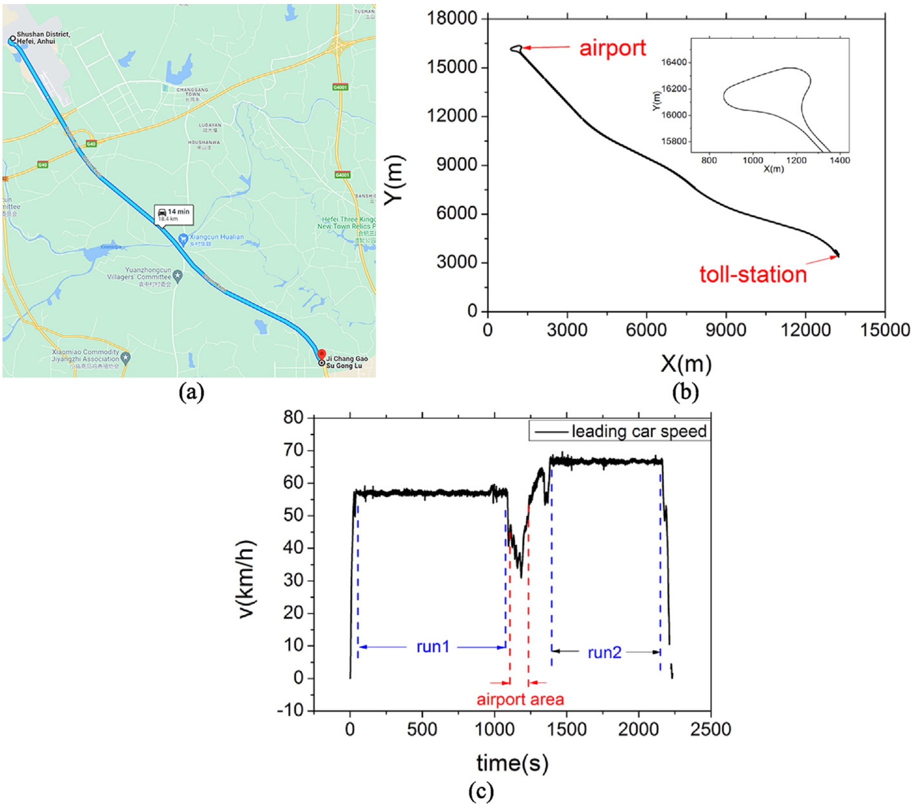

(a) (b) (c)

Fig. 2.32 – (a) Map of the airport highway. (b) The trajectories of cars measured by the GPS installed in the cars. (c) The leading car speed in runs 1 and 2.

and 2. The leading car has a cruise control system, and the car moves at constant speed in each run. Twelve runs have been performed.

2.6.2 Experimental Results

The typical spatiotemporal patterns of the velocity in the experimental traffic flow are shown in figure 2.33. As in the low-speed experiment, one can observe the stripes structure, which exhibits the formation and evolution of slow-down and speed-up oscillations.

Figure 2.34 shows the standard deviation σ_v of the velocity of each car. As in low-speed conditions, the standard deviation σ_v also grows in a concave way. Figure 2.35 compares the growth of σ_v between high speed situation and low speed situation, one can see that the growth of σ_v for the first 11 cars is more rapid in high-speed conditions. However, when the platoon speed reaches 50 km/h, the growth rate of the oscillation of the first 11 cars becomes almost independent of the platoon speed, in which the green data accord well with the red and the black data.

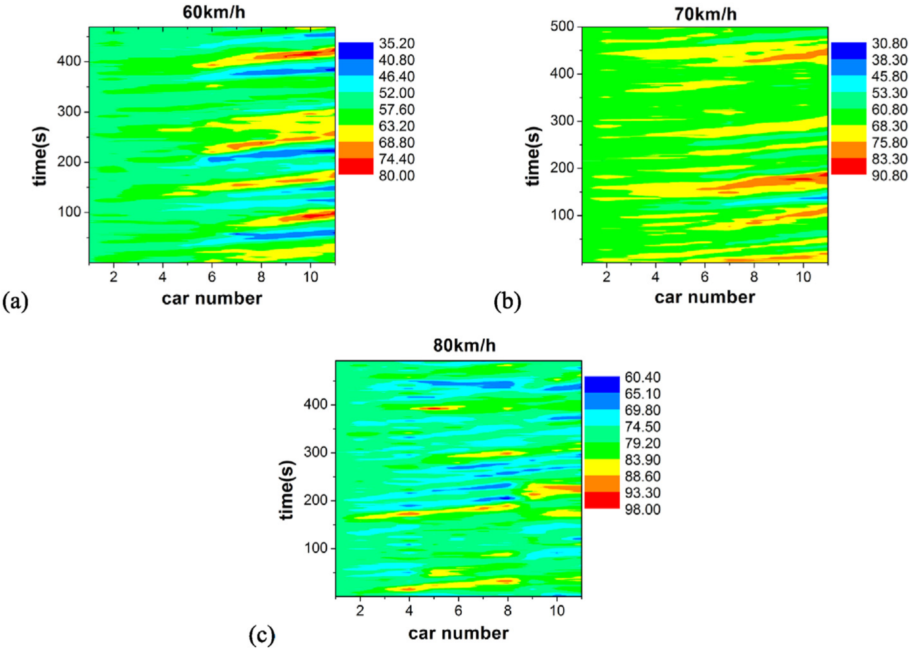

FIG. 2.33 – Typical spatiotemporal patterns in the stationary state in experiments.

2.7 The Lightly Congested Flow Experiment

2.7.1 Experimental Setup

The experiment was performed on Nov. 9, 2019, in the test field affiliated with the Research Institute of Highway, Ministry of Transport, China (Zheng *et al.*, 2021). For a snapshot of the experiment, see figure 2.36. The instruction to the drivers is "Drive as if you were on rush hour expressways. Follow the vehicle ahead closely, whenever safety permits".[14]

We recruited 40 cars/drivers in the experiment and classified the cars/drivers into 8 groups A ∼ H. The order of cars/drivers in each group is always fixed. The number of groups and their order change in different runs. Car/Driver No. is the unique identification for each car in all experiment Runs. Cars in group A are numbered 1 ∼ 5, group B as 6 ∼ 10, …, and group H 36 ∼ 40.

Initially, the cars are stopped bumper-to-bumper. When a Run starts, the first car accelerates to 20 km/h and travels at that speed until the last car

---

[14] Note that how to instruct the drivers is an important issue in traffic flow experiment. Different instructions could possibly lead to different results. For some more details, see Zheng *et al.* (2023).

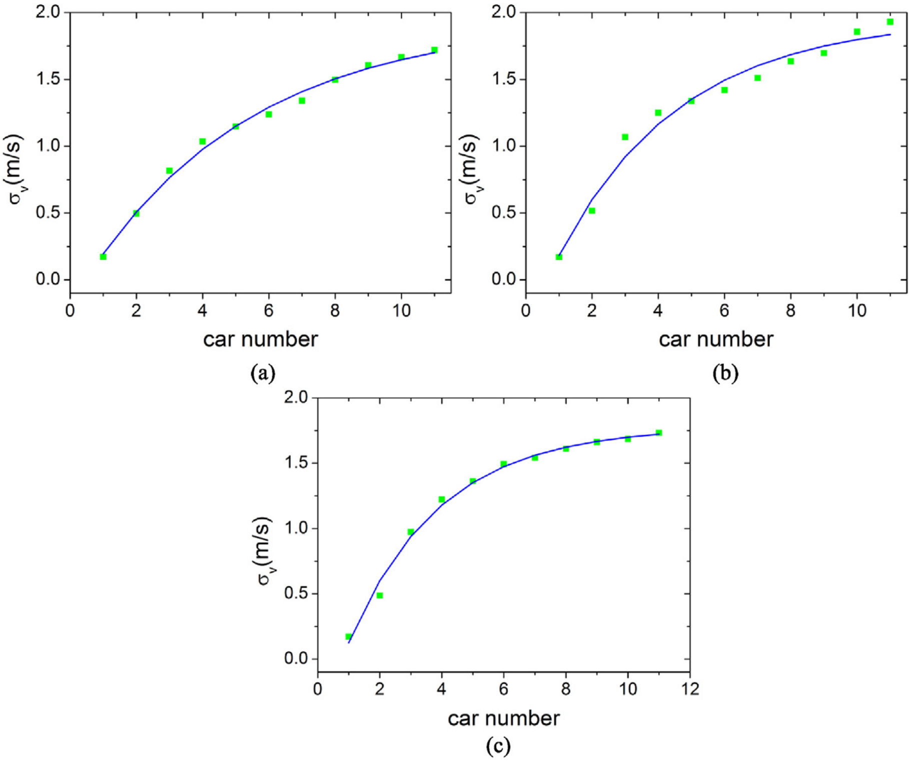

FIG. 2.34 – The standard deviation of the velocity of each car at high speeds. Symbols show experiment results; thick blue line is fitting curve. The leading car speed is (a) 60 km/h, (b) 70 km/h, (c) 80 km/h.

starts up.[15] Then the first car moves to catch up with the last car. Details of the experiment Runs are shown in table 2.3 in chronological order. It is worth mentioning that before the formal runs, we carried out a warm-up preparation run with 40 vehicles so that drivers can be familiar with the track.[16]

2.7.2 Experimental Results

The spatiotemporal evolution diagrams with 40 cars are shown in figure 2.37. For convenience, the car running directions in all runs have been converted to be clockwise in the diagram, and the position of the last car in the platoon is set to 0 at $t = 0$. One can see that, despite having the same initial condition, each Run

---

[15] The aim of the instruction is to dissipate the initial jam. Although the leader did not strictly obey the instruction and moved faster than 20 km/h before the last car started, the initial jam still dissipated as expected.

[16] The warm-up phase lasts about 8 min, which is not long enough for all drivers to get accustomed with the setting.

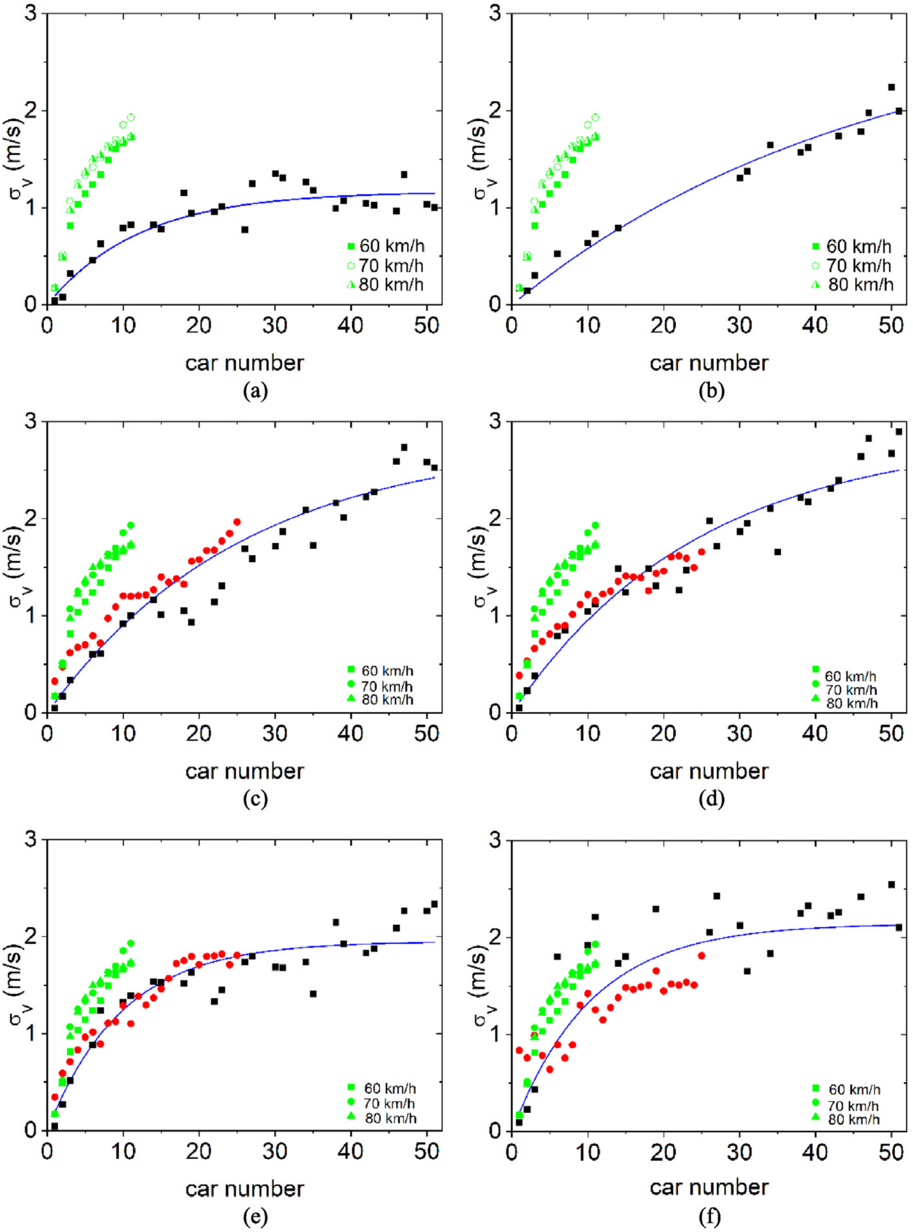

FIG. 2.35 – Standard deviation of velocity of each car. Symbols show experiment results (green for 11 cars experiment, red for 25 cars experiment, black for 51 cars experiment), thick blue line is fitting curve of 51 cars experiment. The leading car speed is (a) 5 km/h, (b) 12 km/h, (c) 25 km/h, (d) 30 km/h, (e) 40 km/h, (f) 50 km/h, for the 25-car and 51-car experiments.

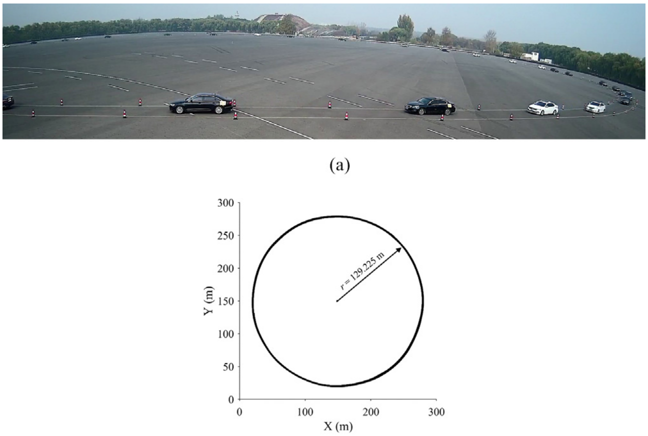

(a)

(b)

FIG. 2.36 – (a) A snapshot of the experiment. Due to the large circumference, the camera is not able to cover the whole track. (b) The trajectories of cars measured by the GPS installed on the cars.

TAB. 2.3 – Details of the experiment run in chronological order.

Run number	Vehicle number	Group number and order	Experiment time	Duration (min)	Traffic direction
1	40	ABCDEFGH	10:42 ~ 11:07	25	Clockwise
2	35	ACDEFGH	11:50 ~ 12:10	20	
3	30^{*}	ACEGHB	12:55 ~ 13:05	10	
4	40^{**}	ACEGHBDF	13:23 ~ 13:48	25	Counterclockwise
5	35^{***}	ACEGBDF	14:46 ~ 15:06	20	
6	40	ACEGBDFH	15:18 ~ 15:43	25	

* One vehicle has Electronic Stability Program (ESP) fault and leaves the track at $t = 530$ s.
** The same vehicle has ESP fault again and leaves the track at $t = 240$ s.
*** GPS signal of one vehicle is missing.

produces a quite different flow pattern, and not all Runs produce the stop-and-go type of clusters, which highlights the stochastic nature of traffic dynamics.

40 vehicles: In Run 1, low-speed clusters emerge and propagate upstream, see figure 2.37a. The propagation speed is about 14 km/h, as indicated by the black lines. The evolution and propagation of the clusters are not in a straightforward manner. Specifically, the first cluster emerges at $t \approx 243$ s (indicated by arrow 1). It propagates until $t \approx 725$ s and disappears (indicated by arrow 2). A second cluster emerges from $t \approx 785$ s (indicated by arrow 3). At $t \approx 820$ s (indicated by arrow 4), the cluster splits into two clusters. The two clusters disappear at $t \approx 935$ s (indicated by arrow 5) and $t \approx 990$ s (indicated by arrow 6), respectively. At $t \approx 1045$ s (indicated by arrow 7), a third cluster emerges, which propagates until the end of the Run.

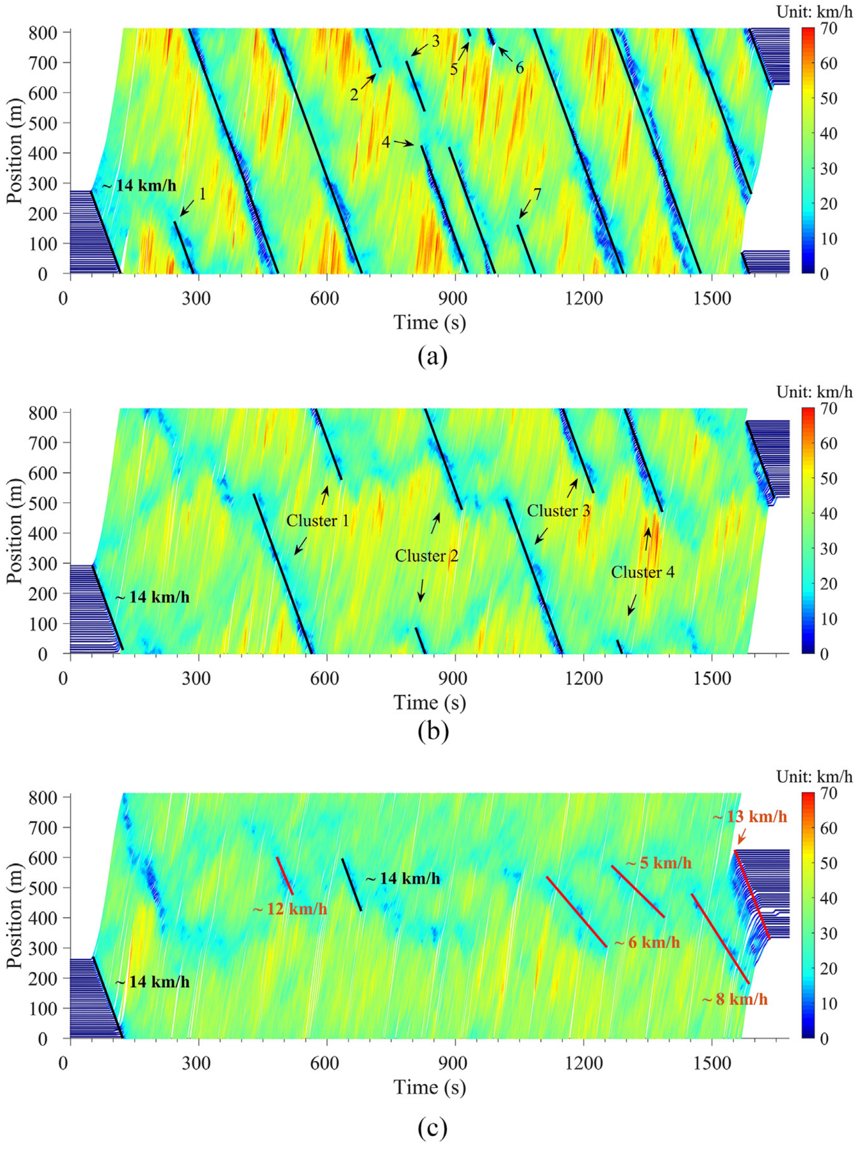

FIG. 2.37 – The spatiotemporal evolution diagrams with 40 cars. (a) Run 1; (b) Run 4; (c) Run 6. The black lines have a slope of 14 km/h.

In Run 4, there form four main clusters successively, see figure 2.37b. The first and the third ones propagate for about 205 s. The second and the fourth ones are much shorter and propagate for about 107 s.

In Run 6, the clusters are rather blurred, see figure 2.37c. The propagation of clusters is not as clearly identifiable as in Runs 1 and 4. The propagation speed is not constant and is mostly smaller than 14 km/h, as indicated by red lines.

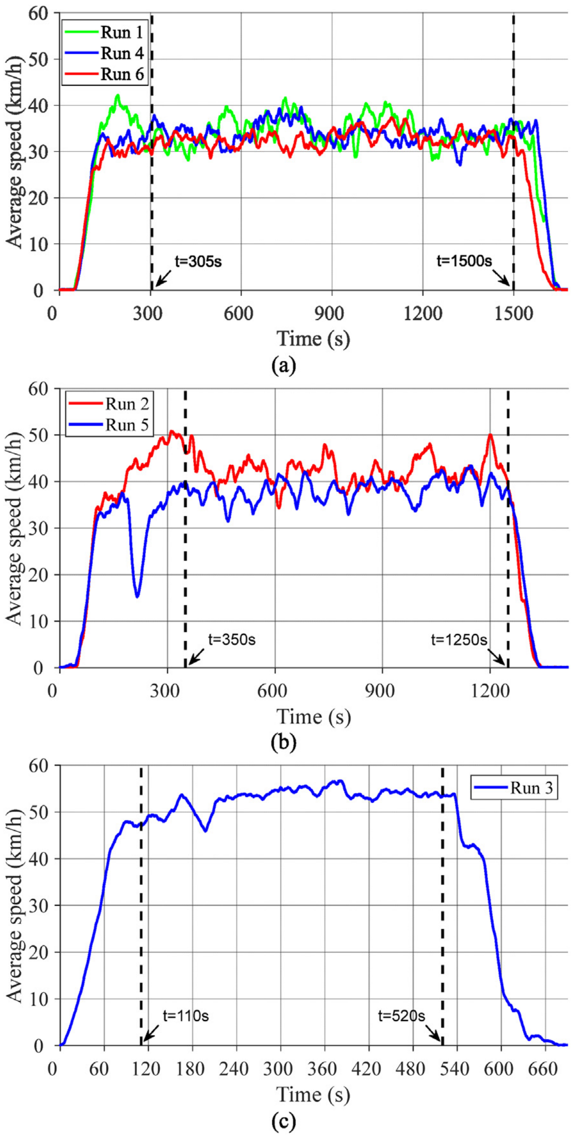

(a)

(b)

(c)

Fig. 2.38 – Time series of average speed. (a) Runs 1, 4, 6; (b) Runs 2, 5; (c) Run 3. The two black dotted lines mark the interval used in the following analysis.

Although the spatiotemporal evolution processes are remarkably different in the three Runs, the average speed is very close to each other. Figure 2.38a compares the time series of the average speed in the three Runs. One can see that the three curves are entangled.

35 vehicles: Figure 2.39 shows the spatiotemporal evolution diagrams with 35 cars. In Run 2, low-speed cluster is still observed to propagate for a rather long time.

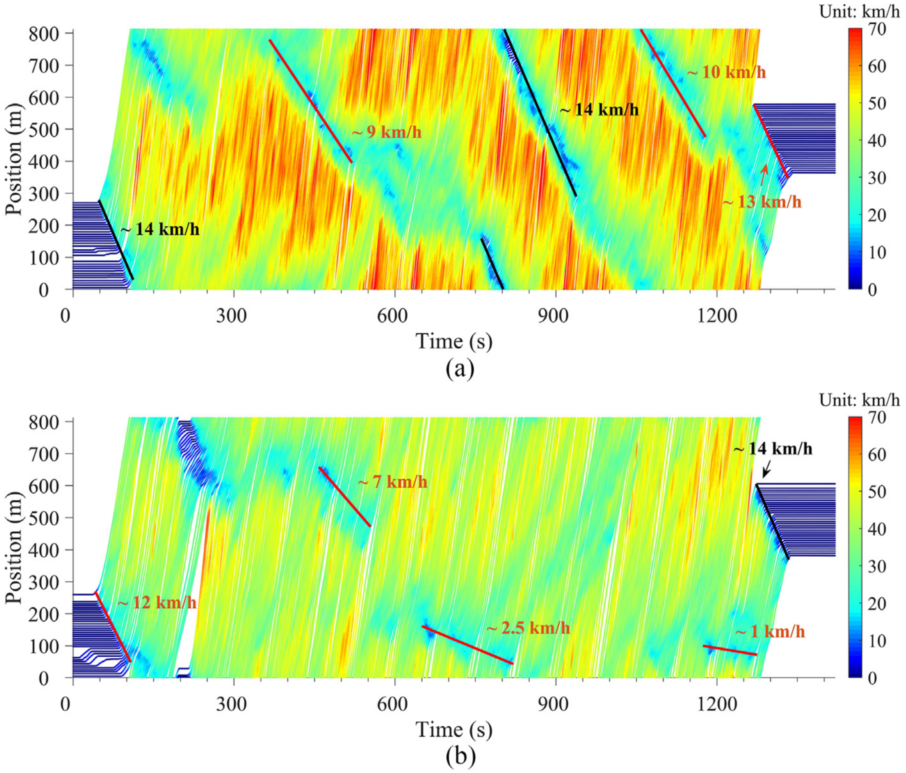

Fig. 2.39 – The spatiotemporal evolution diagrams with 35 cars. (a) Run 2; (b) Run 5. The black lines have a slope of 14 km/h. In (b), a car stops at $t \approx 197$ s because the door is not closed. The driver stops to close the door.

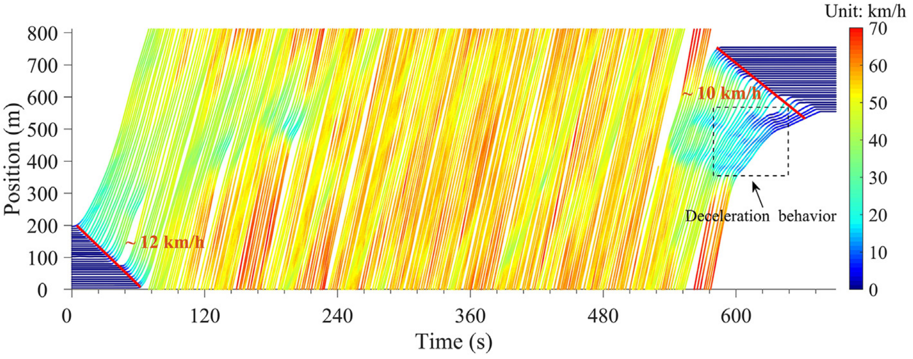

Fig. 2.40 – The spatiotemporal evolution diagram with 30 cars in Run 3.

However, sometimes the propagation speed of the cluster is smaller, as indicated by red lines. In Run 5, the propagation speed of the low-speed cluster is much smaller, as indicated by the red lines.

Figure 2.38b compares the time series of average speed in the two Runs. One can see that the average speed in Run 5 is notably lower.

30 vehicles: Figure 2.40 shows the spatiotemporal evolution diagram with 30 cars. Traffic flow is rather homogeneous. No low-speed cluster emerges. The average speed in this Run is obviously larger than that in other Runs, see figure 2.38c.

References

Ahn S., Laval J., Cassidy M.J. (2010) Effects of merging and diverging on freeway traffic oscillations theory and observation, *Transp. Res. Rec.* 1–8.

Bando M., Hasebe K., Nakayama A., Shibata A., Sugiyama Y. (1995) Dynamical model of traffic congestion and numerical simulation, *Phys. Rev. E* **51**, 1035–1042.

Bertini R.L., Leal M.T. (2005) Empirical study of traffic features at a freeway lane drop, *J. Transp. Eng.* **131**, 397–407.

Cassidy M.J., Rudjanakanoknad J. (2005) Increasing the capacity of an isolated merge by metering its on-ramp, *Transp. Res. B: Method* **39**, 896–913.

Chandler R.E., Herman R., Montroll E.W. (1958) Traffic dynamics: Studies in car following, *Oper. Res.* **6**, 165–184.

Chattaraj U., Seyfried A., Chakroborty P. (2009) Comparison of pedestrian fundamental diagram across cultures, *Adv. Complex Syst.* **12**, 393–405.

Chen D., Ahn S., Laval J., *et al.* (2014) On the periodicity of traffic oscillations and capacity drop: The role of driver characteristics [J], *Transp. Res. B: Method.* **59**, 117–136.

Coifman B., Kim S. (2011) Extended bottlenecks, the fundamental relationship, and capacity drop on freeways [J], *Proc.-Soc. Behav. Sci.* **17**, 44–57.

Dong J., Mahmassani H.S. (2011) Predicting flow breakdown probability and duration in stochastic network models: Impact on travel time reliability, 90th Annual Meeting of the Transportation Research Board, Washington, DC.

Gartner N.H., Messer C.J., Rathi A. (2002) Traffic flow theory – A state-of-the-art report: revised monograph on traffic flow theory.

Gazis D.C., Herman R., Potts R.W. (1961) Car-following theory of steady-state traffic flow, *Oper. Res.* **7**, 499–505.

Gazis D.C., Herman R., Rothery R.W. (1959) Nonlinear follow-the-leader models of traffic flow, Oper. Res. 9, 545–567.

Gipps P.G. (1981) A behavioral car-following model for computer-simulation, *Transp. Res. B: Method* **15**, 105–111.

Herman R., Montroll E., Potts R., Rothery R. (1959) Traffic dynamics: Analysis of stability in car following, *Oper. Res.* **7**, 86–106.

Jiang R., Hu M.B., Zhang H.M., Gao Z.-Y., Jia B., Wu Q.-S. (2015) On some experimental features of car-following behavior and how to model them, *Transp. Res. B: Method* **80**, 338–354.

Jiang R., Hu M.B., Zhang H.M., Gao Z.Y., Jia B., Wu Q.-S., Wang B., Yang M. (2014) Traffic experiment reveals the nature of car-following, *Plos One* **9**, e94351.

Jiang R., Wu Q., Zhu Z. (2001) Full velocity difference model for a car-following theory, *Phys. Rev. E* **64**, 017101.

Kerner B.S., Klenov S.L., Hiller A. (2007) Empirical test of a microscopic three-phase traffic theory [J], *Nonlinear Dyn.* **49**, 525–553.

Laval J., Chen D., Ben Amer K., Guin A., Ahn S. (2009) Evolution of oscillations in congested traffic improved estimation method and additional empirical evidence, *Transp. Res. Rec.* 194–202.

Laval J.A., Leclercq L. (2010) A mechanism to describe the formation and propagation of stop-and-go waves in congested freeway traffic, *Philos. T. Roy. Soc. A: Math. Phy. Eng. Sci.* **368**, 4519–4541.

Li X., Cui J., An S., Parsafard M. (2014) Stop-and-go traffic analysis: Theoretical properties, environmental impacts and oscillation mitigation, *Transp. Res. B: Method* **70**, 319–339.

Mauch M., Cassidy M.J. (2002) Freeway traffic oscillations: Observations and predictions, *Transportation and traffic theory in the 21st century* (M.A.P. Taylor, Ed.). pp. 653–673.

Ngoduy D., Lee S., Treiber M., Keyvan-Ekbatani M., Vu H.L. (2019) Langevin method for a continuous stochastic car-following model and its stability conditions, *Transp. Res. C: Emerg. Technol.* **105**, 599–610.

NGSIM (2006) Next Generation Simulation.

Stern R.E., Cui S., Delle Monache M.L., Bhadani R., Bunting M., Churchill M., Hamilton N., Haulcy R.m., Pohlmann H., Wu F., Piccoli B., Seibold B., Sprinkle J., Work D.B. (2018) Dissipation of stop-and-go waves via control of autonomous vehicles: Field experiments, *Transp. Res. C: Emerg. Technol.* **89**, 205–221.

Sugiyama Y., Fukui M., Kikuchi M., Hasebe K., Nakayama A., Nishinari K., Tadaki S.-i., Yukawa S. (2008) Traffic jams without bottlenecks – Experimental evidence for the physical mechanism of the formation of a jam, *New J. Phys.* **10**, 033001.

Sun J., Li T., Yu M., Zhang H.M. (2018) Exploring the congestion pattern at long-queued tunnel sag and increasing the efficiency by control, *IEEE Trans. Intell. Transp. Syst.* **19**, 3765–3774.

Tadaki S.I., Kikuchi M., Fukui M., Nakayama A., Nishinari K., Shibata A., Sugiyama Y., Yosida T., Yukawa S. (2013) Phase transition in traffic jam experiment on a circuit, *New J. Phys.* **15**, 103034.

Tomer E., Safonov L., Havlin S. (2000) Presence of many stable nonhomogeneous states in an inertial car-following model, *Phys. Rev. Lett.* **84**, 382–385.

Treiber M., Hennecke A., Helbing D. (2000) Congested traffic states in empirical observations and microscopic simulations, *Phys. Rev. E* **62**, 1805.

Treiber M., Kesting A. (2018) The Intelligent Driver Model with stochasticity – New insights into traffic flow oscillations, *Transp. Res. B: Method.* **117**, 613–623.

Wang, C., Coifman, B. (2008) The effect of lane-change maneuvers on a simplified car-following theory, *IEEE T. Intell. Transp.* **9**, 523–535.

Wang Y., Li X., Tian J., Jiang R., (2020) Stability analysis of stochastic linear car-following models, *Transp. Sci.* **54**, 274–297.

Zheng S.-T., Jiang R., Tian J.-F., Li X.-P., Jia B., Gao Z.-Y. (2023) A comparison study on the growth pattern of traffic oscillations in car-following experiments, *Transportmetrica B* **1**(11), 706–724.

Zheng S.-T., Jiang R., Tian J.-F., Zhang H., Li Z.-H., Gao L.-D., Jia B. (2021) Experimental study on properties of lightly congested flow, *Transp. Res. B: Method.* **149**, 1–19.

Zheng Z., Ahn S., Chen D., Laval J. (2011) Freeway traffic oscillations: Microscopic analysis of formations and propagations using wavelet transform, *Transp. Res. B: Method* **45**, 1378–1388.

Zielke B.A., Bertini R.L., Treiber M. (2008) Empirical measurement of freeway oscillation characteristics, *Transp. Res. Rec.* 57–67.

Chapter 3

Car Following Behavior Analysis

In this chapter, we analyze the characteristics of car-following behavior in traffic platoon, including the velocity distribution, the spacing and platoon length analysis, the acceleration and the wave travel time analysis, and so on.

3.1 The Velocity Distribution Analysis

We present the velocity distributions of the cars in the 25-car-platoon experiment. In figure 3.1, the panels (a)–(e) show velocity distributions for different leading car velocities: (a) 50 km/h, (b) 40 km/h, (c) 30 km/h, (d) 15 km/h, (e) 7 km/h. The black squares are experimental results, the blue circles are simulation results of the model proposed in section 5.2, and the red lines are the fitted Normal distribution curves. As shown in figure 3.1, generally the velocity distributions can be well-fitted by Normal distributions. There are two exceptions. One exception is when traffic is stop-and-go at low speeds, there appears another peak probability near zero speeds as shown by the red arrows in figure 3.1d and e. The other exception is when the leading car moves at a low constant velocity (7 km/h) in panel (e), some drivers drive in a peculiar way: they did not step on the gas pedal just as the leading car, and their cars move with constant velocity for some periods of time (see figure 3.2). As a result, there is another peak in the probability distribution at 7 km/h, marked by the blue arrows in figure 3.1e. Consistent with the (concave) growth of σ_v with respect to the position of a car in the platoon, the velocity distributions become flatter for cars further away from the platoon leader.

3.2 The Spacing Analysis

Figure 3.3a, b show two examples of the evolution of the spacing of car No. 1 (which is the second car in the platoon) as well as the velocities of the car and its preceding car in the first set of experiments. In figure 3.3a, the car velocity is nearly constant

DOI: 10.1051/978-2-7598-3193-7.c003
© Science Press, EDP Sciences, 2023

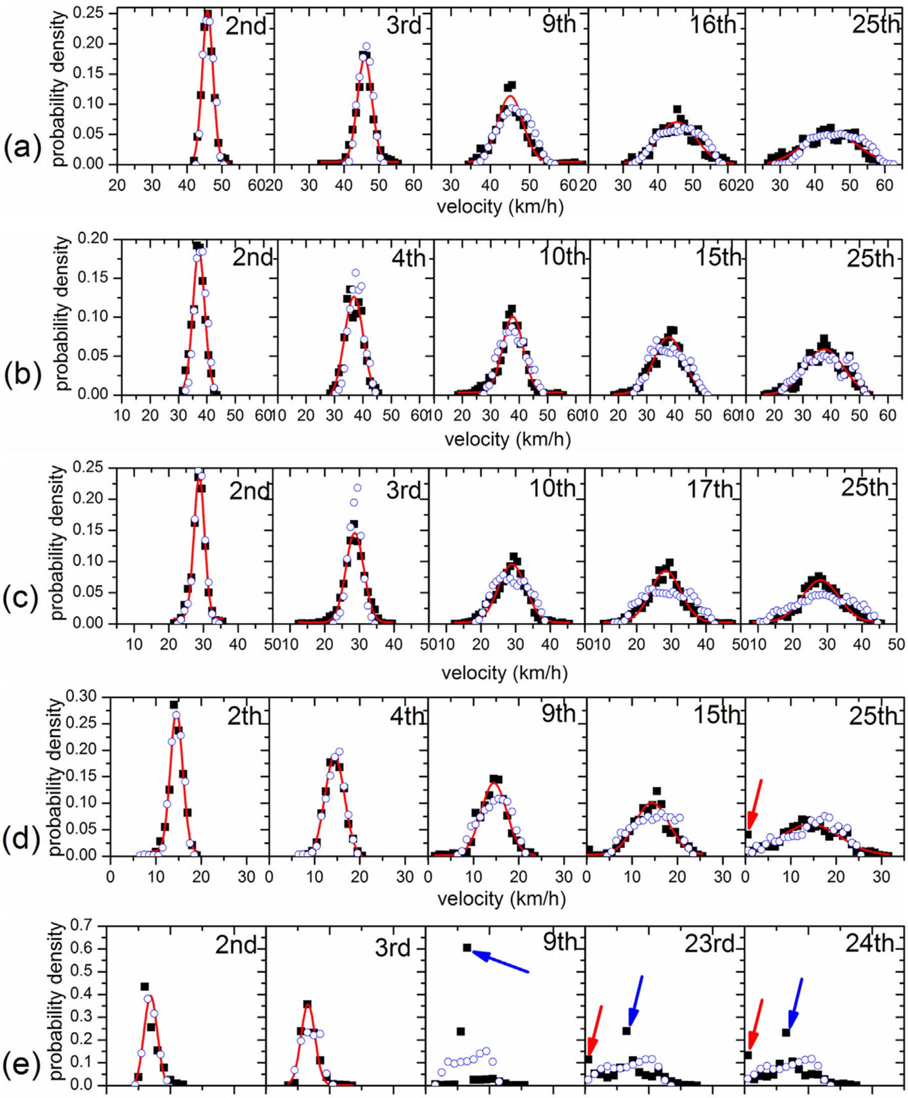

FIG. 3.1 – Velocity distribution of the cars and simulation fits.

and around 25 km/h, and the velocity difference between the car and its preceding one is always small. Before $t = 174$ s, the spacing fluctuates slightly around 15 m. The one-to-one bi-variate relation between density, speed, and flow in traditional traffic flow theory could be correct, provided the observations before $t = 174$ s is the norm. However, after $t = 174$ s, the spacing begins to fluctuate significantly and has

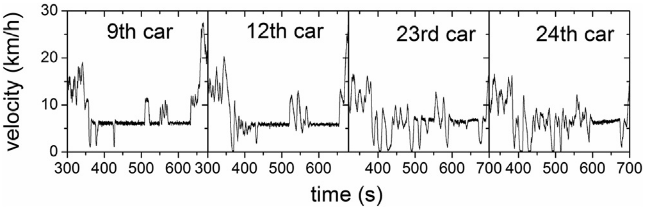

FIG. 3.2 – Examples of the velocity time series of some cars when traffic speed is low.

increased to more than 30 m, even though the traveling speed of that car remains nearly constant. Figure 3.3b shows that the spacing also changes significantly between 15 and 40 m when the cars move with a velocity of around 41 km/h. Figure 3.3c–f shows some more examples of other cars, and similar results are observed.

This feature clearly contradicts the fundamental assumption in traditional traffic flow theory. Here are two possible explanations for this feature. (i) In a certain range of spacing, drivers are not so sensitive to changes in spacing when the velocity differences between cars are small. Only when the spacing is large (small) enough, will they accelerate (decelerate) to decrease (increase) the spacing. (ii) At a given velocity, drivers do not have a fixed preferred spacing. Instead, they change their preferred spacing either intentionally or unintentionally from time to time in the driving process.

Figure 3.4 shows two-time series of the spacing of car No. 1 (the 2nd car in the platoon) as well as the velocities of this car and its preceding car in the first set of experiments. Figure 3.4a shows that the spacing changes significantly between 30 and 60 m when the cars move with a velocity of around 51 km/h. However, figure 3.4b shows that when the cars move with a velocity of around 56 km/h, the spacing fluctuates below 25 m, which is even smaller than the minimum spacing in figure 3.4a.

Figure 3.5a shows the velocity and the spacing of car No. 2 (the 15th car in the platoon) in two different runs in the second set of the 25-car experiment. The velocity of the car fluctuates between about 35 km/h and 58 km/h, and the average velocity equals about 46 km/h in both runs. However, the average spacing of one run (red line) is much larger than the other run (black line). Figure 3.5b shows another similar example.

We have also carried out another set of experiments, studying car-following behaviors in a 3-car-platoon that moves at high speed on the ring highway of Hefei City, see figure 2.23. Since traffic is light in the experiment time period (from 9:55 am to 10:40 am) and the highway has three or four lanes in the experiment section, the platoon was not hindered by other vehicles, and no vehicle was cut in the platoon during the experiment. The leading car in the experiment is asked to move with different constant velocities in different time intervals.

Figure 3.6 shows the experimental results of the high-speed experiment. The ratio σ_v/v_{ave} and $\sigma_{\Delta x}/\Delta x_{\text{ave}}$ equal to 0.012 and 0.182 in panel (a), 0.0128 and 0.139

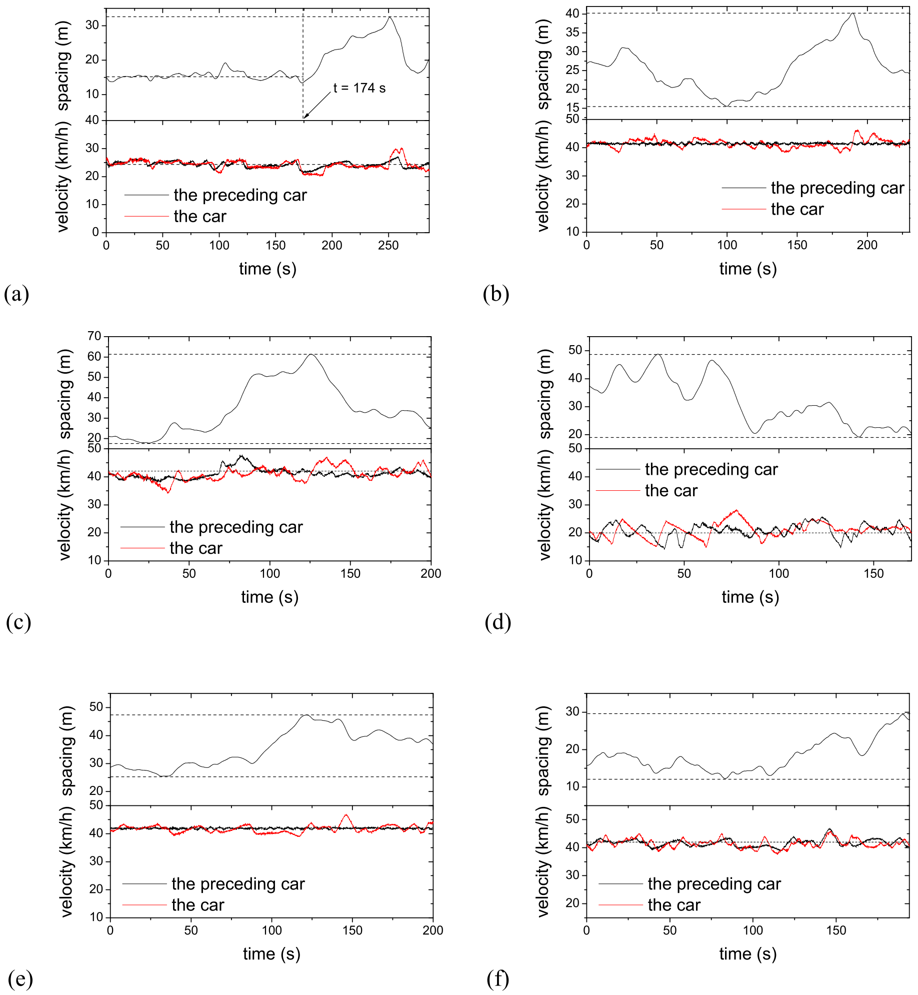

FIG. 3.3 – Evolution of the spacing of a car as well as the velocities of the car and its preceding car. (a, b) Car No. 1 in the 1st set of experiments. (c) Car No. 2 in the 1st set of experiments. (d) Car No. 23 in the 1st set of experiments. (e) Car No. 11 in the 2nd set of experiments. (f) Car No. 12 in the 2nd set of experiments.

in panel (b), 0.048 and 0.242 in panel (c), 0.0426 and 0.205 in panel (d). Here σ_v and $v_{\rm ave}$ are the standard deviation and the average of velocity, $\sigma_{\Delta x}$ and $\Delta x_{\rm ave}$ are standard deviation and the average of spacing. These results show that the fluctuations in spacing are much larger than that in speeds.

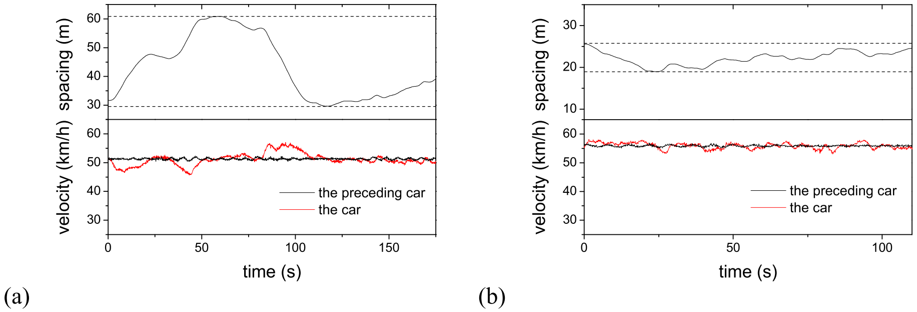

Fig. 3.4 – The spacing of car No. 1 (the 2nd car in the platoon) as well as the velocities of this car and its preceding car in the 1st set of experiments.

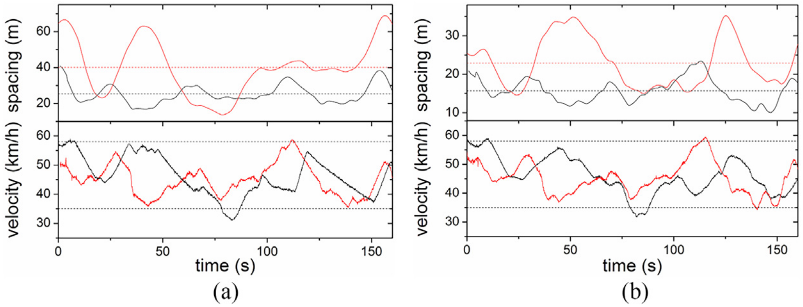

Fig. 3.5 – The velocity and the spacing of car. (a) No. 2 (the 15th car in the platoon). (b) No. 3 (the 16th car in the platoon) in two different runs in the second set of the 25-car experiment. The dashed lines in the top panels show the average spacing.

3.3 The Platoon Length Analysis

Now we study the platoon length L, which is related to the average spacing *via* $s = L/(N-1)$, and the macroscopic density *via* $\rho = 1/s$, where $N = 25$ is the number of cars in the platoon. Figure 3.7a–d show four examples, in which in different runs of the experiment, even if the leading car is asked to move at the same speed, the platoon length could be significantly different while the average velocity of all cars is approximately the same. Figure 3.7e shows an example, in which while the average velocity is smaller when the leading car moves at 20 km/h (compared with 25 km/h), the platoon length is larger. All the experimental facts further demonstrate that traffic states span a 2D region in a speed-spacing plane.

To show the relationship between individual spacing variation and the platoon length variation, we plot in figure 3.8 the spacing of cars and their differences in the second set of experiments where the leading car is asked to move at 60 km/h. First, we plot in figure 3.8a the spacing of cars in the first experimental run at two different time instants (indicated by blue and red arrows in figure 3.7a): $t = 125$ s (black bars)

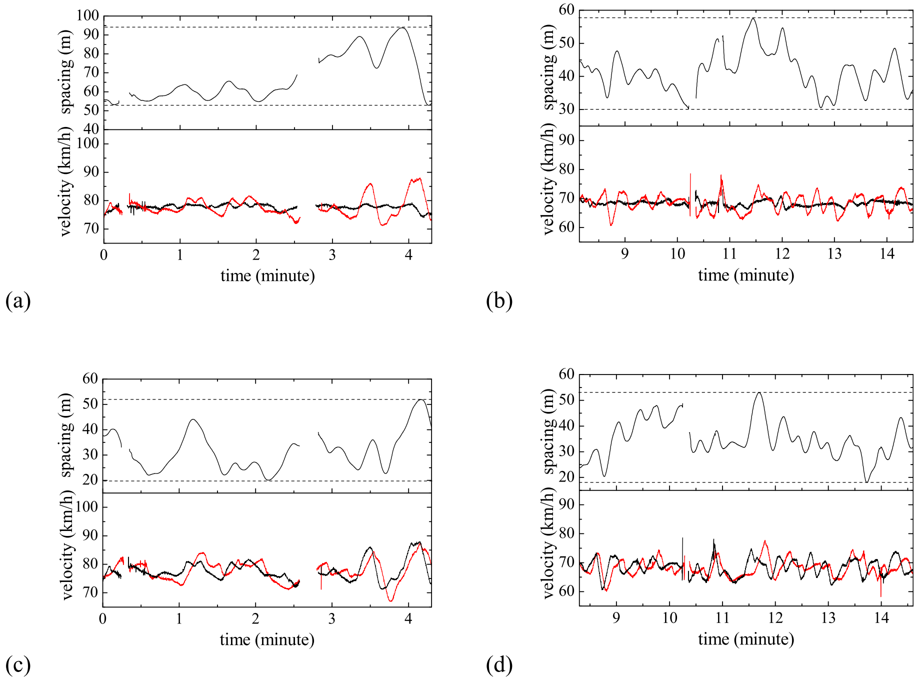

FIG. 3.6 – The velocity and the spacing of the car in the 3-car-platoon experiment on the Hefei ring highway. (a) and (b), the second car, (c) and (d), the third car. Red line corresponds to velocity of the car, and black line corresponds to velocity of preceding car. The gaps in the curves are due to temporary loss of GPS signal when cars move under bridges.

and $t = 200$ s (red bars). We also plot the spacing of the cars at $t = 200$ s in the second experimental run (indicated by the green arrow in figure 3.7a) in figure 3.8a, which are shown by blue bars. The difference in spacing between the two time instants in the first run is shown in figure 3.8b, and that between the first and second run at $t = 200$ s are shown in figure 3.8c. As can be seen from figure 3.8b, the positive differences and the negative differences almost cancel out between the two-time instants in the first run, so the platoon length remains relatively constant in this case (from 1121 to 1054 m, a change of 6%). In the second case, the difference in spacing between the first run and the second run at time $t = 200$ s is systematically positive, producing a large difference in platoon length (from 1121 to 644 m, a 74% change). For the same average speed of travel, the spacing of cars in the second run is systematically lower than that in the first run, therefore its platoon length is significantly shorter, regardless of spacing distribution.

Our experiments above reveal that vehicle spacing (hence platoon length and traffic density) can vary considerably for the same average travel speed. Next, we show the length of the 51-car-platoon in different sets of experiments. To remove the influence of vehicle turning at the two ends of the experimental track, we consider

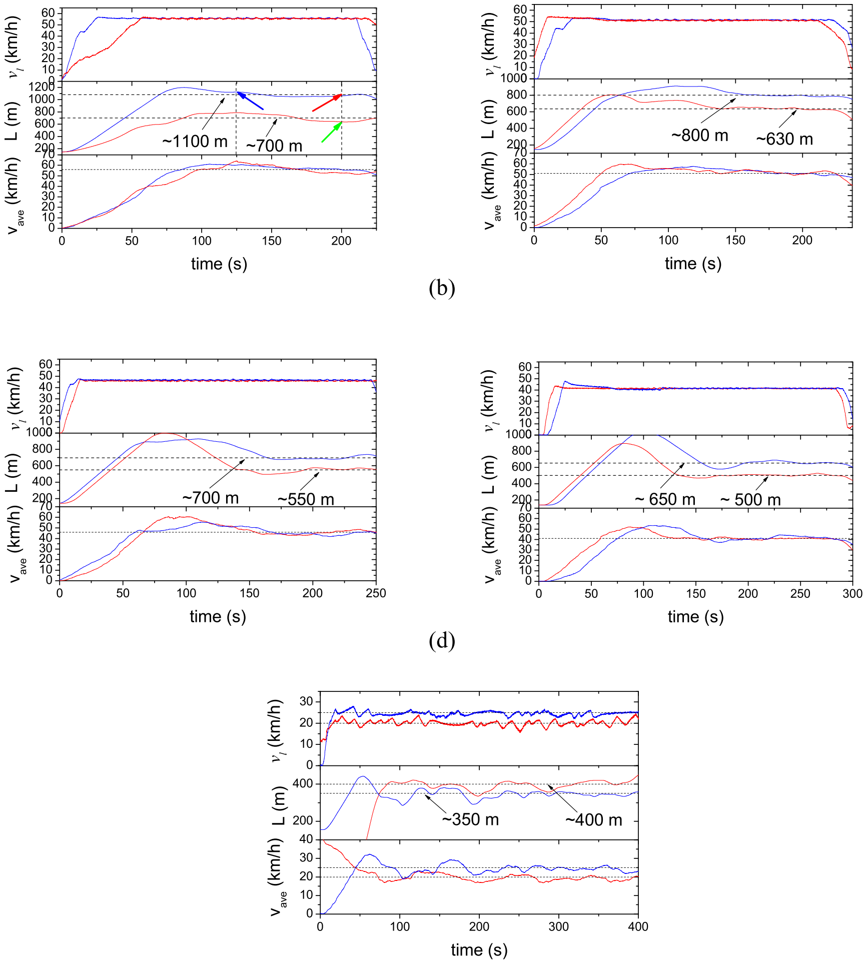

(a) (b) (c) (d) (e)

FIG. 3.7 – Evolution of the velocity of the leading car, the platoon length, and the average velocity of all cars in the platoon. The leading car is asked to move with speeds. (a) 60 km/h, (b) 55 km/h, (c) 50 km/h, (d) 45 km/h, (e) 25 km/h and 20 km/h. The blue and red color lines represent two runs of experiments with the same leading car speeds in panels (a)–(d), and with different leading car speed in panels (e).

the situation that both the leading car and the last car are on the same runway or taxiway. Figure 3.9 shows that the platoon length could be significantly different while the average velocity of all cars (that have velocity measured by the GPS) is approximately the same.

To study the platoon length at high speed, figure 3.10 shows the platoon length (the distance from the leading car to the last car) and average velocity of all cars in two runs for each leading car speed in our 11-car-platoon high-speed experiment.

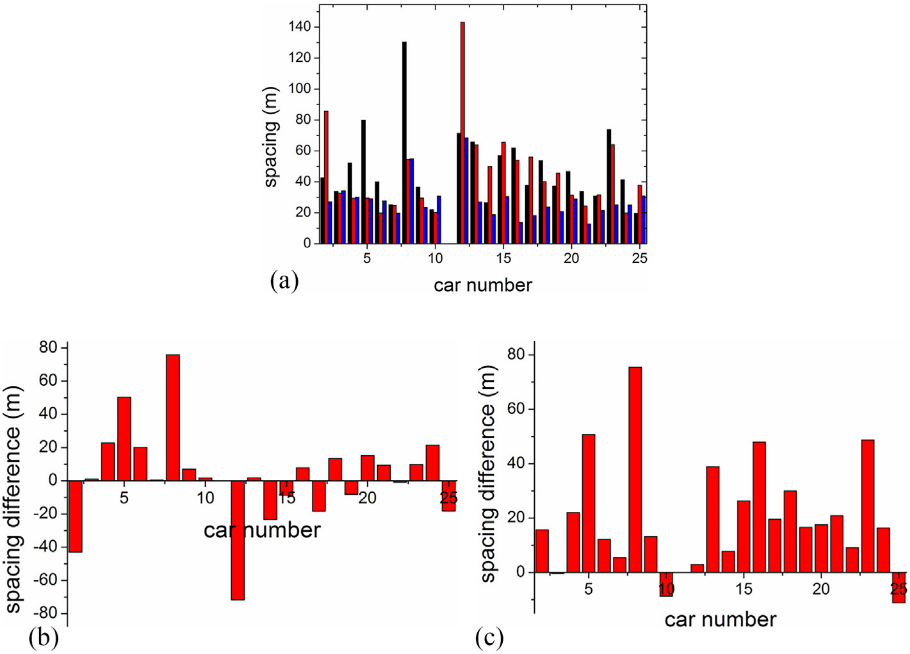

FIG. 3.8 – (a) The spacing of the cars in two different runs in the 2nd set of the experiment. Since the trajectory data of the 11th car are missing in one run of the experiment, the bars corresponding to the spacing of the 12th car show the spacing between the 10th car and the 12th car. Panels (b) and (c) show the difference in spacing between the cars at $t = 150$ s and at $t = 200$ s in the first run, and at $t = 200$ s between the first and the second runs, respectively.

One can see that the platoon length could be significantly different while the average velocity of all cars is approximately the same. Even in the same run, whose leading car speed remains unchanged, the length of the platoon varies much. See figure 3.10c for example, the platoon of run 8 once reaches 503.6 m, and is only 272.9 m for shortest, spanning a range of 230.7 m.

Figure 3.11 shows the average spacing of cars in the stationary state in different runs. One can see that the spacing of the same car sometimes differs significantly from run to run, which indicates strong intra-driver heterogeneity. For example, see figure 3.12, which compares the time series of velocity and spacing of car IDs 4 and 6 in two different runs. Although the sequence of the cars is different, the speed of the cars is essentially the same in different runs, while the spacing is not. For a car of ID 4, the fluctuation of spacing is strong in run 10 but is much weaker in run 2. For a car of ID 6, the fluctuation of spacing is stronger in run 6 than in run 11.

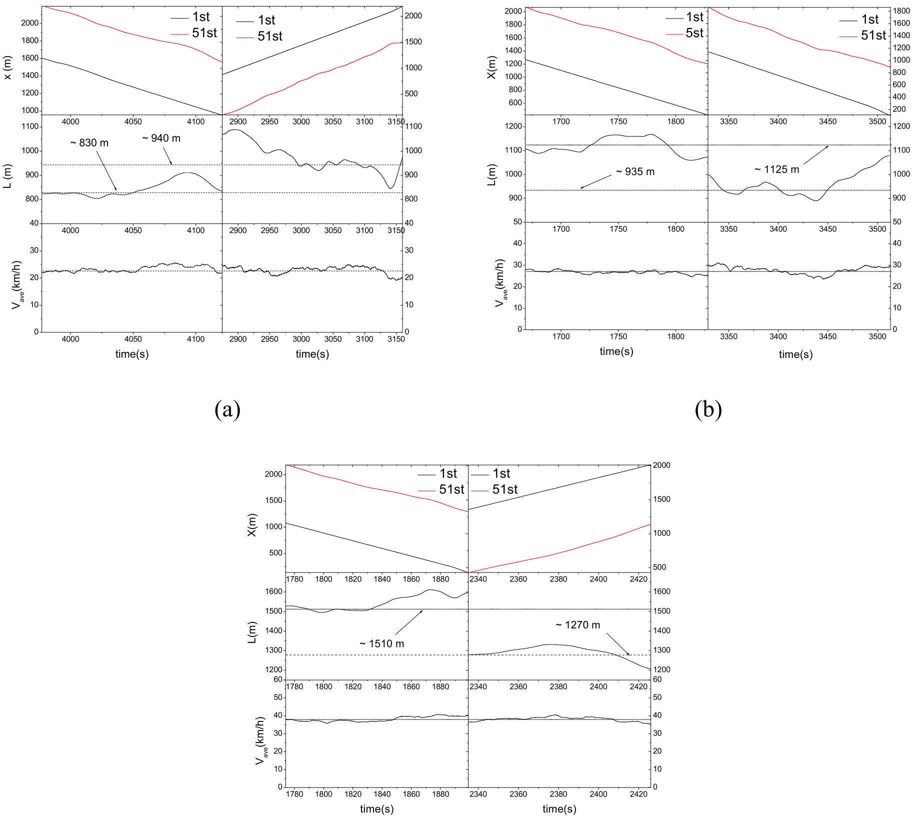

(a)

(b)

(c)

FIG. 3.9 – Evolution of the platoon length and the average velocity of all cars (that have velocity measured by the GPS) in the platoon. The leading car moves with speed. (a) 25 km/h, (b) 30 km/h, (c) 40 km/h.

3.4 The Acceleration Analysis

In this section, the accelerations of the 25-car-platoon experiments will be extracted and analyzed. Since the GPS devices record the speed every $dt = 0.1$ s, we calculate the acceleration *via*

$$a_n(t) = \frac{v_n(t) - v_n(t - dt)}{dt} \tag{3.1}$$

To reduce random fluctuations, we employ the moving average method with a 1 s time window. It should be mentioned that when the time window reaches 2 s, the true acceleration peaks have been damped. We have examined the results by changing the time windows in the range between 0.5 s and 2 s and found only minor

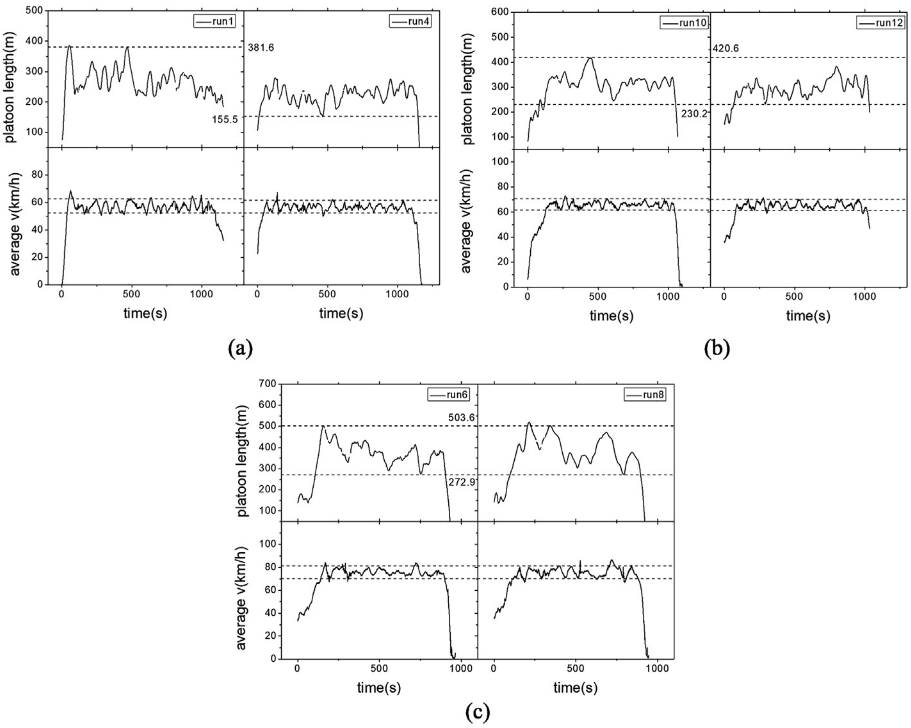

(a) (b) (c)

FIG. 3.10 – Platoon length and average velocity of all cars in two different runs. (a) 60 km/h, (b) 70 km/h, (c) 80 km/h.

quantitative differences in the results. Thus, we choose a time window of 1 s to smooth the acceleration rates.

Then we compare the time series of acceleration with the speed difference between a car and its front car. Figure 3.13 shows two typical examples. One can see that the two-time series exhibit striking similarities, and a time delay in the acceleration time series is manifested. To extract the time delay, the correlation method is used

$$\tau_n = \underset{\tau' \in (0,5)}{\arg\max}\Big(\mathrm{corr}\big(a_n^{\exp}(t), \Delta v_n^{\exp}(t-\tau')\big)\Big) \tag{3.2}$$

where $a_n^{\exp}$ and $\Delta v_n^{\exp}$ are the acceleration and speed difference of vehicle n in the experiments. "corr" is the Pearson correlation coefficient.

Figure 3.14a shows the statistical results of the extracted time delay of the 24 cars. Figure 3.14b shows the distribution of the mean time delay of each driver. The Jarque–Bera test shows that it follows the lognormal distribution (p-value = 0.213). Figure 3.15 shows the Pearson correlation coefficient r between $\Delta v_n^{\exp}(t-\tau_n)$ and $a_n(t)$. As a comparison, we also calculated the r between $d_n^{\exp}(t-\tau_n)$ and $a_n^{\exp}(t)$.

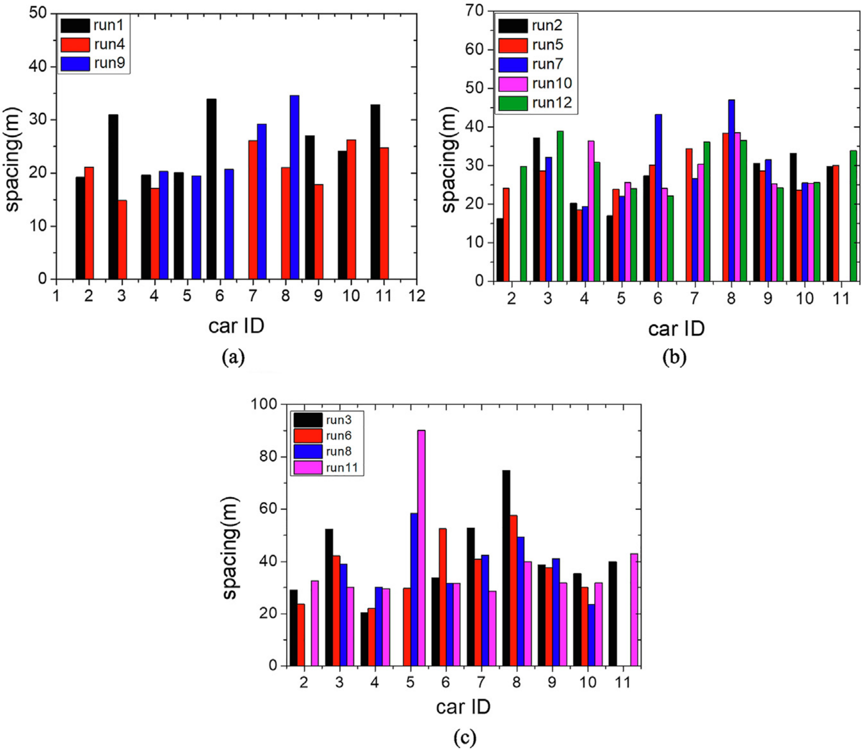

FIG. 3.11 – Average spacing in the stationary state in different runs of (a) 60 km/h, (b) 70 km/h, (c) 80 km/h. The missing bars are due to the missing GPS signals.

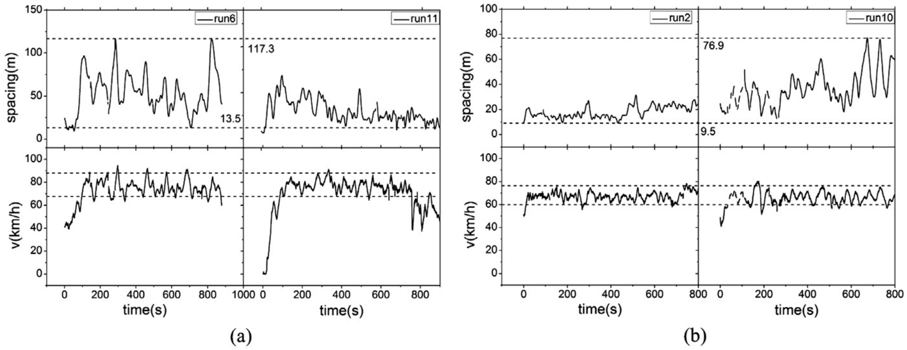

FIG. 3.12 – Spacing and velocity series of two single cars in different runs of 80 km/h, (a) car ID 4 in run 6 and run 11, (b) car ID 6 in run 2 and run 10.

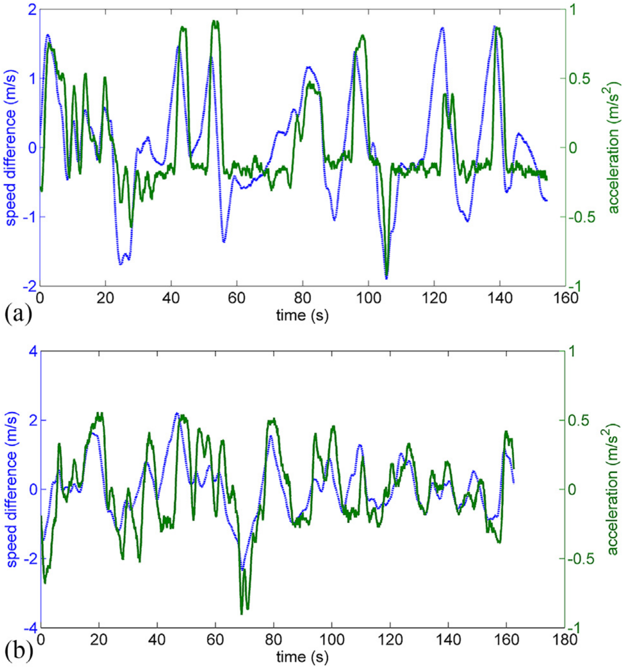

Fig. 3.13 – Two samples of the speed difference and acceleration time series.

One can see that r is much larger between $\Delta v_n^{\text{exp}}(t-\tau_n)$ and $a_n(t)$, which indicates that the speed difference plays a more important role in car-following dynamics, at least in the spacing range concerned, see figure 3.16.

Next, λ_n is calculated through linear regression of $a_n(t)=\lambda_n\Delta v_n(t-\tau_n)$, see figure 3.16a and d for two examples. As a comparison, we show acceleration *vs.* spacing in figure 3.16b and e, which again indicates that the dependence of acceleration on spacing is not so remarkable as on speed difference. The statistical results of λ_n are shown in figure 3.17a. Figure 3.17b shows the distribution of the mean sensitivity of each driver. The Jarque–Bera test shows that it also follows the log-normal distribution (p-value $= 0.3729$).

Now we subtract $\lambda\Delta v(t-\tau)$ from the acceleration. Denote the resulting residual time series as $\xi(t)$. Figure 3.16c and f show two typical examples. We performed an augmented Dickey–Fuller test (ADF) of $\xi(t)$. The result is shown in figure 3.18. One can see that in most cases, $\xi(t)$ is stationary, therefore $\xi(t)$ can be regarded as a Mean Reversion process (Balvers *et al.*, 2000).

To measure the strength of $\xi(t)$, the standard deviations of $a(t)$ and $\xi(t)$ are calculated. Figure 3.19a shows that both σ_a and σ_ξ grow concavely along the platoon. Figure 3.19b shows that (i) the ratio σ_ξ/σ_a is quite large for the several vehicles in the front part of the platoon, which indicates that when its amplitude is small, the growth of the oscillations is mainly determined by the stochastic factors since the speed difference among vehicles is small in the front part of the platoon; (ii) this

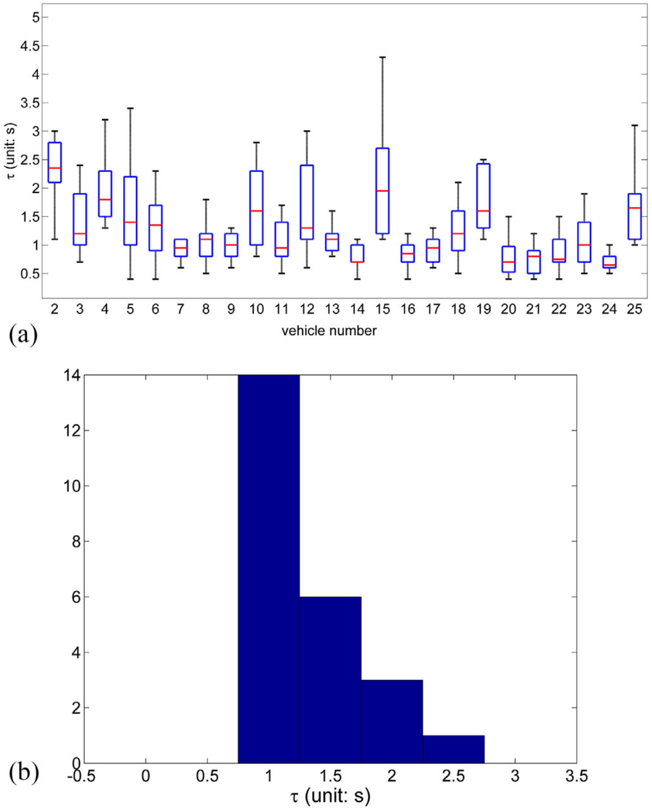

FIG. 3.14 – The time delay τ of the 24 cars. (a) The statistics of time delay of each car in each run, (b) Distribution of mean time delay of the cars over all runs.

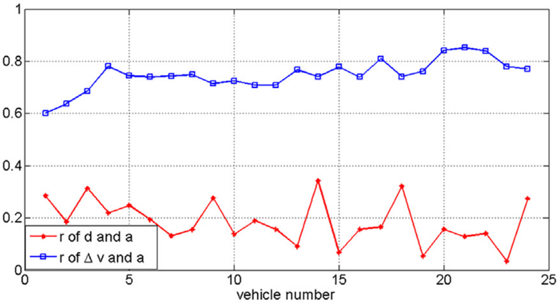

FIG. 3.15 – The Pearson correlation coefficient r between speed difference Δv and acceleration and r between spacing d and acceleration.

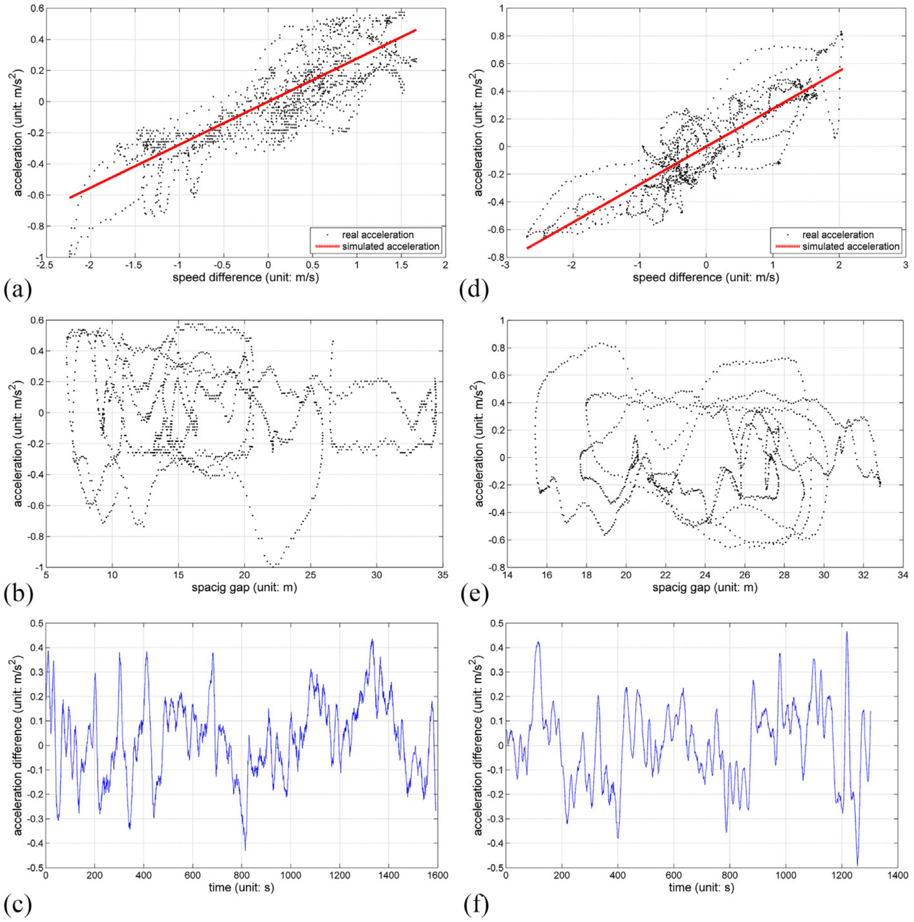

FIG. 3.16 – Two samples of (a, d) acceleration $a(t)$ *vs.* speed difference $\Delta v(t-\tau)$, (b, e) acceleration $a(t)$ *vs.* spacing $d(t-\tau)$, and (c, f) the time series of $\xi(t)$. In (a, d) the red line denotes $a = \lambda \Delta v(t-\tau)$

ratio decreases along the platoon since the speed difference grows along the platoon. Therefore, the growth of the oscillations is determined by the competition between the stochastic factors and the speed difference.

Therefore, we use the Vasicek model (Vasicek, 1977) to approximate $\xi_n(t)$. This model is the first one to capture the mean reversion process and was originally used to describe the evolution of interest rate derivatives, which reads

$$d\xi_n = \kappa(\mu - \xi_n)\,dt + \sigma\,dW_n \tag{3.3}$$

where $W_n(t)$ is a Wiener process, dW_n follows the normal distribution with mean zero and variance dt. σ denotes the instantaneous volatility measuring the amplitude of randomness. μ is the long -term mean level, $\xi_n(t)$ will evolve around the mean level μ in the long run. κ is the speed of reversion, which characterizes the speed at which

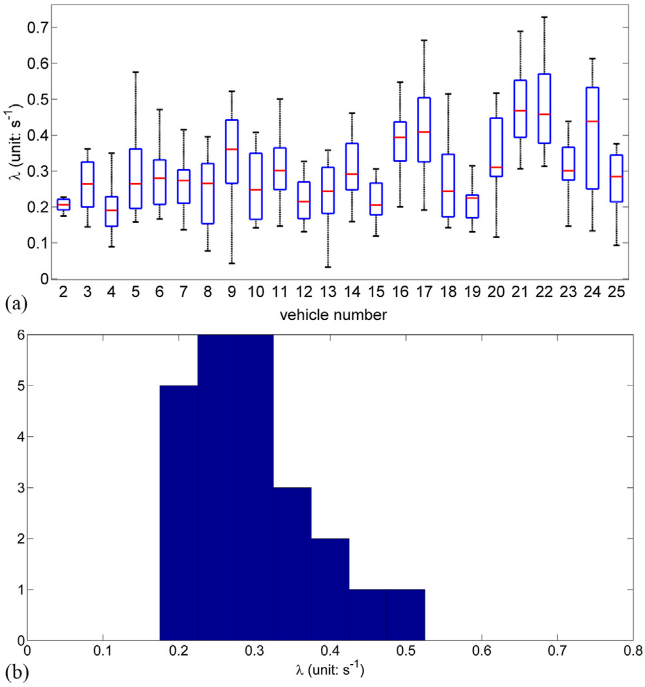

FIG. 3.17 – The statistics of sensitivity λ. (a) Distribution of sensitivity of each car in each run; (b) distribution of mean sensitivity of the cars over all runs.

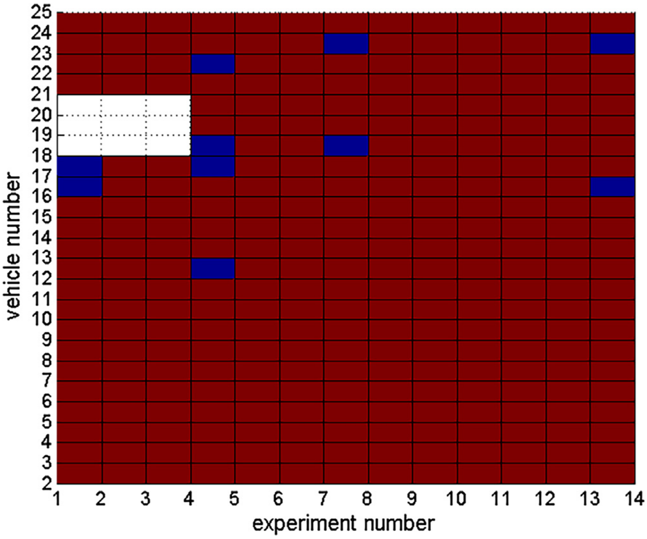

FIG. 3.18 – The result of the augmented Dickey-Fuller (ADF) test. The red grid means that $\xi(t)$ is stationary while the blue means nonstationary. The blanks are the missing data.

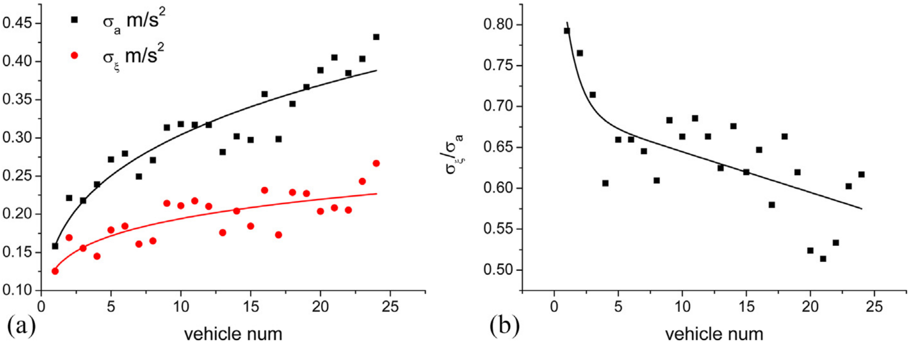

FIG. 3.19 – (a) The standard deviation of the acceleration σ_a and residual σ_ξ. (b) The ratio of σ_ξ/σ_a. The curves are the fitting curves.

ξ_n(t) returns to μ. It is worth mentioing that $\sigma^2/2\kappa$ is the long-term variance. ξ_n(t) will regroup around μ with this variance after a long time.

To calibrate κ and σ, the model is reformulated into the discrete form

$$\xi_n(t) = (1 - \kappa dt)\xi_n(t - dt) + \kappa\mu dt + \sigma dW_n \tag{3.4}$$

The least square method is used in the calibration. The statistical results are shown in figure 3.20. The mean values of κ and σ are 0.11 s^{-1} and 0.08 m/s^2, respectively, overall drivers. Figure 3.20c shows that the range of the mean μ is quite small and very close to zero. This is reasonable, and one can expect that μ tends to zero if the time series becomes longer. Thus, the acceleration residual $\xi_n(t)$ can be approximated by

$$d\xi_n = -\kappa\xi_n dt + \sigma dW_n \tag{3.5}$$

3.5 The Wave Travel Time Analysis

This section analyzes the wave travel time. To this end, Newell's car following model (abbreviated as NCM, see Newell (2002)) and its variants will be introduced. The NCM assumes that the following vehicle's trajectory is the trajectory of the leading vehicle with a translation in time and space. Let n−1 denote the vehicle ahead of vehicle n, and their location and speed are x_{n-1} and x_n, v_{n-1} and v_n, respectively. When vehicle n−1 changes its speed from $v_{n-1} = v$ to $v_{n-1} = v'$, vehicle n will adjust its speed in the same way after a space displacement of s_0 and an adjusting time of τ to reach the preferred spacing for the new speed v'. Under the car-following context, NCM is described by

$$x_n(t) = x_n(t - \tau) + \min\left(\Delta x_n^{\text{free}}(t - \tau), \Delta x_n^{\text{cong}}(t - \tau)\right) \tag{3.6}$$

where the free-moving and congested-moving terms are defined as

$$\Delta x_n^{\text{free}}(t - \tau) = v_{\max}\tau \tag{3.7}$$

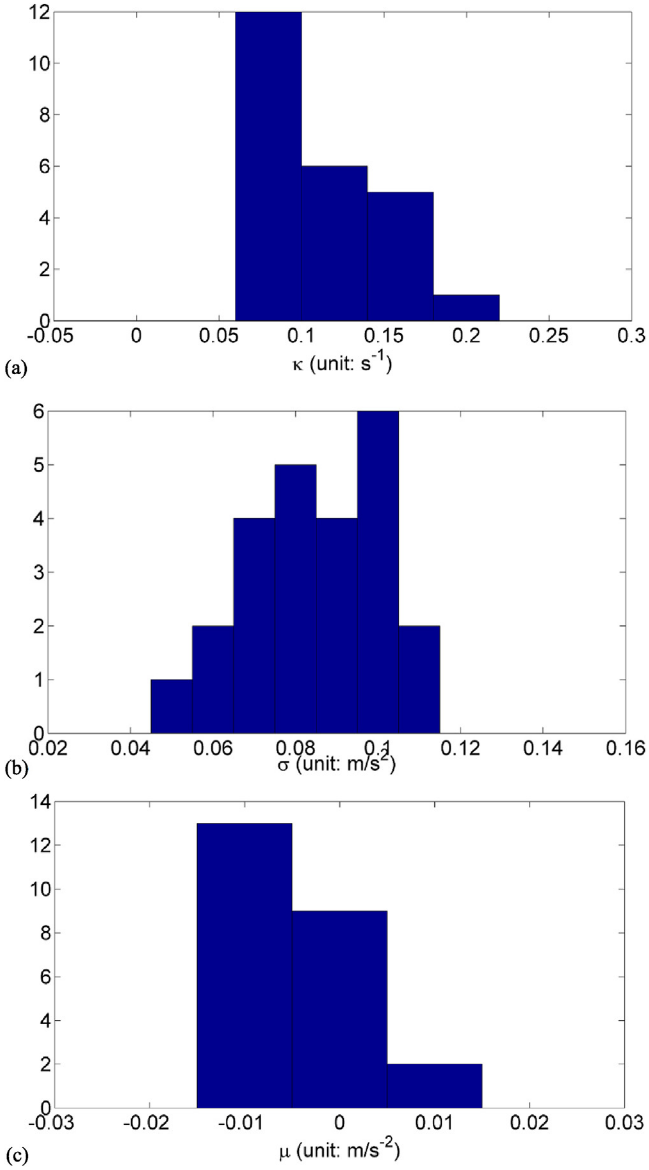

FIG. 3.20 – Statistical results of calibrated parameter. (a) κ, (b) σ, (c) μ.

$$\Delta x_n^{\mathrm{cong}}(t-\tau) = x_{n-1}(t-\tau) - x_n(t-\tau) - \delta \tag{3.8}$$

where $v_{\max}$ is the maximum speed. NCM adopts a single wave speed $-w = -\delta/\tau = -(L_{\mathrm{veh}} + s_0)/\tau$ independent of traffic states. Here L_{veh} is vehicle length. Traffic information, such as speeds, flows, spacing, etc., propagate unchanged along characteristic travelling wave with speeds of either $v_{\max}$ or $-w$.

However, disturbances will never grow or decay in NCM. Laval and Leclercq (2010) reported that vehicle trajectories will deviate from the Newell trajectories (which are generated by the NCM) when the vehicles go through traffic oscillations. To capture these deviations, the congested moving term is revised as Chen *et al.* (2012)

$$\Delta x_n^{\text{cong}}(t) = x_{n-1}(t - \eta_n(t)\tau) - x_n(t - \tau) - \delta\eta_n(t) \tag{3.9}$$

$$\eta_n(t) = \tilde{\tau}_n(t)/\tau \tag{3.10}$$

The term $\tilde{\tau}_n(t)$ is the actual wave travel time, see figure 3.21.

Laval and Leclercq (2010) assumed that: (i) $\eta_n(t) = 1$ under the equilibrium driving states; (ii) there are three kinds of variation patterns of $\eta_n(t)$ when the vehicles are under the nonequilibrium driving states, *i.e.* the concave triangle, the convex triangle and constant patterns, see figure 3.22, where $\eta_n^0 = \eta_n^1 = 1$ and $\varepsilon_n^0 = \varepsilon_n^1$. Here ε_n^0 and ε_n^1 are the changing rate of $\eta_n(t)$ between η_n^0 and η_n^T and between η_n^T and η_n^0, respectively.

Later, Chen *et al.* (2012) examined the traffic oscillations in the NGSIM US101 trajectory data to verify the above assumptions of Laval and Leclercq (2010) and found that: (1) η_n^0 (ε_n^0) may be different from η_n^1 (ε_n^1); (2) η_n^0 and η_n^1 do not necessarily equal 1, and they do not necessarily equal each other. Before entering the oscillation, the vehicle is in the state with $\eta_n(t) = \eta_n^0$. After exiting the oscillation, the vehicle changes into another state with $\eta_n(t) = \eta_n^1$.

However, the NGSIM US101 trajectory data is very short, about 40 s for each trajectory. Thus, it is yet to know whether the assumptions in Chen *et al.* (2012) and

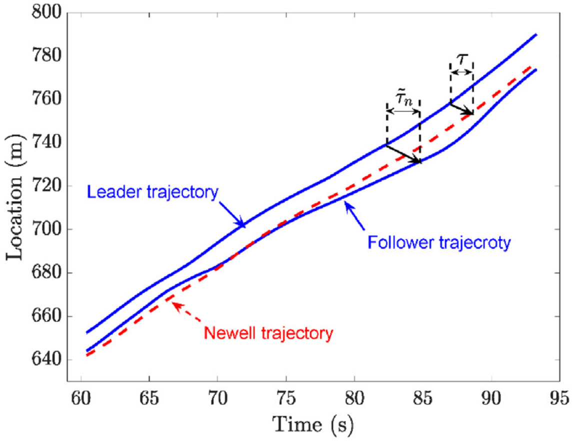

FIG. 3.21 – The measurement of $\tilde{\tau}_n(t)$.

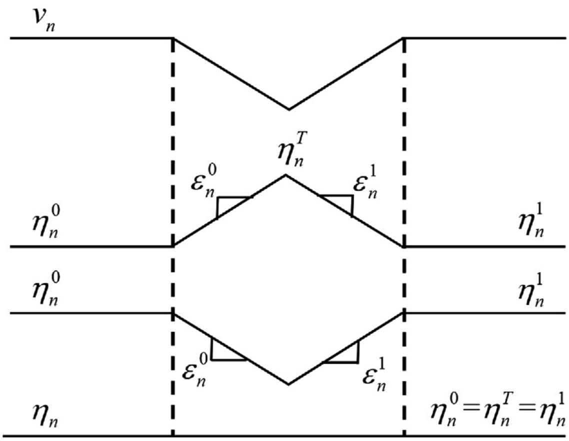

FIG. 3.22 – Variation patterns of $\eta_n(t)$. The dashed line separates the traffic oscillation from the equilibrium states.

Laval and Leclercq (2010) will hold in more extensive scales. In the following section, longer car following trajectories data will be investigated by analyzing the $\tilde{\tau}_n(t)$ time series. Since $\tilde{\tau}_n(t) = \eta_n(t)\tau$, the variation of $\tilde{\tau}_n(t)$ should also exhibit the same pattern as that of $\eta_n(t)$, and the changing rate of $\tilde{\tau}_n(t)$ is equivalent to ε_n but may not be a constant anymore.

3.5.1 Some Observed Features of $\tilde{\tau}_n(t)$ Time Series

During the analysis, the transient states (the acceleration process from stop and the deceleration process to stop) are discarded. Recall that we aim to obtain $\tilde{\tau}_n(t)$ (and thus $\eta_n(t)$). Thus, the first step in data analysis is to extract τ and w by calibrating the Newell model with real trajectories. Once the parameter set (τ and s_0) in the Newell model are obtained, we can calculate w through $w = (L_{\text{veh}} + s_0)/\tau$, and $\tilde{\tau}_n(t)$ can be directly measured once w is given. To find the optimal parameter set (τ and s_0) for the Newell model, the nonlinear optimization problem is solved numerically by minimizing the Root Mean Square Error (RMSE)

$$\text{RMSE} = \sqrt{\frac{1}{M}\sum_{m=0}^{M}\left(d_n(mdt) - d_n^{\text{simu}}(mdt)\right)^2} \tag{3.11}$$

where the length of the time series is Mdt, with $dt = 0.1$ s; $t = mdt$, $m = 0, 1, \ldots, M$. $d_n(t) = x_{n-1}(t) - x_n(t)$ is the spacing from the follower's trajectory to the leader's trajectory. $d_n^{\text{Newell}}(t) = x_{n-1}(t) - x_n^{\text{Newell}}(t)$ is the spacing from the follower's Newell trajectory to the leader's trajectory.

The reason for the choice of equation (3.11) as the fitness function of GA is that the goal is to calibrate τ and w by the trajectory data. As Punzo and Montanino

(2016) have proved, the errors on gaps are equivalent to a convolution of the errors on speed and time, *i.e.*, errors on gap have less degree of freedom than errors on speed. Thus, while the internal and platoon consistency implies that the cumulated differences of speed or speed difference between the simulated and real trajectory are zero in the long run, on average, no such restrictions apply to the gap (Treiber and Kesting, 2013); Punzo *et al.*, 2011. Therefore, the gap, rather than speed, is used for calibration.

Here, we use the GA to solve the optimization problem. The GA optimization is adopted just because it is widely applied in the car following model calibrations, see *e.g.*, Cheu *et al.* (1998), Hamdar *et al.* (2015) and Sharma *et al.* (2019). Sharma *et al.* (2019) showed the good performance of GA in trajectory calibration. For details on the GA heuristic, one may refer to Hamdar *et al.* (2015). Here (τ, s_0) is chromosome, the population size is 20, and their values are initiated randomly. In each iteration, these parents produce 100 children's chromosomes, where the best 10 candidates are kept for the next iteration. The calibration process continues until the number of iterations exceeds 200 (the maximum number of iterations we set) or no improvement more than 0.01 is observed for 20 consecutive iterations. It should be noted that a mutation rate of 1% is applied in all iterations.

With τ and w, the time series of $\tilde{\tau}_n(t)$ is directly measured by Chen *et al.* (2012). Notably, $\eta_n(t)$ is scaled from $\tilde{\tau}_n(t)$ by a constant τ and thus its evolution is equivalent to the evolution of $\tilde{\tau}_n(t)$.

We examine the time series of $\tilde{\tau}_n(t)$ for all trajectories and obtain the following remarks. Note that the speeds of vehicles in the front part of the platoon are quite stable. However, the speeds fluctuate significantly in the rear part of the platoon. Therefore, we show vehicles in the front (rear) of the platoon concerning the situation that the speed of the leading vehicle oscillates slightly (significantly).

(i) No matter the speed of leading vehicle oscillates significantly (figure 3.23) or slightly (figure 3.24), $\tilde{\tau}_n(t)$ might change significantly.
(ii) A follower's $\tilde{\tau}_n(t)$ can vary from run to run even if the leader travels at the same stable speed; see plot (a) *vs.* (b), (c) *vs.* (d) in figure 3.24 for followers following the same leader.
(iii) Sometimes, even if the leader's speed fluctuates significantly, the followers can keep a nearly constant value of $\tilde{\tau}_n(t)$ (see figure 3.25).

Here we analyze the relationship between the standard deviations of $\tilde{\tau}_n(t)$ and the standard deviations of v_n(t). Figure 3.26 shows that the diagram is widely scattered, which means that the fluctuation of speed has little influence on the fluctuation of $\tilde{\tau}_n(t)$, *i.e.* even if the speed severely fluctuates, the wave travel time can keep a nearly constant value; even if the speed remains approximately constant, the wave travel time might change significantly. This implies that $\tilde{\tau}_n(t)$ can be regarded as the personal driving characteristics independent of the driving states.

Now we study the time series of the wave travel time changing rate $\xi_n(t) = d\tilde{\tau}_n(t)/dt$. Since GPS devices collected the speed and location data every 0.1 s, we calculate the changing rate *via* $\xi_n(t) = (\tilde{\tau}_n(t) - \tilde{\tau}_n(t - dt))/dt$, with $dt =$ 0.1 s. We have examined all $\xi_n(t)$ time series and discovered that all of them oscillate

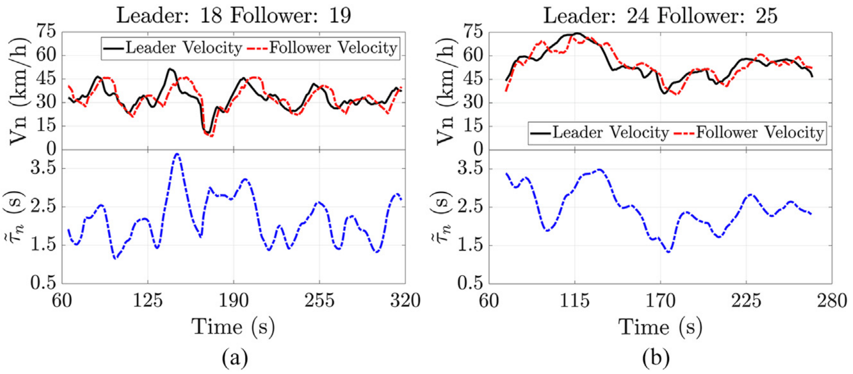

FIG. 3.23 – $\tilde{\tau}_n(t)$, $v_n(t)$ and $v_{n-1}(t)$ time series of the leader–follower pairs, in which speed of the leader remarkably fluctuates. The standard deviation of the leader's speed is (a) 1.96 m/s; (b) 2.49 m/s. The standard deviation of the follower's $\tilde{\tau}_n(t)$ is (a) 0.60 s; (b) 0.53 s.

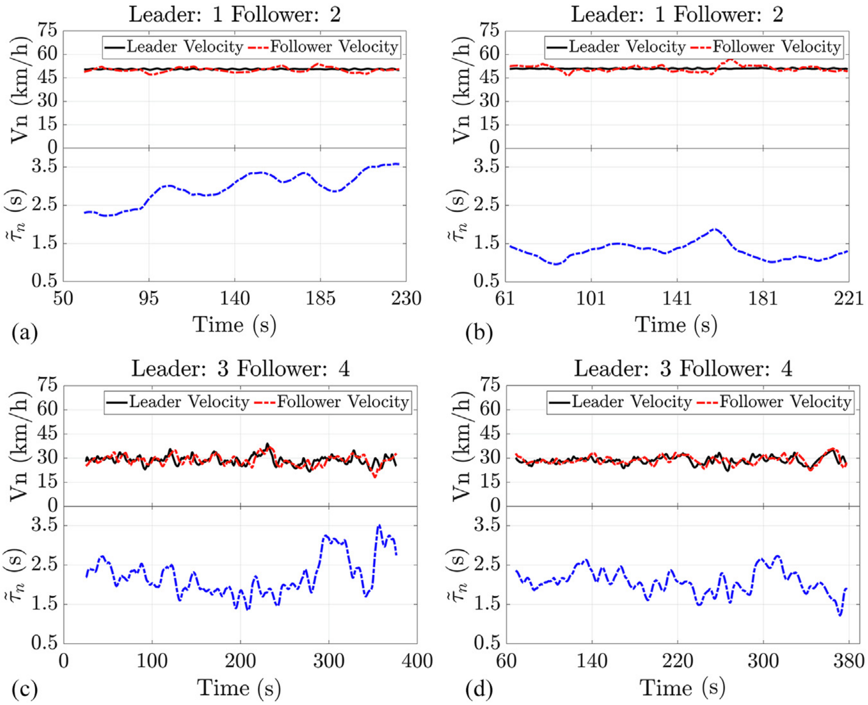

FIG. 3.24 – $\tilde{\tau}_n(t)$, $v_n(t)$ and $v_{n-1}(t)$ time series of the leader–follower pairs, in which speed of the leader only slightly fluctuates. (a) and (b), (c) and (d) are from the same leader–follower pair but two different runs. The standard deviation of the leader's speed is 0.07, 0.06, 0.76, 0.62 m/s in (a)–(d); The standard deviation of the follower's $\tilde{\tau}_n(t)$ is 0.39, 0.21, 0.48, 0.29 s in (a)–(d).

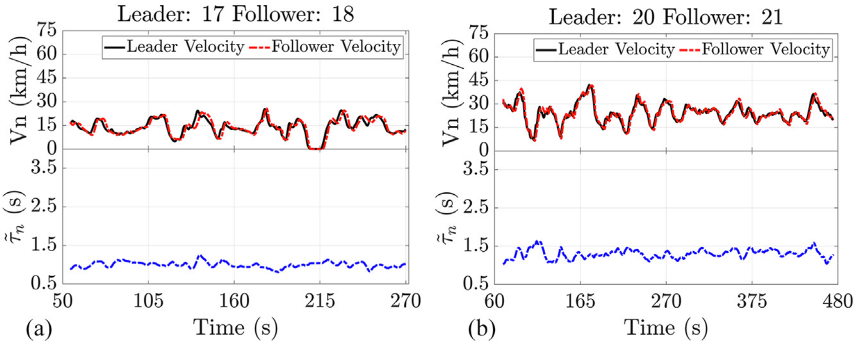

FIG. 3.25 – $\tilde{\tau}_n(t)$, $v_n(t)$ and $v_{n-1}(t)$ time series of the leader–follower pairs. The standard deviation of the leaders speed is (a) 1.43 m/s; (b) 1.68 m/s. The standard deviation of the follower's $\tilde{\tau}_n(t)$ is (a) 0.07 s; (b) 0.11 s.

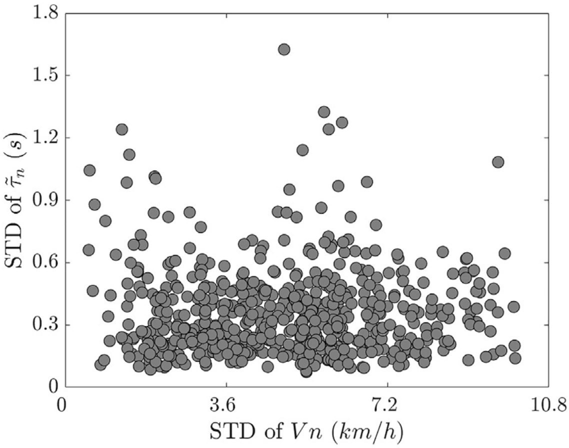

FIG. 3.26 – The relationship between the standard deviation (STD) of $\tilde{\tau}_n$ and the STD of v_n.

around zero. It indicates that the $\xi_n(t)$ time series may follow the mean reversion process, see figure 3.27 for some examples.

To study the feature of the time series of $\xi_n(t)$, we have conducted the Augmented Dickey-Fuller (ADF) test. The results show that 98.72% (616 trajectories of a total of 624 trajectories) of $\xi_n(t)$ time series follows the mean reversion process (Chaudhuri and Wu, 2003). Therefore, we can use the mean reversion model to capture $\xi_n(t)$. The Ornstein–Uhlenbeck process was widely applied to simulate the mean reversion phenomenon. Since $\xi_n(t)$ is the rate of change of the car-to-car wave travel time, the asymptotic expectation should be equal to zero. Otherwise, the wave travel time would tend to plus or minus infinity. Here we assume that $\xi_n(t)$ is governed by the following Ornstein–Uhlenbeck process,

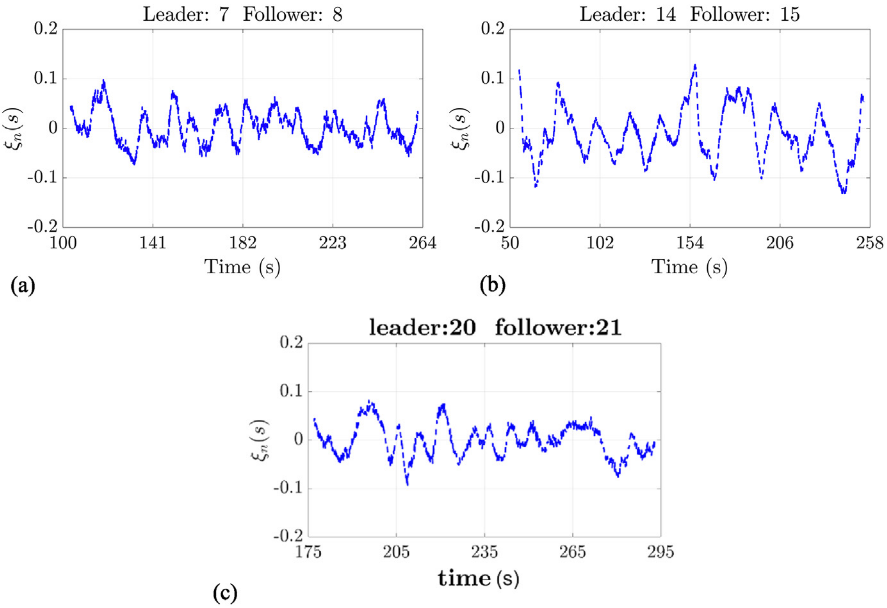

FIG. 3.27 – The time series of $\xi_n(t)$.

$$d\xi_n(t) = -\alpha\xi_n(t)\,dt + \sigma\,dW(t) \tag{3.12}$$

where $W(t)$ is a standard Wiener process; the evolution of $\xi_n(t)$ will evolve around the mean level 0 in the long run; α is the mean reversion speed, which characterizes the rate of evolution in recovering; σ is the volatility rate that measures the amplitude of randomness in the system. Higher σ implies larger randomness.

To calibrate equation (3.12), the maximum likelihood estimation (Tang and Chen, 2009) is applied. To this end, the solution of $\xi_n(t)$ is given as follows (Karatzas and Shreve, 1991)

$$\xi_n(t) = \xi_n(0)e^{-\alpha t} + \sigma\int_0^t e^{-\alpha s}\,dW(s) \tag{3.13}$$

which follows the normal distribution with the mean and variance:

$$\mathrm{E}(\xi_n(t)) = \xi_n(0)e^{-\alpha t} \tag{3.14}$$

$$\mathrm{Var}(\xi_n(t)) = \frac{\sigma^2}{2\alpha}\left(1 - e^{-2\alpha t}\right) \tag{3.15}$$

Then the conditional mean and variance of $\xi_n(t)$ given $\xi_n(t - dt)$ are

$$\mathrm{E}(\xi_n(t)|\xi_n(t - dt)) = \xi_n(t - dt)e^{-\alpha dt} \tag{3.16}$$

$$\mathrm{Var}(\xi_n(t)|\xi_n(t-dt)) = \frac{\sigma^2}{2\alpha}\left(1 - e^{-2\alpha dt}\right) \tag{3.17}$$

Denote the length of time series of ξ_n by Mdt and $t = mdt$, $m = 0, 1,\ldots, M$, the time series of $\xi_n(t)$ is rewritten as $\xi_n(mdt)$ and further simplified as $\xi_n(m)$. Then we can derive the likelihood function. Note that only the marginal distribution of each sample point is not enough. Since $\xi_n(t)$ is a stochastic process, we need to capture the likelihood of a path. That is, at time $1dt$, we should derive the probability of changing from $\xi_n(0)$ to $\xi_n(dt)$, where the probability represents the likelihood of the path $\xi_n(0) \to \xi_n(dt)$. Based on the independently incremental property of Brownian motion, the likelihood function can be represented as follows.

$$L = \phi\left(\sigma^{-1}\frac{\sqrt{2\alpha}}{\sigma}\xi_n(0)\right)\prod_{m=1}^{M}\phi\left(\frac{\xi_n(m) - \left(\xi_n(m-1)e^{-\alpha dt}\right)}{\sqrt{\frac{\sigma^2}{2\alpha}\left(1 - e^{-2\alpha dt}\right)}}\right) \tag{3.18}$$

where ϕ is the density function of the standard normal distribution. Therefore, the maximum likelihood estimators are obtained by

$$\hat{\alpha} = -\frac{1}{dt}\log(\theta_1), \hat{\sigma} = \sqrt{\frac{2\hat{\alpha}\theta_2}{1-\theta_1^2}} \tag{3.19}$$

where

$$\theta_1 = \frac{\sum_{m=1}^{M}\xi_n(m-1)\xi_n(m) - M^{-1}\sum_{m=1}^{M}\xi_n(m)\sum_{m=1}^{M}\xi_n(m-1)}{\sum_{m=1}^{M}\xi_n^2(m-1) - M^{-1}\left(\sum_{m=1}^{M}\xi_n(m-1)\right)^2} \tag{3.20}$$

$$\theta_2 = M^{-1}\sum_{m=1}^{M}\left(\xi_n(m) - \theta_1\xi_n(m-1)\right)^2 \tag{3.21}$$

The statistical results of calibrated parameters are shown in table 3.1, which shows that the estimation results have high statistical significance. It indicates that the Ornstein–Uhlenbeck process delivers satisfactory performance in simulating the $\xi_n(t)$ time series.

TAB. 3.1 – Statistics of α and σ.

Parameter	Number of trajectories	The range of the sample size in each trajectory	Average sample size in each trajectory	Median	Mean	Std	Minimum absolute t-statistics
α	624	[617, 4053]	2062	0.264	0.434	0.506	3.626
σ				0.036	0.043	0.031	422.279

3.5.2 New Experimental Data Analysis

In the 25 car-platoon, the oscillation has not yet fully developed due to the limited platoon length. Therefore, we perform a new set of experiments to mimic the fully developed oscillations and study the evolution of $\tilde{\tau}_n(t)$ in the fully developed oscillations. In the experiments, we use a 5-car platoon. The experiments were carried out in Hefei in 2019, on a remote suburb road with a length of about 4 km. There is no traffic light on the road and no other vehicle intervening in the experiment. The experiment instructions are as follows. Initially, the platoon stops at one end of the road. For the leading car, the driver is asked to

(i) Accelerate to 40 km/h, then maintain the 40 km/h speed for 30 s to 1 min.
(ii) Randomly choose to decelerate to 10 km/h or complete stop with equal probability.
(iii) Maintain the 10 km/h speed or stop for $5 \sim 10$ s, then accelerate back to 40 km/h.
(iv) Maintain the 40 km/h speed for $2 \sim 3$ min.
(v) Repeat the deceleration and acceleration process.
(vi) Maintain the 40 km/h speed until arriving at the other end of the road and decelerate to stop.
(vii) Make a U-turn and prepare for the next round of experiments.

For following cars, the drivers are asked to drive as normal. Overtaking is not allowed. High precise GPS data with an interval of 0.1 s were collected. Figure 3.28 shows the typical speed time series of the five cars in one round of experiments. To study the evolution of $\tilde{\tau}_n(t)$ related to each oscillation, we classify each round into two intervals. Each interval includes one oscillation and the following stationary

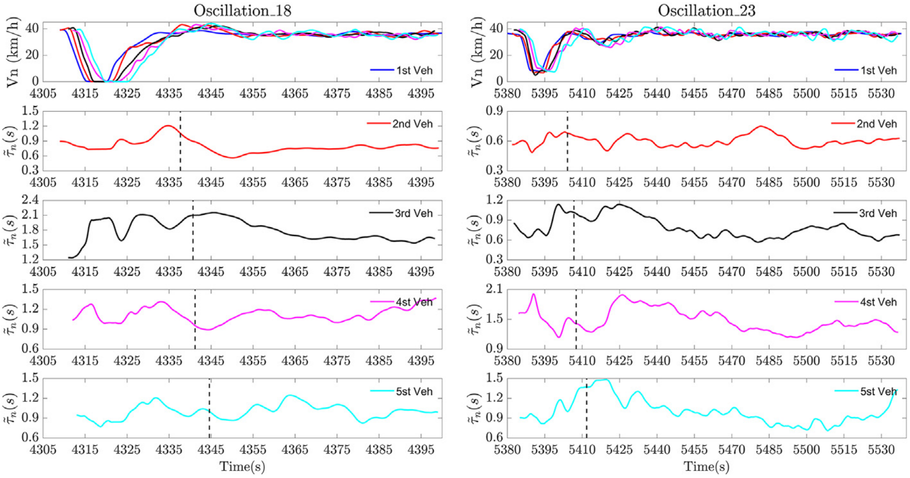

FIG. 3.28 – The speeds and $\tilde{\tau}_n(t)$, respectively. The dashed line roughly separates the oscillation from the stationary traffic flow.

traffic flow. We have extracted 40 intervals. In 19 intervals, the leading car stopped. In 21 intervals, the leading car decelerated to 10 km/h. Figure 3.28 shows one example of $\tilde{\tau}_n(t)$ time series for these two types of oscillations.

We calculate the $\xi_n(t)$ time series from the $\tilde{\tau}_n(t)$ time series. We have four drivers and 40 intervals. Therefore, we have a total 160 $\xi_n(t)$ time series. We perform the ADF test, which indicates that all the 160 $\xi_n(t)$ time series also follow the mean reversion process. Therefore, the Ornstein–Uhlenbeck model is calibrated. The results are given in table 3.2, which also shows that the estimation results have high statistical significance.

TAB. 3.2 – Statistics of α and σ.

Parameter	Number of trajectories	The range of the sample size in each trajectory	Average sample size in each trajectory	Median	Mean	Std	Minimum absolute t-statistics
α	160	[399, 1635]	1116	0.251	0.322	0.202	12.629
σ				0.028	0.031	0.015	343.530

3.6 Indifference Region Analysis

This section studies the spacing-velocity relation of each car in the lightly congested flow experiment, aiming to reveal links between the spacing-velocity relation and spatiotemporal pattern. Firstly, we show that in different Runs, how the spacing-velocity relations vary from car to car. Figure 3.29 shows three examples of the raw data in Runs 4 and 6. One can see that the data in the two Runs are largely overlapped in figure 3.29a. Figure 3.29b shows that the data in Run 4 are largely above the ones in Run 6. Figure 3.29c shows that the data in Run 4 are largely below the ones in Run 6.

The indifference region is an important concept in traffic flow and has been considered in many studies (Tian *et al.*, 2019; Jiang *et al.*, 2015; Boris S. Kerner, 2012; Yeo and Skabardonis, 2009; B. S. Kerner and Klenov, 2003). The indifference region is usually defined in the space of velocity *vs.* spacing, in which drivers are not sensitive to the changes in spacing. If the spacing is larger/smaller than the values of the right/left boundary of the region, drivers usually have the tendency to accelerate/decelerate to decrease/increase the spacing.

Next, we investigate the indifference region of the cars in different Runs. To this end, we consider the situation that the velocity difference is small. Thus, we use the data in which the absolute value of velocity difference is smaller than 1 m/s. To quantify the boundary of the indifference region, we divided the raw data into the interval of 10 km/h (interval i corresponds to velocity between $(i–1) \times 10$ and $i \times 10$ km/h). We use such an interval to ensure that the number of samples in each interval is enough. We calculate the 1st and 99th percentiles of spacing to represent the left and right boundary of the indifference region in each speed interval. The speed intervals with less than 300 data samples are discarded. The box-plot method is adopted to check the outliers in each interval, and the outliers are also discarded.

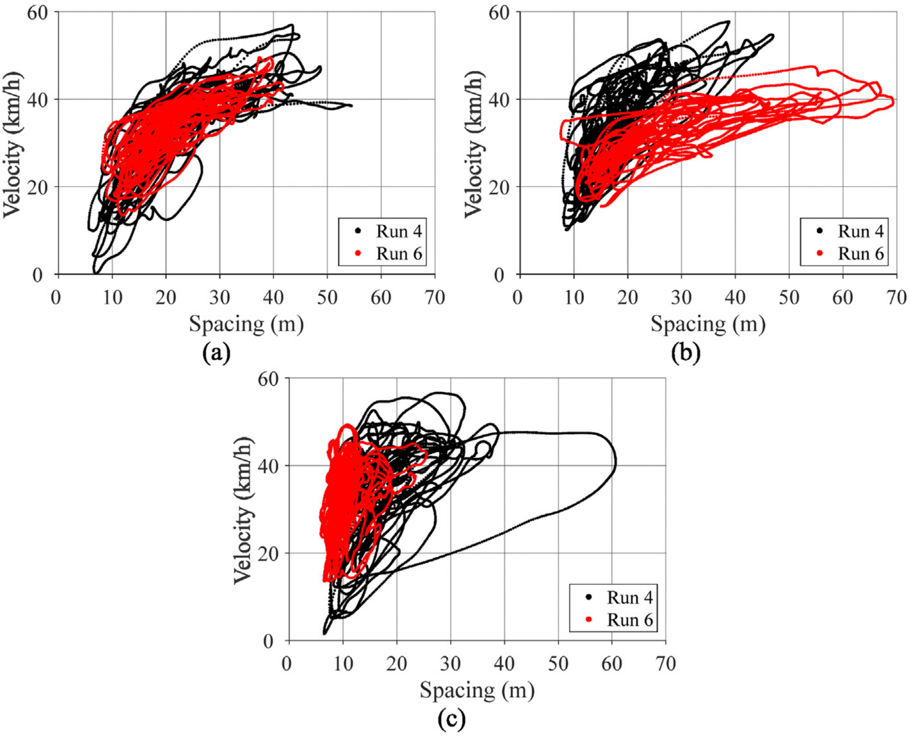

FIG. 3.29 – Three examples of the raw data in Runs 4 and 6. (a) Car No. 1, (b) Car No. 17, (c) Car No. 22.

We compare the Runs corresponding to the same global density. For example, each top panel in figure 3.30 shows the 1st and 99th percentiles of spacing in each speed interval in Runs 2 and 5. The bottom panels show the difference in spacing between the two Runs. We make a paired *t*-test at the 5% significance level, the null hypothesis that there is no significant difference in the 1st percentile of spacing could not be rejected (*p*-value = 0.2357, 0.3511, 0.1262, 0.4050 for speed interval 3 ∼ 6, respectively), while the null hypothesis that there is no significant difference in the 99th percentile of spacing is rejected in three speed intervals (*p*-value = 0.0189, 0.0011, 0.0006 for speed interval 3 ∼ 5, respectively). Note that in intervals 1, 2, 7, and 8 (0 ∼ 10 km/h, 10 ∼ 0 km/h, 60 ∼ 70 km/h, and 70 ∼ 80 km/h), there aren't enough paired samples for hypothesis test.[17]

The test results of Runs 1 *vs.* 4, 1 *vs.* 6, 4 *vs.* 6 are shown in figure 3.31. One can see that except speed interval 40 ∼ 50 km/h of Runs 1 *vs.* 6, the null hypothesis could not be rejected for the 1st percentile of spacing in all other speed intervals. The finding might indicate that the left boundary of the indifference region, which

---

[17] The threshold number of paired samples for hypothesis test is set to 4.

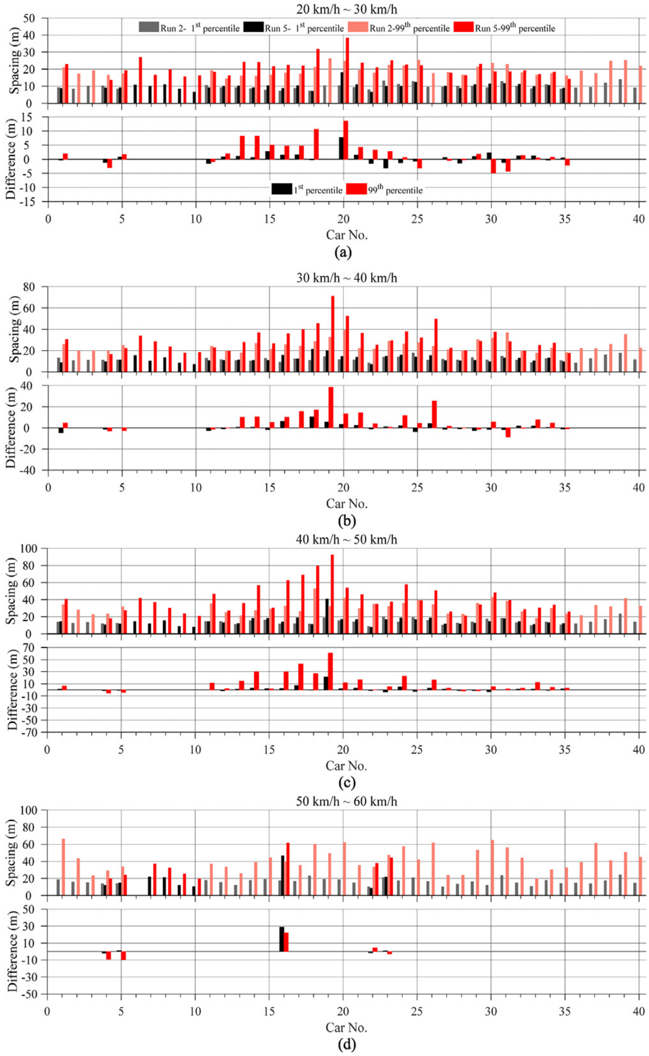

Fig. 3.30 – The comparison of the 1st and 99th percentiles of spacing in Runs 2 and 5. (a) Interval 3; (b) interval 4; (c) interval 5; (d) interval 6. The difference value is from the data of Run j minus the ones of Run i, for $j > i$. The missing data in each Run are due to (i) no sufficient data sample in the speed interval, (ii) cars absence in the Run, or (iii) signal loss.

corresponds to the safety constraint in car following, basically remains unchanged under different spatiotemporal patterns.

On the other hand, the null hypothesis is rejected for the 99th percentile of spacing in about 41% speed intervals. Moreover, in these speed intervals, the averaged value of the 99th percentile of spacing is larger in the Run with a larger index. The spatiotemporal evolution diagrams show that the traffic flow becomes

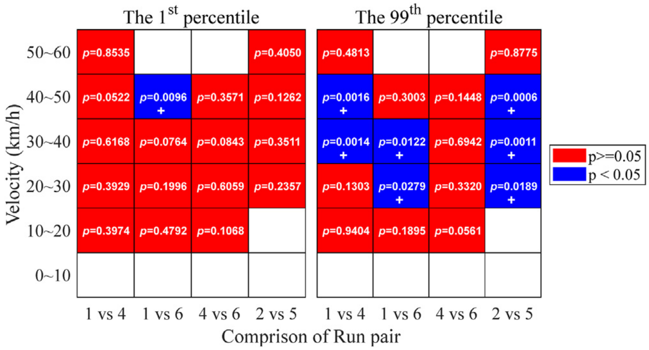

Fig. 3.31 – The paired t-test results concerning the 1st and 99th percentiles of spacing in each speed interval. The number in lattice is the p-value of paired t-test. The symbol "+" means the average value of the 1st or the 99th percentile of spacing across all cars in Run j is larger than that in Run i in the speed interval, for $j > i$.

more homogeneous from Run 1 to 4 to 6, and from Run 2 to 5. Namely, the Run with a larger index is more homogeneous. Roughly speaking, with the experiment going on, drivers become more familiar with the driving conditions and get accustomed to the setting and the situation.[18] Consequently, they tend to be less sensitive to changes in driving conditions, and the indifference region thus expands from the right side. This finding indicates that expansion of the indifference region from the right side might lead to more homogeneous traffic flow.

3.7 Sensitivity Factor Analysis in Car Following

We study the overall difference of sensitivity factor in different Runs in the lightly congested flow experiment. Here we only concern the Runs with the same global density, because as later revealed in this section, the sensitivity factor also depends on the average spacing.

For Runs 1, 4, and 6. We make a paired t-test at the 5% significance level for λ. Figure 3.32a compares λ in Runs 1 and 4. The null hypothesis that there is no significant difference is rejected (p-value = 2.51E-6). The mean value of λ is 0.4243 s^{-1} in Run 1, which is larger than 0.3515 s^{-1} in Run 4. Figure 3.32b compares λ in Runs 4 and 6, and the null hypothesis that there is no significant difference is also rejected (p-value = 4.77E-4). The mean value of λ in Run 4 is larger than 0.3091 s^{-1} in Run 6. We also compare λ in Runs 1 and 6, see figure 3.32c. As expected, they are significantly different (p-value = 9.95E-9).

---

[18] In China, vehicles are left-hand-drive ones. Thus, to observe the traffic state on the track, the driver's vision under clockwise traffic direction (Run 1, 2, 3) is smaller than that under counterclockwise direction (Run 4, 5, 6). Therefore, from Run 1 to Run 4 & 6, and from Run 2 to Run 5, the changing traffic direction might also contribute to the more homogeneous traffic flow.

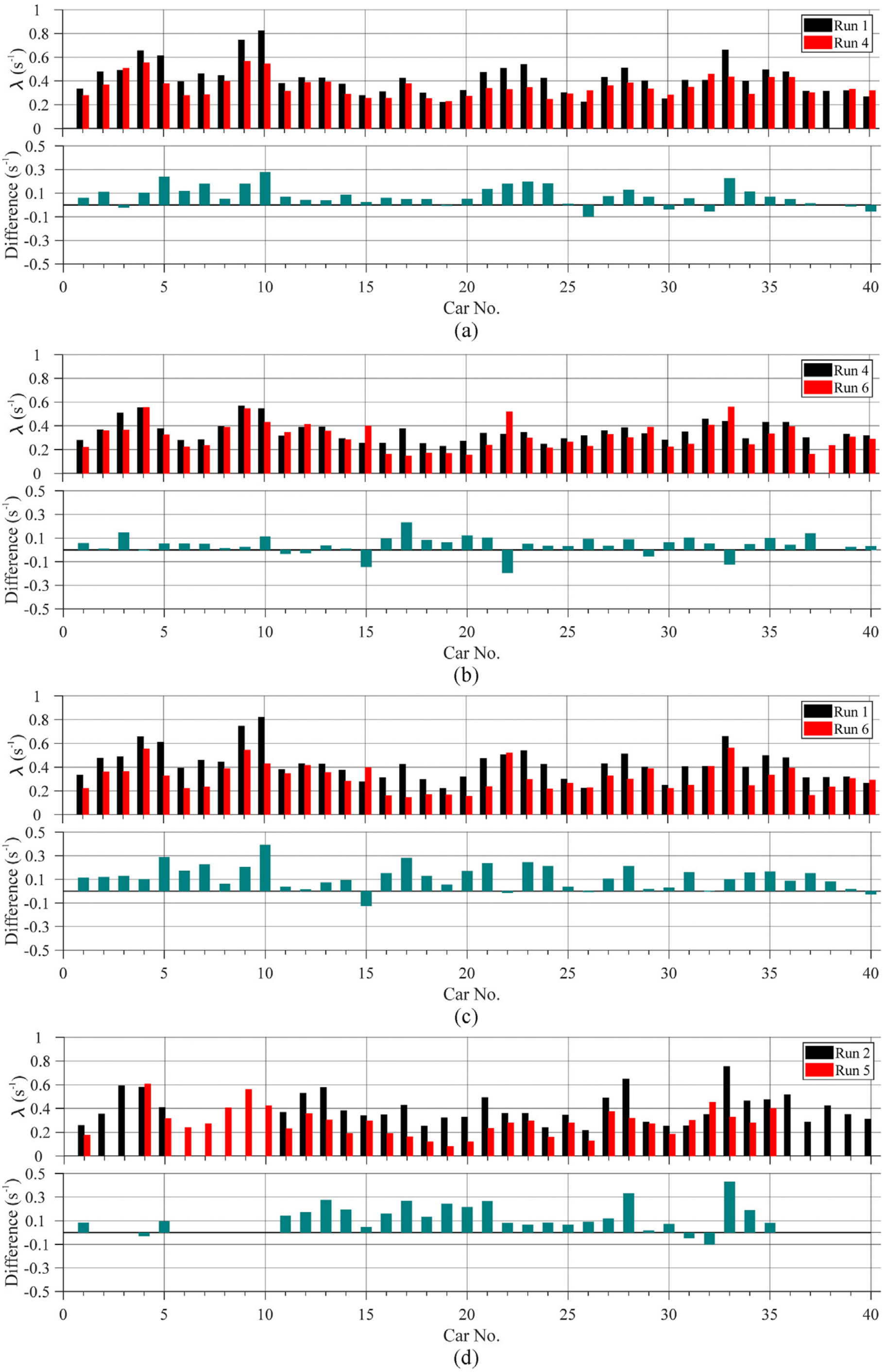

FIG. 3.32 – The comparison of sensitivity factor λ. (a) Runs 1 *vs.* 4; (b) Runs 4 *vs.* 6; (c) Runs 1 *vs.* 6; (d) Runs 2 *vs.* 5. The difference value is from the data of Run i minus the ones of Run j, for $i < j$.

For Runs 2 and 5. Comparison in figure 3.32d shows that λ in Runs 2 and 5 are significantly different (p-value = 8.67E-7). The mean value of λ is 0.3970 s^{-1} in Run 2, which is larger than 0.2814 s^{-1} in Run 5.

Since traffic flow becomes more homogeneous from Run 1 to 4 to 6 and from Run 2 to 5, our analysis thus indicates that the overall sensitivity factor might contribute to the stability of traffic flow in a way that the smaller the sensitivity factor is, the more homogeneous the traffic flow is. As aforementioned, with the experiment going on, drivers become more familiar with the driving conditions and get accustomed to the setting and the situation. Consequently, their sensitivity lowers down, which might make the traffic pattern more homogenous.

To study the specific relation between sensitivity factor λ and traffic pattern, the σ_v (STD of speed) is adopted here to reflect the amplitude of traffic oscillation. We plot the relation between λ and σ_v in figure 3.33. One can see that regardless of the global density, λ grows with the increase of σ_v.

Apart from experience, the sensitivity might also be affected by spacing. To explore this, we plot the relation of λ *vs.* the average spacing of each car. As shown in figure 3.34, there is an inverse relation between λ and average spacing. The drivers' sensitivities decrease with the increase of average spacings.

3.8 Stochasticity Factor Analysis in Car Following

This section investigates the overall difference of σ_ξ (STD of ξ) in different Runs in the lightly congested flow experiment, which reflects the strength of stochasticity in the car following.

For Runs 1, 4, and 6. Figure 3.35a compares σ_ξ in Runs 1 and 4. We make a paired t-test at the 5% significance level, and the null hypothesis that there is no

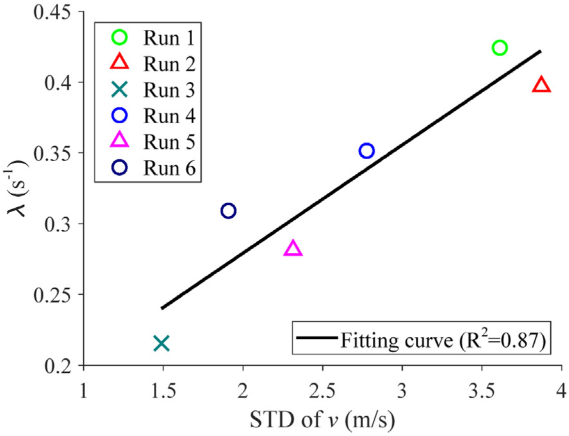

FIG. 3.33 – The relation between λ and σ_v. The scatters are the mean value across all cars in each Run. The fitting curve is given by $y = ax + b$, where $a = 0.0765$, $b = 0.1263$.

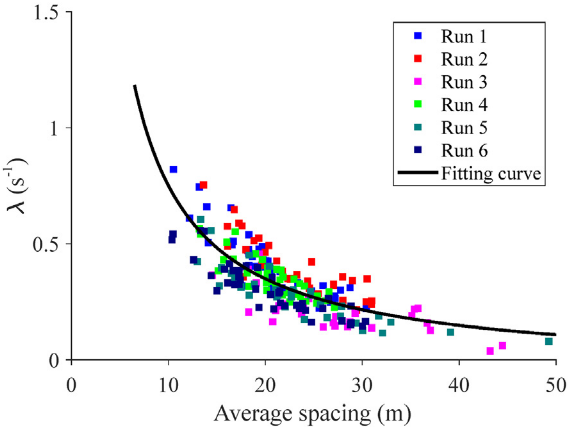

FIG. 3.34 – The relation of λ *vs.* average spacing. The fitting curve is given by $y = a\,x^{-1} + b$, where $a = 8.0312$ and $b = -0.0520$.

significant difference is rejected (p-value = 2.47E-9). The mean value of σ_ξ is 0.4016 m/s^2 in Run 1, which is larger than 0.3448 m/s^2 in Run 4. Figure 3.35b compares σ_ξ in Runs 4 and 6, and the null hypothesis is also rejected (p-value = 7.05E-18). The mean value of σ_ξ in Run 4 is larger than 0.2551 m/s^2 in Run 6. Figure 3.35c compares σ_ξ in Runs 1 and 6, and there is also a significant difference between the two Runs (p-value = 5.84E-22).

For Runs 2 and 5. Comparison in figure 3.35d shows that σ_ξ in Runs 2 and 5 are significantly different (p-value = 3.32E-19). The mean value of σ_ξ is 0.4362 m/s^2 in Run 2, which is larger than 0.2809 m/s^2 in Run 5.

Similar to the analysis of λ, there is also a significant relation between the stochastic effect and macroscopic traffic pattern. The analysis indicates that the weaker the stochastic effect is, the more homogeneous the traffic flow is. On the contrary, a strong stochastic effect is more likely to destabilize traffic flow. This is also supported by our previous finding that traffic instability is due to the accumulation of stochastic disturbances (Tian *et al.*, 2019; Jiang *et al.*, 2018). Generally speaking, with drivers getting more experienced and accustomed to the setting as the experiment goes on, the stochastic effect in car following weakens, which might contribute to the more homogenous traffic pattern.

3.9 Analysis of Competition Between Stochastic and Speed Adaptation Effects

In our previous works (Tian *et al.*, 2019; Jiang *et al.*, 2018), we argued that the growth of oscillations is due to the competition between the stochastic effect and speed adaptation effect. In this subsection, we further examine the consequences of

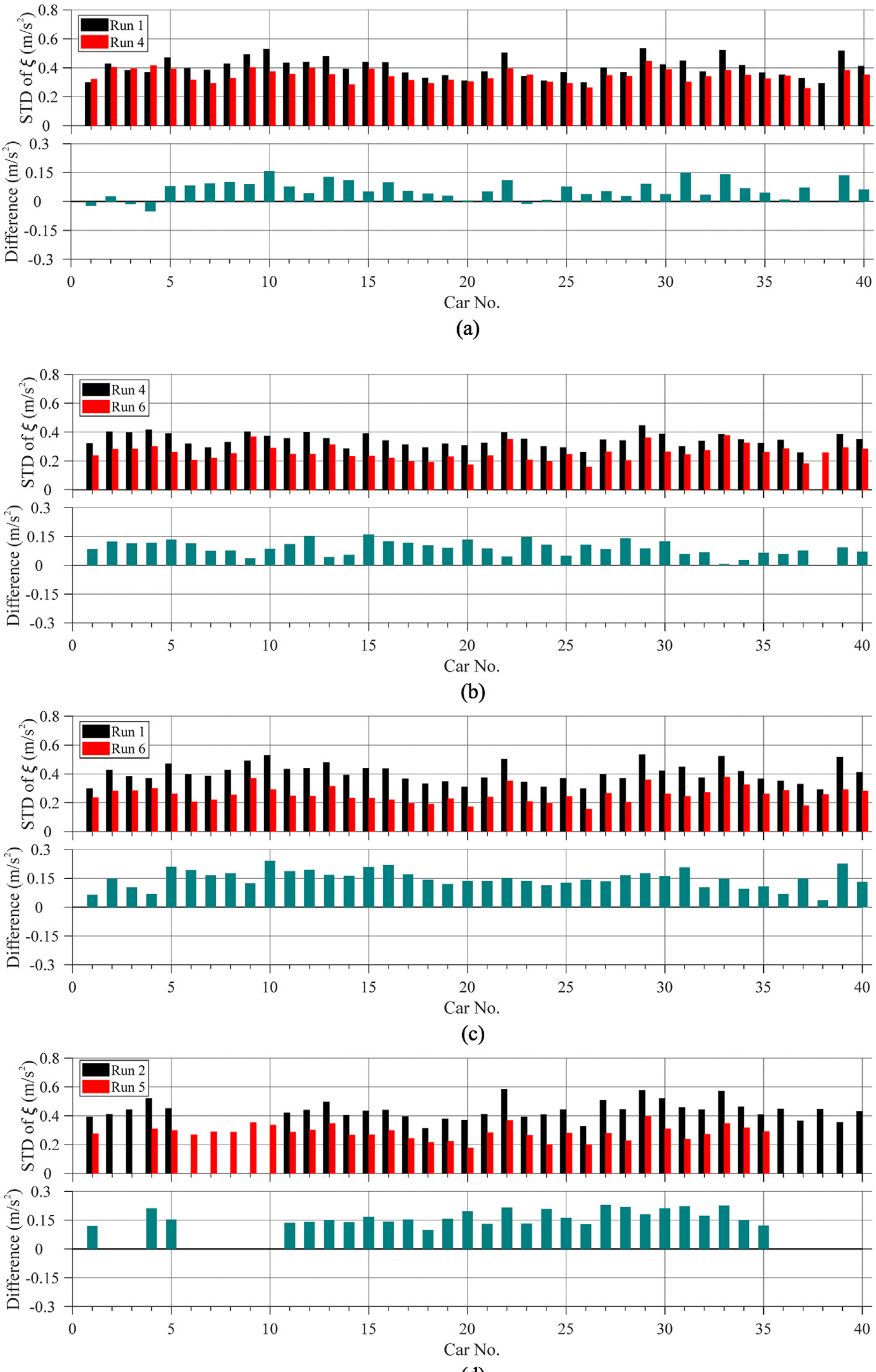

FIG. 3.35 – The comparison of STD of ξ. (a) Runs 1 *vs.* 4; (b) Runs 4 *vs.* 6; (c) Runs 1 *vs.* 6; (d) Runs 2 *vs.* 5. The difference value is from the data of Run i minus the ones of Run j, for $i < j$.

these two competitive forces on traffic flow and reveal the connection between the two effects and traffic states.

The stochastic effect ξ tends to destabilize traffic flow, while the speed adaptation effect $\lambda\Delta v$ tends to stabilize traffic flow. To depict the specific relation between the two effects and traffic instability, we plot the relation of σ_ξ and $\sigma_{\lambda\Delta v}$ (STD of $\lambda\Delta v$) *vs.* σ_v in figure 3.36, respectively. One can see that regardless of the global density, the stronger traffic oscillation corresponds to the stronger stochastic effect and speed adaptation effect. The competition between the speed adaptation effect and stochastic effect leads to a growth pattern of their ratio $\sigma_{\lambda\Delta v}/\sigma_\xi$, see figure 3.37a.

Figure 3.37b compares the ratio $\sigma_{\lambda\Delta v}/\sigma_\xi$, which grows with the increase of σ_v. One can see that the ratio in Run 3 is far below 1, which indicates that the stochastic effect plays a dominant role in the car following when the oscillation amplitude is

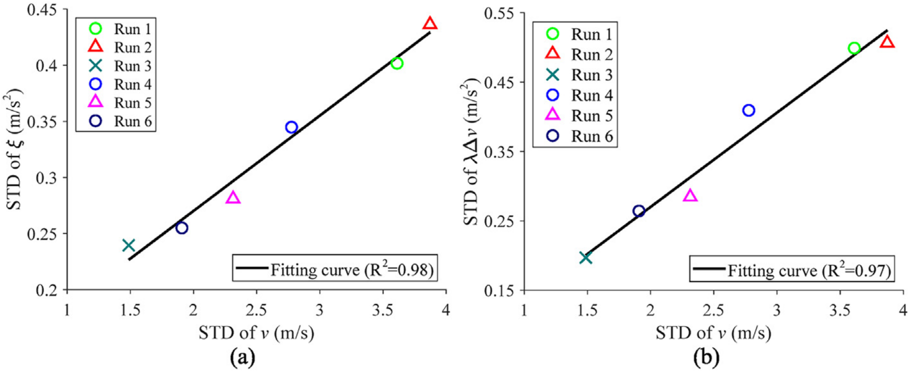

FIG. 3.36 – The relation between (a) σ_ξ, (b) $\sigma_{\lambda\Delta v}$ and σ_v. The scatters are the mean value across all cars in each Run. The fitting curve is given by $y = ax + b$: (a) $a = 0.0850$, $b = 0.1002$; (b) $a = 0.1359$, $b = -0.0017$.

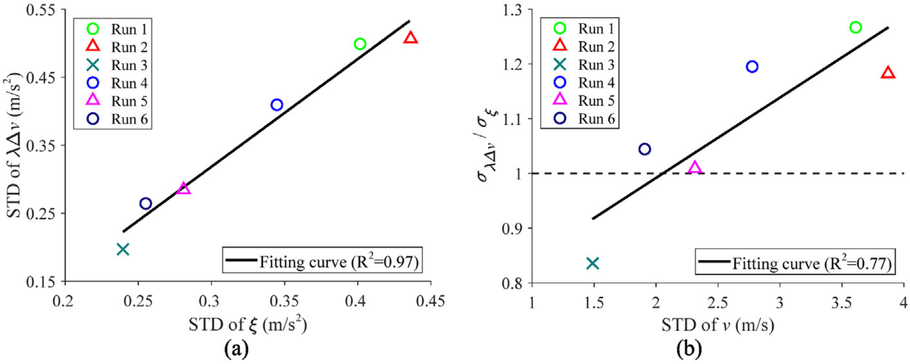

FIG. 3.37 – The competition relation between stochastic and speed adaption effects. The scatters are the mean value across all cars in each Run. The fitting curve is given by $y = ax + b$: (a) $a = 1.5840$, $b = -0.1566$; (b) $a = 0.1467$, $b = 0.6985$.

small. This is consistent with the finding in our platoon experiment that the growth of the oscillations is mainly determined by the stochastic factors for the several vehicles in the front part of the platoon (Tian *et al.*, 2019). Then, with the increase of oscillation amplitude, the speed adaptation effect gradually exceeds the stochastic effect, which would suppress the further growth of oscillation.

References

Balvers R., Wu Y.R., Gilliland E. (2000) Mean reversion across national stock markets and parametric contrarian investment strategies, *J. Finance* **55**(2), 745–772. doi: https://doi.org/10.1111/0022-1082.00225.

Chaudhuri K., Wu Y.R. (2003) Random walk *versus* breaking trend in stock prices: Evidence from emerging markets, *J. Banking & Finance* **27**(4), 575–592. doi:https://doi.org/10.1016/s0378-4266(01)00252-7.

Chen D., Laval J., Zheng Z., Ahn S. (2012) A behavioral car-following model that captures traffic oscillations, *Trans. Res. Part B: Methodol.* **46**(6), 744–761. doi:https://doi.org/10.1016/j.trb.2012.01.009.

Cheu R.L., Jin X., Ng K.C., Ng Y.L., Srinivasan D. (1998) Calibration of FRESIM for Singapore Expressway using genetic algorithm, *J. Trans. Eng.-Asce* **124**(6), 526–535. doi:https://doi.org/10.1061/(asce)0733-947x(1998)124:6(526).

Hamdar S.H., Mahmassani H.S., Treiber M. (2015) From behavioral psychology to acceleration modeling: Calibration, validation, and exploration of drivers' cognitive and safety parameters in a risk-taking environment, *Trans. Res. Part B: Methodol.* **78**, 32–53. doi:https://doi.org/10.1016/j.trb.2015.03.011.

Jiang R., Hu M. B., Zhang H.M., Gao Z.-Y., Jia B., Wu Q.-S. (2015) On some experimental features of car-following behavior and how to model them, *Trans. Res. Part B: Methodol.* **80**, 338–354. doi:https://doi.org/10.1016/j.trb.2015.08.003.

Jiang R., Jin C.-J., Zhang H.M., Huang Y.-X., Tian J.-F., Wang W.,...,Jia B. (2018) Experimental and and empirical investigations of traffic flow instability, *Trans. Res. Part C: Emerging Technol.* **94**, 83–98. doi:https://doi.org/10.1016/j.trc.2017.08.024.

Karatzas I., Shreve S.E. (1991) *Brownian motion and stochastic calculus*. Springer, New York.

Kerner B.S. (2012) Complexity of spatiotemporal traffic phenomena in flow of identical drivers: Explanation based on fundamental hypothesis of three-phase theory, *Phys. Rev. E* **85**(3), 036110. doi:https://doi.org/10.1103/PhysRevE.85.036110.

Kerner B.S., Klenov S.L. (2003) Microscopic theory of spatial-temporal congested traffic patterns at highway bottlenecks, *Phys. Rev. E* **68**(3), 036130. doi:https://doi.org/10.1103/PhysRevE.68.036130.

Laval J.A., Leclercq L. (2010) A mechanism to describe the formation and propagation of stop-and-go waves in congested freeway traffic, *Philos. Trans. R. Soc. Math. Phys. Eng. Sci.* **368** (1928), 4519–4541. doi:https://doi.org/10.1098/rsta.2010.0138.

Newell G.F. (2002) A simplified car-following theory: a lower order model, *Trans. Res. Part B: Methodol.* **36**(3), 195–205. doi:https://doi.org/10.1016/s0191-2615(00)00044-8.

Punzo V., Borzacchiello M.T., Ciuffo B. (2011) On the assessment of vehicle trajectory data accuracy and application to the Next Generation SIMulation (NGSIM) program data, *Trans. Res. Part C: Emerging Technol.* **19**(6), 1243–1262. doi:https://doi.org/10.1016/j.trc.2010.12.007.

Punzo V., Montanino M. (2016) Speed or spacing? Cumulative variables, and convolution of model errors and time in traffic flow models validation and calibration, *Trans. Res. Part B: Methodol.* **91**, 21–33. doi:https://doi.org/10.1016/j.trb.2016.04.012.

Sharma A., Zheng Z., Bhaskar A. (2019) Is more always better? The impact of vehicular trajectory completeness on car-following model calibration and validation, *Trans. Res. Part B: Methodol.* **120**, 49–75. doi:https://doi.org/10.1016/j.trb.2018.12.016.

Tang C.Y., Chen S.X. (2009) Parameter estimation and bias correction for diffusion processes, *J. Econo.* **149**(1), 65–81. doi:https://doi.org/10.1016/j.jeconom.2008.11.001.

Tian J., Zhang H.M., Treiber M., Jiang R., Gao Z.-Y., Jia B. (2019) On the role of speed adaptation and spacing indifference in traffic instability: Evidence from car-following experiments and its stochastic model, *Trans. Res. Part B: Methodol.* **129**, 334–350. doi:https://doi.org/10.1016/j.trb.2019.09.014.

Treiber M., Kesting A. (2013) *Traffic flow dynamics: Data, models and simulation.* Springer, Berlin Heidelberg.

Vasicek O. (1977) An equilibrium characterization of the term structure, *J. Financ. Econ.* **5**(4), 627–627.

Yeo H., Skabardonis A. (2009) *Understanding stop-and-go traffic in view of asymmetric traffic theory.* Paper presented at the Transportation and Traffic Theory 2009: Golden Jubilee.

Chapter 4

Cellular Automaton Models

Abstract. Cellular automaton (CA) is a dynamic system in which spatially-discrete cells have discrete states, and evolve according to spatially-localized discrete-time update rules (Hanson, 2009). In CA, space is divided into many units by regular meshes. Each element in these regular grids is called a cell, which has a finite set of discrete states. All cells follow the same discrete-time local update rules. The basic idea of CA is to use a large number of simple components, simple links, and simple rules running in parallel in time and space, to simulate complex and rich phenomena (Jia *et al.*, 2007; Wolfram, 1982). CA is an important theoretical framework for studying complex system behavior, and also one prototype of AI (Duan *et al.*, 2012). Up to now, CA has been widely used in social, economic, and scientific research fields, including biology (Edelstein-Keshet, 2017)), ecology (Hogeweg, 1988), physics (Krug and Spohn, 1988), chemistry (Krug and Spohn, 1988; Lodder *et al.*, 1988), environmental science (Parsons and Fonstad, 2007), society and economy (Goldenberg *et al.*, 2002), financial (Bartolozzi and Thomas, 2004), and so on. In the CA traffic flow models, the road is classified into cells. Each cell can be empty or occupied by at most one vehicle (except in multi-value CA models, in which each cell can hold more than one vehicle, see *e.g.*, Nishinari and Takahashi (2000). Time is discretized and each time step usually corresponds to 1 s. As a result, velocity and acceleration are also discretized.

4.1 The Basic CA Models

4.1.1 The NaSch Model

The first CA traffic flow model can be traced back to the Wolfram 184 model (Wolfram, 1982), in which each vehicle moves deterministically. In one time step, vehicles either stay motionless (if the cell in front is occupied) or move forward by one cell (if the cell in front is empty). Cremer and Ludwig (1986) proposed another CA model. However, these early models did not attract the attention of the traffic flow community until the proposal of the NaSch model.

DOI: 10.1051/978-2-7598-3193-7.c004
© Science Press, EDP Sciences, 2023

The parallel update rules in the NaSch model are as follows.
Step 1. Acceleration:

$$\tilde{v} = \min\,(v + a, v_{\max})$$

Step 2. Deceleration:

$$\tilde{v} = \min\,(\tilde{v},\ d)$$

Step 3. Randomization:

$$v' = \begin{cases} \max(\tilde{v} - b, 0), & \text{if } r < p, \\ \tilde{v}, & \text{otherwise.} \end{cases}$$

Step 4. Vehicle movement:

$$x' = x + v'$$

Here x (x') and v (v') denote positions and speeds at the current and next time step. x_l is the position of the leading vehicle. $d = x_l - x - l_{\text{veh}}$ is the space gap between the two vehicles and l_{veh} is vehicle length. $v_{\max}$ is the maximum speed of vehicles. a and b are acceleration and randomization deceleration, respectively, which are usually set to be 1. p is the randomization probability.

Figure 4.1 shows the fundamental diagram of the NaSch model on a circular road with length 1000 L_{cell}. The parameters are shown in table 4.1. Two different traffic states are classified. When the density is smaller than the critical density ρ_c, the traffic is in free flow, see figure 4.2a. When $\rho > \rho_c$, the jams appear spontaneously, see figure 4.2b.

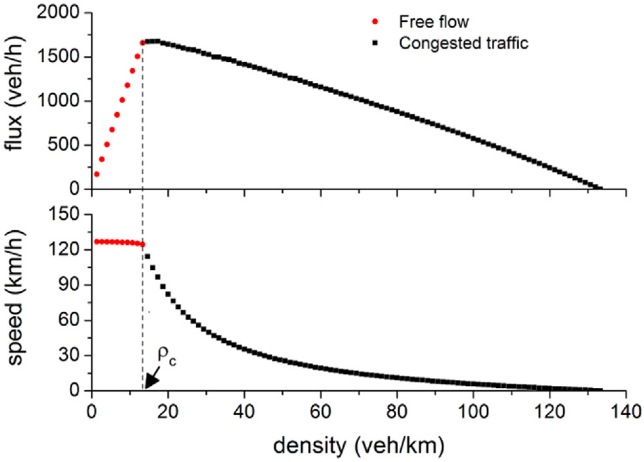

FIG. 4.1 – The fundamental diagram of the NaSch model on a circular road. This figure describes the averaged flow as a function of the global density (number of vehicles divided by the circumference). The averaged flow is product of the global density and the average speed of all vehicles on the road.

TAB. 4.1 – Parameter values of the NaSch model. Taken from Nagel and Schreckenberg (1992).

Parameters	L_{cell}	L_{veh}	$v_{\max}$	a	b	p
Units	m	L_{cell}	L_{cell}/s	$L_{\text{cell}}/\text{s}^2$	$L_{\text{cell}}/\text{s}^2$	–
Values	7.5	1	5	1	1	0.3

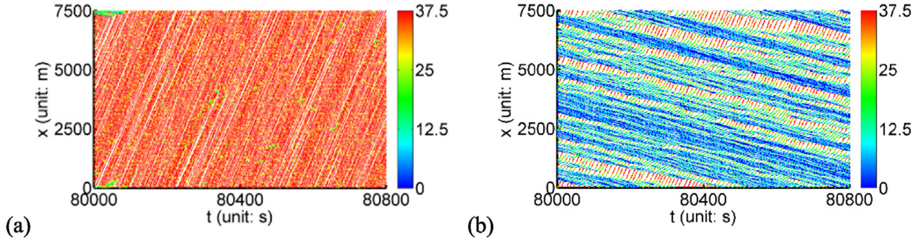

FIG. 4.2 – The spatiotemporal diagrams of NaSch model on the circular road. (a) $\rho = 13$ veh/km; (b) $\rho = 53$ veh/km. The color bar indicates speed (m/s).

As recently revealed, stochastic factors play a nontrivial role in traffic flow dynamics. Traffic flow instability might be due to the cumulative effect of stochastic factors (Jiang *et al.*, 2014, 2015, 2018; Laval *et al.*, 2014; Treiber and Kesting, 2013). Randomization in the NaSch model characterizes the stochastic factors, which enables the model to depict the spontaneous formation of jams in congested flow. This feature makes NaSch model a milestone in traffic flow studies, which has been cited 2401 times according to Web of Science (accessed on 23/09/2018). Moreover, the NaSch model has been widely used in transportation applications. For example, it has been used as a microscopic simulator in the TRANSIMS developed at Los Alamos National Laboratory (Nagel and Rickert, 2001) and in urban traffic simulation in Dallas/Fort Worth area (Rickert and Nagel, 1997).

4.1.2 The Slow-To-Start Model

In the NaSch model, the transition from free flow to congested flow is not of the first order. To depict the first-order transition in traffic flow, the slow-to-start rules are introduced (Barlovic *et al.*, 1998; Benjamin *et al.*, 1996; Fukui and Ishibashi, 1997; Schadschneider and Schreckenberg, 1997; Takayasu and Takayasu, 1993). Here we review the velocity-dependent-randomization (VDR) rule (Barlovic *et al.*, 1998), which is the simplest one. In the VDR model, the only difference from the NaSch model is that the randomization is not a constant, it depends on the velocity as follows,

$$p(v) = \begin{cases} p_0, & \text{if } v = 0, \\ p, & \text{otherwise.} \end{cases}$$

Figure 4.3 shows the fundamental diagram of the VDR model, in which there are two critical densities. Below ρ_{c1}, the traffic is in free flow; above ρ_{c2}, the traffic is in a jam. When the density is in the range $\rho_{c1} < \rho < \rho_{c2}$, the traffic flow is metastable. When starting from homogeneous traffic, free flow is maintained, see figure 4.4a. When starting from mega-jam, the traffic is in jam. Moreover, the first-order transition from free flow to jam could appear spontaneously, see figure 4.4b.

TAB. 4.2 – Parameter values of the VDR model taken from Barlovic *et al.* (1998).

Parameters	L_{cell}	L_{veh}	$v_{\max}$	a	b	p_0	p
Units	m	L_{cell}	L_{cell}/s	$L_{\text{cell}}/\text{s}^2$	$L_{\text{cell}}/\text{s}^2$	–	–
Values	7.5	1	5	1	1	0.75	1/64

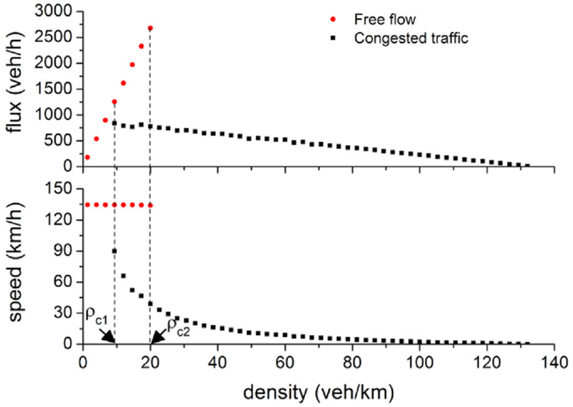

FIG. 4.3 – The fundamental diagram of the VDR model on a circular road. The parameters are shown in table 4.2.

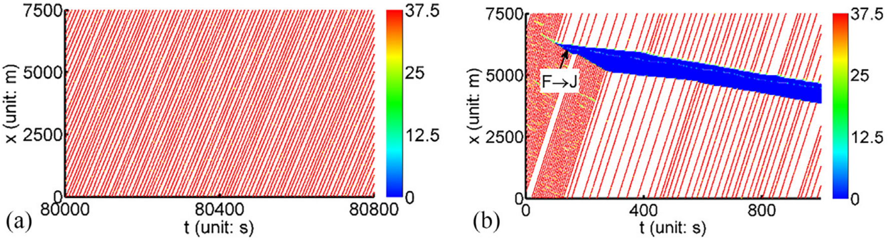

FIG. 4.4 – The spatiotemporal diagrams of VDR model on the circular road. (a) $\rho = 15$ veh/km, start from homogeneous initial condition; (b) $\rho = 20$ veh/km.

4.1.3 The Kerner-Klenov-Wolf Model for Synchronized Traffic Flow

The Kerner-Klenov-Wolf (KKW, Kerner *et al.* (2002)) model is one of the first CA models (the other is the comfortable driving model in section 4.2.1) within the framework of three-phase traffic theory, in which the 2D region of steady state and the speed adaptation effect is explicitly considered. The update rules consist of deterministic and stochastic rules.
Step 1. Dynamical part of all KKW models:

$$\tilde{v} = \max(0, \min(v_{\max}, v_s, v_c)).$$

where,

$$v_s = d.$$

$$v_c = \begin{cases} v + a & \text{for } x_l - x > G(v), \\ v + a \ \mathrm{sign}(\Delta v) & \text{for } x_l - x \leq G(v). \end{cases}$$

Step 2. Stochastic part of all KKW models:

$$v' = \max(0, \min(\tilde{v} + a\eta, v + a, v_{\max}, v_s)).$$

where,

$$\eta = \begin{cases} -1, & \text{if } r < p_{\mathrm{b}}, \\ 1, & \text{if } p_{\mathrm{b}} \leq r < p_{\mathrm{b}} + p_{\mathrm{a}}, \\ 0, & \text{otherwise.} \end{cases}$$

$$p_b = \begin{cases} p_0, & \text{if } v = 0, \\ p, & \text{if } v > 0. \end{cases}$$

$$p_a = \begin{cases} p_{\mathrm{a}1}, & \text{if } v < v_p \\ p_{\mathrm{a}2}, & \text{if } v \geq v_p. \end{cases}$$

Step 3. Vehicle movement:

$$x' = x + v'$$

Here $\Delta v = v_l - v$ is the speed difference and v_l is the speed of the leading vehicle. v_{s} is the safe speed that must not be exceeded to avoid collisions. v_c describes the rule of "speed change", which means the acceleration behavior depends on whether the leading vehicle is within a synchronized space gap. The synchronized space gap can be defined as linear form: $G(v) = L_{\mathrm{veh}} + kv$ or nonlinear form: $G(v) = L_{\mathrm{veh}} + v + \beta v/(2a)$, in which k and β are the positive parameters. The sign function is defined as

$$\operatorname{sign}(\Delta v)=\begin{cases}-1 & \text{if } \Delta v<0,\\ 0 & \text{if } \Delta v=0,\\ 1 & \text{if } \Delta v>0.\end{cases}$$

The steady state corresponds to a 2D region bounded by $q = \rho v_s = (1 - \rho L_{\text{veh}})$ (U: related to safe speed), $q = \rho v_{\max}$ (F: related to maximum speed) and $q = (1 - \rho L_{\text{veh}})/k$ (L: related to the linear form of synchronized space gap), see figure 4.5. The rule $v_c = v + a\ \operatorname{sign}(\Delta v)$ corresponds to the speed adaptation effect, which occurs when the traffic state is in the 2D region.

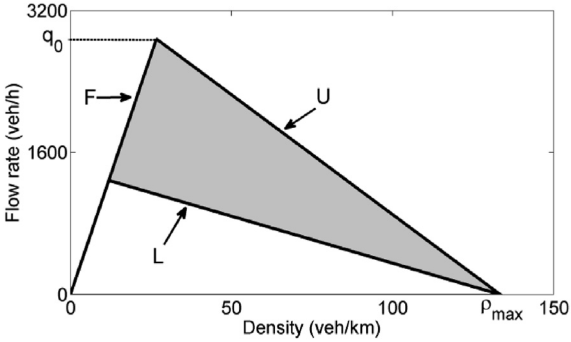

Fig. 4.5 – The 2D region of KKW model.

Figure 4.6 shows simulation results of the fundamental diagram of the KKW model on a circular road with length $L = 7500$ m. Each cell corresponds to $L_{\text{cell}} = 0.5$ m. The parameter values are shown in table 4.3. One can see that three density ranges are classified by two critical densities. When the density $\rho < \rho_{c1}$, the traffic

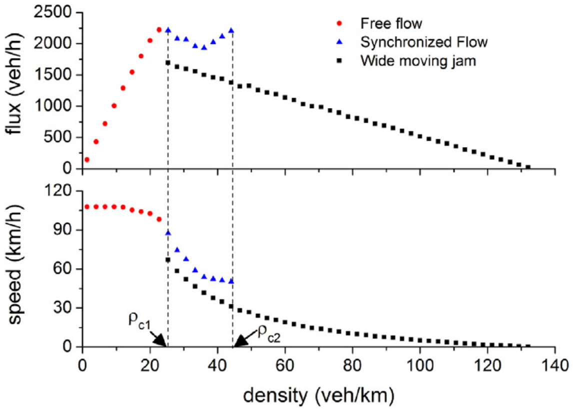

Fig. 4.6 – The fundamental diagram of the KKW model on a circular road. The parameters are shown in table 4.3.

TAB. 4.3 – Parameter values of the KKW model taken from Kerner *et al.* (2002).

Parameters	L_{cell}	L_{veh}	$v_{\max}$	a	k	p	p_0	$p_{\text{a}1}$	$p_{\text{a}2}$	v_p
Units	m	L_{cell}	L_{cell}/s	$L_{\text{cell}}/\text{s}^2$	–	–	–	–	–	L_{cell}/s
Values	0.5	15	60	1	2.55	0.04	0.425	0.2	0.052	28

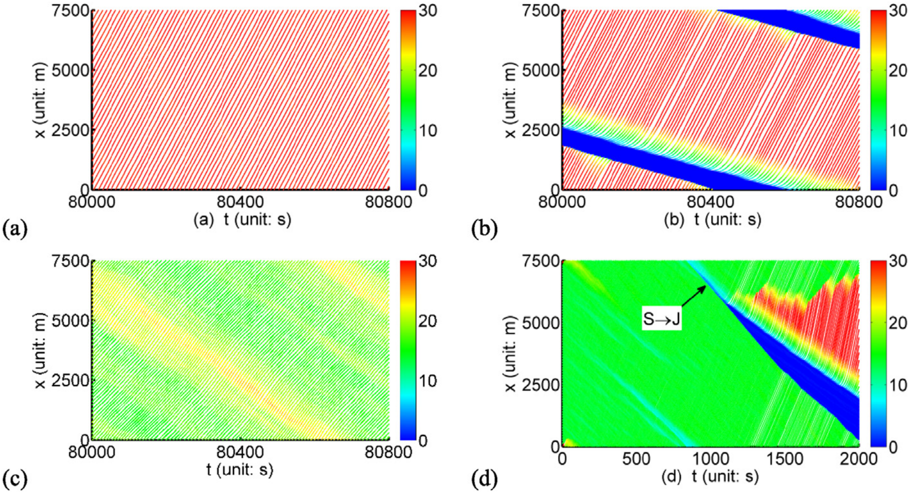

FIG. 4.7 – The spatiotemporal diagrams of KKW model on the circular road. (a) $\rho = 15$ veh/km; (b) $\rho = 31$ veh/km; (c) $\rho = 31$ veh/km; (d) $\rho = 47$ veh/km.

flow is in a free flow state, see figure 4.7a. When the density is larger than $\rho_{\text{c}1}$, traffic flow is a coexistence of free flow and jams if initially starting from a mega-jam, see figure 4.7b. When the density $\rho_{\text{c}1} < \rho < \rho_{\text{c}2}$, the traffic flow will be in synchronized flow if starting from a homogeneous configuration, see figure 4.7c. When $\rho > \rho_{\text{c}2}$, synchronized flow cannot be maintained even if starting from a homogeneous configuration. Jams will emerge spontaneously, see figure 4.7d. We also notice that in the simulation results, the flow rate in synchronized flow changes non-monotonically, which might be related to the choice of parameters.

To simulate the concave growth pattern, the following parameter values are adopted *via* calibration: $L_{\text{veh}} = 15L_{\text{cell}}$, $k = 2.55$ s, $a = 5L_{\text{cell}}/\text{s}^2$, $v_p = 28L_{\text{cell}}/\text{s}$, $p_0 = 0.425$, $p_{\text{a}1} = 0.2$, $p_{\text{a}1} = 0.052$, $p = 0.08$, $v_{\max} = 60L_{\text{cell}}/\text{s}$. Figure 4.8a shows that the formation of oscillations can be reproduced. Figure 4.8b shows that the standard deviation increases faster in the simulation than in the empirical data in the initial stage. In particular, the standard deviation of the second vehicle has reached about 1.5 m/s, much larger than that in the experimental data. However, later the growth rate of the standard deviation in the model becomes slower than the empirical one.

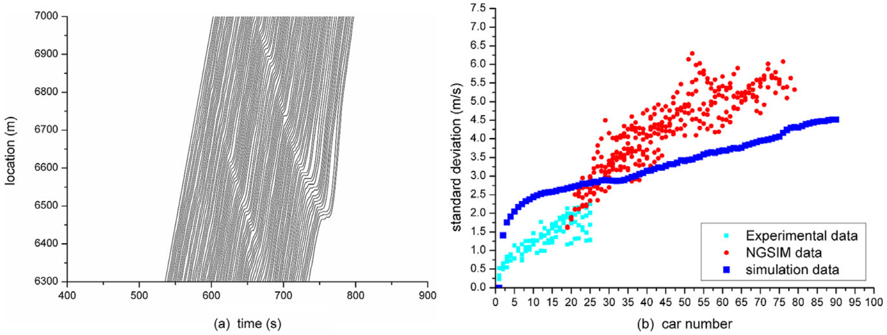

FIG. 4.8 – The simulation results of trajectories by KKW model, (b) the corresponding standard deviation of velocities of vehicles.

4.2 The Generalized NaSch Models

Models of this class such as (Tian *et al.*, 2012a, 2012b, 2015, 2016, 2017; Jia *et al.*, 2011; Gao *et al.*, 2007, 2009; Zhao *et al.*, 2009) are all based on the following generalized NaSch rules.
Step 1. Acceleration/deceleration:

$$\tilde{v} = \min\left(v + \hat{a}, \hat{d}, \hat{v}\right)$$

Step 2. Randomization with probability $\hat{p}$:

$$v' = \begin{cases} \min(\tilde{v} - \hat{v}_r, 0), & \text{if } r < \hat{p}, \\ \tilde{v}, & \text{otherwise.} \end{cases}$$

Step 3. Vehicle movement:

$$x' = x + v'$$

In different models, the formulations of $\hat{a}$, $\hat{d}$, $\hat{v}$, $\hat{v}_r$, and $\hat{p}$ are different.

4.2.1 The Comfortable Driving Model and Its Variants

Knospe *et al.* (2000) proposed the comfortable driving (CD) model that considers the desire of the drivers for smooth and comfortable driving. In this model, the formulations of $\hat{a}$, $\hat{d}$, $\hat{v}$, $\hat{v}_r$, and $\hat{p}$ are as follows.

(i) $\hat{a} = \begin{cases} a, & \text{if } (s_l = 0 \text{ and } s = 0) \text{ or } t_h \geq t_s, \\ 0, & \text{otherwise.} \end{cases}$

(ii) $\hat{d} = d + \max\left(v_{\text{anti}} - g_{\text{safety}}, 0\right)$.

(iii) $\hat{v} = v_{\max}$

(iv) $\hat{v}_r = b$

$$\text{(v)}\quad \hat{p} = \begin{cases} p_{\mathrm{b}}, & \text{if } s_l = 1 \text{ and } t_h < t_s, \\ p_0, & \text{if } v_n = 0\ , \\ p_{\mathrm{d}}, & \text{otherwise.} \end{cases}$$

Here $v_{\mathrm{anti}} = \min(d_l, v_l)$. s and s_l are the status of the brake light of the vehicle and its leader ($s = 1(0)$ means the brake lights are on (off)). $t_h = d/v$ is the time gap. t_s is the safe time headway, which is defined as $t_s = \min(v, h)$. The slow-to-start rule is applied to simulate the wide moving jams in which standing vehicles in the previous time step have a higher randomization probability p_0 than the moving vehicles with p_d. Moreover, $b \geq a$ should be satisfied to simulate the wide-moving jams. The brake light state s' in the next time step is determined as follows.

$$s' = \begin{cases} 1, & \text{if } \tilde{v} < v \text{ or } (p = p_{\mathrm{b}} \text{ and } v' < v), \\ 0, & \text{otherwise.} \end{cases}$$

Figure 4.9 shows the fundamental diagram of the model. Three density ranges can be classified. In the synchronized flow branch, a phase separation phenomenon will occur and the system is the coexistence of the free flow phase and congested flow phase (figure 4.10a). Note that the congested flow consists of both synchronized flow and jams. In other words, the model cannot correctly reproduce the synchronized flow. With the increase of the density, the free flow region shrinks (see figure 4.10a

TAB. 4.4 – Parameter values of CD model taken from Knospe *et al.* (2000).

Parameters	L_{cell}	L_{veh}	$v_{\max}$	a	b	p_{b}	p_0	p_{d}	g_{safety}	h
Units	m	L_{cell}	$L_{\mathrm{cell}}/\mathrm{s}$	$L_{\mathrm{cell}}/\mathrm{s}^2$	$L_{\mathrm{cell}}/\mathrm{s}^2$	–	–	–	L_{cell}	s
Values	1.5	5	20	1	1	0.94	0.5	0.1	7	6

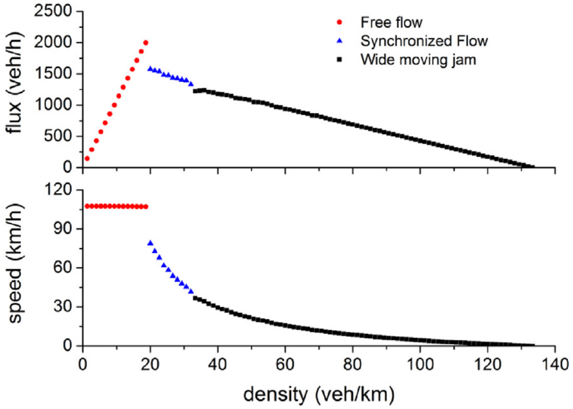

FIG. 4.9 – The fundamental diagram of CD model on a circular road with length 7500 m. The parameters are shown in table 4.4.

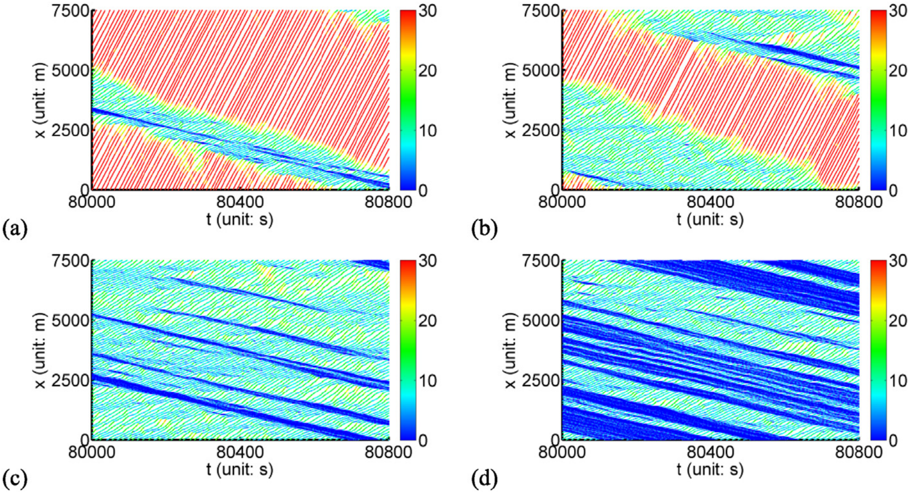

FIG. 4.10 – The spatiotemporal diagram of the CD model on the circular road. (a) $\rho = 23$ veh/km; (b) $\rho = 27$ veh/km; (c) $\rho = 49$ veh/km; (d) $\rho = 76$ veh/km.

and b). In the wide moving jam branch, the free flow region disappears and only the congested flow exists (figure 4.10c). If one continues to increase the density, the jams will gradually invade the synchronized flow (figure 4.10c and d). Unfortunately, the metastable states, the F → S and S → J transitions cannot be simulated by the CD model.

Tian *et al.* (2017) found that in the CD model, when the leading vehicle decelerates sharply, there is not enough time for the following vehicle to smoothly adapt its speed due to the reaction delay. As a result, jam emerges, and synchronized flow cannot be maintained. To overcome this deficiency, the braking rule is revised by introducing a desired time gap larger than 1 s, named the desired time gap brake light (DTGBL) model. In the DTGBL model, the formulations of $\hat{a}$, $\hat{d}$, $\hat{v}$, $\hat{v}_r$, and $\hat{p}$ are as follows.

$$\text{(i)}\quad \hat{a} = \begin{cases} a_1, & \text{if } (s_l = 0 \text{ or } t_h \geq t_s) \text{ and } v > 0 \\ a_2, & \text{otherwise} \end{cases}$$

$$\text{(ii)}\quad \hat{d} = \left\lceil \left(d_n + \max\left(v_{\text{anti}} - g_{\text{safety}}, 0\right)\right) / T \right\rceil$$

$$\text{(iii)}\quad \hat{v} = v_{\max}$$

$$\text{(iv)}\quad \hat{v}_r = b$$

$$\text{(v)}\quad \hat{p} = \begin{cases} p_{\mathrm{b}}, & \text{if } s_l = 1 \text{ and } t_h < t_s, \\ p_0, & \text{if } v = 0, \\ p_{\mathrm{d}}, & \text{otherwise.} \end{cases}$$

where the brake light rule in the CD model is applied. Here $\lceil x \rceil$ returns the minimum integer no smaller than x.

The steady states of the DTGBL model are considered. In the deterministic limit $p_\mathrm{b} = 1$, $p_\mathrm{d} = 0$, and $p_0 = 0$, the steady states are given by $v_n = \min(d_{n,\mathrm{eff}}/T,\ v_{\max})$. Thus the unique relationship between speed and space gap is established.

Nevertheless, in traffic flow, stochastic factors play an important role. Figure 4.11a, b show two examples of the velocities of a car (which is asked to move with constant speed) and its following car, as well as the gap between the two cars in Jiang *et al.*'s traffic experiment (Jiang *et al.*, 2014). One can see that while the speed of the following car fluctuates weakly, the gap changes significantly. This demonstrates that the steady states do not exist in real traffic and the traffic state actually dynamically spans a two-dimensional speed-gap region.

In the DTGBL model, when the various randomizations are considered, the traffic state is able to dynamically span a two-dimensional speed-gap region as in the experiment, see figure 4.11c.

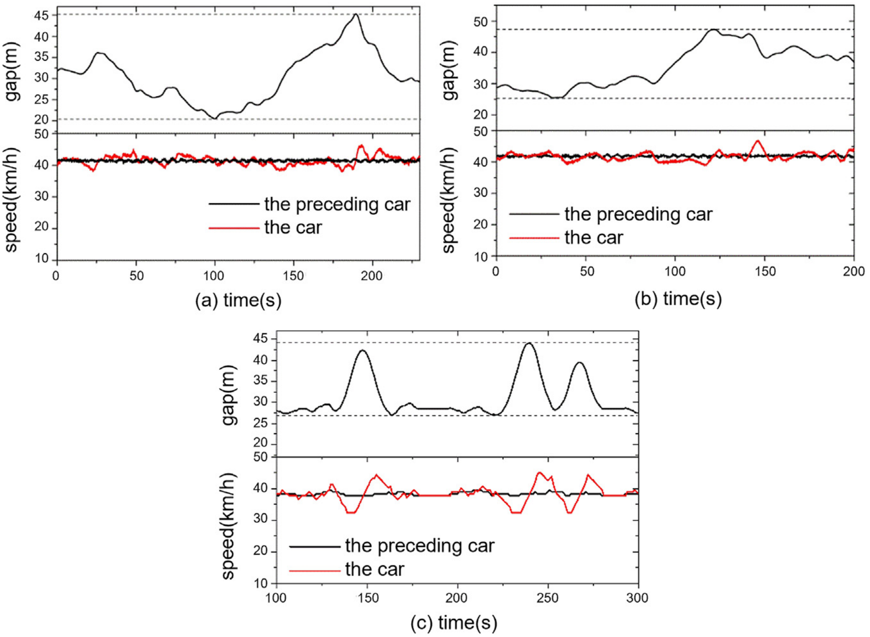

Fig. 4.11 – (a, b) The evolution of speeds of a car and its preceding car and their gaps taken from the real car following experiments. The preceding car in (a) is the same as that of (b), while the following cars are different. (c) Simulation results with the DTGBLM with the parameters in table 4.5 Note that if the leading car moves with constant speed, then its brake light is always off. As a result, for the following car, its randomization is always equal to p_d so our model reduces to the NaSch model. Therefore, we introduce randomization probability $p = 0.9$ to the leading car to activate its brake light so that the following car can move with our model rule. In order to show the variation trend, the original discrete simulation results are smoothed by the moving average method with the smoothing width $w = 15$.

Compared with the CD model, the highlight feature is that the desired time gap is set as $T > 1$. Figure 4.12 shows the fundamental diagram of this model, which can reproduce the free flow, the synchronized flow, the jam as well as F → S (figure 4.13a), S → J transition (figure 4.13b). Also note that the fluctuation of speed in synchronized flow is reasonable, see figure 4.14.

TAB. 4.5 – Parameter values of DTGBL model taken from Tian *et al.* (2017).

Parameters	L_{cell}	L_{veh}	$v_{\max}$	T	p_{b}	p_0	p_{d}	g_{safety}	h	a_1	a_2	b
Units	m	L_{cell}	L_{cell}/s	s	–	–	–	L_{cell}	s	$L_{\text{cell}}/\text{s}^2$	$L_{\text{cell}}/\text{s}^2$	$L_{\text{cell}}/\text{s}^2$
Values	1.5	5	20	1.8	0.94	0.5	0.1	7	6	2	1	1

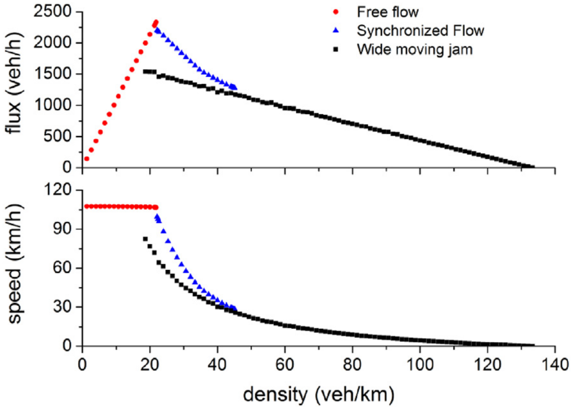

FIG. 4.12 – The fundamental diagram of DTGBL model with length 3000 m. The parameters are shown in table 4.5.

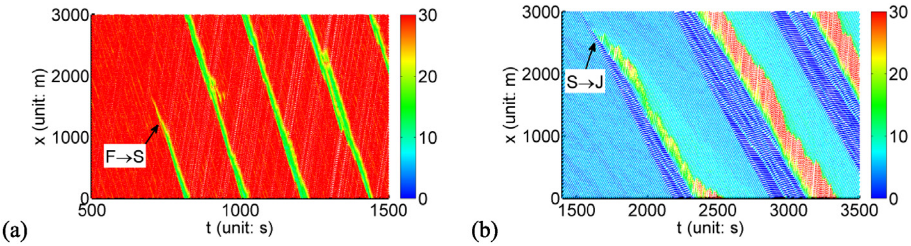

FIG. 4.13 – The spatiotemporal pattern of (a) $\rho = 22$ veh/km, describes F → S, (b) $\rho = 67$ veh/km, describes S → J transition.

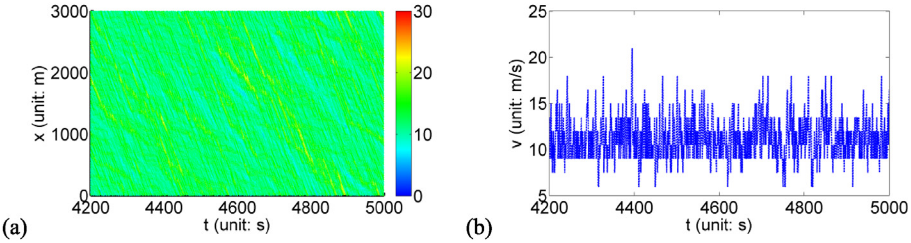

FIG. 4.14 – The simulation results of the spatiotemporal diagram. (a) $\rho = 37$ veh/km; (b) The time series of the velocity of a single vehicle.

Figure 4.15 simulates the 25-vehicle-platoon experiment for DTGBLM. The jam initial condition is adopted and the leading vehicle (No. 1) moves with the constant speed v_l. The disturbance evolution process of DTGBLM is in pretty good agreement with that of the experiment. Figure 4.16 compares the spatiotemporal patterns of the speeds of the car platoon. One can see that the simulation results are very similar to the experimental ones.

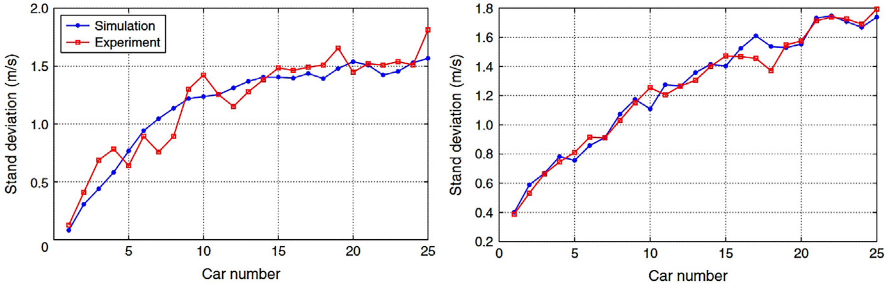

FIG. 4.15 – The standard deviation of the time series of the speed of each car. Car number 1 is the leading car. In (a, b), the experimental leading vehicle was asked to move with the constant speed $v_{\mathrm{l,exp}} = 50$ and 30 km/h respectively. The simulation results of DTGBLM are obtained with parameter values: $L_{\mathrm{cell}} = 0.5$ m, $L_{\mathrm{veh}} = 15L_{\mathrm{cell}}/\mathrm{s}$, $a_1 = 1L_{\mathrm{cell}}/\mathrm{s}$, $v_{\max} = 45L_{\mathrm{cell}}/\mathrm{s}$, and $p_{\mathrm{d}} = 0.3$. Other parameters are the same as in table 4.5. In the simulation, the velocity of the leading car is set by: $v_{\mathrm{l},} = [v_{\mathrm{l,exp}}/L_{\mathrm{cell}}]$, where $[x]$ is the integer nearest to x.

4.2.2 Two-State Model and Its Improved Version

The Two-State (TS model, Tian *et al.* (2015)) model has considered two driver states: a defensive one, and a normal one. The defensive state is activated if $v > d_{\mathrm{anti}}/T$. Otherwise, the drivers are assumed to be in the normal driving state. In the TS model, the formulations of $\hat{a}$, $\hat{d}$, $\hat{v}$, $\hat{v}_r$, and $\hat{p}$ are as follows.

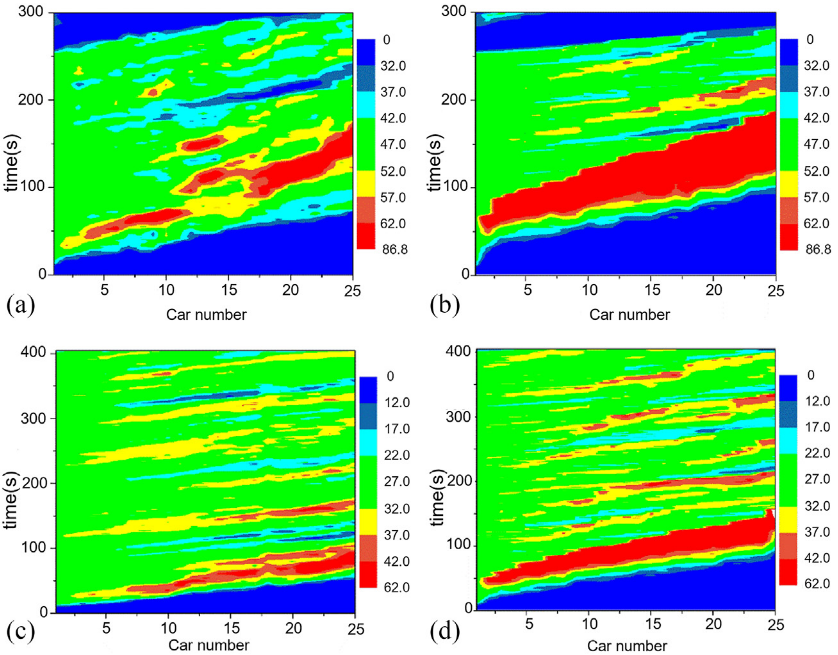

FIG. 4.16 – The spatiotemporal patterns of the platoon traffic. The car speed is shown with different colors (unit: km/h) as a function of time and car number. The left panels show the experimental results and the right panels show the simulation results of the DTGBLM. In (a, b) and (c, d), the experimental leading vehicle was asked to move with the constant speed $v_{\mathrm{l,exp}} = 50$ and 30 km/h respectively.

$$\text{(i)}\quad \hat{a} = a$$

$$\text{(ii)}\quad \hat{d} = d + \max\left(v_{\text{anti}} - g_{\text{safety}}, 0\right)$$

$$\text{(iii)}\quad \hat{v} = v_{\max}$$

$$\text{(iv)}\quad \hat{v}_r = \begin{cases} a & \text{if } v \leq d_{\text{anti}} \,/\, T, \\ b_{\text{defense}} & \text{otherwise.} \end{cases}$$

$$\text{(v)}\quad \hat{p} = \begin{cases} p_{\mathrm{b}}, & \text{if } v = 0 \text{ and } t_{st} > t_{\mathrm{c}}, \\ p_{\mathrm{c}}, & \text{else if } 0 \leq v \leq d_{\text{anti}} \,/\, T, \\ p_{\mathrm{a}}, & \text{otherwise.} \end{cases}$$

Here $v_{\text{anti}} = \min(d_l, v_l + a, v_{\max})$ is the anticipated speed of the leading vehicle, in which d_l is the space gap of the leading vehicle. The effectiveness of the anticipation is controlled by g_{safety}. Accidents are avoided only if $\hat{v}_r \geq g_{\text{safety}}$.

Figure 4.17 shows the simulation results of the fundamental diagram of the two-state model. One can see that the model can reproduce the free flow, the synchronized flow, the jam, and the F → S (figure 4.18a) and S → J transitions (figure 4.18b).

TAB. 4.6 – Parameter values of TS model, taken from Tian *et al.* (2015).

Parameters	L_{cell}	L_{veh}	$v_{\max}$	T	p_{a}	p_{b}	p_{c}	a	b_{defense}	g_{safety}	t_c
Units	m	L_{cell}	L_{cell}/s	s	–	–	–	$L_{\text{cell}}/\text{s}^2$	$L_{\text{cell}}/\text{s}^2$	L_{cell}	s
Values	7.5	1	5	1.8	0.95	0.55	0.1	1	1	2	8

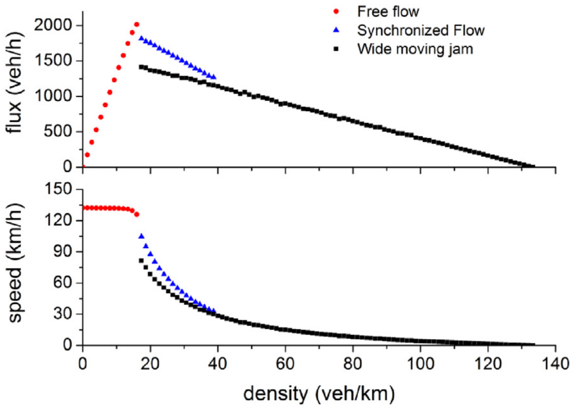

FIG. 4.17 – The fundamental diagram of the TS model on a circular road with length 3000 m. The parameters are shown in table 4.6.

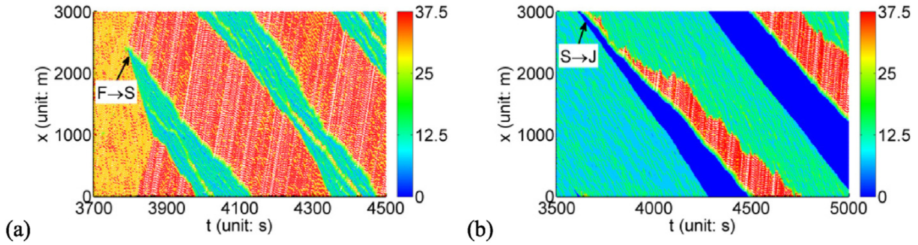

FIG. 4.18 – The spatiotemporal diagrams of TS model with the density (a) $\rho = 25$ veh/km and (b) $\rho = 67$ veh/km.

However, in the TS model, the growth of oscillation magnitudes of vehicles in a car platoon is much faster than that reported in the experiment (figure 4.19).

To make the TS model more realistic, the safe speed v_{safe}, and the logistic function for the randomization probability p_{defense} are introduced into the TS model. The two new variables are defined as follows:

$$v_{\text{safe}} = \left[-b_{\max} + \sqrt{b_{\max}^2 + v_l^2 + 2 b_{\max} d_n} \right]. \tag{4.1}$$

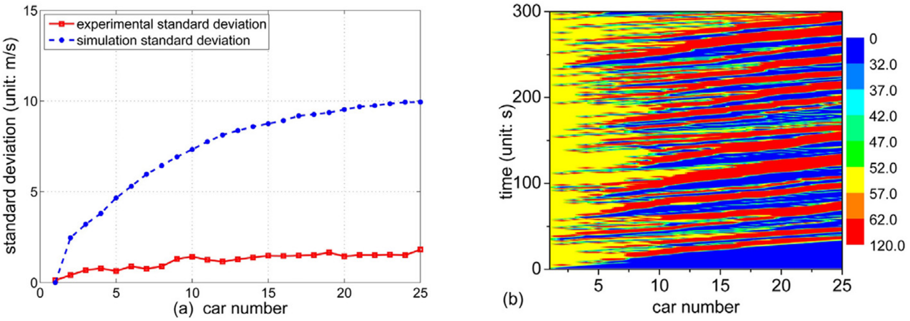

FIG. 4.19 – (a) Comparison of the simulation result and experiment result of the standard deviation of the velocities of the cars and (b) the spatiotemporal patterns of the platoon traffic when the leading vehicle moves with the constant speed $v_{\text{leading}} = 54$ km/h. The color bar in (b) indicates speed. In the real experiment, the leading vehicle was required to move with $v_{\text{leading}} = 50$ km/h.

$$p_{\text{defense}} = p_{\text{c}} + \frac{p_{\text{a}}}{1 + e^{\alpha(v_c - v_n)}}. \tag{4.2}$$

where α and v_c are the steepness and midpoint of the logistic function, respectively. v_l is the speed of the preceding car, $b_{\max}$ is the maximum deceleration of the car. The round function $[x]$ returns the integer nearest to x.

The safe speed v_{safe} is applied to take into consideration kinematic restraints restricting the maximum safe speed of a vehicle when its space gap is d and the preceding car moves with v_l. It is calculated based on the assumption that (i) the driver's reaction time is equal to one-time step, *i.e.*, 1 s; (ii) the maximum deceleration of the vehicle is $b_{\max}$; (iii) the preceding car decelerates with $b_{\max}$ and the deceleration of the considered vehicle is restricted to $b_{\max}$ as well. Note that equation (4.2) heuristically defines p_{defense} as a function of the speed based on the observations. Figure 4.20 illustrates the shape for the randomization probability p_{defense} defined by equation (4.2). When the speed v is lower than v_c, the randomization probability is greatly reduced.

Since safe speed is introduced, the model been named the two-state model with safe speed (TSS model, Tian *et al.* (2016)). In the TSS model, the formulations of $\hat{v}$, $\hat{v}_r$, and $\hat{p}$ change into:

$$\hat{v} = \min(v_{\max},\ v_{\text{safe}}).$$

$$\hat{v}_r = \begin{cases} a, & \text{if } v < b_{\text{defense}} + \lfloor d_{\text{anti}}/T \rfloor, \\ b_{\text{defense}}, & \text{otherwise.} \end{cases}$$

$$\hat{p} = \begin{cases} p_{\text{b}}, & \text{if } v = 0 \\ p_{\text{c}}, & \text{else if } 0 < v \leq d_{\text{anti}}/T \\ p_{\text{defense}}, & \text{otherwise.} \end{cases}$$

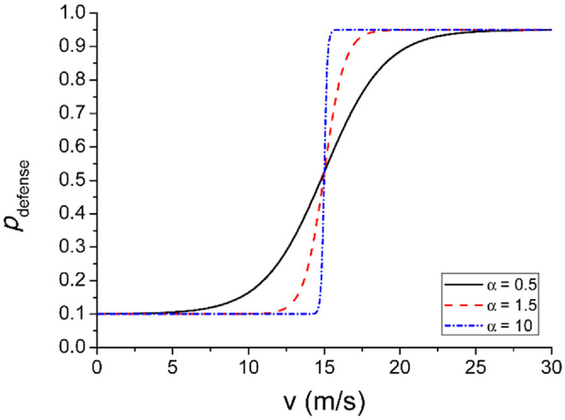

FIG. 4.20 – The logistic form of p_{defense} for $v_c = 15$ m/s, $v_{\max} = 30$ m/s, $p_{\text{c}} = 0.1$, and $p_{\text{a}} = 0.85$.

Here $\lfloor x \rfloor$ returns the maximum integer no greater than x.

Figure 4.21 shows the simulation results of the fundamental diagram of the improved two-state model. One can see that the model can well reproduce the three phases of traffic flow. Figure 4.22 shows that both the F $\longrightarrow$ S and the S $\longrightarrow$ J transition can be well depicted. Moreover, the growth of oscillation magnitudes of vehicles in a car platoon is consistent with that reported in the experiment (not shown here, see (Tian *et al.*, 2016)). Note that in the improved two-state model, the synchronized flow could coexist with the free flow (see figure 4.22a), and traffic oscillations exist in the synchronized flow (see figure 4.23).

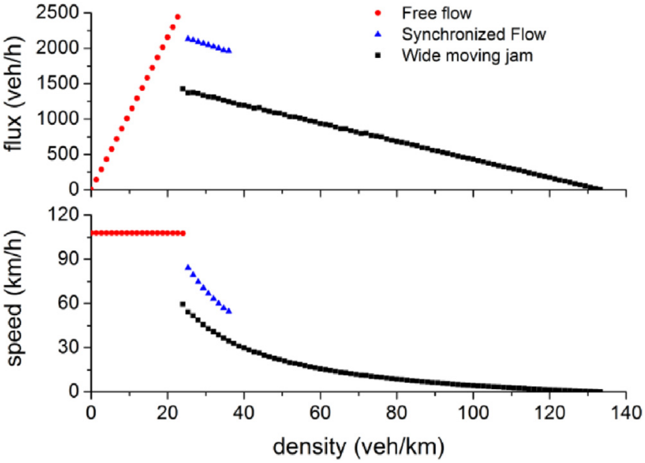

FIG. 4.21 – The fundamental diagram of the TSS model on a circular road with length 3000 m. The parameters are shown in table 4.7.

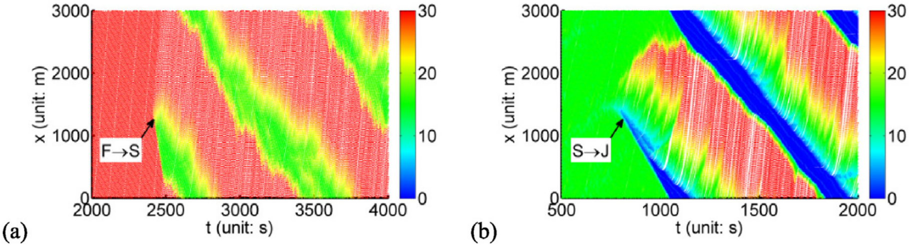

FIG. 4.22 – The spatiotemporal diagrams of TSS model on the circular road. (a) $\rho = 24$ veh/km; (b) $\rho = 38$ veh/km.

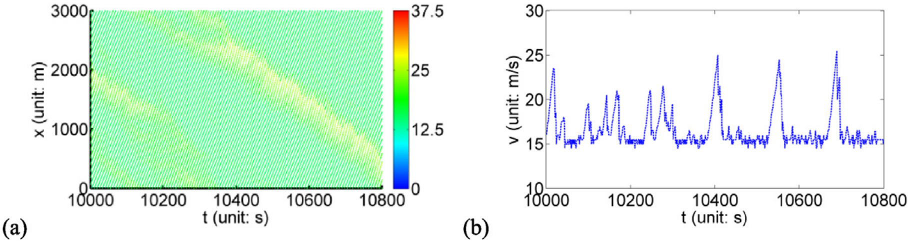

FIG. 4.23 – The simulation results of spatiotemporal diagram. (a) $\rho = 33$ veh/km; (b) The time series of velocity of a single vehicle.

To simulate the concave growth pattern of traffic oscillations, TSSM is adopted to simulate the 25-vehicle-platoon experiment. To quantitatively reproduce the concave growth pattern, p_b changes from 0.52 to 0.4, other parameters are the same as that in table 4.7.

TAB. 4.7 – Parameter values of TSS model taken from Tian *et al.* (2016).

Parameters	L_cell	L_veh	v_max	T	p_a	p_b	p_c
Units	m	L_cell	L_cell/s	s	–	–	–
Values	0.5	15	60	1.8	0.85	0.52	0.1
Parameters	a	b_max	b_defense	g_safety	v_c	α	
Units	$L_\mathrm{cell}/\mathrm{s}^2$	$L_\mathrm{cell}/\mathrm{s}^2$	$L_\mathrm{cell}/\mathrm{s}^2$	L_cell	L_cell/s	s/L_cell	
Values	1	7	2	20	30	10	

Figure 4.24 indicates the capability of the TSSM in predicting the observed growth of the disturbances along the platoon. Figure 4.25 shows that the formation and evolution of the simulated oscillations (right panels) look very similar to that of Jiang's experimental data (left panels).

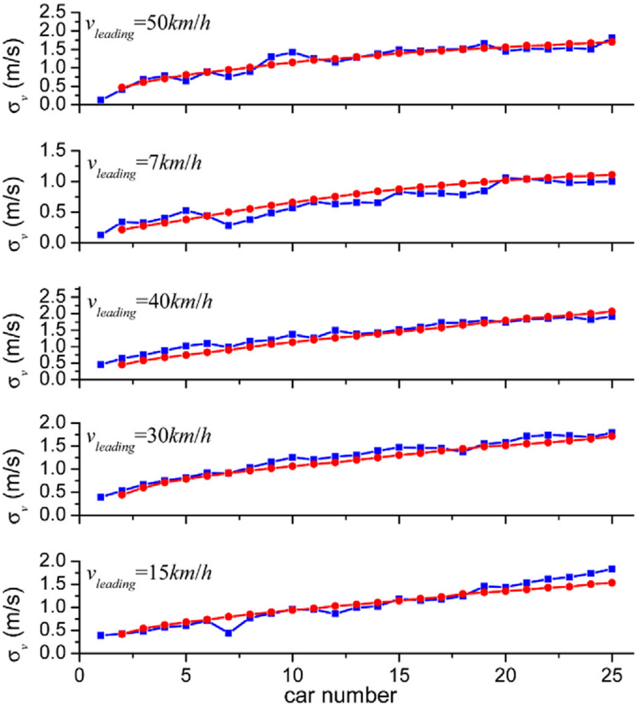

Fig. 4.24 – Comparison of the simulation results (symbol solid red lines) and experiment results (symbol solid blue lines) of the standard deviation of the speed of the cars. Car number 1 is the leading car.

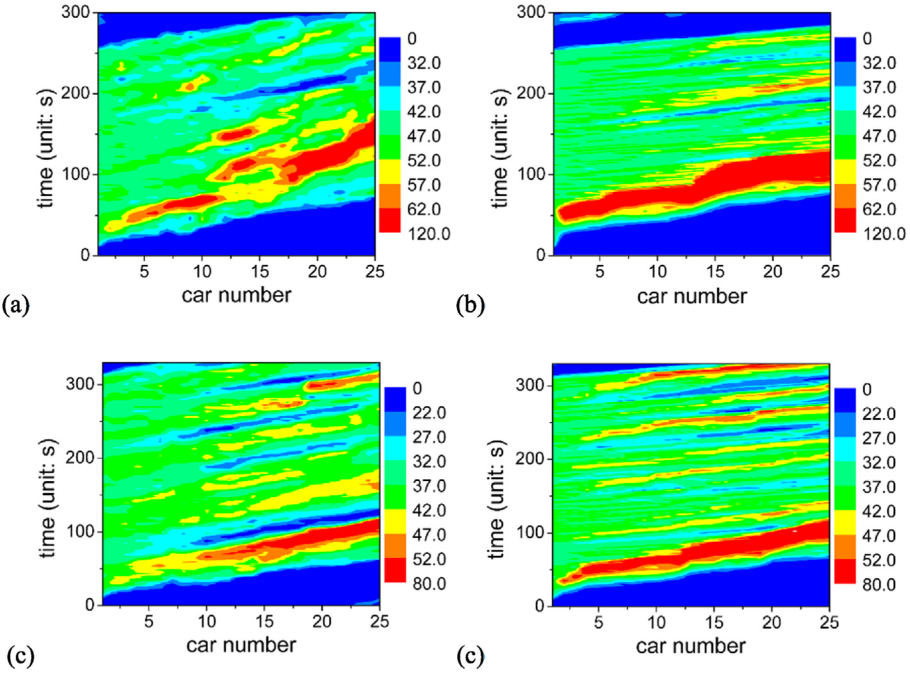

FIG. 4.25 – The spatiotemporal patterns of the platoon traffic. The car speed is shown with different colors (unit: km/h) as function of time and car number. The left and right Panels show the experimental results and the simulation results of TSSM. In (a, b) and (c, d), the leading vehicle of the platoon is required to move with $v_{\text{leading}} = 50$ and 30 km/h, respectively. In the simulation, the speed of the leading car of the platoon is set as $[v_{\text{leading}}/3.6/L_{\text{cell}}]$. The color bar indicates speed.

References

Barlovic R., Santen L., Schadschneider A., Schreckenberg M. (1998) Metastable states in cellular automata for traffic flow, *Eur. Phys. J. B-Condens. Matter Complex Syst.* **5**, 793–800.

Bartolozzi M., Thomas A.W. (2004) Stochastic cellular automata model for stock market dynamics, *Phys. Rev. E* **69**, 046112.

Benjamin S.C., Johnson N.F., Hui P. (1996) Cellular automata models of traffic flow along a highway containing a junction, *J. Phys. A: Math. Gen.* **29**, 3119.

Cremer M., Ludwig J. (1986) A fast simulation model for traffic flow on the basis of Boolean operations, *Math. Comput. Simul.* **28**, 297–303.

Duan X., Wang C., Liu X. (2012) Cellular automata theory research and simulation applications. Science Press, Beijing.

Edelstein-Keshet L. (2017) How the lizard gets its speckled scales, *Nat.* **544**, 170–171.

Fukui M., Ishibashi Y. (1997) Effect of delay in restarting of stopped cars in a one-dimensional traffic model, *J. Phys. Soc. Jpn.* **66**, 385–387.

Gao K., Jiang R., Hu S.-X., Wang B.-H., Wu Q.-S. (2007) Cellular-automaton model with velocity adaptation in the framework of Kerner's three-phase traffic theory, *Phys. Rev. E* **76**, 026105.

Gao K., Jiang R., Wang B.-H., Wu Q.-S. (2009) Discontinuous transition from free flow to synchronized flow induced by short-range interaction between vehicles in a three-phase traffic flow model, *Phys. A: Stat. Mech. Appl.* **388**, 3233–3243.

Goldenberg J., Libai B., Muller E. (2002) Riding the saddle: How cross-market communications can create a major slump in sales, *J. Mark.* **66**, 1–16.

Hanson J. (2009) Emergent phenomena in cellular automata, *Encycl. Compl. Syst. Sci.* 768–778.

Hogeweg P. (1988) Cellular automata as a paradigm for ecological modeling, *Appl. Math. Comput.* **27**, 81–100.

Jia B., Gao Z.-Y., Li K.-p., Li X.-G. (2007) Models and simulations of traffic system based on the theory of cellular automaton, *Sci., Beijing* **123**, 2002.

Jia B., Li X.-G., Chen T., Jiang R., Gao Z.-Y. (2011) Cellular automaton model with time gap dependent randomisation under Kerner's three-phase traffic theory, *Trans.* **7**, 127–140.

Jiang R., Hu M.-B., Zhang H., Gao Z.-Y., Jia B., Wu Q.-S. (2015) On some experimental features of car-following behavior and how to model them, *Trans. Res. Part B: Methodol.* **80**, 338–354.

Jiang R., Hu M.-B., Zhang H., Gao Z.-Y., Jia B., Wu Q.-S., Wang B., Yang M. (2014) Traffic experiment reveals the nature of car-following, *PloS one* **9**, e94351.

Jiang R., Jin C.-J., Zhang H., Huang Y.-X., Tian J.-F., Wang W., Hu M.-B., Wang H., Jia B. (2018) Experimental and empirical investigations of traffic flow instability, *Trans. Res. Part C: Emerging Technol.* **94**, 83–98.

Kerner B.S., Klenov S.L., Wolf D.E. (2002) Cellular automata approach to three-phase traffic theory, *J. Phys. A: Math. Gen.* **35**, 9971.

Knospe W., Santen L., Schadschneider A., Schreckenberg M. (2000) Towards a realistic microscopic description of highway traffic, *J. Phys. A: Math. Gen.* **33**, L477.

Krug J., Spohn H. (1988) Universality classes for deterministic surface growth, *Phys. Rev. A* **38**, 4271.

Laval J.A., Toth C.S., Zhou Y. (2014) A parsimonious model for the formation of oscillations in car-following models, *Trans. Res. Part B: Methodol.* **70**, 228–238.

Lodder R.A., Hieftje G.M., Selby M. (1988) Applications of cellular automata: Attractors and fractals in analytical chemistry? *TrAC Trends Anal. Chem.* **7**, 240–244.

Nagel K., Rickert M. (2001) Parallel implementation of the TRANSIMS micro-simulation, *Parallel Comput.* **27**, 1611–1639.

Nagel K., Schreckenberg M. (1992) A cellular automaton model for freeway traffic, *J. De Phys. I* **2**, 2221–2229.

Nishinari K., Takahashi D. (2000) Multi-value cellular automaton models and metastable states in a congested phase, *J. Phys. A: Math. Gen.* **33**, 7709.

Parsons J.A., Fonstad M.A. (2007) A cellular automata model of surface water flow, *Hydrol. Proc.: An Int. J.* **21**, 2189–2195.

Rickert M., Nagel K. (1997) Experiences with a simplified microsimulation for the Dallas/Fort-Worth area, *Int. J. Mod. Phys. C* **8**, 483–503.

Schadschneider A., Schreckenberg M. (1997) Traffic flow models with 'slow-to-start' rules, *Annalen der Physik* **509**, 541–551.

Takayasu M., Takayasu H. (1993) 1/f noise in a traffic model. *Fractals* **1**, 860–866.

Tian J.-f., Yuan Z.-z., Jia B., Fan H.-q., Wang T. (2012a) Cellular automaton model in the fundamental diagram approach reproducing the synchronized outflow of wide moving jams, *Phys. Lett. A* **376**, 2781–2787.

Tian J.-f., Yuan Z.-z., Treiber M., Jia B., Zhang W.-y. (2012b) Cellular automaton model within the fundamental-diagram approach reproducing some findings of the three-phase theory, *Phys. A: Stat. Mech. Appl.* **391**, 3129–3139.

Tian J., Jia B., Ma S., Zhu C., Jiang R., Ding Y. (2017) Cellular automaton model with dynamical 2D speed-gap relation, *Trans. Sci.* **51**, 807–822.

Tian J., Li G., Treiber M., Jiang R., Jia N., Ma S. (2016) Cellular automaton model simulating spatiotemporal patterns, phase transitions and concave growth pattern of oscillations in traffic flow, *Trans. Res. Part B: Methodol.* **93**, 560–575.

Tian J., Treiber M., Ma S., Jia B., Zhang W. (2015) Microscopic driving theory with oscillatory congested states: model and empirical verification, *Trans. Res. Part B: Methodol.* **71**, 138–157.

Treiber M., Kesting A. (2013) *Traffic flow dynamics, Traffic flow dynamics: Data, models and simulation*, Springer-Verlag Berlin Heidelberg, 983–1000.

Wolfram S. (1982) Cellular automata as simple self-organizing systems, *Caltech preprint CALT-68-938*.

Zhao B.-H., Hu M.-B., Jiang R., Wu Q.-S. (2009) A realistic cellular automaton model for synchronized traffic flow, *Chin. Phys. Lett.* **26**, 118902.

Chapter 5

Car Following Models

Abstract. Car following models describe traffic flow dynamics by the formulation of acceleration in terms of the interactions between consecutive vehicles on the lane. Traditional car following models assumes that in the steady state, there is a unique relationship between speed and spacing that corresponds to the fundamental diagram of traffic flow at the macroscopic level. However, our previous chapter has shown that these models cannot reproduce the concave growth pattern of traffic oscillations. Therefore, a new car following models is needed to reproduce the new observed characteristics of oscillations. To this end, this chapter first extends the traditional models and then new models are also proposed.

5.1 The Extensions of Traditional Models

By removing the fundamental notion and letting the spacing of a car could change significantly even if its preceding car moves at a constant speed, congested traffic states of a car could span a 2D region in the speed-spacing plane in traditional models. Thus, we name these new models 2D models.

(i) The 2D OV and FVD models:

We assume that the relationship between speed and spacing is determined by $V(\Delta x) = \max(11.6(\tanh(0.086(m \cdot \Delta x - 25)) + 0.913), 0)$ with a parameter m, which changes with time in the OV and FVD models (see equations (2.5) and (2.6)). For simplicity, we assume that m is a uniformly distributed random number between m_1 and m_2, and m changes in the range with rate p (*i.e.*, in each time step Δt in the simulation, $m \to m'$ with probability $p\ \Delta t$ and remains unchanged with probability $1 - p\ \Delta t$). In the simulations, the parameters are $p = 0.15\ \mathrm{s}^{-1}$, $m_1 = 0.8$, $m_2 = 1.2$. Other parameters are the same as before.

(ii) The 2D ID model:

We suppose that the drivers do not always maintain a constant value of desired time headway T. For simplicity, we assume that T is a uniformly distributed random number between T_1 and T_2, and T changes in the range with rate p. In the simulation, the parameters are $T_1 = 0.5$ s, $T_2 = 1.9$ s, $p = 0.15\ \mathrm{s}^{-1}$. Other parameters are the same as before.

DOI: 10.1051/978-2-7598-3193-7.c005
© Science Press, EDP Sciences, 2023

(iii) The 2D inertial model:

Similar to the 2D ID model, we assume that T is a uniformly distributed random number between T_1 and T_2, and T changes in the range with rate p. The parameters are $p = 0.15\ \mathrm{s}^{-1}$, $T_1 = 1.6$ s, and $T_2 = 2.4$ s. Other parameters are the same as before.

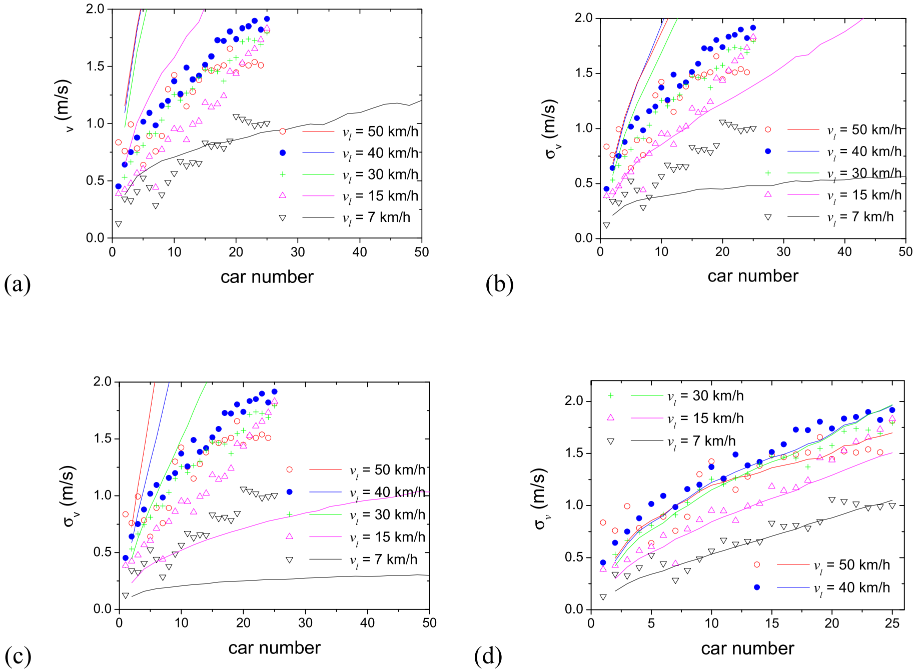

FIG. 5.1 – Simulation results (solid lines) of the standard deviation σ_v of the time series of the velocity of each car. (a) The 2D OV model, (b) the 2D FVD model, (c) the 2D inertial model, and (d) the 2D ID model. The scatter points are from the experiment.

The curves of the standard deviation of the velocities of the cars in the 2D models are shown in figure 5.1. One can see that although the simulation results are still quantitatively different from the experimental ones in figure 5.1a–c, the growth of the disturbances changes from a convex way into a concave way, which is qualitatively consistent with the experimental ones. This implies that the feature of traffic flow stability has qualitatively changed after removing the fundamental notion. As for the 2D ID model, the growth of the disturbances is not only qualitatively but also quantitatively in good agreement with the experimental ones, as shown in figure 5.1d.

5.2 The Insensitivity Model

In this section, we propose the car-following model based on the assumption that in certain ranges of speed and spacing, drivers are insensitive to changes in spacing when the velocity differences between cars are small. It is supposed that there is a two-dimensional region R in the velocity-spacing plane in which car i moves as follows. If the absolute value of the velocity difference with the preceding car $i-1$ is smaller than a threshold, *i.e.*, $|\Delta v_i| < \Delta v_c$, then the driver is not sensitive to either the velocity difference or the spacing, and he/she does not wish to change the speed. However, as it is not possible for the driver to control the accelerator pedal exactly to always maintain a constant velocity, the acceleration of the car changes randomly from $a(t)$ to[19]

$$a(t+\Delta t) = \max(\min(a(t)+\xi, 0.1), -0.1) \tag{5.1}$$

in each time step $\Delta t = 0.1$. Here ξ is a uniform random acceleration within the range $[-0.02, 0.02]$. On the other hand, if $|\Delta v_i| > \Delta v_c$, then the driver becomes sensitive to the velocity difference. In this case, the car moves as

$$\frac{dv_i}{dt} = \lambda \Delta v_i \tag{5.2}$$

Finally, if the state of the car is outside of the region R in the velocity-spacing plane, the driver becomes sensitive to both velocity difference and spacing. In this case, the car movement is modeled by the full velocity difference (FVD) model

$$\frac{dv_i}{dt} = \kappa[V(\Delta x_i) - v_i] + \lambda \Delta v_i \tag{5.3}$$

where V is the optimal velocity (OV) function, κ and λ are sensitivity parameters.

The two-dimensional region R is set to be bounded by five straight lines $v = 0.5(\Delta x - 6.8)$, $v = 0.22\Delta x + 5.5$, $v = \Delta x - 6$, $v = v_{\max}$, and $v = 0$. The OV function used is $V(\Delta x) = \max(\min(v_{\max}, 0.7(\Delta x - 6)), 0)$, see figure 5.2. To avoid car collision, we set $v = 0$ if $\Delta x \leq 6$.

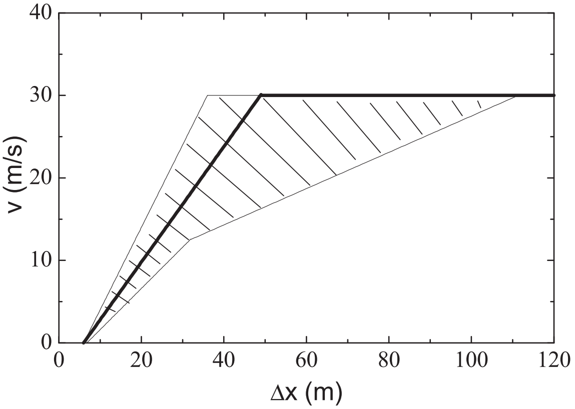

Fig. 5.2 – The two-dimensional region R (hatched) and the OV function (thick lines).

---

[19] All variables in this section are measured in SI units with time in seconds and space in meters, unless otherwise mentioned.

We would like to mention that Kerner first adopted the 2D region (in the flow-density or speed-density plane) hypothesis and proposed several microscopic models based on the assumption, such as the Kerner–Klenov model (Kerner and Klenov, 2002), and the Kerner–Klenov–Wolf cellular automaton model (Kerner *et al.*, 2002). In these models, drivers always try to adapt to the velocity of the preceding cars, subject to stochastic acceleration and deceleration. Kerner's models, in particular the Kerner–Klenov model, were sometimes criticized due to their complex formulation of stochastic acceleration and deceleration. Compared with Kerner's model, we have introduced a threshold Δv_{c}, beyond which the stochastic factors are neglected and below which the speed adaptation is neglected. Our formulation of stochastic factors is much simpler and easier to understand.

Now we present the simulation results of the model. In the simulations, the parameters are set as $\kappa = 0.4$, $\lambda = 0.35$, $v_{\max} = 30$, $\Delta v_{\mathrm{c}} = \min(\max(0.6, 0.054 v_i + 0.15), 1.0)$. As in the experiment, we consider a standing platoon of 25 cars. We let the leading car move as did the leading car in the experiment. The curves of the standard deviation of the velocities of the cars in the model are shown in figure 5.3. One can see that the simulation results are not only qualitatively but also quantitatively in good agreement with the experimental ones.

Figure 5.4a shows an example of the evolution of the spacing of car No. 2 and the velocity of car No. 2 (the following car) and No. 1 (the preceding car). One can see that the velocity fluctuation is small, but the spacing fluctuation is large, which is consistent with the experimental results shown in figure 3.3. Figure 5.4b shows an example of the evolution of velocity and spacing of one car (No. 20) in different runs. One can see that while the average velocity is almost the same, the spacing fluctuation as well as the average spacing is significantly different, which is consistent with the experimental results shown in figure 3.5.

Figure 5.5 shows the evolution of the platoon length, in which the movement of the leading car is the same. As in the experiment, while the average velocity of the cars is essentially the same, the platoon length could be different under different runs, see figure 3.7.

However, the difference in platoon length is not so large as in the experiment. Moreover, when the leading car velocity is small, the difference in platoon length under different runs is small. For example, the simulation shows that the platoon length is always around 420 m when the leading car moves at speed 25 km/h, and the platoon length is always around 370 m when the leading car moves at speed 20 km/h. This is because the 2D region becomes narrow with the decrease of speed. As a result, the phenomenon presented in figure 3.7 has not been reproduced. One possible reason is that the heterogeneity of cars/drivers has not been considered in our simulations, which is clearly demonstrated in figure 5.6. The driver of car No. 3 tends to drive with spacing much smaller than that of the driver of car No. 10, although their average velocity is roughly the same.

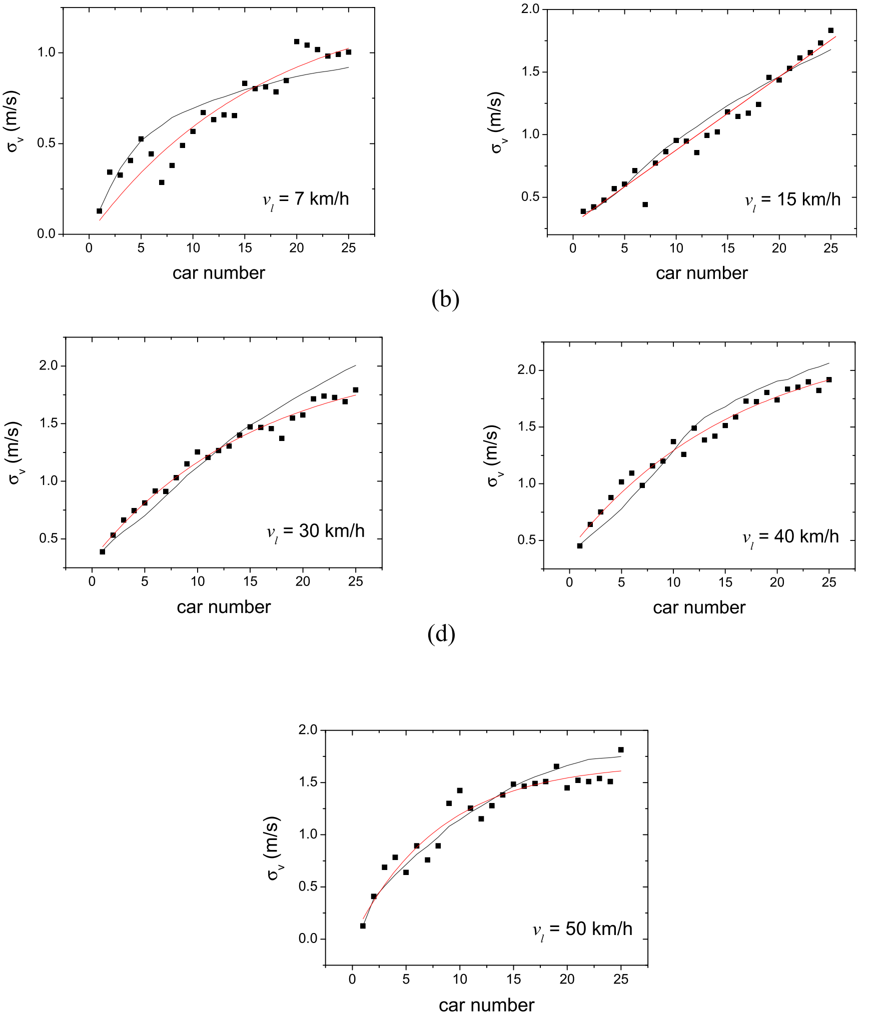

(a) (b) (c) (d) (e)

FIG. 5.3 – Comparison of the simulation results of the insensitivity model (black solid lines) and experiment results (scattered data) of the standard deviation of the velocities of the cars. The red lines are fitted lines for the experimental data.

5.3 The Speed Adaption Model

In this section, we propose the car following model to capture the essential findings in our analysis presented earlier in section 3.4. The essential features of the model are as follows: (i) when the spacing between vehicles is in the indifference region $[d^{\min}, d^{\max}]$, the acceleration of vehicles will be determined by the speed adaptation and the stochastic part; (ii) when the spacing is outside the indifference region, the

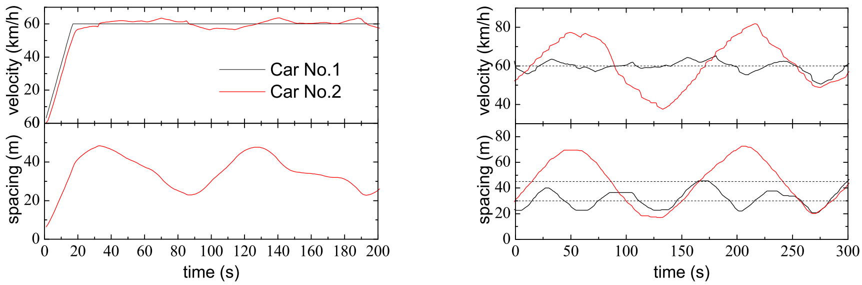

(a) (b)

FIG. 5.4 – (a) Simulation results of evolution of the spacing of car No. 2 and the velocity of car No. 2 and No. 1; (b) Simulation results of evolution of the velocity and spacing of car No. 20 in two different runs. The two dashed lines in the bottom panel show the average spacing of the two runs. The leading car moves at speed 60 km/h.

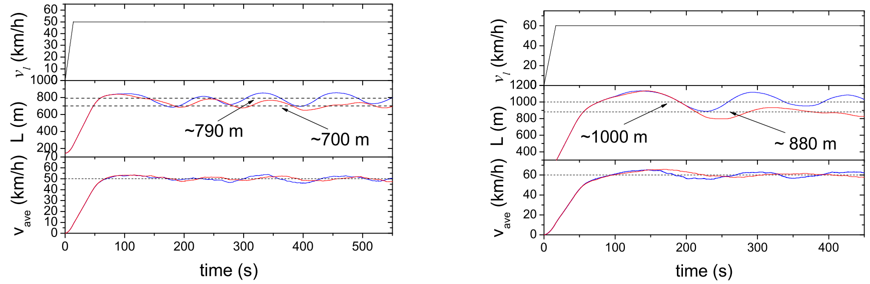

(a) (b)

FIG. 5.5 – Simulation results of evolution of the velocity of the leading car, the platoon length, and the average velocity of all cars in the platoon. The leading car moves with velocity (a) 50 km/h, (b) 60 km/h.

normal deterministic car following acceleration is used. Taking the revised IDM (Horiguchi and Oguchi, 2014) as an example, the new model is specified as follows:

$$\begin{aligned}
&\text{if } d_n^{\min} \le d_n \le d_n^{\max}\\
&\qquad a_n(t) = \min(\lambda \Delta v_n(t-\tau) + \xi_n,\ \lambda(v_{\max} - v_n(t)))\\
&\text{else}\\
&\qquad a_n(t) = \min\left(a\left(1 - \left(\frac{v_n(t)}{v_{\max}}\right)^4\right) a\left(1 - \left(\frac{d_n^{\min} + d_n^{\max}}{2d_n(t)}\right)^2\right)\right)
\end{aligned} \tag{5.4}$$

where ξ_n is determined by equation (3.5). The boundaries of the indifference region are determined by

$$d_n^{\min} = \max\left(v_n(t)\,T_{\min} - \frac{v_n(t)\Delta v_n(t)}{2\sqrt{ab}}, 0\right) + s_0 \tag{5.5}$$

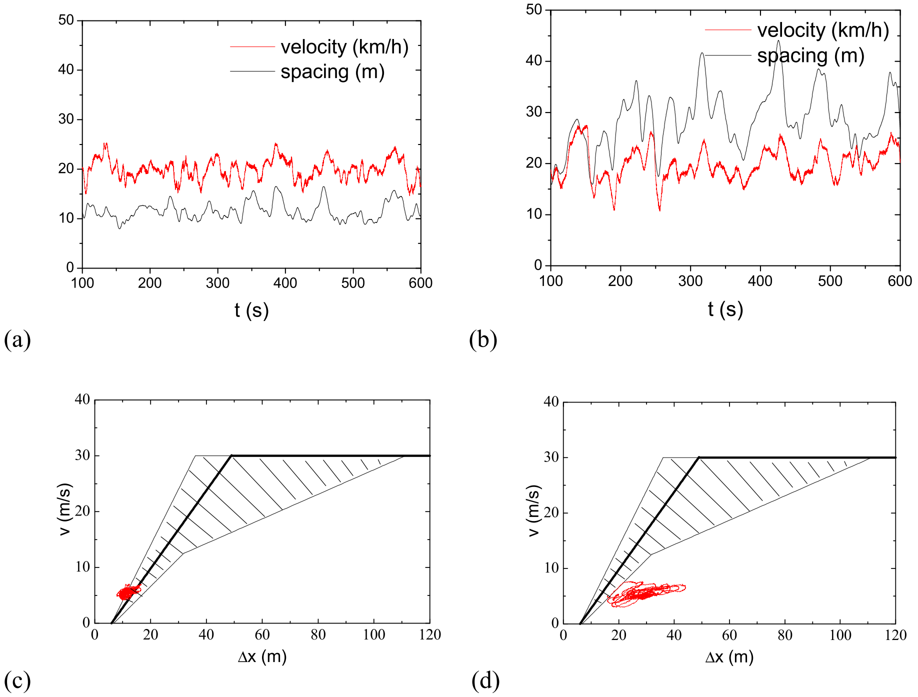

FIG. 5.6 – (a) and (b) show velocity and spacing of cars No. 3 and No. 10, respectively, in which the leading car moves with velocity 20 km/h. (c) and (d) show the same data (red) in the spacing-velocity space. In (c) and (d), the background is the two-dimensional region R (hatched) and the OV function (thick lines) used in the simulations.

$$d_n^{\max} = \max\left(v_n(t)\, T_{\max} - \frac{v_n(t)\Delta v_n(t)}{2\sqrt{ab}}, 0 \right) + s_0 \tag{5.6}$$

In the indifference region, the term $\lambda(v_{\max} - v_n)$ is applied to ensure that the vehicle's speed v_n will not exceed the maximum speed $v_{\max}$.

To quantitatively reproduce the concave growth of speed variance or standard deviations (STDs) in the platoon, we calibrate the model parameters, using a Generic Algorithm. The fitness function is to minimize the difference between the simulated STDs and experimental ones. The calibrated parameters are shown in table 5.1. Moreover, the Fast Fourier transform analysis (FFT, (Li *et al.*, 2010)) of the speed time series of the last vehicle is performed to compare the simulated and experimental oscillation frequencies in the platoon. Figures 5.7 and 5.8 show that the concave growth pattern is quantitatively reproduced by the new model, and the spatiotemporal evolution of traffic flow has been captured.

Yuan *et al.* (2017) reported a linear relationship between the speed in congestion and the queue discharge rate: the queue discharge rate increases with the speed in congestion. Next, we examine whether this feature can be captured in the new model.

TAB. 5.1 – Model parameter values.

Parameters	Description	Unit	Value
$v_{\max}$	Maximum speed	m/s	30
$T_{\min}$	Minimum desire time gap	s	0.6
$T_{\max}$	Maximum desire time gap	s	1.7
a	Maximum acceleration	m/s^2	0.85
b	Desire deceleration	m/s^2	1.5
s_0	Minimum standing gap	m	2.0
τ	Reaction delay	s	1.3
λ	Sensitivity	s^{-1}	0.27
κ	Sensitivity	s^{-1}	0.09
σ	Acceleration strength	m/s^2	0.07

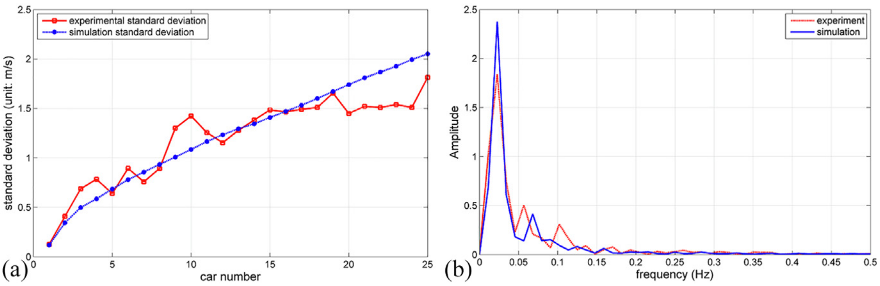

FIG. 5.7 – (a) The standard deviations of the car following platoon; (b) the corresponding FFT spectra for detrended speed data of the last vehicle. Car number 1 is the leading car. The leading car moves with $v_{\text{leading}} = 50$ km/h.

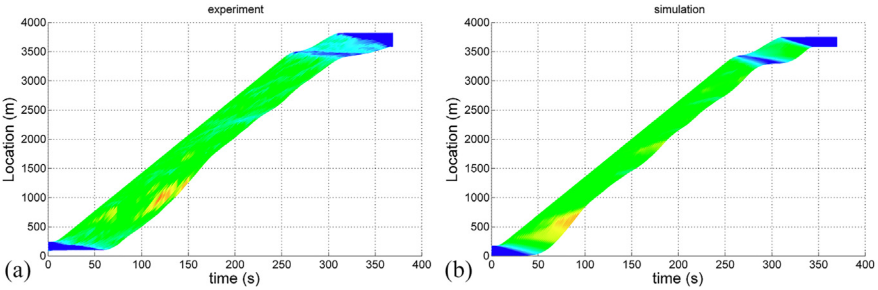

FIG. 5.8 – The spatiotemporal diagrams of the car following platoon. (a) Experimental result; (b) simulation one. The leading car moves with $v_{\text{leading}} = 50$ km/h.

In the simulation, a 25-car following platoon has been simulated. The leading car moves with speed v_{leading} when its location $x < x_0$. As a result, the average speed of the congested traffic in the platoon equals v_{leading}. The leading car accelerates freely when $x > x_0$. The discharge rate is calculated by $24/(t_2 - t_1)$, where t_1 and t_2 denote the time for the leading car and the last car to pass the location $x = x_{\text{de}}$ downstream of x_0, respectively, see figure 5.9a. Figure 5.9b shows that the linear relationship between the congested speed and discharge rate is well simulated.

Moreover, the sensitivity analysis is performed to examine the role of reaction delay and indifference region boundary in traffic flow dynamics.

Firstly, their influence on oscillation growth is investigated. Figure 5.10 shows the impact of reaction delay in the case $v_{\text{leading}} = 50$ km/h. One can see that reaction delay only has a slight effect. The oscillation only grows a little faster even if the reaction delay increases from 0.5 s to 2.0 s. In the case of other leading speeds, similar results are observed.

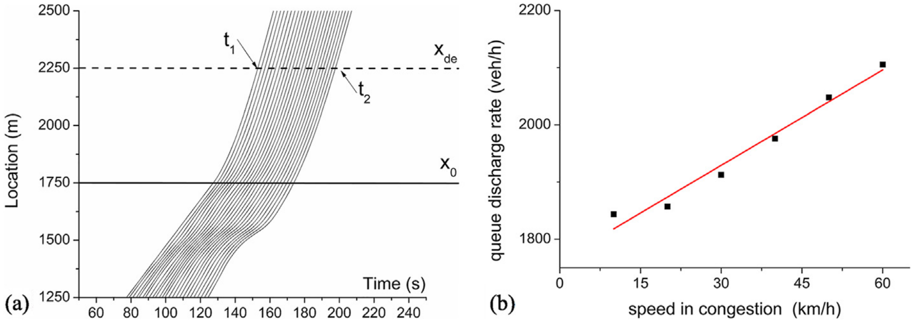

FIG. 5.9 – (a) A sample of the trajectories of the queue discharge simulation. (b) The relation between queue discharge rate and the speed of congested traffic. The two locations $x_0 = 1750$ m, $x_{\text{de}} = 2250$ m. In the sample in (a), $v_{\text{leading}} = 10$ m/s.

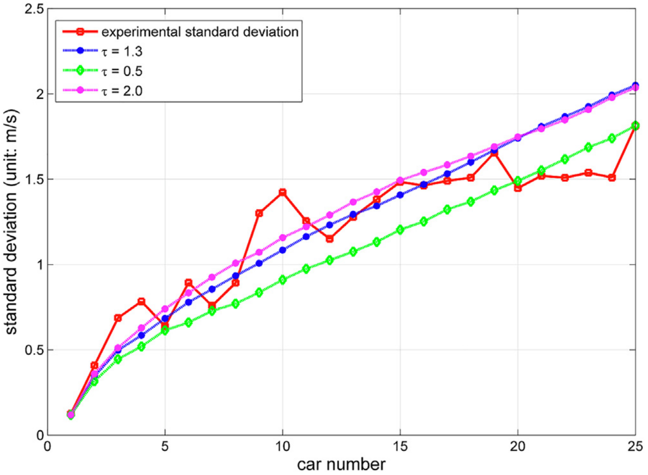

FIG. 5.10 – Standard deviations of the car following platoon. The platoon leader moves with $v_{\text{leading}} = 50$ km/h.

Figure 5.11 shows the influence of the indifference region boundary. The lower boundary depends on $T_{\min}$ and the upper one depends on $T_{\max}$. The boundary has a significant impact on the oscillation growth rate. With the increase of $T_{\max}$ or the decrease of $T_{\min}$ (*i.e.*, with the expansion of the indifference region), the oscillation grows much faster.

Figure 5.12 shows the simulation results of the spacing-speed relationship of one leader–follower pair, in which the leader moves with a constant speed of 50 km/h. It can be seen that the state of the follower moves between the boundaries

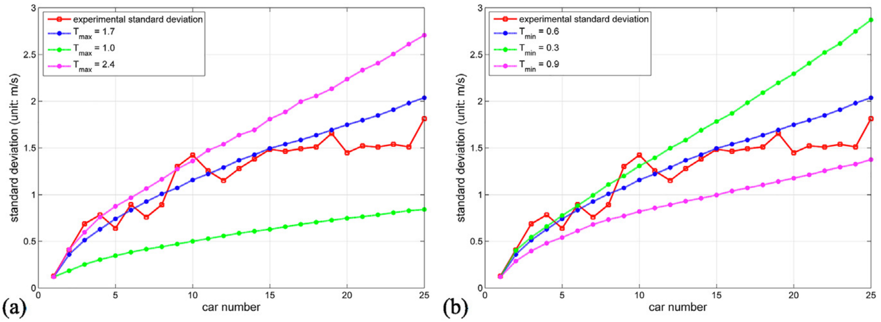

FIG. 5.11 – Standard deviations of the car following platoon. The platoon leader moves with $v_{\text{leading}} = 50$ km/h. In the case of other leading speed, similar results are observed. (a) The impact of $T_{\max}$; (b) The impact of $T_{\min}$.

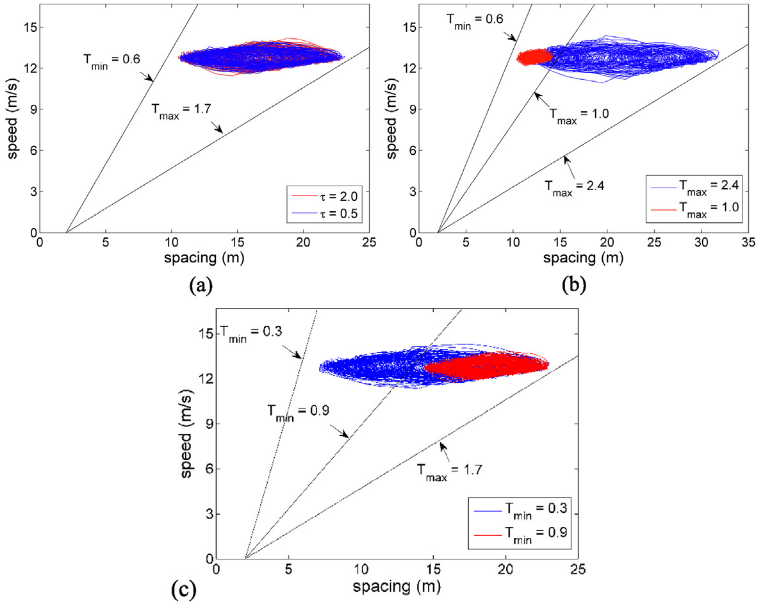

FIG. 5.12 – The spacing-speed relationship of one leader–follower pair.

of $d^{\min} = vT_{\min} + s_0$ and $d^{\max} = vT_{\max} + s_0$. The speed fluctuation changes significantly with the variations of the boundaries. When only the reaction delay changes, the speed fluctuation changes slightly. This might explain why reaction delay has a small influence on oscillation growth, but the indifference boundary has a large influence on oscillation growth.

Next, we study the impacts of reaction delay and indifference region boundary on the discharge rate. Figure 5.13a and b show that τ and $T_{\min}$ have only a slight quantitative impact on the discharge rate. However, the discharge rate decreases significantly with the increase of $T_{\max}$, as shown in figure 5.13c.

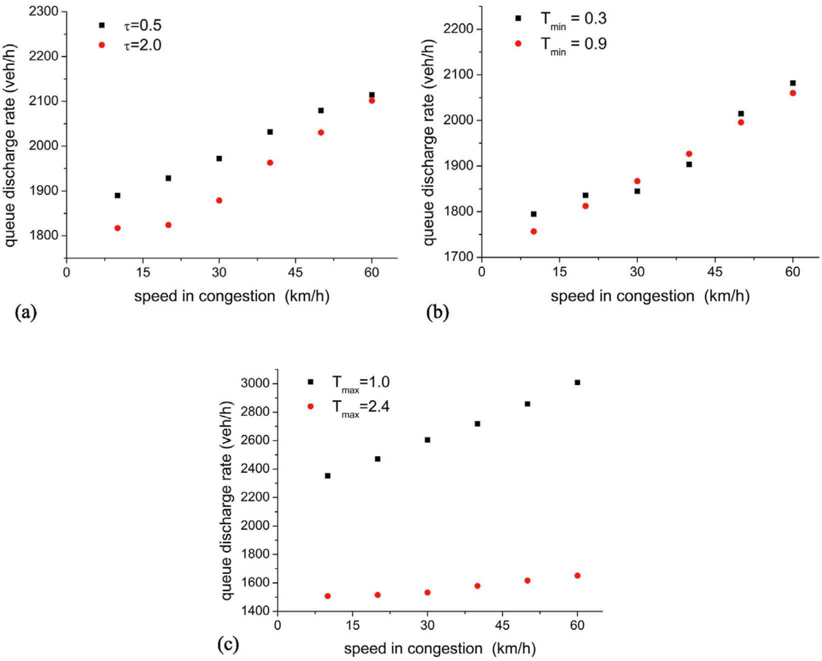

FIG. 5.13 – Impact of (a) τ, (b) $T_{\min}$, (c) $T_{\max}$ on discharge flow rate.

5.4 The Variants of Newell Model

Based on the analysis in section 3.5, a simple car following model is proposed.

$$v_n^{\text{free}}(t) = \min\big(v_{\max}, v_n(t-\tau) + a_n(t-\tau)\tau\big) \tag{5.7}$$

$$x_n(t) = x_n(t-\tau) + \min\big(v_n^{\text{free}}(t-\tau)\tau, \max(x_{n-1}(t-\tau) - x_n(t-\tau) - w\tilde{\tau}_n(t), 0)\big) \tag{5.8}$$

The wave travel time $\tilde{\tau}_n(t)$ is updated by the following equations (see the derivations in the Appendix).

$$\tilde{\tau}_n(t) = [\tilde{\tau}_n(t-\tau) + \varsigma_n(t-\tau)]_{\tilde{\tau}_{\min}}^{\tilde{\tau}_{\max}} \tag{5.9}$$

where $\varsigma_n(t)$ follows the normal distribution with mean $\mu_n^{\varsigma} = 0$ and variance $\sigma_n^{\varsigma} = \tau\tilde{\sigma}$, where $\tilde{\sigma} = \frac{\sigma}{\sqrt{2\alpha}}$. It should be noted that $\tilde{\tau}_n(t) \geq \tilde{\tau}_{\min} = L_{\text{veh}}/w$ is imposed to avoid accidents and $\tilde{\tau}_n(t)$ is bounded up by $\tilde{\tau}_{\max}$ to restrict the influence of the leading car when the gap is large enough. The acceleration $a_n(t)$ of vehicle n is captured *via* the TWOPAS model in (Allen *et al.*, 2000):

$$a_n(t) = a\left(1 - \frac{v_n(t)}{v_{\max}}\right) \tag{5.10}$$

Theorem: Assuming that the vehicles move according to the stochastic Newell model per equations (5.7)–(5.10) and there is a car following platoon with $N+1$ vehicles (0 to N) in a lane, the leading vehicle (with number 0) moves with a constant speed $\overline{v}$, then speed standard deviations of vehicle n at time t can be approximated by $\sqrt{n}\sigma_n^{\varsigma}$.

Proof: According to the new model, the movement of vehicles in congestion can be approximated by

$$x_n(t+\tau) = x_{n-1}(t) - w\tilde{\tau}_n(t+\tau) \tag{5.11}$$

$$x_n(t) = x_{n-1}(t-\tau) - w\tilde{\tau}_n(t) \tag{5.12}$$

thus

$$v_n(t) = v_{n-1}(t-\tau) - \frac{w}{\tau}(\tilde{\tau}_n(t+\tau) - \tilde{\tau}_n(t)) \approx v_{n-1}(t-\tau) - \frac{w}{\tau}\varsigma_n(t) \tag{5.13}$$

which yields

$$v_n(t) \approx \overline{v} - \sum_{i=1}^{n} \frac{w}{\tau}\varsigma_i(t-(n-i)\tau) \tag{5.14}$$

Since ς_n is independent among vehicles,

$$\text{Var}(v_n(t)) \approx \frac{w^2}{\tau^2}\sum_{i=1}^{n}\text{Var}(\varsigma_i(t-(n-i)\tau)) = n\frac{w^2}{\tau^2}\left(\sigma_n^{\varsigma}\right)^2 = nw^2\tilde{\sigma}^2 \tag{5.15}$$

Thus,

$$\text{STD}(v_n(t)) \approx \sqrt{n}w\tilde{\sigma} \tag{5.16}$$

Figure 5.14 compares the model simulation results with the analytical results calculated by equation (5.16). It can be seen that equation (5.16) can predict the speed standard deviations of the vehicles along the platoon quite well.

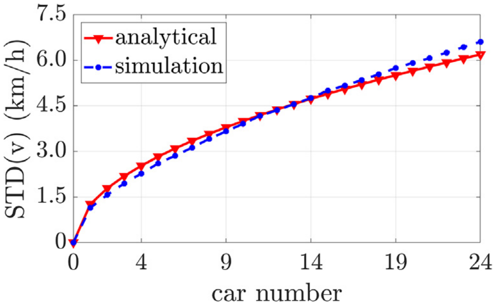

FIG. 5.14 – The standard deviation of speed. Car number 0 is the leading car and the leading vehicle runs at a constant speed of 40 km/h. "analytical" is the results calculated by equation (5.16). "simulation" is the model simulation results. The parameters are $v_{\max} = 80$ km/h, $a = 0.5$ m/s^2, $\tau = 1.1$ s, $\tilde{\sigma} = 0.055$ s, $s_0 = 2.0$ m and $\tilde{\tau}_{\max} = 2.5$ s.

In this section, several different simulations are conducted to investigate the performance of the new model. Firstly, the bottleneck road system is simulated to examine whether the empirically observed congested pattern of traffic flow can be reproduced. Secondly, we investigate the new model's ability to simulate the speed and gap of individual cars in the car following process. Finally, the platoon oscillation evolutions are simulated to examine whether macroscopic characteristics of the car-following platoon, including the concave growth patterns of speed standard deviations and the platoon length, can be quantitatively reproduced. In all simulations, the vehicle length is set as $l_{\text{veh}} = 5$ m.

5.4.1 Empirical Congested Pattern Simulation

There are two different congested patterns in the empirical spatiotemporal traffic flow patterns in NGSIM data, which were collected on a 640 m segment on southbound US 101 in Los Angeles, CA, on June 15th, 2005 between 7:50 am and 8:35 am, see figure 5.15a and b. Figure 5.15a shows that the jams emerge from the congested traffic flow in the bottleneck region and then propagate upstream along the road, while in figure 5.15b, no jams emerge from the congested traffic flow. Chen *et al.* (2012) argued that the rubbernecking in the road median (due to the construction crew) was a likely cause for the formation of oscillations in figure 5.15a, and the rubbernecking zone is located at [320, 420] m.

In the simulation, we consider a road with a length $L_{\text{road}} = 10$ km. The rubbernecking zone is set to be located at $[0.8L_{\text{road}}, 0.8L_{\text{road}} + L_{\text{bottleneck}}]$ with the length $L_{\text{bottleneck}} = 100$ m. When vehicles enter the rubbernecking zone, the drivers have a probability p_{rub} to rubberneck which will lead them to decelerate with a deceleration d_{rub} for h_{rub} second. We also assume that rubbernecking occurs at most once for the drivers in the bottleneck region. The road is initially assumed to be filled with cars that are uniformly distributed with density k and speed $v_{\max}$. The leading car going beyond L_{road}, it will be removed from the simulation. Figure 5.15c and d

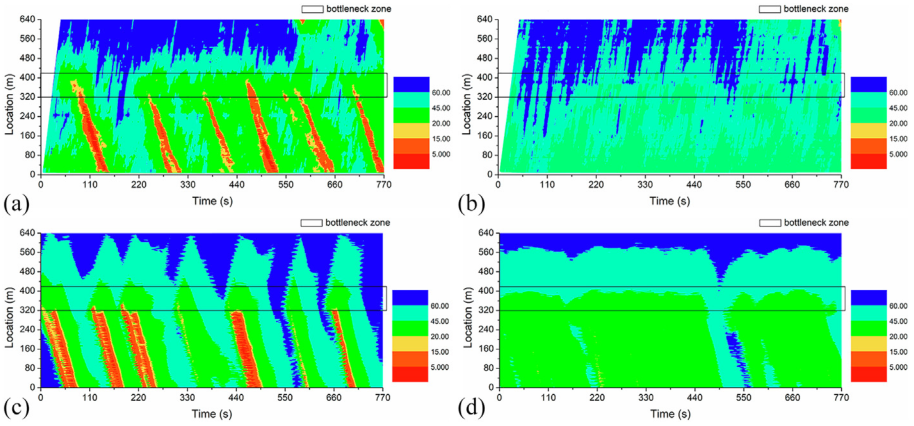

FIG. 5.15 – Empirical spatiotemporal patterns of the velocity on Lane 1 (a) and Lane 5 (b) from the NGSIM trajectory dataset were collected on a 640 m segment on southbound US 101. The simulation of congested traffic flow on an open road with a rubberneck bottleneck with (c) $p_{\text{rub}} = 0.05$, $d_{\text{rub}} = 2.25\ \text{m/s}^2$, $h_{\text{rub}} = 6.0$ s and (d) $p_{\text{rub}} = 0.5$, $d_{\text{rub}} = 0.6\ \text{m/s}^2$, $h_{\text{rub}} = 2.0$ s. The color bar indicates speed (unit: m/s). The parameter values are: $v_{\max} = 80$ km/h, $a = 1.0\ \text{m/s}^2$, $\tau = 1.1$ s, $\tilde{\sigma} = 0.055$ s, $s_0 = 2.0$ m and $\tilde{\tau}_{\max} = 2.5$ s. (c) and (d) shows simulation results only on the 640 m road section in the vicinity of the rubbernecking zone.

show the simulation results of the proposed stochastic Newell model. Specifically, one can see that, figure 5.15c has produced the oscillations observed in figure 5.15a while no oscillation is produced in figure 5.15d, consistent with figure 5.15b.

5.4.2 Vehicle Trajectory Simulation

In this section, the stochastic Newell model is used to calibrate the trajectory of the 5-car-platoon experiments reported in chapter 3. Particularly, we calibrate the inter-vehicle gap. In the calibration process, we use the Genetic Algorithm (GA), and the trajectory of each paired leading-following vehicle is used. In each run, we still consider the Root Mean Squared Error (RMSE) defined in equation (3.11), where the simulated trajectory is generated by the new model. To calibrate each trajectory pair, we perform 200 runs of simulation, and the parameter set that minimizes the RMSE is chosen.

Note that in the 5-car-platoon experiment, each driver experienced 40 oscillations. We randomly choose 20 oscillations for calibration. Data from the other 20 oscillations are used for validation. The calibration and validation results for each driver are shown in table 5.2. One can see that the errors are rather small.

TAB. 5.2 – The calibration and validation results of the stochastic Newell model.

	Calibration		Validation	
	RMSE of spacing (m)	RMSE of velocity (m/s)	RMSE of spacing (m)	RMSE of velocity (m/s)
Veh2	1.5	0.6	2.0	0.6
Veh3	2.8	0.7	2.7	0.8
Veh4	2.0	0.7	2.6	0.7
Veh5	2.6	0.8	3.1	0.8

Figure 5.16 shows two examples of the simulated trajectory. Figure 5.16a shows a calibrated trajectory, in which the leading car completely stops. Figure 5.16b shows a trajectory of validation, in which the leading car decelerates to 10 km/h. The real data and one realization of simulated spacing and speed are plotted as a blue line and a red line, respectively. The corresponding 5%–95% probability band is shown as a gray area. The difference between simulation results and real data is quite small – the RMSE for spacing is 0.69 m and 1.54 m, respectively, and the RMSE for speed is 0.64 m/s, and 0.59 m/s, respectively. These results show that the stochastic Newell model can well reproduce the spacing and speeds of the followers.

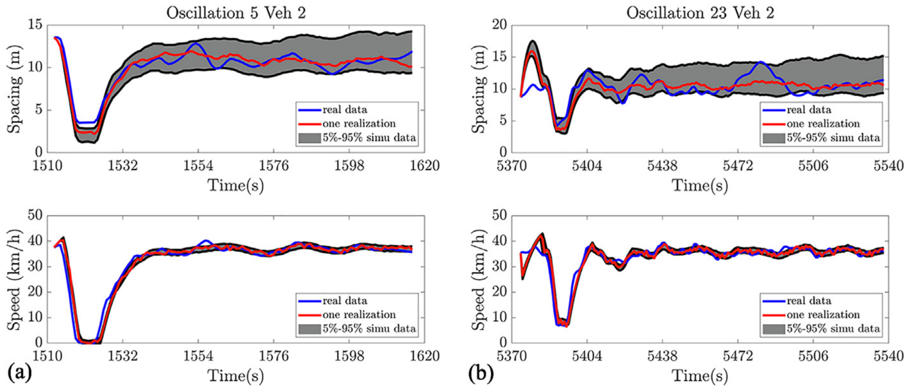

FIG. 5.16 – The spacings and speeds of the simulated vehicle. The parameters are: $v_{\max} = 51.81$ km/h, $a = 1.63$ m/s^2, $\tau = 0.9$ s, $\tilde{\sigma} = 0.025$ s, $s_0 = 2.17$ m and $\tilde{\tau}_{\max} = 2.95$ s.

5.4.3 Platoon Oscillation Simulation

Here we show that the new model can reproduce the concave growth of platoon oscillations. The parameter values are still calibrated by the GA to minimize the averaged RMSE (ARMSE) of inter-vehicle gaps defined in equation (3.11) over the 24 following vehicles using the 25-car platoon experiment data. The data of $v_{\text{leading}} = 40$ km/h are used for calibration. The data of $v_{\text{leading}} = 30$ km/h and 50 km/h are used for validation. The calibrated parameter values are $v_{\max} = 75.47$ km/h, $a = 1.03$ m/s^2, $\tau = 1.4$ s, $\tilde{\sigma} = 0.1$ s, $s_0 = 1.6$ m and $\tilde{\tau}_{\max} = 2.51$ s. The calibration and validation results are shown in table 5.3. One can see that the errors are also rather small.

Tab. 5.3 – The calibration and validation results of the stochastic Newell model and the calibration results of LL model.

	Stochastic Newell model			LL model
	40 km/h	30 km/h	50 km/h	40 km/h
ARMSE of spacing (m)	6.7	4.7	12.4	7.5
ARMSE of velocity (m/s)	0.7	0.6	1.0	0.7
ARMSE of the STD of speed (m/s)	0.1	0.1	0.2	0.7
RMSE of platoon length (m)	22.9	26.2	37.6	50.8

Typical simulation results using the stochastic Newell model are shown in the left panel in figure 5.17. It can be seen that: (1) the simulated speed standard deviation increases in a concave way along the platoon and agrees with the experimental results quite well, see the left plot of figure 5.17a; (2) the platoon length also agrees with the experimental results very well, see the left plot of figure 5.17b; (3) the simulated spatiotemporal patterns (see figure 5.17c) reproduce the stripes in the experimental ones (figure 2.2) denoting oscillations that arise, develop and propagate along the platoon.

Finally, we compare the proposed stochastic Newell model with the LL model. We use only a subset of 25-car platoon data with $v_{\text{leading}} = 40$ km/h to demonstrate that the simulation results of the LL model are quantitatively and qualitatively different from the experimental results. Note that in the LL model, a vehicle will enter the non-equilibrium model once it detects a deceleration wave and that initiates the deviation from Newell's model. In this process, the deceleration wave serves as a trigger but its value is not specified in the LL model. In this paper, we set that as parameters and examine its sensitivity. Specifically, the threshold of a deceleration wave is set as follows. Denote $\delta v = v_n(t - \delta t) - v_n(t)$ as the speed change of vehicle n in a time interval δt. If $\delta v \geq \delta v_c$ and $\delta t \leq \delta t_c$, we assume that vehicle n is experiencing a deceleration wave. Accordingly, once the deceleration wave reaches the follower, vehicle $n + 1$, it will enter the non-equilibrium state with η_{n+1} evolving per the LL model. Note that, if vehicle n experiences multiple deceleration-acceleration cycles in a short time before η_{n+1} completes the prescribed pattern triggered by the first deceleration wave, we assume that η_{n+1} takes its full course to complete the prescribed pattern. This is equivalent to merging the impacts of the multiple deceleration-acceleration cycles in the leader.[20]

---

[20] Note that the car-following behavior under such closely-spaced oscillations was not addressed in the LL model. Our treatment may not be ideal and could decrease the frequency of oscillations reproduced, but we should still be able to see the oscillation formation and propagation.

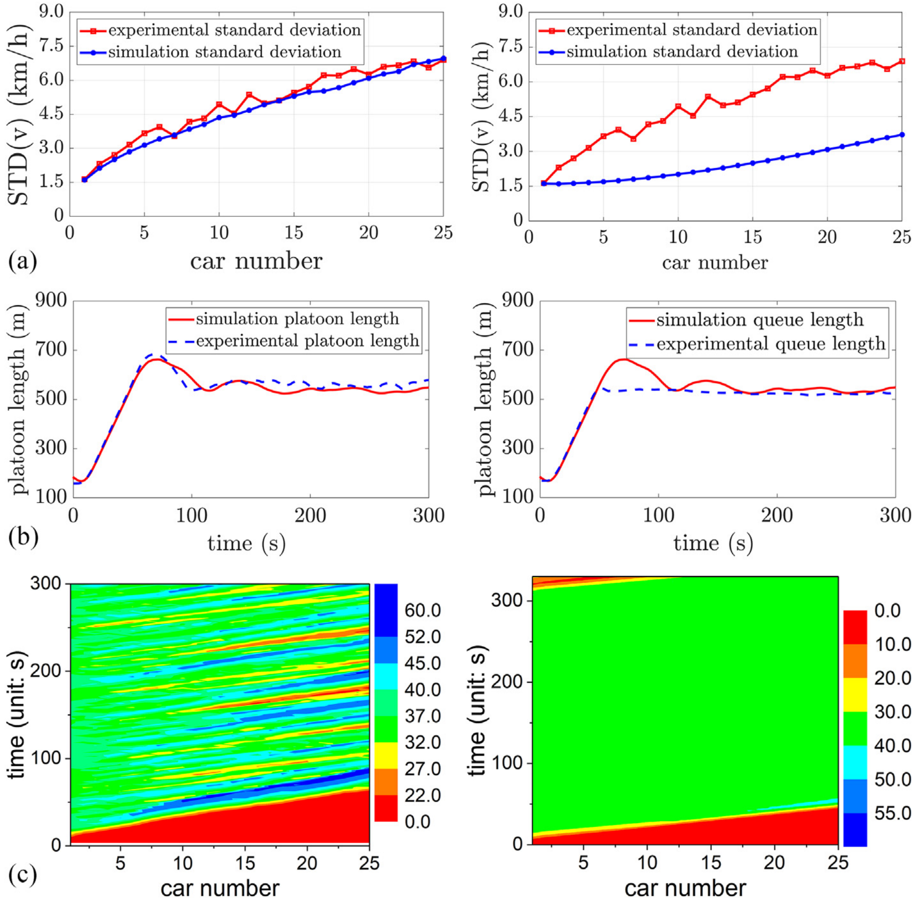

FIG. 5.17 – (a) The standard deviation of speed, (b) the platoon length, and (c) the simulated spatiotemporal diagrams of the stochastic Newell model (left panel) and the LL model (right panel). Car number 1 is the leading car. The leading car moves with $v_{\text{leading}} = 40$ km/h.

In the platoon experiment, the leading car is asked to move at a constant speed. However, since neither the driver nor the cruise control system can control the gas pedal exactly, the speed slightly fluctuates, for example, see figure 5.18.

Notably, for the trigger of the deceleration wave in the LL model, we need the threshold δt_c and δv_c. We found that, in the example of $v_{\text{leading}} = 40$ km/h, when $\delta v_c > 0.9$ m/s, the leading car does not experience any deceleration wave no matter what δt_c is. Thus, no oscillation will develop from the followers. In our simulations, we set $\delta t_c = \tau$, and $\delta v_c = 0.5$ m/s, which are quite sensitive to speed fluctuations. The results from the LL model are shown in the right panel in figure 5.17 and the last column in table 5.3. The other parameters are calibrated by minimizing the ARSME of gaps: $v_{\max} = 68.7$ km/h, $s_0 = 2.48$ m, $\tau = 1.4$ s, $a = 1.83$ m/s^2,

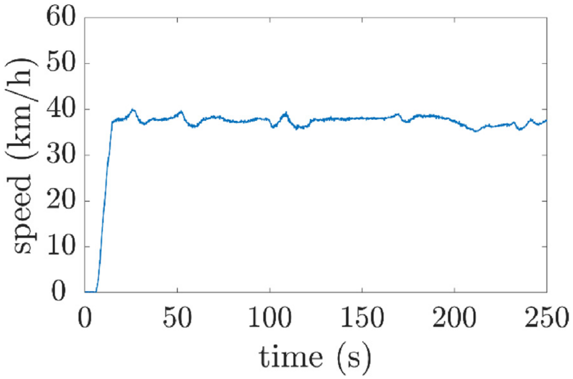

FIG. 5.18 – The example of speed series of the leading car in the platoon experiments with $v_{\text{leading}} = 40$ km/h. Note that the actual velocity of a car is slightly smaller than that shown by the speedometer in the car for safety reasons.

$\eta_n^T = 1.13$, and $\varepsilon = 13$ h^{-1}. One can see that concerning speed standard deviation, there is a significant quantitative difference between the simulation and the experimental results. Moreover, the oscillation grows in a convex way (see figure 5.17b), which is qualitatively different from the experimental finding.

5.5 The Improved 2D-ID Model

Although in section 5.1, we have shown that the 2D-ID model could reproduce the concave grown pattern, however, figure 5.19 shows the flow-density and speed-density diagrams of 2D-IDM, which is formed from the initial homogeneous distribution. The free flow branch ($K < K_c$) and the wide moving jam branch ($K > K_c$) can be identified, while the synchronized flow branch is not reproduced (see figure 5.21 for the comparison). In the free flow branch, vehicles move at the maximum speed with some fluctuations (see figure 5.20a). In the wide-moving jam branch, large localized disturbances emerge from the free flow and propagate in a downstream direction. Then, the speeds of some vehicles fall to zero and the wide moving jams appear, which propagate in the upstream direction (see figure 5.20b). Therefore, the transition reproduced by 2D-IDM is the unrealistic $\text{F} \rightarrow \text{J}$ transition.

We argue that the failure to reproduce the synchronized traffic flow in 2D-IDM can be attributed to the difference between driving behaviors at high speeds and at low speeds has not been considered. In order to keep safety, drivers tend to be more defensive in the high-speed state, in particular under the circumstance that the actual space gap is smaller than the desired space gap. Based on this fact, an improved model based on the IDM (Treiber and Kesting, 2013) is proposed as follows:

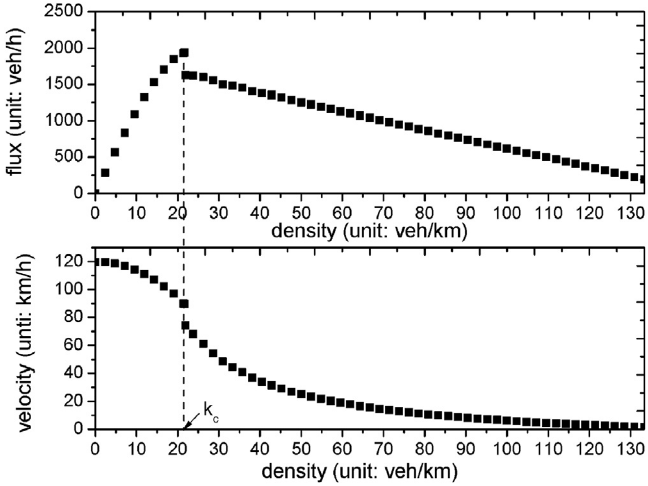

FIG. 5.19 – Flow-density and speed-density diagrams of 2D-IDM. In the simulation, the parameters are set as: $v_{\max} = 120$ km/h, $a_{\max} = 0.73$ m/s^2, $b = 1.67$ m/s^2, $d_0 = 2$ m, $T_1 = 0.5$ s, $T_2 = 1.9$ s, $p = 0.015$, and $L_{\text{veh}} = 5$ m.

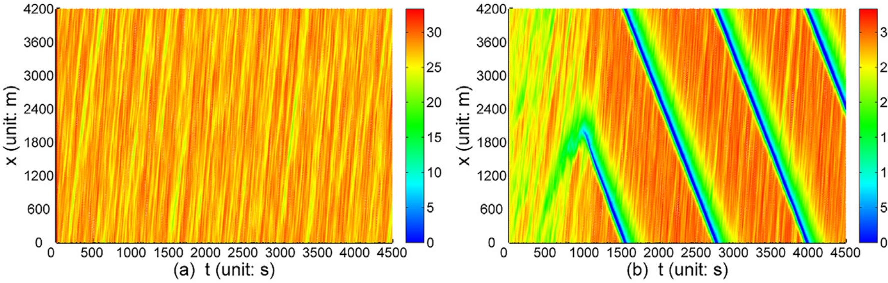

(a) t (unit: s)

(b) t (unit: s)

FIG. 5.20 – The spatiotemporal diagrams of velocities (Unit: m/s) in 2D-IDM on the circular road. In (a, b) the density $k = 19$, 22 veh/km, respectively.

$$
\begin{aligned}
&\text{If} \quad d_{n,\text{desired}}(t) \le d_n(t) \\
&\quad a_n(t) = a_{\max}\left(1 - \left(\frac{v_n(t)}{v_{\max}}\right)^4\right)\left(1 - \left(\frac{d_{n,\text{desired}}(t)}{d_n(t)}\right)^2\right) \\
&\text{else} \\
&\begin{cases}
\text{If } v_n(t) \le v_{\text{c}} \\
\quad a_n(t) = a_{\max}\left(1 - \left(\dfrac{d_{n,\text{desired}}(t)}{d_n(t)}\right)^2\right) \\
\text{else} \\
\quad a_n(t) = \min\left(a_{\max}\left(1 - \left(\dfrac{d_{n,\text{desired}}(t)}{d_n(t)}\right)^2\right), -b\right)
\end{cases}
\end{aligned}
\tag{5.20}
$$

where v_c is the critical velocity. $T(t)$ is still the desired time gap but redefined as:

$$T(t+\Delta t) = \begin{cases} T_1 + rT_2 & \text{if } r_1 < p_1 \text{ and } v_n(t) \leq v_c, \\ T_3 + rT_4 & \text{if } r_1 < p_2 \text{ and } v_n(t) > v_c, \\ T(t) & \text{otherwise.} \end{cases} \tag{5.21}$$

where r and r_1 are still two independent random numbers between 0 and 1. These revisions have considered the situation that when vehicles are at high speeds ($v_n(t) > v_c$), drivers tend to become more defensive. The improved 2D-IDM is abbreviated as 2D-IIDM in the text below.

It is worth mentioning that the two-dimensional regions in the velocity-spacing plane in 2D-IDM and 2D-IIDM are different from that of the Kerner–Klenov model (Kerner and Klenov, 2002) and Kerner–Klenov–Wolf model (Kerner *et al.*, 2002). Drivers do not have preferred spacing in the KK and KKW models. Within the synchronized distance, drivers are not sensitive to the changes in spacing when the velocity differences between vehicles vanish. In contrast, in 2D-IDM and 2D-IIDM, at a given speed, drivers have a preferred spacing. However, the preferred spacing is not fixed, drivers change their preferred spacing either intentionally or unintentionally from time to time.

Firstly, we simulate traffic flow on a circular road and an open road with a bottleneck as one normally tests a traffic flow model. We study whether the synchronized traffic flow and the widening synchronized pattern (WSP) can be simulated or not. Next, car-following behaviors have been simulated to test whether 2D-IIDM can preserve the advantage of 2D-IDM to reproduce the experimental evolution feature of disturbances and the spatiotemporal patterns as revealed in 25-car platoon experiment. In the simulation, the parameters are set as: $v_{\max}$ =120 km/h, $v_c = 50.4$ km/h, $a_{\max} = 0.8$ m/s^2, $b = 1.5$ m/s^2, $d_0 = 2.0$ m, $T_1 = 0.5$ s, $T_2 = 1.9$ s, $T_3 = 0.9$ s, $T_4 = 1.5$ s, $p_1 = p_2 = 0.015$, and $L_{\text{veh}} = 5$ m.

The following two initial configurations are used in the simulations: 1) all vehicles are homogeneously distributed on the road; 2) all vehicles are distributed in a megajam. Figure 5.21 shows the flow-density and velocity-density diagrams of 2D-IIDM. In the branch where the density is smaller than K_1, there is only free flow on the road (figure 5.22a). Compared with that of 2D-IDM, there are two branches in the density region $K_1 < K < K_2$. In this region, the upper branch exhibits the synchronized traffic flow (figure 5.22b), which initiates from the initial homogeneous distribution; the lower branch is the coexistence state of free flow and wide moving jam (figure 5.22c), which comes from the initial megajam. When the density is larger than K_2, the synchronized flow is unstable, and wide moving jams will appear finally. Figure 5.22d shows the spontaneous S → J transition, which is consistent with the observed empirical phenomenon. Therefore, the synchronized traffic flow, the metastable states, and the S → J transition are successfully depicted in 2D-IIDM.

Road bottlenecks include flow-conserving ones (like gradients, a local decrease of the speed limit, local road narrowings inducing a locally increased time gap, and so on) or rubbernecking bottlenecks, and flow-non-conserving ones, such as on-ramps, off-ramps. We consider a rubbernecking bottleneck on an open road

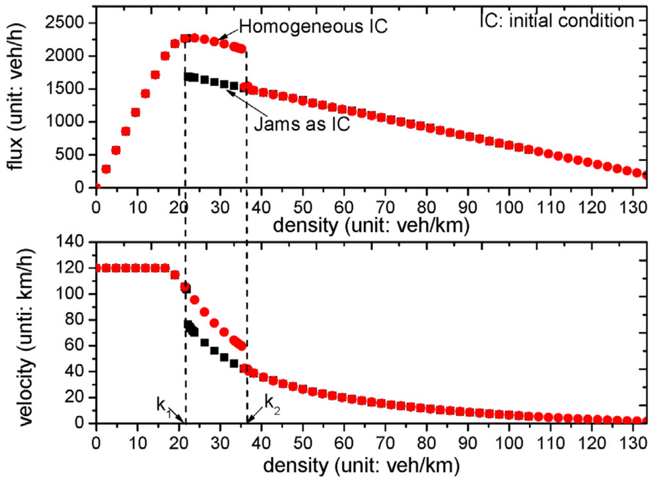

FIG. 5.21 – Flow-density and speed-density diagrams of 2D-IIDM.

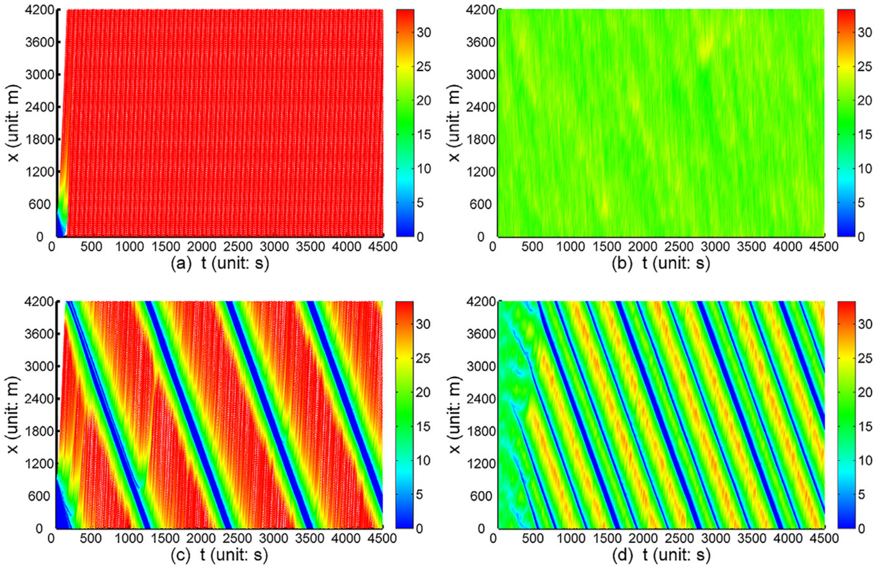

FIG. 5.22 – The spatiotemporal diagrams of velocities (Unit: m/s) in 2D-IIDM on the circular road. From (a) to (d), the density k is 19, 31, 31, 43 veh/km. In (a, c) the traffic starts from a megajam. In (b, d) the traffic starts from a homogenous distribution.

(Chen *et al.*, 2012). It should be noted that any type of flow-conserving bottleneck as well as on-ramp bottlenecks will have the same effect.

The rubbernecking zone is located at $[0.9L_{\text{road}}, 0.9L_{\text{road}} + 300]$m, where the road length $L_{\text{road}} = 700$ km. When vehicles enter this zone, at each simulation time step, they have a probability γ to rubberneck which will cause their speeds to decrease instantaneously by $\varphi\%$. Rubbernecking only can occur at most once in this zone. Initially, the road section is assumed to be filled with vehicles uniformly distributed with density ρ and their velocities are set to $v_{\max}$. For the leading vehicle, it will be removed when it goes beyond L_{road}. The second car becomes a new leading car and it moves freely. At the road section entrance, no vehicle is inserted. This simulation setup is used because a high flow rate cannot be achieved by using the usual boundary setup.

Figure 5.23 presents the simulation results in the road segment $[0.9L_{\text{road}} - 4000, 0.9L_{\text{road}} + 2000]$m. Figure 5.23a shows the spatiotemporal features of the Widening Synchronized flow (WSP), where only the upstream front propagates upstream and no wide-moving jams appear. Figure 5.23b gives the Local Synchronized Pattern (LSP) where the synchronized flow is only localized in the vicinity of the bottleneck region. Figure 5.23c shows the General Pattern (GP) that wide moving jams continuously emerge in synchronized traffic flow. Figure 5.23d shows the Dissolving General Pattern (DGP) that only one wide moving jam emerges in synchronized traffic flow and there is the LSP near the bottleneck region. Therefore, most of the empirical findings, especially the WSP, are successfully simulated by 2D-IIDM.

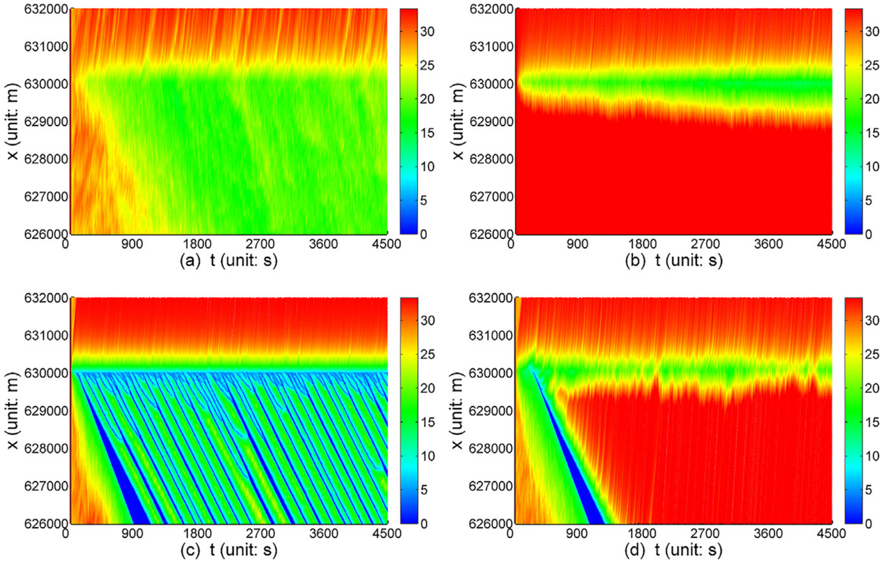

FIG. 5.23 – The spatiotemporal diagrams of 2D-IIDM on an open road with a rubbernecking. (a) $\rho = 22.8$ veh/km, $\gamma = 0.025, \varphi = 2\%$ (WSP), (b) $\rho = 16$ veh/km, $\gamma = 0.04, \varphi = 7\%$ (LSP), (c) $\rho = 22.8$ veh/km, $\gamma = 0.03, \varphi = 30\%$ (GP) and (d) $\rho = 22.8$ veh/km, $\gamma = 0.02, \varphi = 10\%$.

5.6 The E2D-ID Model

To reproduce the experimental findings in section 2.5, the E2D-IDM model is proposed as follows.

$$a_n(t) = a_{\max}\left(1 - \left(\alpha_n(t)\frac{v_n(t)}{v_{\max}}\right)^{\delta} - \left(\frac{v_n(t)\,T_n(t) + d_0 - \frac{v_n(t)\Delta v_n(t)}{2\sqrt{a_{\max}b}}}{d_n(t)}\right)^2\right) \tag{5.22}$$

where $\alpha_n(t)$ is an additional parameter, which is assumed to change over time in each simulation time step as follows.

$$\alpha_n(t) = \begin{cases} \max(1.0, \beta v_n(t) + \gamma) & \text{with the probability } p_1 \\ \alpha_n(t - \Delta t) & \text{otherwise} \end{cases} \tag{5.23}$$

The curve $\alpha_n(t) = \max(1.0, \beta v_n(t) + \gamma)$ decreases with the increase in speed $v_n(t)$ until reaches 1. This roughly means that the first deceleration term in the IDM model is underestimated and the acceleration is thus overestimated at low and intermediate speed. Actually, when $v_n(t)$ is small, $\left(\frac{v_n(t)}{v_{\max}}\right)^{\delta} \approx 0$. Under the circumstance, the role of $\alpha_n(t)$ is not so important. When $v_n(t)$ is in an intermediate range, $\left(\frac{v_n(t)}{v_{\max}}\right)^{\delta} \gg 0$, introducing $\alpha_n(t)$ becomes nontrivial.

In the E2D-IDM, the change of desired time gap $T_n(t)$ is different from that in 2D-IDM, which is set to

$$T_n(t) = \begin{cases} T_1 + \big(T_{2,n}(t) - T_1\big) r_1 & \text{with the probability } p_2 \\ T_n(t - \Delta t) & \text{otherwise} \end{cases} \tag{5.24}$$

$$T_{2,n}(t) = \begin{cases} T_{21} + (T_{22} - T_{21}) r_2 & \text{with the probability } p_3 \\ T_2(t - \Delta t) & \text{otherwise} \end{cases} \tag{5.25}$$

Here r_1 and r_2 are two uniformly distributed random number between 0 and 1. Note that the larger threshold $T_{2,n}$ also changes over time, which is adopted to enhance the intra-heterogeneity of drivers.

In the simulations, we still set $v_{\max} = 30$ m/s, $l = 5$ m. The time step is still $\Delta t = 0.1$ s, other parameters are calibrated. Table 5.4 shows the calibration

TAB. 5.4 – Calibration results of E2D-IDM model.

Parameters	Lower bound	Upper bound	Calibrated
$a_{\max}$	0.5	2.5	0.6296
b	0.5	2.5	1.7963
δ	2.0	4.0	3.7407
d_0	1.0	2.5	2.4722
T_1	0.4	1.0	0.4111
T_{21}–T_1	0.5	1.5	0.5185
T_{22}–T_{21}	2.0	4.0	3.4444
p_2	0	1.0	0.00189
p_3	0	1.0	0.01593
β	−0.2	0	−0.1083
γ	1.5	3.5	2.7500
p_1	0	1.0	0.00028

results. Figures 5.24 and 5.25 show simulation results of the speed standard deviation in the E2D-IDM model, which agrees pretty well with the experimental ones.

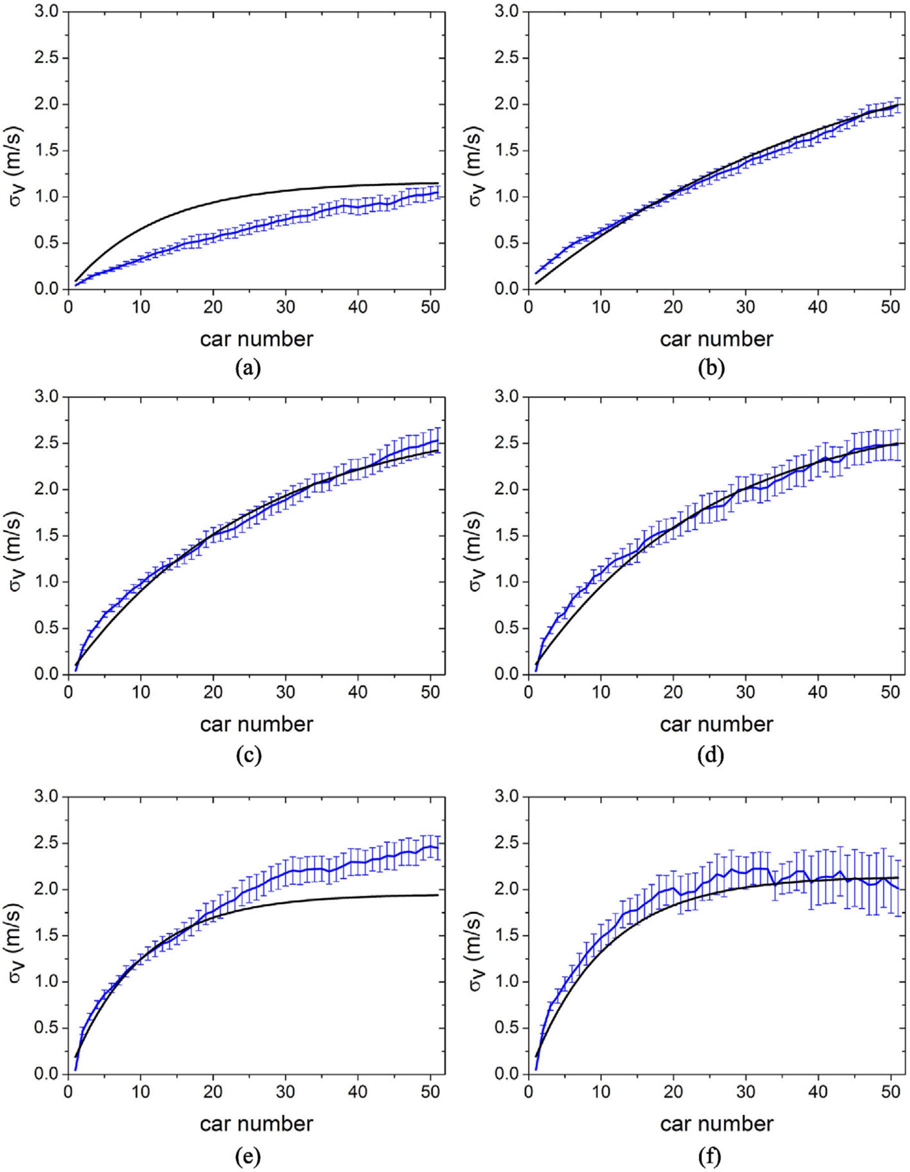

Fig. 5.24 – Standard deviation of velocity of each car at low speed in simulation of E2D-IDM (blue) compared with fitting curve (black). The leading car speed is (a) 5 km/h, (b) 12 km/h, (c) 25 km/h, (d) 30 km/h, (e) 40 km/h, (f) 50 km/h.

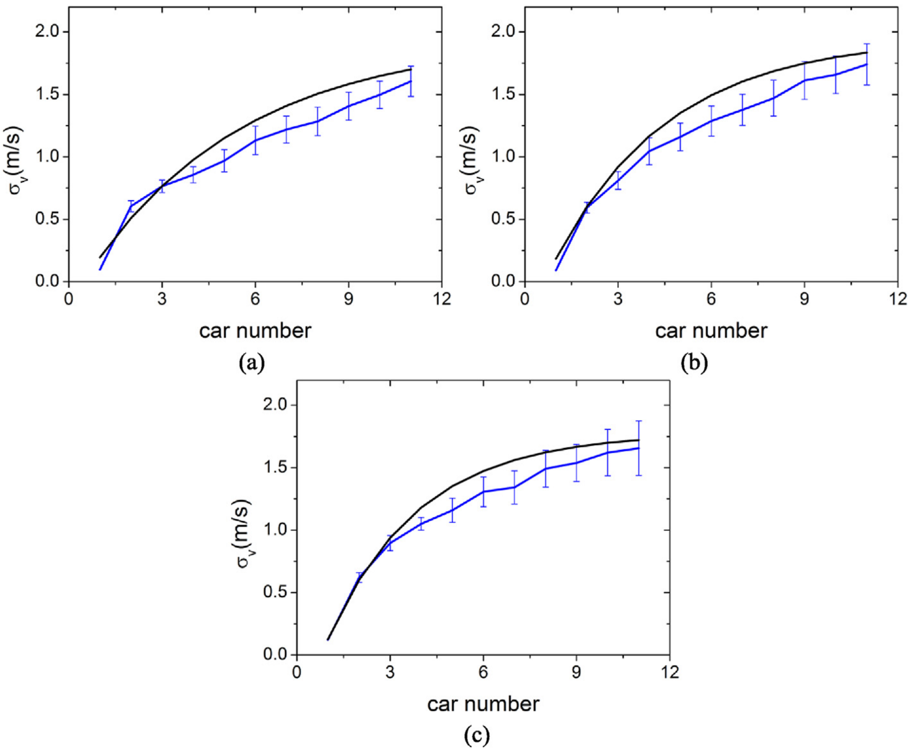

FIG. 5.25 – Standard deviation of velocity of each car at high speed in simulation of E2D-IDM (blue) compared with fitting curve (black). The leading car speed is (a) 60 km/h, (b) 70 km/h, (c) 80 km/h.

References

Allen R.W., Harwood D., Chrstos J.P., Glauz W.D. (2000) *The capability and enhancement of VDANL and TWOPAS for analyzing vehicle performance on upgrades and downgrades within IHSDM.* Turner-Fairbank Highway Research Center.

Chen D., Laval J., Zheng Z., Ahn S. (2012) A behavioral car-following model that captures traffic oscillations, *Transp. Res. B: Method.* **46**, 744-761.

Horiguchi R., Oguchi T. (2014) A study on car following models simulating various adaptive cruise control behaviors. *Int. J. Intell. Transp. Syst. Res.* **12**, 127–134.

Karatzas I., Shreve S.E. (1998) *Brownian motion, Brownian motion and stochastic calculus.* Springer, pp. 47–127.

Kerner B.S., Klenov S.L. (2002) A microscopic model for phase transitions in traffic flow. *J. Phys. A: Math. Gen.* **35**, L31.

Kerner B.S., Klenov S.L., Wolf D.E. (2002) Cellular automata approach to three-phase traffic theory. *J. Phys. A: Math. Gen.* **35**, 9971.

Li X., Peng F., Ouyang Y. (2010) Measurement and estimation of traffic oscillation properties, *Transp. Res. B: Method.* **44**, 1–14.

Treiber M., Kesting A. (2013) Traffic flow dynamics. *Traffic flow dynamics: Data, models and simulation.* Springer-Verlag, Berlin Heidelberg, pp. 983–1000.
Yuan K., Knoop V.L., Hoogendoorn S.P. (2017) A microscopic investigation into the capacity drop: Impacts of longitudinal behavior on the queue discharge rate. *Transp. Sci.* **51**, 852–862.

Appendix

Since $\frac{d\tilde{\tau}_n}{dt} = \xi_n$, the distribution of $\varsigma_n(t) = \tilde{\tau}_n(t+\tau) - \tilde{\tau}_n(t) = \int_t^{t+\tau} \xi_n(s)\,ds$ follows the normal distribution with the mean and variance:

$$\mu_n^{\varsigma} \triangleq \mathrm{E}\left(\int_t^{t+\tau} \left(\xi_n(0)e^{-\alpha s} + \sigma \int_0^s e^{-\alpha u}\,dW_n(u)\right)ds\right) = \frac{\xi_n(0)}{\alpha}\left(e^{-\alpha t} - e^{-\alpha(t+\tau)}\right) \tag{A1}$$

$$\left(\sigma_n^{\varsigma}\right)^2 \triangleq \sigma^2 E\left(\int_t^{t+\tau} \int_0^s e^{-\alpha u}\,dW_n(u)\,ds\right)^2 \tag{A2}$$

Denote $Y(t) \triangleq \int_0^t e^{-\alpha u}\,dW_n(u)$, Ito's rule (Karatzas and Shreve, 1998) implies that

$$\int_t^{t+\tau} Y(s)\,ds = (t+\tau)Y(t+\tau) - tY(t) - \int_t^{t+\tau} se^{-\alpha s}\,dW_n(s) \tag{A3}$$

Then we have,

$$\begin{aligned}\left(\sigma_n^{\varsigma}\right)^2 &= \sigma^2 \mathrm{E}\left((t+\tau)Y(t+\tau) - tY(t) - \textstyle\int_t^{t+\tau} se^{-\alpha s}\,dW_n(s)\right)^2 \\ &= \sigma^2 \left(\begin{array}{l} (t+\tau)^2 E(Y(t+\tau))^2 + t^2 E\left(\int_0^t e^{-\alpha s}\,dW_n(s)\right)^2 + E\left(\int_t^{t+\tau} se^{-\alpha s}\,dW_n(s)\right)^2 \\ -2(t+\tau)E\left(\int_0^{t+\tau} e^{-\alpha s}\,dW_n(s) \int_t^{t+\tau} se^{-\alpha s}\,dW_n(s)\right) \\ -2t(t+\tau)E\left(\int_0^{t+\tau} e^{-\alpha s}\,dW_n(s) \int_0^t e^{-\alpha s}\,dW_n(s)\right) \\ +2tE\left(\int_0^t e^{-\alpha s}\,dW_n(s) \int_t^{t+\tau} se^{-\alpha s}\,dW_n(s)\right) \end{array}\right)\end{aligned} \tag{A4}$$

Since the quadratic variation of Brownian motion $(W(t))$, denoted by $\langle W(t), W(t)\rangle$, is time t, and $W^2(t) - t$ is a martingale, we have,

$$E\left(\int_t^{t+\tau} e^{-\alpha s}\,dW_n(s)\right)^2 = \int_t^{t+\tau} e^{-2\alpha s}\,\mathrm{d}s \tag{A5}$$

$$E\left(\int_t^{t+\tau} se^{-\alpha s}\,dW_n(s)\right)^2 = \int_t^{t+\tau} s^2 e^{-2\alpha s}\,\mathrm{d}s \tag{A6}$$

$$E\left(\int_t^{t+\tau} e^{-\alpha s} dW_n(s) \int_t^{t+\tau} s e^{-\alpha s} dW_n(s)\right) = \int_t^{t+\tau} s e^{-2\alpha s} d\mathrm{s} \tag{A7}$$

$$E\left(\int_0^{t} e^{-\alpha s} dW_n(s) \int_t^{t+\tau} s e^{-\alpha s} dW_n(s)\right) = 0 \tag{A8}$$

Hence,

$$\left(\sigma_n^{\varsigma}\right)^2 = \sigma^2\left(\frac{\tau^2}{2\alpha} - \frac{\tau e^{-2\alpha t}}{2\alpha^2} + \frac{e^{-2\alpha t} - e^{-2\alpha(t+\tau)}}{4\alpha^3}\right) \tag{A9}$$

Since $t \gg 1$ in the simulation, we can let

$$\mu_n^{\varsigma} \approx 0 \tag{A10}$$

$$\sigma_n^{\varsigma} \approx \frac{\tau\sigma}{\sqrt{2\alpha}} \tag{A11}$$

to simplify the model. Furthermore, since $\tilde{\tau}_n(t)$ is bounded by $\tilde{\tau}_{\min}$ and $\tilde{\tau}_{\max}$, therefore, $\tilde{\tau}_n(t)$ is updated by $\tilde{\tau}_n(t+\tau) = [\tilde{\tau}_n(t) + \varsigma_n(t)]_{\tilde{\tau}_{\min}}^{\tilde{\tau}_{\max}}$ and $\varsigma_n(t) \sim N\left(0\frac{\tau\sigma}{\sqrt{2\alpha}}\right)$.

Chapter 6

Outlook

There are several directions of this book that can be enhanced by future research, which are listed below.

I. For the data acquisition and analysis

(1) Whether the synchronized flow could coexist with free flow. Models that can simulate the synchronized flow can be divided into two types, *i.e.*, the one that can simulate the coexistence of synchronized flow and free flow and the one that cannot. However, up to now, it is still unknown whether the coexisting state does exist in reality.

(2) The hysteresis phenomenon. Up to now, the hysteresis phenomenon is analyzed by the macroscopic traffic flow data or the short-time vehicle trajectories. For the macroscopic traffic flow data, it is hard to clarify behind behavioral mechanism, which is also overshadowed by the driving stochasticity when the short-time vehicle trajectories were applied. Therefore, long-time vehicle trajectories are necessary to pin down the subject.

(3) The analysis and modeling of driving behavior in a high-speed state. Due to the fast speed, driving at high speed has higher requirements for the driver's response-ability, concentration, driving habits and driving methods. The driving behavior of drivers at high speeds is also different from that of low and medium speeds. But the trajectory data used for analysis at present are mostly collected at low or medium speeds, and there is little trajectory data in high speed. Therefore, on the basis of collecting the trajectory data at high speeds, the following behavior in high speed and the following behavior at the transition from high speed to low speed are worth studying.

II. For the cellular automaton models

(1) In real traffic flow, with the increase of the density, the free flow branch bends downward. The lowest speed in the free flow can be as low as 70–80 km/h. However, in the cellular automaton models, the free flow branch is almost a straight line. The lowest speed in free flow is very close to the maximum speed. Therefore, how to

DOI: 10.1051/978-2-7598-3193-7.c006
© Science Press, EDP Sciences, 2023

capture the feature of the free flow branch is a common task for cellular automaton modeling.

(2) Most, if not all, cellular automaton models that can describe synchronized traffic flow reasonably well have very small cell sizes of 1.5 m (5 cells per vehicle), or even 0.5 m. In a way, this counteracts the very cellular automaton idea of abstraction of all the dynamics to very small integers. Instead, with 20 or more different speed levels and 5 cells per vehicle, one could say that these models resemble more a coarse-grained conventional car-following model with discrete update time (iterated map) than a cellular automaton although, conceptionally, they are still cellular automata. Therefore, how to develop a classic cellular automaton with only one cell per vehicle describing all three phases and having realistic propagation velocities of information, particularly traffic waves, is also challenging.

(3) The rules of many models are usually based on behavioral assumptions. The data validation and justification of these assumptions are absent. Furthermore, there are many other important driving behaviors that should be considered and their impacts on traffic flow worth to be investigated, such as risk driving and distraction.

III. For the car following models

(1) The driving behavior analysis and modeling in various traffic environment. Driving behavior is greatly affected by the external environment. While driving, drivers will rely on vision and hearing to obtain traffic environment information and make corresponding responses. Therefore, in different traffic environments, such as different visibility, different road slope and curvature, the driving behavior may be different. The trajectory data applied in this book are collected under normal conditions (straight road, circular road, normal weather conditions), but there is still a lack of trajectory data under some other traffic environments (such as roads with slopes, or in the rain, snow or fog condition, etc.), Therefore, the analysis and modeling of driving behavior in unconventional traffic environment is of great significance for a comprehensive understanding of driving behavior.

(2) The driving behavior analysis and modeling considering the physiological and psychological characteristics of drivers. The driver is a life body with independent personal physiological characteristics and complex psychological behaviors. During driving, many external factors will affect the driver's psychology and physiology, which will lead to a change in driving behavior. For example, if the driver is stimulated and becomes nervous, a series of physiological reactions such as breathing aggravation and heart rate acceleration will appear, and psychological changes such as distraction and decline in judgment will appear, which will eventually lead to a change of driving behavior. At present, the study of driving behavior is mainly from the vehicle driving index, such as speed and acceleration, the impact of the driver's physiological and psychological characteristics on driving behavior is ignored. With the development of data acquisition technology, more and more researchers began to organize real vehicle platoon experiments and collect trajectory data with GPS

equipment. For such research, because the participants are controllable, it provides the possibility to collect the physiological and psychological data of drivers. Therefore, if researchers collect the driver's physiological and psychological characteristics variables while collecting the vehicle trajectory, and further consider the physiological and psychological characteristics in the driving behavior analysis and modeling, will make the driving behavior simulation model more humanized.

(3) Models based on machine learning and other data-based methods. In recent years, with more and more driving trajectory data collected, the application of machine learning and data mining technology in traffic flow modeling is becoming more and more popular. However, the main achievements are based on the black box models, few of which consider the behavioral characteristics of the car following behavior. It is worth studying to build a data simulation model that incorporates behavioral characteristics.